Fine structure in $d-f$ and $f-f$ transitions of Tm^{3+} and systematic investigation of $3d^5 - 3d^4 4s$ absorption of Mn^{2+} doped fluorides

DISSERTATION

zur Erlangung des Doktorgrades

des Fachbereichs Physik der

Universität Hamburg

vorgelegt von

Marcus True

aus Friedrichshafen

Hamburg
2004

Gutachter der Dissertation	Prof. Dr. G. Zimmerer
	Prof. Dr. G. Huber
Gutachter der Disputation	Prof. Dr. G. Zimmerer
	Dr. S. Kück
Dekan des Fachbereichs Physik	Prof. Dr. G. Huber
Vorsitzende des Promotionsausschusses	Prof. Dr. C. Hagner
Datum der Disputation	22.10.2004

Abstract

Research on novel luminescent materials applicable in efficient mercury-free discharge lamps has been motivated in line with a joint cooperation between industry and universities. In the framework of this BMBF project photoluminescence spectroscopy of rare earth (RE) and transition metal ion doped fluoride crystals has been performed in order to characterize luminescence and energy transfer processes.

$LiCaAlF_6$ (LiCAF) single crystals, singly and co-doped with Tm^{3+} and Mn^{2+}, have been successfully grown by Czochralski technique and investigated spectroscopically in the vacuum-ultraviolet (VUV) to visible spectral region using synchrotron radiation, F_2 operated excimer laser, and supplementary techniques. The iso-structural $LiSrAlF_6$ (LiSAF) compounds have been obtained by solid state reaction. However, the doping concentrations of the Tm^{3+} and Mn^{2+} doped LiCAF and LiSAF compounds are surprisingly low (of the order 0.01%), being close to the detection limit of the trace analysis. This fact imposes severe restraints on the prospective energy transfer in these hosts.

On the other hand, the optically thin crystals are well suited for absorption and excitation spectroscopy of the (partially) allowed inter-configurational $4f^{11}5d \rightarrow 4f^{12}$ transition of Tm^{3+}. A rich fine structure, mainly consisting of electronic and vibronic lines, is observed in high resolution emission spectra due to transitions to the Stark levels in the crystal field. The splitting of the ground state is determined, and zero-phonon lines of $f \rightarrow f$ transitions are assigned. Supplementary results have been obtained for BaY_2F_8:Tm^{3+}. Fine structure in $d \rightarrow f$ emission spectra has been revealed in the respective hosts for the first time.

The substitutional lattice sites and corresponding charge compensation of Tm^{3+} in LiCAF and LiSAF were investigated by analyzing the fine structure in emission as well as in excitation, being in agreement with the theoretical results of defect and rare earth doping studies in the respective hosts. Drastic differences have been observed in high resolution emission spectra due to $f \rightarrow f$ transitions excited via the $4f^{11}5d$ states (with excimer laser) compared to those excited via the $F^- \rightarrow Tm^{3+}$ charge transfer state at our setup.

A series of Mn^{2+} doped fluoride samples, namely LiCAF, LiSAF, $BaMgF_4$, $KMgF_3$, and MgF_2, has been analyzed in terms of $3d^5 \rightarrow 3d^5$ transitions and intense absorption bands due to $3d^5 \rightarrow 3d^4 4s$ transitions in the VUV spectral region. The oscillator strengths of these bands in LiCAF:Mn^{2+} are determined from absorption spectroscopy in good agreement with sparse values from the literature.

For the first time a systematic analysis of Mn^{2+} in fluorides using synchrotron radiation is presented, associating the observed peaks due to $3d^5 \rightarrow 3d^4 4s$ transitions with the corresponding sub-levels of the crystal field splitted ground state. The influence of the local symmetries of different substitutional lattice sites is demonstrated.

Kurzfassung

Forschung an neuen Leuchtstoffen zur Anwendung in effizienten, quecksilberfreien Entladungslampen wurde durch ein Verbundprojekt zwischen Industrie und akademischen Instituten motiviert. Im Rahmen dieses BMBF-Projekts wurde Photolumineszenz-Spektroskopie an Fluoridkristallen dotiert mit *Seltenen Erd-* (RE) und *Übergangsmetall*-Ionen zur Charakterisierung der Lumineszenz- und Energietransfer-Prozesse durchgeführt.

$LiCaAlF_6$ (LiCAF) Einkristalle einfach und ko-dotiert mit Tm^{3+} und Mn^{2+} konnten erfolgreich mit dem Czochralski-Verfahren gezogen werden, und spektroskopisch im Vakuumultraviolettem (VUV) bis sichtbaren Bereich mit Synchrotronstrahlung, F_2 betriebenem Exzimerlaser, und ergänzenden Methoden untersucht werden. Proben von $LiSrAlF_6$ (LiSAF) mit gleicher Kristallstruktur wurden mittels Festkörperreaktion hergestellt. Die Konzentrationen der Tm^{3+} und Mn^{2+} dotierten LiCAF und LiSAF Proben sind erstaunlich niedrig (von der Größenordnung 0.01%), nahe der Nachweisgrenze der durchgeführten Spurenanalyse. Dies impliziert drastische Einschränkungen bezüglich des Energietransfers in den Wirtsgittern.

Andererseits sind die optisch dünnen Kristalle gut geeignet zur Untersuchung mit Absorptions- und Anregungsspektroskopie der (teils) erlaubten interkonfiguralen $4f^{11}5d \rightarrow 4f^{12}$ Übergänge in Tm^{3+}. Eine vielfältige Feinstruktur, bestehend aus elektronischen und vibronischen Linien, wurde in den hochaufgelösten Emissionsspektren beobachtet, resultierend aus den Übergängen zu den Stark-Niveaus im Kristallfeld. Die Aufspaltung des Grundzustandes in LiCAF:Tm^{3+} wurde ermittelt, und Nullphononen-Linien konnten den $f \rightarrow f$ Übergängen zugeordnet werden. Ergänzende Resultate wurden für BaY_2F_8:Tm^{3+} erzielt. Erstmals wurde Feinstruktur in den $d \rightarrow f$ Emissionsspektren der entsprechenden Wirtsgitter nachgewiesen.

Der bevorzugte Einbauplatz und die damit verbundene Ladungskompensation von Tm^{3+} in LiCAF und LiSAF folgt aus der Analyse der Feinstruktur in Emissions- und Anregungsspektren, in guter Übereinstimmung mit den Resultaten einer theoretischen Untersuchung der Defektbildung von RE in den entsprechenden Kristallen. Drastische Unterschiede wurden in den hochaufgelösten $f \rightarrow f$ Spektren beobachtet, jeweils angeregt über die d Niveaus (mit Exzimerlaser) bzw. den $F^- \rightarrow Tm^{3+}$ Ladungstransfer an unserem Messplatz.

Eine Reihe von Mn^{2+} dotieren Fluoridkristallen, nämlich LiCAF, LiSAF, $BaMgF_4$, $KMgF_3$ und MgF_2, wurden hinsichtlich der $3d^5 \rightarrow 3d^5$ Übergänge und der starken Absorptionbanden im VUV Spektralbereich untersucht, die $3d^5 \rightarrow 3d^4 4s$ Übergängen zugeordnet wurden. Die Oszillatorenstärken dieser Bänder in LiCAF:Mn^{2+}, bestimmt aus den Absorptionsspektren, sind in guter Übereinstimmung mit den wenigen Werten aus der Literatur.

Erstmals wurde eine systematische Analyse mit Synchrotronstrahlung von Mn^{2+} in Fluoriden präsentiert, welche die beobachteten Banden $3d^5 \rightarrow 3d^4 4s$ Übergängen von den jeweiligen Unterniveaus des im Kristallfeld aufgespaltetem Grundzustandes zuordnet. Der Einfluß der lokalen Symmetry der verschiedenen Einbauplätze wurde nachgewiesen.

Contents

List of Figures

List of Tables

Chapter 1

Introduction

1.1 Motivation

As conventional Cathode Ray Tube (CRT) monitors slowly fade from the mass market, alternatives to the currently popular Liquid Crystal Displays (LCD) are heavily investigated. Besides displays employing polymer or organic phosphors, Plasma Display Panels (PDP) have been developed relying on a mercury discharge similar to energy saving lamps [JUE00].

The demand for energy saving, environmentally compatible lighting sources is not accounted for by conventional energy saving lamps. The essential discharge, which requires the presence of a small amount of mercury, imposes an environmental hazard which the consumer is not aware of. Since only one UV photon of high energy is converted into one visible photon [RON02], the overall energy efficiency is with 30% close to the maximum achievable by this process including energy losses in the discharge. Furthermore the slow warm-up period necessary to evaporate the mercury is a limitation which prevents applications requiring rapid response times, e.g. break or flash lights and photocopier machines.

One approach to obtain efficient phosphor materials is based on the concept of photon cascade emission (down conversion, quantum cutting). The high energy of photons resulting from a rare gas discharge can be converted into two visible photons, which would double the quantum efficiency and dispose of the mercury. Experimentally, an internal quantum efficiency of 195% has been demonstrated in $LiGdF_4:Eu^{3+}$ under selective excitation [WEG99a, WEG99b], however, the external efficiency achieved was merely 32% [FEL01].

New luminescent materials are required. The pure rare gas discharge of Xenon emits light at predominantly 172 nm with a discharge efficiency comparable to that of mercury. However, the conventional phosphors have to be replaced since a wide transparency is needed up to the vacuum-ultraviolet (VUV). Fluorides are a good choice over the conventional oxides whose bandgap is usually too small. Special attention has to be paid to the stability against degradation under irradiation. In this respect oxides are often advantageous over fluorides.

Research focused on the energy levels in the VUV spectral region requires a specialized experimental setup. The unique *Superlumi* station [ZIM91] at HASYLAB, DESY, Germany, allows time-resolved photo-luminescence spectroscopy with synchrotron radiation in the VUV-visible spectral region at high resolution and is therefore well-suited for this purpose. Thus, the search for efficient energy transfer via down conversion in Tm^{3+} and Mn^{2+} co-doped fluorides has been motivated in line with the BMBF project "VUV Leuchtstoffe für quecksilberfreie Entladungslampen", a research collaboration for finding evidence of efficient lighting materials based on mercury-free discharge.

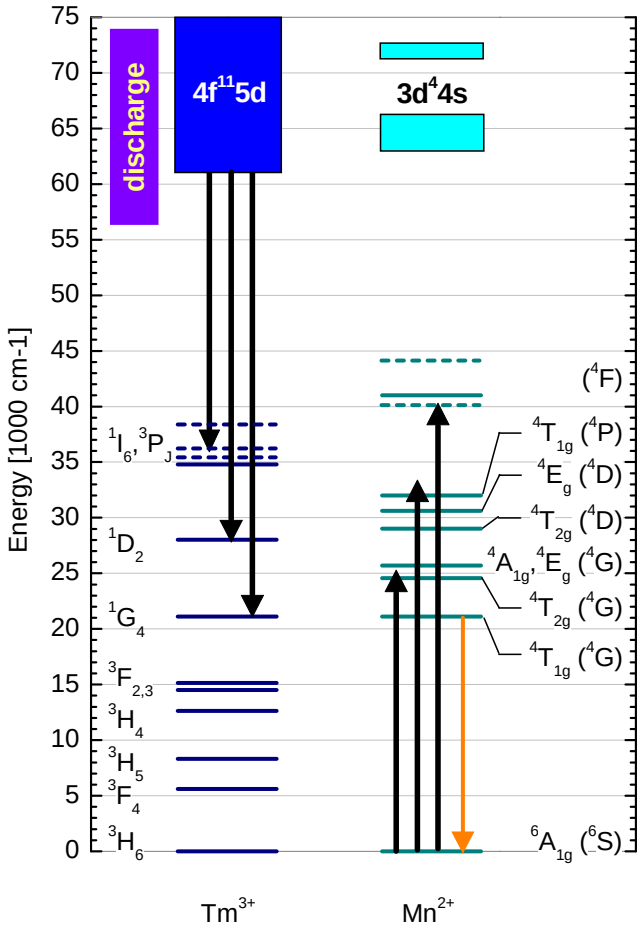

Figure 1.1: Prospective energy transfer scheme of Tm^{3+} and Mn^{2+} ions. The energy levels are those of $LiCaAlF_6$ determined in this work.

The Tm^{3+} ion has a similar energy level structure as Pr^{3+} which has been shown to exhibit high quantum efficiencies in many hosts [KUE03]. The $4f^{12}$ and $4f^{11}5d$ energy levels of Tm^{3+}

are shifted to higher energies, and as opposed to Pr^{3+} a low quantum efficiency is expected for transitions only within the $4f$ configuration in singly doped crystals [PIP74, SOM74].

Therefore inter-ionic energy transfer between Tm^{3+} and transition metals such as Mn^{2+} is a prospective possibility. Up to now energy transfer between rare earth and transition metal ions has been observed in the red or IR spectral region, e.g. from Cr^{3+} to Tm^{3+} [ARM89a, ARM89b] used in high-power laser systems based on Cr^{3+}, Tm^{3+}, Ho^{3+} (CTH) in YAG [QUA90, BEC92] having a quantum efficiency of nearly two.

Czochralski grown $LiCaAlF_6$ (LiCAF) single crystals, which possess an extraordinary large band gap up to 89 300 cm^{-1} (down to 112 nm), have been chosen as primary host to be investigated in this thesis along with the iso-structural $LiSrAlF_6$ and various other fluorides. The divalent Ca^{2+} and trivalent Al^{3+} lattice sites offer many prospective possibilities for co-doping with rare earth and transition metal ions.

Figure 1.1 shows possible energy transfer schemes within Tm^{3+} and Mn^{2+} co-doped fluorides, the energy level positions are those of LiCAF:Tm^{3+} and LiCAF:Mn^{2+} determined in this work. The noble gas discharge is overlapping very well with strong $4f^{12} \rightarrow 4f^{11}5d$ absorption of Tm^{3+}, which relaxes non-radiatively to the lowest $5d$ state after excitation. Emission due to the spin-forbidden $d \rightarrow f$ transition is observed with a lifetime of at least 1 μs, while the fast, spin-allowed component is not identified. It may be of low intensity and hidden in the background noise due to the very low doping concentration of Tm^{3+} analyzed.

Thus, the long-living spin-forbidden state would be well-suited as starting level for a cross relaxation energy transfer to Mn^{2+} as indicated by wide arrows. Subsequently, emission predominantly in the visible due to $f \rightarrow f$ transitions in Tm^{3+} as well as a due to intra-configurational $^4T_{1g}(G) \rightarrow {}^6A_{1g}$ transition of Mn^{2+} in the visible is expected at internal quantum efficiency higher than 100%.

The unintended and surprisingly low doping concentrations in the LiCAF and LiSAF samples put severe restraints on possible energy transfer. On the other hand, the optically thin samples are well suited for absorption and excitation spectroscopy of the (partially) allowed inter-configuration transition of Tm^{3+} and Mn^{2+}.

Furthermore, strong absorption bands of Mn^{2+} in the VUV region have been observed which are rarely discussed in the literature. A detailed investigation along with the $3d^5$ levels in various fluorides has been performed to gain deeper insight into the nature of these VUV bands, deciding on the prospective transfer applicability of Mn^{2+}. Therefore, the pure and singly doped compounds are analyzed in terms of the energy level structure and energy transfer processes until final conclusions on the co-doped systems are drawn.

1.2 Rare earth elements

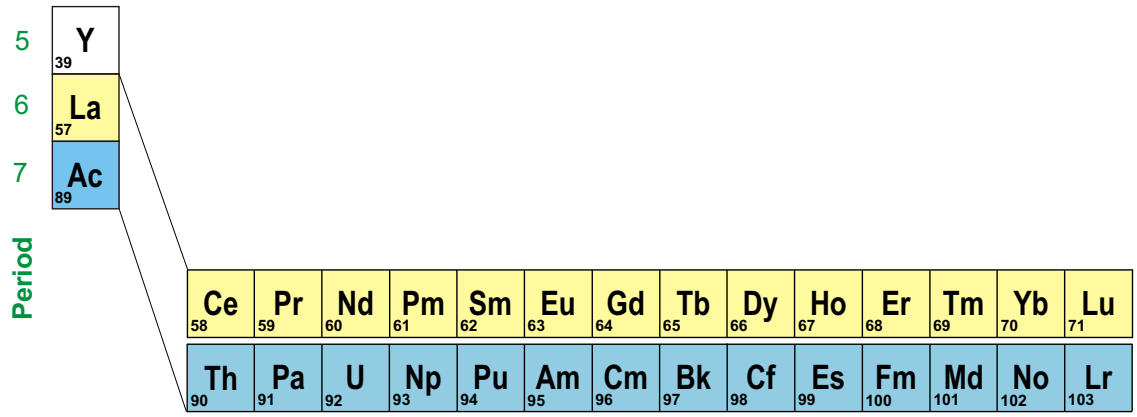

Figure 1.2: The rare earth elements in the Periodic Table of Elements.

The rare earth (RE) elements have been discovered in 1787, when Lieutenant Carl Axel Arrhenius (1757-1824) found in the dumps of the Ytterby quarry on the island of Roslaga near Stockholm (Sweden) an exceptionally heavy piece of black rock, which he called yttria. This stone was sent to, among others, Johan Gadolin (1760-1852), professor at Åbo University, who suspected that a new element was contained in the sample. More than a century passed by until all RE elements were separated from the original oxides [KRO03, GRE98].

The lanthanide series (elements 57 to 71) and the actinide series (elements 89 to 103) as well as Yttrium are shown in Figure 1.2. Both series are located in the Periodic Table of Elements (Appendix B) in group 3 and the 6^{th} ($4f5d$ electronic configuration) and 7^{th} ($5f6d$) period. The terms *rare earths* and *lanthanides* are used for describing elements 57 to 71 inclusively, which is more common than the pedantically more appropriate term *lanthanoides*. According to the latest IUPAC (`http://www.chem.qmul.ac.uk/iupac/`) recommendation, both terms are endorsed. Scandium is chemically different and does not occur naturally with the other elements, therefore it is usually not included.

In fact the rare earths are not particularly rare, but prior to 1945 long and tedious processes were required to purify the metals from their oxides. Ion-exchange and solvent extraction processes are used today to produce 99.999% pure (5N) low-cost RE. Their abundance in the earth's crustal rocks ranges from cerium (the 25^{th} most abundant element with 60 ppm) to thulium and lutetium (0.4 ppm), which is still more common than antimony or thallium. Several of the lanthanides form during the fission of uranium and plutonium.

The RE ions have many scientific and industrial applications in optics (Section 1.4). Their compounds are used as catalysts in the production of petroleum and synthetic products. Rare

earths are used in lamps, lasers, scintillators, phosphors, permanent magnets (neodymium, dysprosium, samarium), rechargeable batteries (lanthanum), automotive catalysts (cerium), and many other applications. A pyrophoric mixed rare-earth alloy called *Mischmetall* (50% Ce, 25% La, 25% other light lanthanides) combined with 30% iron has been discovered in 1903 to make flints for cigarette lighters. The addition of <1% *Mischmetall* or lanthanide silicides improves the strength and workability of low alloy steels.

1.2.1 Rare earth resources

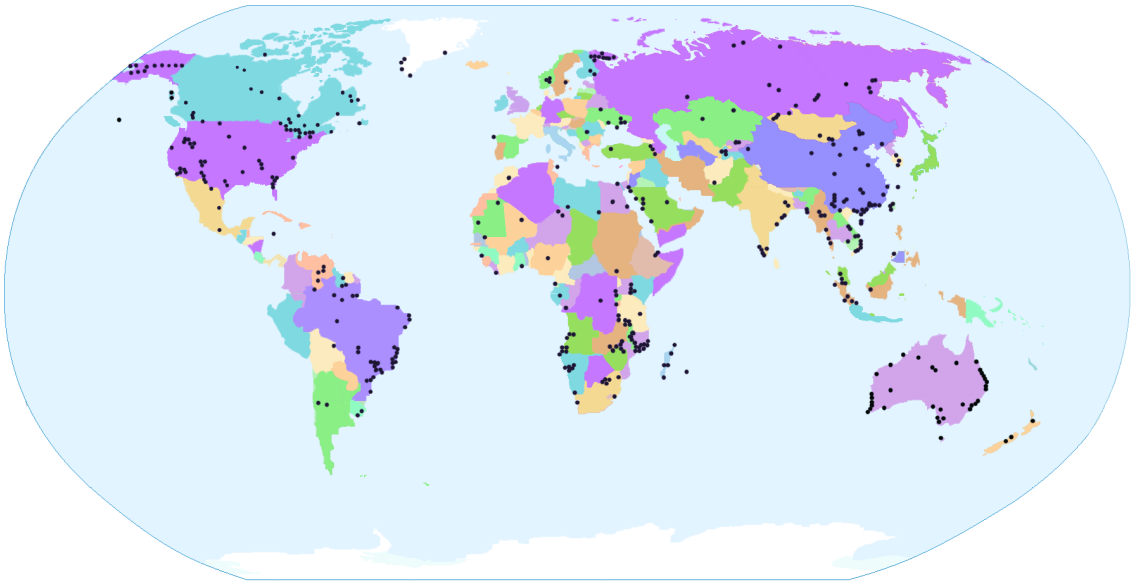

Figure 1.3: Rare earth mines, deposits, and occurrences world wide are shown as black dots, adopted from [ORR02].

Rare earth elements naturally occur in minerals like monazite and others, which are found in numerous sites around the world (Figure 1.3). China has the biggest world deposit of RE minerals discovered so far with more than 43 million (metric) tonnes, followed by Russia with 19 million tonnes, the United States with 13 million tonnes, and Malawi (Africa) with over 11 million tonnes. Detailed data of 848 mines, deposits, and occurrences world wide is tabulated in [ORR02].

The overall production increased from 1000 tonnes per year at the beginning of the 20^{th} century to 16 000 tonnes in 1966. At this time prices dropped significantly. At the end of the 20^{th} century 80 000 tonnes are produces world wide [FRA00, HED00]. However, the consumption decreased by a factor of two since 1990, mainly because the industry changed to fluid-cracking catalysts that contain significantly less rare earths.

1.2.2 Properties of rare earths

Rare earth elements possess a number of similar chemical properties, which made them hard to distinguish and to separate in former times. They are relatively soft silver-like or gray metals, which are highly conductive, malleable, and ductile. The hardness increases slightly with higher atomic number. There are very small differences in solubility and complex formation between the rare earths. They are very reactive, form oxides when exposed to air, commonly bind to water, are strong reducing agents, and react with most non-metals to form binaries on heating.

		Z	ρ	T_{melt}	T_{boil}	A
Yttrium	Y	39	4.472	1799	3609	30
Lanthanum	La	57	6.146	1193	3743	30
Cerium	Ce	58	6.689	1068	3633	60
Praseodymium	Pr	59	6.640	1208	3563	7
Neodymium	Nd	60	6.800	1297	3373	25
Promethium	Pm	61	7.264	1373	3273	$4.6 \cdot 10^{-20}$
Samarium	Sm	62	7.353	1345	2076	5
Europium	Eu	63	5.244	1099	1800	1
Gadolinium	Gd	64	7.901	1585	3523	4
Terbium	Tb	65	8.219	1629	3503	0.7
Dysprosium	Dy	66	8.551	1680	2840	3.5
Holmium	Ho	67	8.795	1734	2993	0.8
Erbium	Er	68	9.066	1770	3141	2.3
Thulium	Tm	69	9.321	1818	2223	0.32
Ytterbium	Yb	70	6.570	1097	1469	2.2
Lutetium	Lu	71	9.841	1925	3675	0.4

Table 1.1: Chemical properties of the RE elements. Z atomic number; ρ density (g/cm^3); T_{melt}, T_{boil} melting and boiling point (K); A earth's crustal abundance (ppm) [CHR98].

Table 1.1 shows general properties of the rare earth elements, the data has been taken from [WIN04, CHR98, KAY93, JAM92] and references therein. Due to difficulties in determining the crustal abundance accurately, the values from several sources differ considerably. Each rare earth metal is more common in the earth's crust than silver, gold or platinum, while Y, La, Ce, and Nd are even more abundant than lead. Most compounds are strongly paramagnetic.

With increasing atomic number, the radius of each trivalent ion decreases considerably (Figure 1.4). This was recognized by V.M. Goldschmidt (1888-1947) and is referred to as *lanthanide contraction*, with a reduction of the ionic radius by 18 pm from La^{3+} to Lu^{3+}. Data on ionic radii in different local surroundings is listed for selected elements in Appendix D.

There is little tendency to vary the valence, usually the rare earths are incorporated as trivalent cations. However, divalent ions have been studied extensively in the past, especially

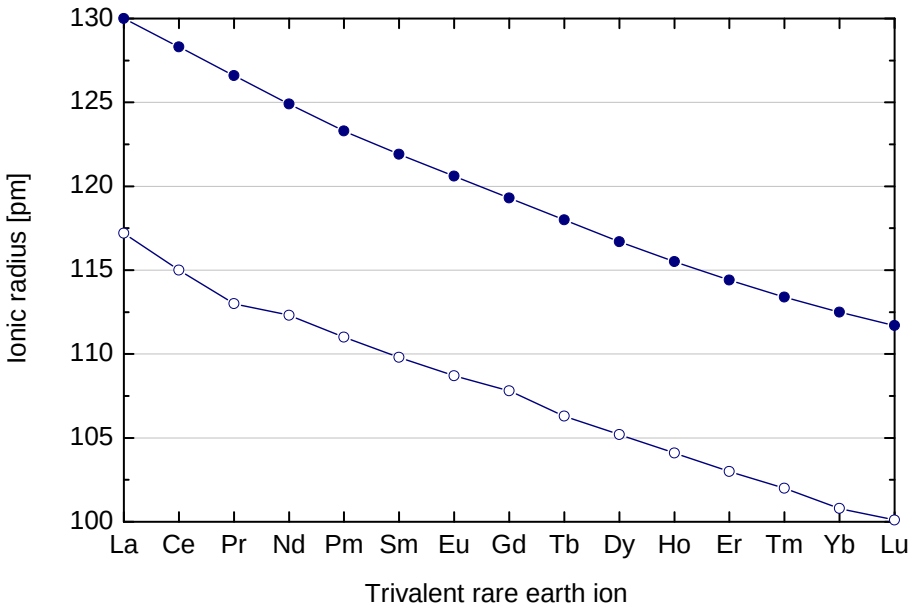

Figure 1.4: Ionic radii of the trivalent RE ions in eight- (•) and six-fold (◦) coordination. The decrease of size with increasing atomic number is referred to as *lanthanide contraction*.

Sm^{2+}, Yb^{2+}, and Eu^{2+} [RUB91]. Rare earth compounds tend to be pale colors, resulting from weak, narrow, parity-forbidden $4f \rightarrow 4f$ optical transitions (Section 2.4).

1.2.3 Thulium

The story of this element began with Carl Gustav Mosander splitting the initially discovered *yttria* into three new elements, *yttria proper*, *erbia*, and *terbia*. In 1878 Jean Charles Galissard de Marignac, professor of Chemistry at the University of Geneva, separated two new earths, *erbia* and *ytterbia*. Marignac's *erbia* was split by Per Theodor Cleve (1804-1905) into *erbia proper* and two new elements, which he named Thulium (after *Thule*) and Holmium in 1879. Analysis of Holmium showed later that it also contained Dysprosium.

Cleve himself, and many sources afterwards, have written that *Thule* is the ancient name for Scandinavia, which is not the case. *Thule* was the most northern habitable region of the world to the ancient Greeks, and it has been associated with early reports on Iceland, Norway, or the Shetland Islands [KRO03, GRE98].

The element is silver-gray, soft, malleable, and ductile. There are 25 isotopes known, with atomic masses ranging from 152 to 176. Although the only naturally occurring isotope ^{169}Tm is stable, there are 15 unstable isotopes. ^{170}Tm, having a half-life of 129 days, is prepared by irradiating ^{169}Tm in a nuclear reactor and utilized in portable X-ray sources.

1.3 Transition metal elements

The elements ranging from $3d^2 4s^2$ (Ti) to $3d^{10} 4s$ (Cu) are considered transition metals. They share similar chemical properties (Section 1.3.1). Many crystals containing transition metal ions in various valence states exhibit broad and intense $3d \rightarrow 3d$ emission bands. Special attention is paid to Manganese (Section 1.3.2) in the scope of this thesis.

1.3.1 Properties of transition metals

The transition metal elements are quite similar in their physical and chemical properties. This is due to the fact, that for the elements in this series the inner $3d$ shell is being filled with electrons, whereas the outer filled $4s$ shell remains unchanged. Common properties include high tensile strength, density, hardness, high melting and boiling points.

The transition metals show variable oxidation states, increasing in number towards the middle, and decreasing again towards the end of the series. All oxidation states can be exhibited in Mn^{N+} ranging from $N = 1 \ldots 7$. In general, the lower oxidation states are found in ionic compounds, whereas the higher ones preferentially occur in covalent compounds.

The filling of the $3d$ orbitals, however, is irregular, since for chromium ($3d^5 4s$) and copper ($3d^{10} 4s$) an electron from the $4s$ shell is promoted to a $3d$ orbital. In chromium the $3d$ and $4s$ levels are fully occupied by unpaired electrons due to electron repulsion interaction.

Generally, various colored compound or complexes can be formed with transition metals.

1.3.2 Manganese

Torben Olof Bergman (1735-1784), professor of chemistry at Uppsala, separated pyrolusite (MnO_2) from lime and magnesia alba, but failed to reduce the ore. In 1774 a friend of Bergman, Carl Wilhelm Scheele, completed a three years investigation, called it Manganese, and described it as “the calx of a metal different from any then known”. Bergman’s assistant, Johan Gottlieb Gahn (1745-1818), succeeded in isolating Manganese from pyrolusite as an element [KRO03, GRE98].

Manganese is the 12th most abundant element and 3rd most abundant transition metal, exceeded only by iron and titanium, reaching an overall abundance of 0.106% in the earth’s crustal rocks. Several silicates, oxides and carbonates containing Manganese are of economical importance, such as hausmannite (Mn_2O_4), rhodochrosite ($MnCO_3$), manganite ($Mn_2O_3 \cdot H_2O$), and pyrolusite (MnO_2), while the latter probably has been used for glass fabrication already since the ancient times of the Pharaohs. Large world deposits are located in the former USSR, Gabon, South Africa, Brazil, Australia, India, and China. Around 90% are used in steel manufacture, mostly in the form of ferromanganese alloys.

Generally, Manganese is moderately reactive. At higher temperature, it reacts vigorously with oxygen, nitrogen, chlorine and fluorine, and combines directly with B, C, Si, P, As, and S. Due to its formidable range of oxidation states, oxides are known based on Mn^{2+} to Mn^{7+}. The representative $KMnO_4$ (Mn^{7+}) is of intense purple color due to a charge transfer band. As strongly oxidizing agent, it is used in industry for the production of saccharin and benzoic acids, or medically for disinfection and water purification.

In this work Mn^{2+} doped fluoride crystals have been grown and investigated spectroscopically. For the first time, systematic investigations on the energy difference of extraordinary strong excitation bands due to $3d^5 \rightarrow 3d^4 4s$ transitions are presented in a variety of fluoride crystals (Section 5.5).

1.4 Applications

Electronic transitions of $3d \rightarrow 3d$ states in transition metal ions and $4f \rightarrow 4f$ in rare earths are typically in the visible range, and selection rules of the spin- and parity-forbidden transitions are partly lifted (Section 2.4).

Thus, these elements can be efficient luminescent materials commonly used in light emitting devices such as fluorescent tubes (Section 1.4.1), display panels (Section 1.4.2), and lasers (Section 1.4.3). Potential applications arise that require phosphors with favorable energy transfer properties in the vacuum-ultra-violet (VUV) spectral region, therefore the new and improved luminescent materials are needed.

Manifold applications based on RE ions are further found in scintillators or optical fibers based on Er^{3+}.

1.4.1 Fluorescent tubes

In conventional fluorescent tubes, an electric discharge is generated within a low-pressure noble gas and mercury environment. Even though the mercury pressure is considerably lower than the noble gas pressure, ionization of mercury occurs preferentially, since the ionization potential of Hg (10.43 eV) is less than that of Ar (15.76 eV) [HEN83]. The addition of a noble gas further enhances ionization of the mercury vapor at a lower voltage potential. This is due to a large number of Ar being promoted to an excited state by electron impact, sub-sequentially colliding and exciting mercury atoms according to

$$Ar^* + Hg \rightarrow Ar + Hg^+ + e^-$$

This phenomenon is known as *Penning ionization* and is used in other types of discharge lamps as well. Emission by recombination of mercury ions with electrons occurs predominantly at

254 nm and 185 nm, and also to a small percentage at lower energies. In order to convert this luminescence into visible light a mixture of crystalline phosphors is applied on the inner walls of the tube. The first UV phosphors are based on Sb^{3+} (blue emission) and Mn^{2+} (orange emission) impurities in halo-phosphates, yielding white light. Thirty years later, in 1970, narrow line emitters in a tri-color setup were proposed to improve the color rendering index (CRI) value [KOE71, THO71]. RE ions provide naturally narrow line luminescence in the visible and are well suited for this purpose. A lamp phosphor based on Eu^{3+}, Tb^{3+}, and Eu^{2+} was developed soon afterwards [VER74].

Nowadays, a total quantum yield of better than 90% is achieved. The phosphors currently used in fluorescent lamps are based on rare earth ions, in particular Y_2O_3:Eu^{3+} in the red, $GdMgB_5O_{10}$:Ce^{3+},Tb^{3+} in the green, and $BaMgAl_{10}O_{17}$:Eu^{2+} in the blue spectral region, while the latter compound suffers most from degradation effects.

However, the presence of mercury, which is contained in the amount of 2-10 mg in each lamp, is an environmental hazard and is preferably replaced by a pure noble gas discharge. Currently, Penning mixtures based on Xenon seem to have promising efficiencies, while several substances are investigated for various applications in order to enhance the Penning effect. Furthermore, the emission characteristics of the Xenon discharge are not influenced by the ambient temperature as opposed to the mercury discharge.

Emission from the Xenon discharge consists mainly of two broad bands in the vacuum-ultraviolet (VUV), the monomer (147 nm) and the strong dimer band (172 nm). New phosphors are required for converting the VUV emission into visible light at competing efficiency. Since the exciting photons have about 50% higher energy than those of the mercury discharge, even a quantum efficiency of 100% would be disadvantageous in terms of energy [RON02].

The process of *down conversion* (photon cascade emission, quantum cutting), in which every absorbed photon yields the emission of more than one photon of lower energy, is well known in the field of spectroscopy. Concerning lamp phosphors down conversion within $LiGdF_4$:Eu^{3+} has been achieved with internal quantum efficiency of 195%, resulting from strong Gd-Eu interaction [WEG99b]. However, the external quantum yield when exciting ${}^6G_J$ states of Gd^{3+} is significantly lower with 32% due to non-radiative processes [FEL01].

In this work, the energy transfer capabilities of Tm^{3+} and Mn^{2+} doped fluorides have been investigated in terms of photon cascade emission.

1.4.2 PDP, OLED, Polymer

The physics of displays is closely connected to fluorescent tubes. Old-fashioned *Cathode Ray Tubes* (CRT) consist of a screen with red, green, and blue phosphor pixels that are excited by fast electrons, commonly used in computer monitors and television devices. The market for modern flat displays has grown rapidly, replacing increasingly CRT. An overview of novel

displays can be found in [JUE00, JUE98]. While the widely used *Liquid Crystal Displays* (LCD) are nonorganic, nonemissive devices that require an external light source or a back lighting system, self-emissive alternatives are under development.

Plasma Display Panels (PDP) consist of a matrix of plasma discharge cells. By applying a certain voltage between two transparent display electrodes on the front glass plate of the display, each cell generates a Xenon discharge with subsequent emission of red, green, or blue light. The intensity of each color is controlled by varying the number and width of voltage pulses applied to the respective sub-pixel during a picture frame. In practice, the luminescent properties of PDP are so far limited due to a low discharge efficiency and unwanted properties of the phosphors currently available (color pureness, afterglow, or degradation effects).

A different approach, which sidesteps the need for efficient VUV phosphors, are displays based on *Polymers* or *Organic Light-Emitting Diodes* (OLED). They consist of a series of thin films between two conductors. When electrical current is applied, light emission is stimulated in the organic luminescent materials.

1.4.3 Lasers

Rare earth ions, such as Tm^{3+}, doped into various crystals are well-known to exhibit laser operation as active ion, which is usually emitting in the IR spectral region. In combination with other rare earth or transition metal ions a variety of lasers has been rendered possible.

Recently, a comprehensive overview of transition metal and rare earth ion doped crystals for application as tunable solid-state lasers presents details on laser operation in the spectral range between 270 nm and 4500 nm based on $3d \rightleftarrows 3d$ and $4f \rightleftarrows 5d$ transitions [KUE01]. Upconversion laser processes of crystals doped with rare earth ions have been reviewed extensively [SHE96].

The $^3H_4$ multiplet, e.g., can be efficiently pumped via a cross-relaxation process by diode laser operating at 800 nm, thus population inversion is achieved of the $^3F_4 \rightarrow {}^3H_6$ transition. Known laser crystals include Tm^{3+} doped $YAlO_3$, $Y_3Al_5O_{12}$ (YAG) and $Y_3Sc_{2.5}Ga_{2.5}O_{12}$ (YSGG) [CAI75, STO90], YVO_4 [SAI92], Y_2SiO_5 [LI93], $LiYF_4$ [PIN94], and KY_3F_{10} [BRA00, BRA01].

After Yb^{3+}-sensitized materials were originally investigated for infrared quantum counters [EST67], co-doping with rare earths such as Tm^{3+} proved to show efficient upconversion laser operation in several crystals [JOH71, FAR94]. Further lasers based on Tm^{3+} include $LiYF_4$:Tm^{3+} [NGU89, HER92], $LiYF_4$:Tm^{3+}, Yb^{3+} [HEI95, DIE98], and BaY_2F_8 :Tm^{3+}, Yb^{3+} [THR94]. Recently, an orange and red upconversion laser has been presented, based on an avalanche pumping mechanism of Pr^{3+}, Yb^{3+} in BaY_2F_8 (BYF) [OSI01, OSI03a, OSI03b]. Efficient tunable laser operation has been observed in diode-pumped Yb,Tm:$KY(WO_4)_2$ around 1.9 μm [BAT02]. BYF with Tm^{3+} concentrations ranging from 2 to 18 at.% varies its emis-

sion wavelength from 1927 nm up to 2030 nm, while the nature of the transition changes from purely electronic to vibronic [COR04].

Applications of IR-visible upconversion materials besides lasers are three-dimensional displays [DOW96], visualization of IR light [POL87], and security marking of official documents.

Solid state lasers based on Tm^{3+} and Ho^{3+} have many applications in remote sensing, medical, and military technologies. Tm^{3+}, Ho^{3+}, Er^{3+} in $Y_3Al_5O_{12}$ (YAG) has been demonstrated to lase at room temperature [FAN87, FAN88, HUB88]. A high-power laser based on Cr^{3+}, Tm^{3+}, Ho^{3+} (CTH) in YAG has been conceived soon afterwards [QUA90, BEC92]. Q-switched Cr,Tm:YAG and CTH:YAG laser operation emitting at 2 μm wavelength has been achieved with maximum pulse energy of 0.7 and 0.5 J, respectively, and corresponding pulse widths of 140 ns and 165 ns [LI00]. The extraordinary high efficiency is due to the Cr^{3+} to Tm^{3+} energy transfer [ARM89a, ARM89b] having a quantum efficiency approaching two. These characteristics generate large interest for a wide range of applications, e.g. in the medical field [BIC95].

The $LiCaAlF_6$ (LiCAF) crystal host investigated in this work (cf. Section 4.2) is also a well-known laser material, extensively investigated in the past, in particular in terms of crystal growth (cf. Section 3.1) and recently in terms of color centers and defects experimentally [KIR04, SAT02a, SAT02b] as well as theoretically [AMA03, AMA04]. An optically pumped tunable solid-state laser based on the $5d \rightarrow 4f$ of Ce^{3+} in $LiYF_4$ [EHR78, OKA94] and LiCAF [MAR94b] has been reported. Recently, improved laser operation of LiCAF:Ce^{3+} and $LiLuF_4$:Ce^{3+} was observed at output energies 60 mJ and 27 mJ, respectively [SHI01b].

1.5 Outline of this thesis

In this introductory chapter the motivation and feasibility have been outlined concerning the design of a novel phosphor with prospective energy transfer capability (quantum cutting) between Tm^{3+} and Mn^{2+}. The rare earth and transition metal elements are introduced briefly in terms of history, general properties, and its various applications as luminescent materials.

The basic theoretical aspects of ions incorporated into a dynamic lattice are presented in Chapter 2. The intra-configurational $4f^n \rightarrow 4f^n$, inter-configurational $4f^n \rightarrow 4f^{n-1}5d$, and charge transfer (CT) transitions of trivalent rare earth ions are discussed. Peculiarities of $3d^n$ transition metal ions are outlined, with special attention being paid to Mn^{2+} ($3d^5$).

Experimental methods applied during this work are covered in Chapter 3. The $LiCaAlF_6$ crystal, target of primary investigation, was grown by Czochralski technique singly and co-doped with Tm^{3+} and Mn^{2+} at the *Institut für Laserphysik, Universität Hamburg* (Section 3.1). Iso-structural $LiSrAlF_6$ crystals with corresponding doping concentrations were formed by solid state reaction, confirmed to be single phase by X-ray powder diffractometry. Further Mn^{2+} doped crystals $BaMgF_4$, $KMgF_3$, and MgF_2 as well as BaY_2F_8 singly and co-doped

with Tm^{3+} and Mn^{2+} have been obtained for extended analysis. The investigated crystals are introduced in Section 3.2. Emission, excitation, and absorption spectroscopy has been carried out at our experimental setup *Superlumi* at HASYLAB, DESY. The available monochromators and detectors offer a variety of spectroscopic techniques, including time-resolved and high-resolution excitation and emission measurements (Section 3.3). Supplementary high resolution emission spectra have been obtained with excimer laser excitation at the *Debye Institute, Universiteit Utrecht, Netherlands*, briefly described in Section 3.4.

The experimental data has been divided into three parts: results on fluoride crystals singly doped with Tm^{3+} are presented in Chapter 4, including host-related, CT, inter- and intra-configurational energy transfer processes. Electronic and vibronic $4f^n \rightarrow 4f^n$ and $4f^n \rightarrow 4f^{n-1}5d$ transitions are analyzed by high resolution emission spectroscopy in terms of Stark splitting, site-selective excitation, and phonon replica.

Chapter 5 comprises a detailed study of various Mn^{2+} doped fluorides. The spin- and parity-forbidden $3d^5 \rightarrow 3d^5$ transitions are clearly observed by excitation spectroscopy at the Fluorolog setup of the *Institut für Laserphysik* (Section 5.3). A convenient evaluation of the large number of samples has been achieved by computational methods developed in this work (Section 5.4). The results allow conclusions on the intense VUV excitation bands observed in all crystals under investigation (Section 5.5), while little attention has been paid to these bands in the literature.

Final conclusions are drawn concerning inter-ionic energy transfer of the Tm^{3+} and Mn^{2+} co-doped $LiCaAlF_6$ crystal in Chapter 6.

Since further research on the inter-ionic energy transfer hinted by the initially investigated $LiCaAlF_6$ and $LiSrAlF_6$ crystals appeared to be rewarding, several samples of the well-known upconversion and laser host BaY_2F_8 doped with Tm^{3+} and Mn^{2+} had been ordered for extended analysis. However, the doping concentrations determined by trace analysis as well as the spectra disagree with the nominal values. Hence, a reliable analysis would require further experiments beyond the scope of this thesis. The results of the BaY_2F_8 samples in question are presented in Appendix A for future reference.

Chapter 2

Theoretical aspects

2.1 Energy level structure of free ions

From general considerations, the Hamiltonian of a free ion many-electron system can be written as

$$\mathcal{H}_{fi} = \mathcal{H}_0 + \mathcal{H}_{er} + \mathcal{H}_{so} \tag{2.1}$$

where $\mathcal{H}_0$ is the kinetic and potential energy in the central field approximation (Section 2.1.1), $\mathcal{H}_{er}$ is the residual Coulomb repulsion between the electrons, and $\mathcal{H}_{so}$ is induced by spin-orbit coupling (Section 2.1.2).

2.1.1 Central field approximation

In order to obtain a separable Schrödinger equation for an N electron system, an average (effective) spherical potential is assumed for each electron i *(central field approximation)*, generated by the nucleus charge and the other $N-1$ electrons *(self-consistent field approximation)*.

The Hamiltonian for a multi-electron system, neglecting spin and other relativistic effects is

$$\mathcal{H} = \sum_i \left(-\frac{\hbar^2}{2\mu} \triangle_{r_i} - \frac{Ze^2}{4\pi\epsilon_0 r_i} \right) + \sum_{i<j} \frac{e^2}{4\pi\epsilon_0 r_{ij}} \tag{2.2}$$

where μ is the reduced mass of the electron-nucleus system, r_i is the distance of electron i to the nucleus of charge Ze, and $r_{ij} = |r_i - r_j|$ is the distance between electron i and j. The first term accounts for the *kinetic energy*, the second for the *nuclear potential energy*, and the third for the *electron repulsion*.

The central field approximation assumes that the latter term contains a large spherically symmetric component, hence it can be written $\mathcal{H} = \mathcal{H}_0 + \mathcal{H}_{er}$ with

$$\mathcal{H}_0 = \sum_i \left(-\frac{\hbar^2}{2\mu} \triangle_{r_i} - \frac{Ze^2}{4\pi\epsilon_0 r_i} + U(r_i) \right) \tag{2.3}$$

$$\mathcal{H}_{er} = \sum_{i<j} \frac{e^2}{4\pi\epsilon_0 r_{ij}} - \sum_i U(r_i) \tag{2.4}$$

$\mathcal{H}_0$ is a sum of terms for each electron, and the respective solutions of the time-independent Schrödinger equation can be written as product of the eigenstates of the single electron wave function

$$\psi_0 = \prod_i |n_i l_i m_l m_s\rangle \tag{2.5}$$

characterized by the principal quantum number n, the orbital angular momentum l_i, the magnetic quantum number m_l, and the spin quantum number m_s. The sub-index i is omitted for m_{l_i} and m_{s_i}. In the central field approximation, m_l and m_s are degenerate.

$\mathcal{H}_{er}$ is treated as a perturbation. $U(r)$ depends on the wave function of all electrons and can be solved iteratively by the self-consistent field approach.

For more general systems, the Hartree-Fock approach can be used to iteratively compute the potential in terms of perturbation theory, which takes into account exchange interaction.

Quantum numbers

The *quantum numbers* for $\mathcal{H}_0$ in the central field approximation take values as follows:

- the principal quantum number $n = 1, 2, \ldots$
- the angular momentum quantum number $l = 0, 1, 2, \ldots, (n-1)$
- the magnetic quantum number $m_l = -l, (-l+1), \ldots, (l-1), l$
- the spin quantum number $m_s = \pm\frac{1}{2}$

The solution of the central field approximation is degenerate in m_l and m_s.

2.1.2 Coupling schemes

The angular momenta of electrons in a partially filled sub-shell couple to total angular momenta, depending on the dominant interaction. The orbital motion and the

magnetic spin moment are coupled via the magnetic interaction of the spin magnetic moment with the magnetic field of the orbital motion. Hence, consider the Hamiltonian $\mathcal{H} = \mathcal{H}_0 + \mathcal{H}_{er} + \mathcal{H}_{so}$ with

$$\mathcal{H}_{so} = \sum_{i=1}^{N} \zeta(r_i) \left(\vec{l_i} \cdot \vec{s_i} \right) \tag{2.6}$$

ζ is the spin-orbit coupling constant of the particular system, $\vec{l_i}$ the orbital momentum, and $\vec{s_i}$ the spin of electron i.

LS coupling

For ions with small Z the most important residual interaction is the electrostatic repulsion between electrons.

$$\mathcal{H}_{er} \gg \mathcal{H}_{so}$$

In this case the eigenstates of $\mathcal{H}_0 + \mathcal{H}_{er}$ are considered, treating $\mathcal{H}_{so}$ as a perturbation. The ordering of the energy levels is given by *Hund's rule*. The orbital angular momenta are coupled first to form the total orbital angular momentum $\vec{L} = \sum_N \vec{l_i}$. The spin angular momenta are summed likewise to the total spin angular momentum $\vec{S} = \sum_N \vec{s_i}$. The total spin and orbital momenta finally couple to $\vec{J} = \vec{L} + \vec{S}$.

This is known as the *Russell-Saunders approximation* or LS coupling. The resulting states are described by their basis function ${}^{2S+1}L_J$, which is $(2J+1)$-fold degenerate in M_J.

jj coupling

In ions with large Z values the spin-orbit coupling is much stronger than the residual Coulomb interaction.

$$\mathcal{H}_{er} \ll \mathcal{H}_{so}$$

It is appropriate to couple the spin and orbital angular momenta of each electron separately $\vec{j_i} = \vec{l_i} + \vec{s_i}$, yielding the total angular momentum $\vec{J} = \sum_N \vec{j_i}$. The basis function is denoted $[(l_1, s_1)\, j_1, \ldots, (l_N, s_N)\, j_N]\, J$. The jj coupling case is usually only considered for the heaviest elements, i.e. the actinides, or for lighter atoms in highly ionized states.

Intermediate coupling

The $4f$ rare earth ions are a case of intermediate coupling, neither LS nor jj coupling are appropriate. The eigenfunctions can be expressed in a different basis set, commonly denoted in terms of Russell-Saunders states ${}^{2S+1}L_J$. The theoretical treatment is more advanced, however, and beyond the scope of this thesis.

2.2 Ions in a static crystal field

Optically active ions incorporated in a crystal lattice experience interactions with the lattice, which influences the optical properties described by

$$\mathcal{H} = \mathcal{H}_{fi} + \mathcal{H}_{cf} \tag{2.7}$$

where $\mathcal{H}_{fi} = \mathcal{H}_0 + \mathcal{H}_{er} + \mathcal{H}_{so}$ is the free-ion Hamiltonian (Equation 2.1) and $\mathcal{H}_{cf}$ accounts for the static crystal field interaction.

The changes introduced into the energy level structure depend on the magnitude of each quantity. Two cases will be discussed: the weak ligand field ($\mathcal{H}_{cf} \ll \mathcal{H}_{so}$), which is appropriate for the rare earths (Section 2.2.1), and the strong ligand field ($\mathcal{H}_{so} \ll \mathcal{H}_{cf}$), which has to be considered for the $3d$ transition metals (Section 2.2.3). The inter-configurational $4f \rightarrow 5d$ transitions of the rare earths are also strongly influenced by the crystal field (Section 2.4).

2.2.1 Rare earth ions in a static crystal field

The $4f^n$ shell is well shielded by filled outer $5s$ and $5p$ orbitals [BUR62, RAY63, STE66] as shown for Gd^+ in Figure 2.1. For the trivalent RE the situation is very similar, except for the missing $5d$ shell.

The $4f$ energy levels of free RE ions are only slightly perturbed by the crystal field, and the energies do not change much with changing the ligands. In high resolution measurements, however, considerable variations are observable. The shielding effect decreased with increasing atomic number [STE66].

Assuming Russell-Saunders coupling the crystal field splitting $\left(\approx 100\ \mathrm{cm}^{-1}\right)$ is much lower than spin-orbit coupling $\left(\approx 1000\ \mathrm{cm}^{-1}\right)$ or the term separation $\left(\approx 10\,000\ \mathrm{cm}^{-1}\right)$, corresponding to the order

$$\mathcal{H}_{cf} \ll \mathcal{H}_{so} \ll \mathcal{H}_0$$

The outer $5d$ shell is much more sensitive to the crystal field, since it is not shielded by filled $5s$ and $5p$ orbitals. Therefore, the $4f \rightarrow 5d$ transition energies are shifted considerably by the

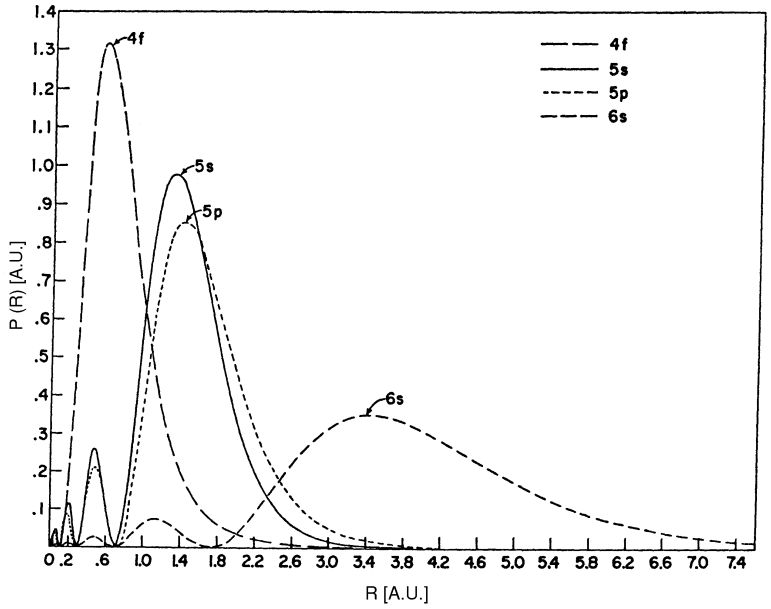

Figure 2.1: Radial charge distribution $P(R)$ of the Gd^+ radial wave function for $4f$, $5s$, $5p$, and $6s$ orbitals. R is the distance from the nucleus [DIE68].

crystal field of the surrounding. In order to determine the energy levels and eigenfunctions of RE ions in a lattice, the matrix elements of the perturbed Hamiltonian can be calculated in the one-electron approximation. The crystal field Hamiltonian can be written

$$\mathcal{H}_{cf} = \sum_{k,q} B_q^k \hat{C}_q^k$$

where B_q^k are parameters containing the structure of the local crystal field, and $\hat{C}_q^{\ k}$ are tensor operators [HUT64].

This accounts for the *nephelauxetic effect*, introducing a red-shift to the free ion levels and further lifting of the M_j degeneracy. The red-shift increases with increasing covalency of the surroundings. For the rare earth ions the $4f$ levels only experience a weak nephelauxetic effect due to the shielding of $5d$ orbitals.

2.2.2 Kramers theorem

In the preceeding section ions in a static lattice have been generally introduced. Besides more complex *ab initio* calculations, the crystal field splitting can be determined qualitatively from group theoretical considerations. The individual crystal levels can be classified by irreducible representations Γ_1, Γ_2, ... of the symmetry group to which they belong to.

An alternative representation based on a coordinate system having the principal symmetry axis chosen as z-axis, introducing a *crystal quantum number* μ associated with the irreducible representations [HEL49]. An extended definition is given by Dieke [DIE68], which is followed in this description.

Axis	$\mu(J$ integer)	μ (J half-integer)
Twofold	0^+, 0^-, 1^+, 1^-	$^1/_2$
Threefold	0^+, 0^-, 1	$^1/_2$, $^3/_2$
Fourfold	0^+, 0^-, 1, 2^+, 2^-	$^1/_2$, $^3/_2$
Sixfold	0^+, 0^-, 1, 2, 3^+, 3^-	$^1/_2$, $^3/_2$, $^5/_2$

Table 2.1: Values taken by the crystal quantum number μ according to [DIE68]. Levels having a super-index $^+$ or $^-$ are singly, all others doubly degenerate.

Table 2.1 shows the possible values of the crystal quantum number μ, depending on the manifold of symmetry axes. For the cubic point groups the description using μ-values is insufficient and the irreducible representations Γ_n have to be used.

However, the preceeding considerations are only based on the geometrical symmetry of the lattice. As consequence of the *time-reversal symmetry* additional degeneracy of states is introduced, depending on the number of electrons and the local symmetry [KRA30]. Since magnetic fields are not invariant under time-reversal operations, this degeneracy is lifted if magnetic fields are present. States having $-\mu$ and $+\mu$ are usually degenerate due to time-reversal.

J	0	$\frac{1}{2}$	1	$\frac{3}{2}$	2	$\frac{5}{2}$	3	$\frac{7}{2}$	4	$\frac{9}{2}$	5	$\frac{11}{2}$	6	$\frac{13}{2}$	7	$\frac{15}{2}$	8	$\frac{17}{2}$	9
Single	1	-	-	-	-	-	1	-	1	-	-	-	2	-	1	-	1	-	2
Double	-	1	-	-	1	1	-	2	1	1	1	2	1	3	1	2	2	3	1
Triple	-	-	1	-	1	-	2	-	2	-	3	-	3	-	4	-	4	-	5
Quadruple	-	-	-	1	-	1	-	1	-	2	-	2	-	2	-	3	-	3	-
Total	1	1	1	1	2	2	3	3	4	3	4	4	6	5	6	5	7	6	8

Table 2.2: Degeneracy of ions in cubic surrounding from purely geometrical considerations according to [DIE68]. Levels having an index $^+$ or $^-$ are singly, all others doubly degenerate.

The number of singly, doubly, triply, and quadruply degenerate Stark levels as well as the total number of observed states in *cubic* symmetry is given in Table2.2, depending on the J-value of the respective energy level.

In *non-cubic* symmetry, if the number of electrons is odd (J is half-integer), all levels are doubly degenerate, hence a free ion level splits into $\left(J+\frac{1}{2}\right)$ sub-levels. If the number of

electrons is even (J integer), all levels are nondegenerate, if not at least a three-fold local symmetry axis is present. If there is an m-fold axis present ($m = 3, 4, 6$), the levels with $\mu = 0$ and $\mu = m/2$ are singly, all others doubly degenerate. With higher local symmetry, additional degeneracy of states is introduced.

The Stark splitting of $^3H_6$ in Tm^{3+} ($4f^{12}$) is taken as example. If the surrounding had not at least a three-fold symmetry axis, all Stark levels would be non-degenerate, leading to 13 sub-levels for the ground state ($J = 6$). In octahedral (O_h) symmetry, a splitting in only six sub-levels would be expected.

The local symmetry of the substitutional Ca^{2+} site is C_{3i} (S_6), neglecting symmetry lowering charge compensation or lattice distortions. This corresponds to a three-fold symmetry axis with inversion symmetry, hence the ground state splits into eight sub-levels.

No statement is possible about the selection rules and corresponding intensities of transitions between Stark levels. Not all transitions are observed in the spectra.

2.2.3 Transition metal ions in a static crystal field

The spin-orbit coupling in $3d^n$ transition metals (≈ 100 cm^{-1}) is much weaker than the large contributions of the crystal field ($\approx 10^4$ cm^{-1}) and therefore neglected,

$$\mathcal{H}_{so} \ll \mathcal{H}_{cf} \tag{2.8}$$

Thus, the splitting energy and degeneracy are determined by the crystal field strength and symmetry. It should be noted that spin-orbit coupling has to be considered again for discussing splitting of sharp lines and transition probabilities between the energy levels.

The weak, medium, and strong field cases of the crystal field and the electrostatic repulsion interaction of the electrons are distinguished.

Medium crystal field

If the crystal field energy is of the same order as the residual electron repulsion,

$$\mathcal{H}_{cf} \approx \mathcal{H}_{er}$$

the configuration interaction between states of the same reduced representation but of different electronic configuration has to be considered.

Weak crystal field

If the crystal field energy is much smaller than the residual electrostatic interaction,

$$\mathcal{H}_{cf} \ll \mathcal{H}_{er}$$

the levels can be denoted according to their free ion terms $\left({}^{2S+1}L\right)$ which are $(2S+1)(2L+1)$ degenerate.

Strong crystal field

If the crystal field energy is much larger than the residual electrostatic interaction between the electrons,

$$\mathcal{H}_{cf} \gg \mathcal{H}_{er} \tag{2.9}$$

the energy levels are only determined by the number of electrons in t_2 and e orbitals and split in $(2S+1)(\Gamma)$ degenerate states ${}^{2S+1}\Gamma(t_2^n e^{N-n})$.

	O_h	T_d	D_{4h}
S	A_{1g}	A_1	A_{1g}
P	T_{1g}	T_1	$A_{2g} + E_g$
D	$E_g + T_{2g}$	$E + T_2$	$A_{1g} + B_{1g} + B_{2g} + E_g$
F	$A_{2g} + T_{1g} + T_{2g}$	$A_2 + T_1 + T_2$	$A_{2g} + B_{1g} + B_{2g} + 2E_g$
G	$A_{1g} + E_g + T_{1g} + T_{2g}$	$A_1 + E + T_1 + T_2$	$2A_{1g} + A_{2g} + B_{1g} + B_{2g} + 2E_g$
H	$E_g + 2T_{1g} + T_{2g}$	$E + T_1 + 2T_2$	$A_{1g} + 2A_{2g} + B_{1g} + B_{2g} + 3E_g$

Table 2.3: Splitting of $3d$ terms in O_h, T_d, and D_{4h} symmetry. States of odd parity have been omitted. The spin multiplicity (omitted) of the free ion states is conserved for the crystal field terms.

By crystal field perturbation these levels split in sub-levels denoted by $\left({}^{2S+1}\Gamma\right)\left({}^{2S+1}L\right)$, which is shown in Table 2.3 for terms in d configuration in local symmetries O_h (octahedral), T_d (tetrahedral), and at lower symmetry D_{4h}. The spin multiplicity of the free ion states is conserved for the crystal field terms. For example in O_h symmetry S and P states do not split (yielding A_{1g} and T_{1g} levels, respectively), while D states result in two terms E_g and T_{2g}. $\left({}^{2S+1}\Gamma\right)$ represent terms adopted from the Mulliken symbols for atomic and molecular orbitals:

A non-degenerate orbital, symmetric to the principle axis C_n

B non-degenerate orbital, anti-symmetric to the principle axis C_n

E doubly degenerate orbital

T triply degenerate orbital

g (subscript) symmetric to center of inversion (*gerade* parity)

u (subscript) anti-symmetric to center of inversion (*ungerade* parity)

1 (subscript) symmetric with respect to axis C_2 perpendicular to C_n

2 (subscript) anti-symmetric with respect to axis C_2 perpendicular to C_n

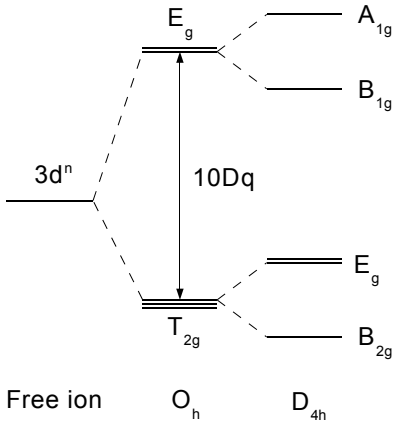

Figure 2.2: Splitting of the $3d^n$ free ion level by the crystal field in O_h and D_{4h} symmetry.

A $3d^n$ free ion level is split by the crystal field in O_h (octahedral) local symmetry in the E_g and T_{2g} sub-levels which are doubly and triply degenerate, respectively (Figure 2.2). If the symmetry is lowered to D_{4h} (square planar) the terms found in octahedral configuration are further split into two sub-levels each.

In the weak, intermediate and strong crystal field the radial and angular part of the electron repulsion interaction can be represented as a linear combination by the Slater-Condon-Shortley parameters F_0, F_2, and F_4. Racah recognized that the relationships $B = F_2 - 5F_4$ and $C = 35F_4$ appeared frequently. In particular, the energy of transitions between states of the same spin multiplicity $(2S + 1)$ as the ground state depends only on B. Thus, a substitutional set of *Racah parameters* B, C and the *crystal field splitting parameter* Dq is used for spectroscopic purposes, where energy differences are measured.

Tanabe and Sugano calculated the determinants of the interaction for d^2 to d^8configuration in octahedral symmetry [TAN54a]. The results are depicted in *Tanabe-Sugano diagrams* [TAN54b], which have been employed for quantitative evaluation of the spectra (Section 5.1).

Ground state splitting

In the free ion all five d orbitals are degenerate. The non-spherical environment in local surrounding introduces a *ground state splitting* in ions with more than one d electron into two sub-sets, a triply degenerate t_{2g} and a doubly degenerate set labeled e_g [TIP70]. The energy separation designated by $10Dq$ [KEE86] is typically of the order of several thousand wavenumbers in fluorides.

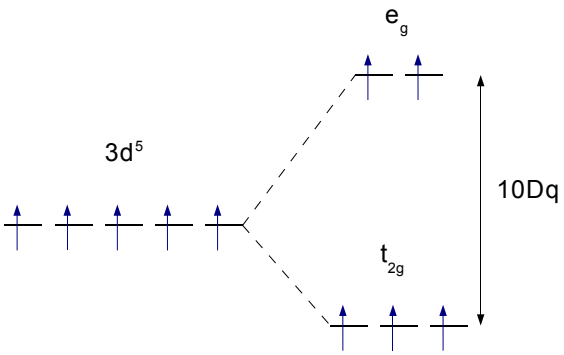

Figure 2.3: Ground state splitting of d^5 ions in crystalline environment into the lower triply degenerate t_{2g} and the upper doubly degenerate e_g level.

In a weak crystal field usually met in fluorides Mn^{2+} manifests in the high-spin ground state, which is split into the lower triply degenerate t_{2g} and the higher doubly degenerate e_g sub-levels as shown in Figure 2.3. If the local symmetry is reduced below octahedral, the remaining degeneracy of the ground state levels is further lifted (Figure 2.2). This splitting is observed in excitation (or absorption) as transitions to higher crystal-field states as predicted by Tanabe-Sugano diagrams (Section 5.1).

A theoretical framework based on perturbation theory has been proposed for the ground state splitting of Mn^{2+} [SIU88], which leads to an identical treatment with that for the Gd^{3+} ground state $^8S_{7/2}$.

The splitting of the ground state of various Mn^{2+} doped fluoride crystals is analyzed in terms of Tanabe-Sugano computation (cf. Section 5.3) as first step of an investigation of intense VUV bands attributed to $3d^5 \rightarrow 3d^4 4s$ transitions (Section 5.5).

2.3 Ions in a vibrating lattice

If an ion as optically active center is incorporated in a crystal, the lattice vibrations (phonons) influence the spectra. The additional term supplementary to the static crystal field Hamiltonian (Section 2.2) yields

$$\mathcal{H} = \mathcal{H}_{fi} + \mathcal{H}_{cf} + \mathcal{H}_{ep} \tag{2.10}$$

$\mathcal{H}_{fi}$ is the free ion Hamiltonian (Equation 2.1), $\mathcal{H}_{cf}$ accounts for the static crystal field (Equation 2.7), and $\mathcal{H}_{ep}$ is the kinetic and interionic energy of the lattice ions. It should be noted that the free ion crystal field Hamiltonian depends both on the electronic and ionic coordinates.

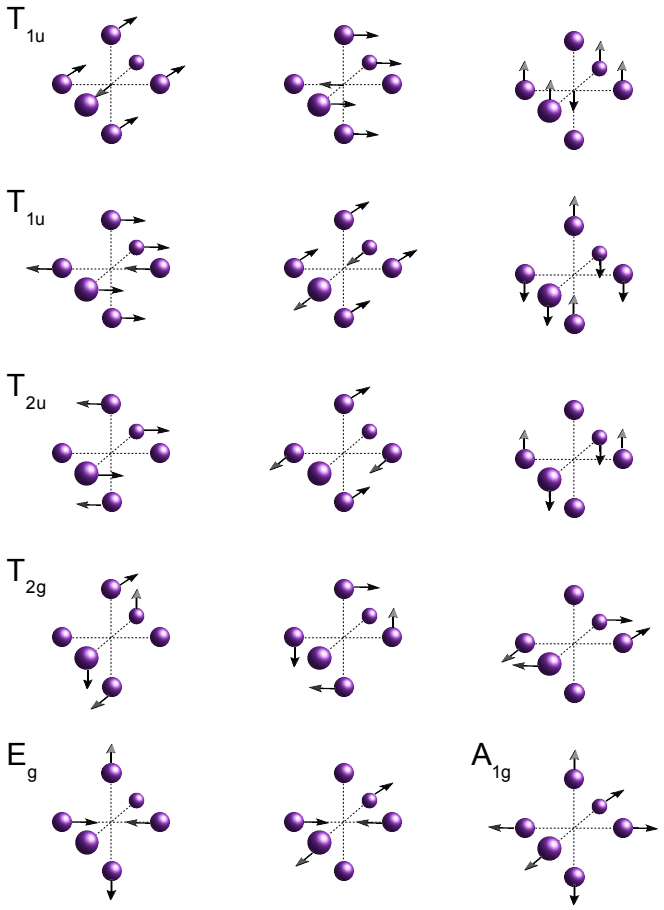

Figure 2.4: Normal vibrating modes of an optically active ion surrounded by six ligands.

Lattice vibrations can be depicted as periodic displacement of ions. Figure 2.4 shows irreducible representations of an optically active ion surrounded by six equidistant neighboring ions, adopted from [HEN89]. The symmetry classifications are also shown.

The interaction between the electronic state and the vibrating modes of a crystal lattice

(phonons) is determined by the *electron-phonon coupling*. Within this context, certain simplifications lead to the *configurational coordinate model* (see, e.g., [WIL51, HEN89, BLA94]).

The simplest case is a linear chain of identical atoms at equilibrium distance a with nearest-neighbor harmonic interaction. The corresponding Hamiltonian describes a coupled mode of oscillation with a normal coordinate Q_{k_n}. The solution of the corresponding Hamiltonian are *phonons*, quanta $|n_k\rangle$ of vibrational energy $\sum \left(n_k + \frac{1}{2}\right) \hbar\omega_k$, representing the eigenstates as product $\prod |n_k\rangle$.

The general case of a three-dimensional lattice containing different types of ions implies different optical and acoustical dispersion branches. It is useful to represent the lattice distortion by irreducible representations of the equilibrium symmetry (Figure 2.4, adopted from [HEN89]).

Electron-phonon coupling

The interaction of an optically active ion with the dynamic lattice is described by

$$\mathcal{H}_{ep} = \sum_k \left[\frac{p_k^2}{2M_k} + V_{pot}\left(r_{k,0} + q_k\right) \right] \tag{2.11}$$

where p_k is the momentum of the kth oscillating ion with mass M_k, $r_{k,0}$ is its equilibrium position, and q_k is the displacement.

In order to solve the corresponding Schrödinger equation, the *Born-Oppenheimer* or *adiabatic approximation* [BOR27] is introduced to decouple the electronic and ionic coordinates. Under the reasonable assumption that the ionic motion is much slower than the electronic motion, the eigenstates can be expressed as product terms of the electronic and the vibrational functions *(Born-Oppenheimer states)*. Usually one representative vibrational lattice mode is chosen, the *breathing mode* A_{1g}, in which the ligands pulsate symmetrically about the optically active ion. The distance of this ion to the first ligand is defined as configurational coordinate Q.

Configurational coordinate diagram

Figure 2.5 shows two electronic states in the *single configurational coordinate diagram* (with equilibrium positions of the ground state $Q = 0$ and excited state Q_0, respectively, where the configurational coordinate Q represents the *deviation* of ion-ligand distance from its equilibrium position. A large difference ΔQ of two states corresponds to a strong electron-phonon coupling. The transition of an electron from the lower to the upper configuration at $Q = 0$ is indicated by an arrow. A higher vibrational mode of the upper configuration is excited predominantly, which will subsequently relax to the lowest vibrational state. Subsequent

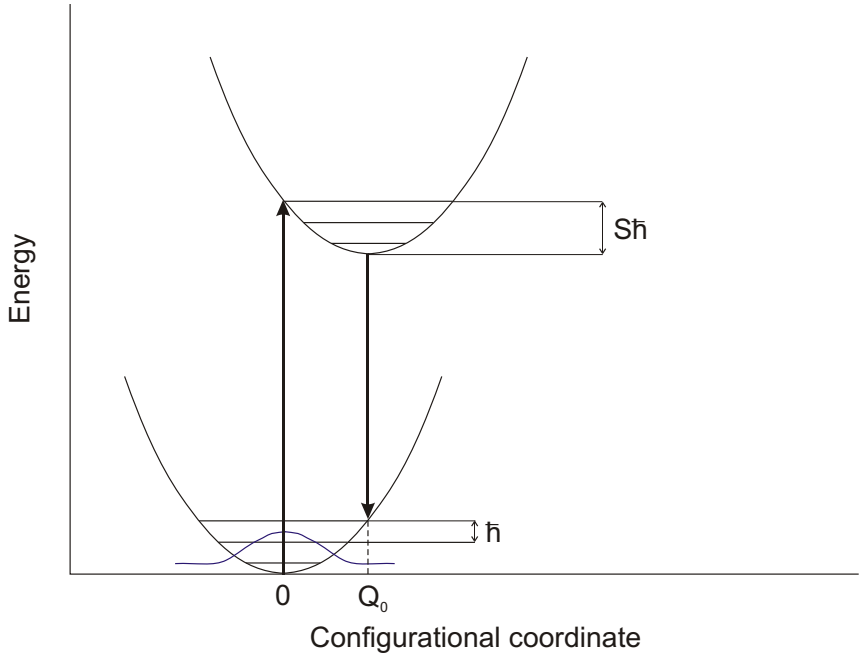

Figure 2.5: Single configuration coordinate diagram of two electronic states at equilibrium positions $Q = 0$ and $Q = Q_0$. S denotes the Huang-Rhys factor.

emission to the ground state occurs at lower energy than in excitation, which is known as Stokes' shift (see, e.g., [HEN89]).

This model is often used to discuss optical properties, and several observations can be explained:

- Stokes' law,
- the widths of absorption or emission bands and their temperature dependence,
- quenching of luminescence induced by temperature (Section 2.6).

The strength of electron-lattice coupling is described by the *Huang-Rhys* factor

$$S = \frac{1}{2}\frac{M\omega^2}{\hbar\omega}\left(Q - Q_0\right)^2 \tag{2.12}$$

where M is the effective ionic mass, ω is the vibrational frequency, and Q_0 is the coordinate of the equilibrium position of the excited state. The vertical line at $Q = 0$ intersects the upper parabola at the higher vibrational level $S\hbar\omega$.

The Huang-Rhys factor S is correlated to the number of emitted phonons as can be seen in Figure 2.6. The upper part ($S = 20$) shows a rich phonon structure, while little intensity

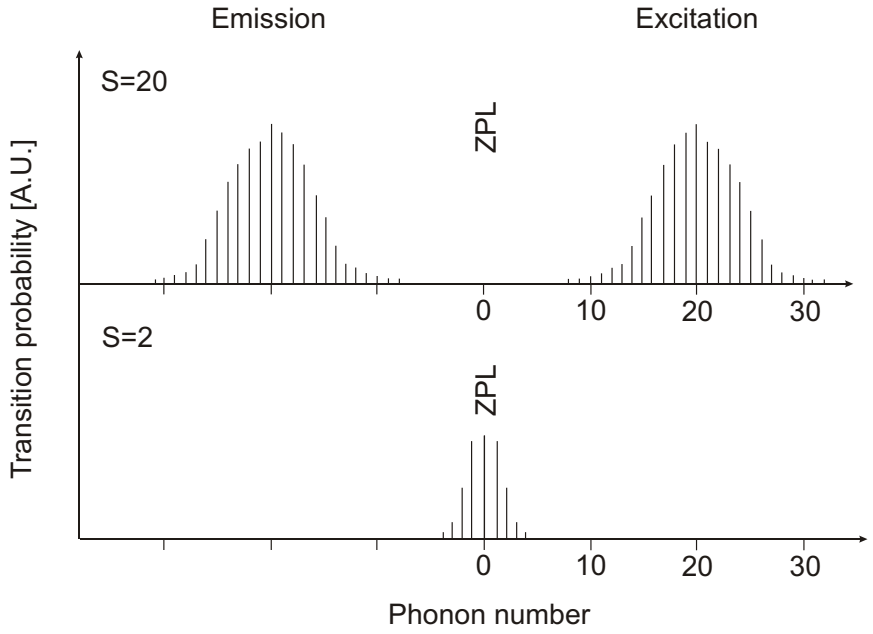

Figure 2.6: Calculated spectral shape in the configurational coordinate model for $S = 20$ (upper graph) and $S = 2$ (lower graph). Values taken from [YAM99].

is contained in the ZPL. In compounds having weak phonon-interaction the ZPL becomes much more pronounced ($S = 2$).

The emission (on the left) as well as excitation (right) transition probabilities in the configurational coordinate model are shown, neglecting selection rules and line widths of transitions. The ZPL results from the radiative transition between the lowest vibrational modes of different electronic states, i.e. without involving phonons [STU67]. Thus, the energy of the ZPL is equal in excitation and emission. Its intensity equals $I_0 \exp(-S)$, I_0 being the total intensity. If the ground state of two electronic states coincide $Q = Q_0$, the Huang-Rhys parameter becomes $S = 0$ and all intensity I_0 is contained in the ZPL.

For $S > 0$ the intensity of the ZPL is reduced and *phonon sidebands* appear on the low-energy side in emission. At elevated temperature additional anti-Stokes' sidebands are observed on the opposing side of the ZPL. In the strong coupling case in emission and excitation spectra only structureless bands show up that cannot be resolved due to strong phonon sidebands.

Considering real crystals, not only the breathing mode, but also many vibrational modes are present. Therefore, besides temperature effects, the vibronic sidebands will appear broader. The ZPL ($m = 0$) has the natural (experimental) line width, vibronics ($m \gtrless 0$) have larger widths $m\hbar\omega$ due to coupling to the lattice, according to [HEN89]. In practice, the description given by the single configurational coordinate diagram is not suitable for describing phonon

energies, since coupling to one breathing mode is not representative for the whole spectrum and selection rules may change the observation considerably.

Experimental issues

There are several methods for determining the electron-phonon coupling strength experimentally. Electron-phonon coupling for $f \rightarrow f$ transitions of the trivalent rare earth ions has been studied intensively in the past decade [HEL41, YEN64, KRU66, KUS69] and more recently (Section 4.5). The influence of the host lattice on electron-phonon coupling of rare earth and transition metal ions has been investigated in detail [VIN00].

High-resolved emission spectra are presented in this work, revealing a rich vibronic fine-structure of Tm^{3+} $5d \rightarrow 4f$ (Section 4.5.2) and $4f \rightarrow 4f$ transitions (Section 4.5.1) being subject to intermediate coupling. However, the quantitative determination of the electron-phonon coupling strength to the lattice is hampered by the occurrence of numerous overlapping electronic and vibronic lines and the lack of theoretical calculations for the investigated host crystals.

2.4 Radiative transitions

The spectra of trivalent RE ions depend on the influence of the crystal host as discussed for the static (Section 2.2) and dynamic (Section 2.3) lattice.

The selection rules for optical transitions (Section 2.4.1) of these ions are partly relaxed by electron-lattice interactions and symmetry effects. In particular, the spin- and parity-forbidden $4f^n \rightarrow 4f^n$ transitions (Section 2.4.2) are observed as narrow lines and account for the emission characteristics in the IR, visible and UV spectral region.

In recent years intensive research focused on the $4f^{n-1}5d \rightarrow 4f^n$ transitions (Section 2.4.3), which occur at higher energies (UV to VUV) and are therefore hidden by the fundamental absorption of crystals having a smaller band gap. In fluorides, however, the $5d$ levels are located in the transparency range of these wide band gap hosts.

2.4.1 Selection rules

Electronic transitions observed are primarily of electric or magnetic dipole character, merely quadrupole transitions may play a subordinate role. Regarding the corresponding oscillator strengths, magnetic dipole transitions are of the order of 10^{-8}, electric dipole transition rather 10^{-5} to 10^{-8} [HEN89]. Judd and Offelt found theoretically an expression for the oscillator strength between electric dipole transitions of the ground configuration $4f^N$, assuming small extension of excited configurations [JUD62, OFE62]. In the Russell-Saunders approximation, the following selection rules apply.

Laporte (symmetry) selection rule

The orbital quantum number l for electric dipole transitions has to change according to

$$\Delta l = \pm 1$$

In other words, the initial and final states must have opposite parity.

Due to several interactions with the electronic wave function of the ion, however, the Laporte selection rule is relaxed [FOR69]:

1. *Electron-phonon interaction.* In the case of an octahedral surrounding, e.g., there exist *gerade* (even) and *ungerade* (odd) type vibrational modes. Hence, even type transitions gain partly odd character and become allowed by coupling to vibrational modes.
2. *Interaction with higher orbitals.* By mixing with the wave function of higher orbitals, e.g. d and p orbitals, odd character can be added to the wave function. This interaction is depending on the symmetry and is, in general, more pronounced in non-centrosymmetric surroundings.
3. *Interaction with ligand orbitals.* Contrary to purely ionic crystals, covalency accounts for mixing with the wave function of the ligands, thus possibly introducing odd character to the optically active ion.

In local surroundings without inversion symmetry the Laporte selection rule is further relaxed by admixture of states having opposite parity compared to the $4f^n$ states. Consequently, $f \rightarrow f$ transitions are observed much weaker on lattice sites having inversion symmetry.

The Tm^{3+} doped crystals (Section 3.2.1) investigated in this work have one regular site with inversion symmetry, which can be changed by local charge compensation.

Spin selection rule

Electric dipole transitions require the spin to be conserved.

$$\Delta S = 0$$

The spin-selection rule is relaxed in presence of spin-orbit coupling, since the wave function cannot be factorized strictly to $\psi = \psi_{space} \cdot \psi_{spin}$. Hence, spin-forbidden features are expected in the spectra. For transition metal ions with weak spin-orbit coupling they appear as weak bands, whereas intensity for rare earths is somewhat increased due to the stronger spin-orbit coupling.

Selection rule for the total quantum number J

In the case of $4f$ rare earth ions the selection rule derived by Judd and Ofelt [JUD62, OFE62] from calculations of crystal spectra intensities become for *electric dipole transitions*

$$|\Delta J| \leq 6$$

with the exception of the following $J \rightarrow J$ transitions: $0 \rightarrow 0$ is forbidden, and $0 \rightarrow 1$, $0 \rightarrow 3$, $0 \rightarrow 5$ appear extraordinary weakly in RE ions having an even number of electrons [DIE68]. For *magnetic dipole transitions* the selection rule reads

$$|\Delta J| = 0, \pm 1$$

with the exception of the $J \rightarrow J$ transition $0 \rightarrow 0$.

2.4.2 Intra-configurational $4f^n \rightarrow 4f^n$ transitions

Trivalent RE ions in $4f^1$ (Ce^{3+}) to $4f^{13}$ (Yb^{3+}) configuration possess partially filled $4f$ shells, which account for their characteristic emission. The energy levels are only weakly affected by the environment due to shielding by outer $5s$ and $5p$ electrons (Section 2.2.1) and may change by some 100 cm^{-1} in different hosts (Section 4.1.1).

The number of free ion $4f^n$ levels becomes quite large in the middle of the RE series (Figure 2.7). Thus, especially for the $4f^4$ to $4f^{10}$ electronic configurations, several levels usually form a *block of states*, in which non-radiative multi-phonon relaxation predominantly occurs (Section 2.6). RE ions have the fairly unique property of emitting narrow, weak lines in solid phase in the infrared, visible, and UV part of the spectrum.

The $4f^n$ energy level diagram of trivalent RE ions incorporated in LaF_3 has been accurately investigated by Carnall *et al.* [CAR89, CAR88, CAR83, CAR70] and is shown in Figure 2.8. La^{3+} is the largest of the trivalent lanthanides (Table D), and the local symmetry for the substitutional ion is rather low (C_2 or C_{2v}). For the investigation of fluorides at high resolution, this data is more appropriate for comparison than the well-known *Dieke diagram*, which comprises trivalent lanthanides in $LaCl_3$ [DIE68].

Each $^{2S+1}L_J$ level is split into up to $(2J+1)$ sublevels by the crystal field Stark effect, further depending on the local symmetry (Section 2.2.1). In Figure 2.8, the broader bands corresponding to one value of J consists of the respective crystal field split energy levels in LaF_3.

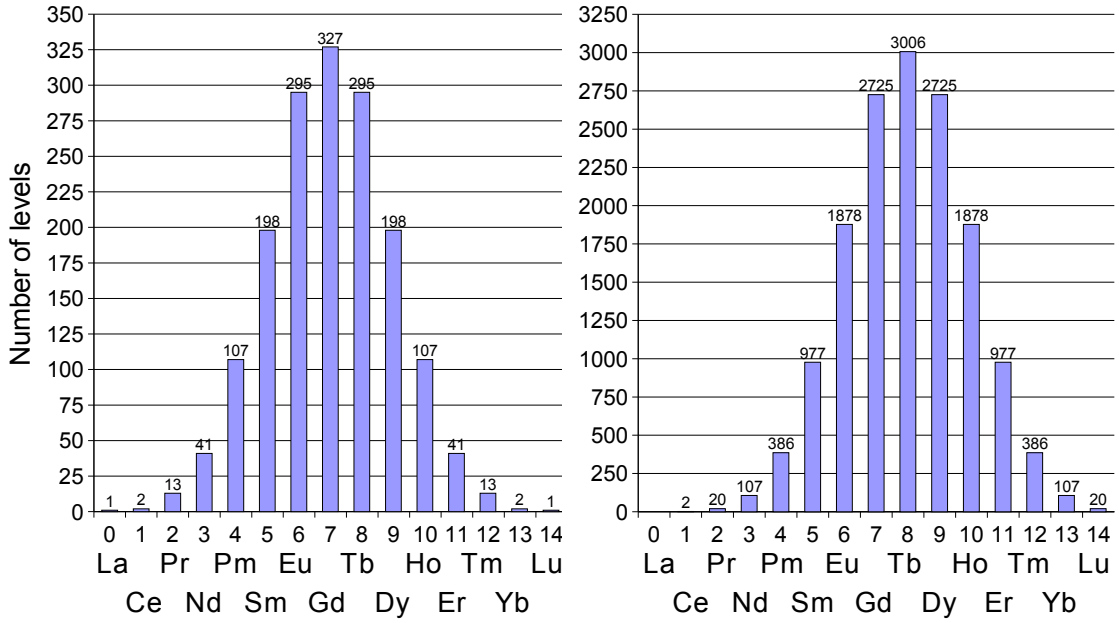

Figure 2.7: Total number of free ion $4f^n$ (left) and $4f^{n-1}5d$ (right) energy levels of the trivalent RE ions. Values taken from [DIE68].

2.4.3 Inter-configurational $4f^{n-1}5d \rightarrow 4f^n$ transitions

In addition to the $f \rightarrow f$ transitions of the trivalent RE ions, transitions involving the $4f^{n-1}5d$ states are frequently observed. The $f \rightarrow d$ excitation usually commence in the vacuum ultraviolet (VUV) spectral region above 50 000 cm^{-1} (below 200 nm) and is extended over several thousand wavenumbers. The energy depends more on the local environment than that of the $4f$ states, since they are not shielded by filled outer shells.

Emission due to $d \rightarrow f$ transitions is usually originating from the lowest onset of the $5d$ states. Excitation into higher d levels is followed by a fast non-radiative relaxation via the d states and subsequent spin-allowed or spin-forbidden transition to lower f levels. This is frequently observed for RE doped crystals, and the spin-forbidden $d \rightarrow f$ transition to higher $4f$ states in LiCAF:Tm^{3+} and LiSAF:Tm^{3+} has been established in this thesis (Section 4.3).

In Ce^{3+} the $4f \rightarrow 5d$ transition energy is the lowest among the RE ions. The closest $4f$ level $^2F_{7/2}$ is still much lower in energy. Furthermore, due to the parity- and spin-allowed nature of the $d \rightarrow f$ transition, the decay time of the Ce^{3+} emission is extraordinary fast [SHI96]. In LaF_3:Ce^{3+} the fast decay time is experimentally determined to be 20 ns [MOS94], and that in LiCAF:Ce^{3+} 25 ns [GEK03].

While fine structure of $d \rightarrow f$ transitions in the UV of light rare earth ions has been inves-

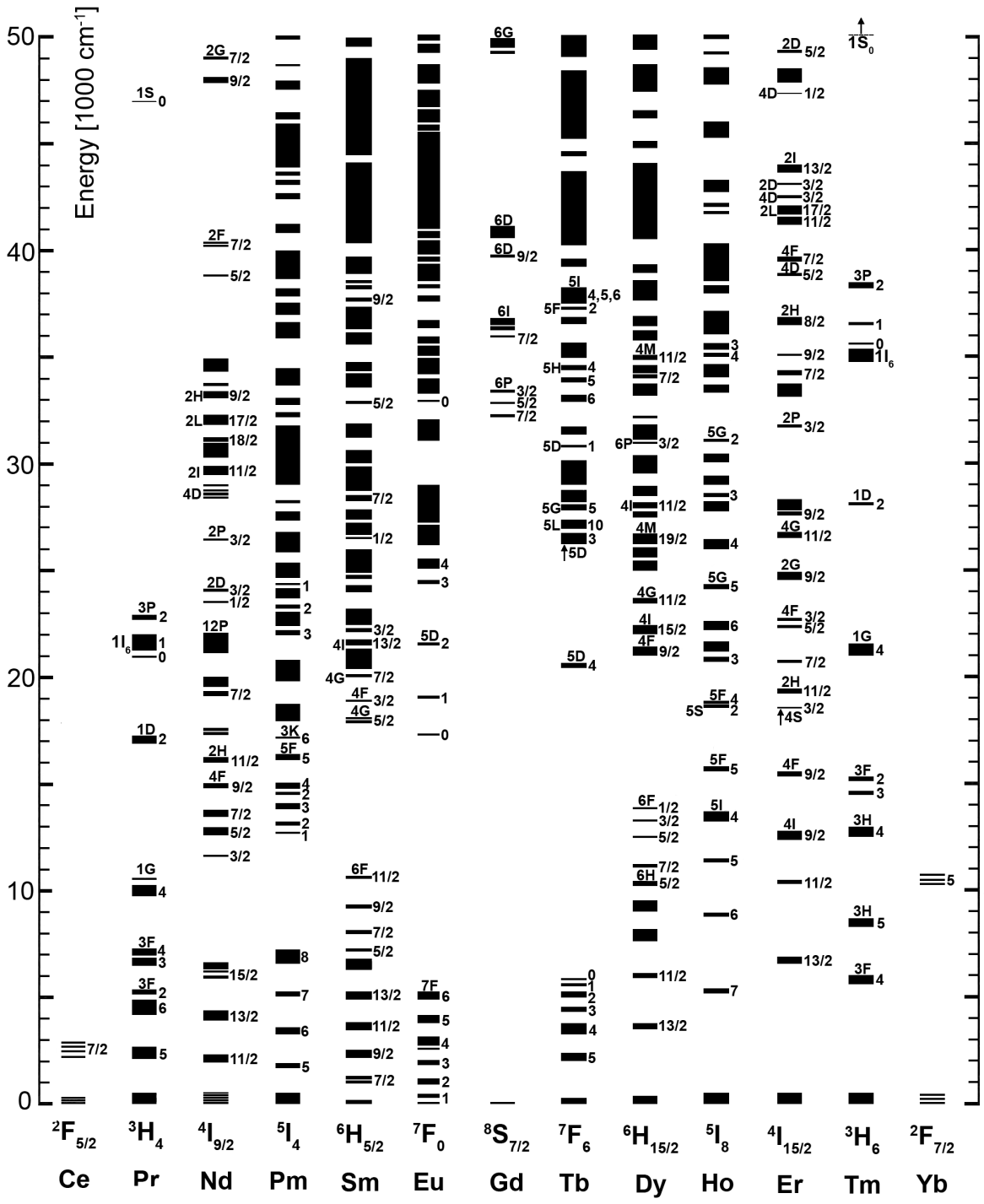

Figure 2.8: The $4f^n$ energy level diagram of trivalent rare earth ions in LaF_3 [CAR88].

tigated thoroughly, the heavier RE, subject to intermediate coupling, are located at higher energies in the VUV which requires a specialized setup. Due to resolution limitations in experiments with heavier RE, the $d \rightarrow f$ transitions are observed usually as broad bands without any structure. The heavier RE ions are subject to intermediate coupling, thus fine structure is expected and observed for the first time in Tm^{3+} doped LiCAF, LiSAF, and BYF crystals (Sections 4.5.2 and 4.5.5).

The energy of the onset of the $5d$ states can be predicted roughly by an empirical method [DOR00], if at least the data for one RE ion is known in the particular host (Section 4.1.2).

2.5 Charge transfer transitions

Charge transfer (CT) transitions are transitions involving ligands and/or central ions, while the charge configuration is changed.

In general, there are four different types of CT transitions:

1. Ligand to Metal (LMCT)

   An electron is promoted from a low-lying ligand orbital to the ligand field orbitals, which have large contributions from the metal orbitals.

2. Metal to Ligand (MLCT)

   The promotion of an electron from a low-lying metal orbital to unoccupied ligand field orbitals is characteristic for strong-field ligands such as CO and CN^-.

3. Metal to Metal (inter-valence)

   If more than one type of metal ions is present, including one type in different oxidation states, transitions between their orbitals can occur.

4. Intra-Ligand

The CT transition is usually described by an electron being promoted from one orbital to another. On the other hand, this process may be regarded merely as large spacial expansion of the charge distribution around the optically active ion rather than an actual *transfer* [PIE00].

The width of a CT state ranges from 5000 to 10 000 cm^{-1} and a large Stokes' shift of several thousand wavenumbers. CT transitions are generally very intense, while the spin selection rule still applies. The intensity is due to the displacement of the charge across the typical inter-atomic distance, thus producing a large transition dipole moment and a large oscillator strength. The Laporte selection rule is only applicable for inter-valence CT transitions.

The CTS energy can be estimated based on the concept of optical electronegativities by Jørgensen (Section 2.5.1), and a practical model predicting CT transfer energies in fluorides is discussed for RE ions (Section 2.5.2), as well as peculiarities of Mn^{2+} (Section 2.5.3).

2.5.1 Energy estimation of charge transfer states

Jørgensen has realized that the energy of a charge transfer state (CTS) depends on the ionization potential of the donor and the electron affinity of the acceptor ion. In chemistry, these properties are successfully described in the (empirical) model of electronegativities. Consequently, a model of optical electronegativities has been developed [JOR62, JOR70] which allows the prediction of CT transitions.

The distance between both ions is further influencing the energy in the particular ion surrounding. This requires to be accounted for by introducing additional parameters. With increasing distance between both ions the CT band is shifted to lower energy.

The energy of a CT transition can be parameterized by

$$E_{CT} = \chi(X) - \chi(M) + q(\Delta\chi(M)) + \frac{4}{3}D \tag{2.13}$$

where $\chi(X)$ and $\chi(M)$ are the optical electronegativity of ligand and metal, $\Delta\chi(M)$ is the difference in optical electronegativity for M^{n+} and $M^{(n-1)+}$, D is the spin-pairing energy parameter ($\approx 7B$) for d electrons, and q is the number of d electrons.

This equation can be simplified to

$$\nu'_{CT} = 30000\ \mathrm{cm}^{-1} \cdot (\chi_{opt}(X) - \chi_{uncorr}(M)) \tag{2.14}$$

where $\nu'_{CT} = \nu_{obs} - f(D)$, and $f(D) = [\langle S(S+1)\rangle - S(S+1)]$ with $\langle S(S+1)\rangle = q(q+2)/4 - [(2l+2)q(q+1)]\,/\,[2(4l+1)]$ being the average value of $S(S+1)$ for the configuration l^q. $f(D)$ ranges from $-\frac{20}{3}$ to $+2$ for different d^n configurations. The optical electronegativity $\chi_{opt}(X)$ of the anion is approximately the Pauling electronegativity.

The practical application is hampered by missing values for the site-dependent optical electronegativities in the literature. The estimates which can be obtained leave still some uncertainty.

2.5.2 Charge transfer transitions in Rare Earth Ions

CT transitions of LMCT type are commonly exhibited as broad bands in excitation spectra of RE ions. The CT excitation in fluorides is located at higher energies compared to oxides or chlorides.

Using measured $O^{2-} \rightarrow Ln^{3+}$ charge transfer energies in YF_3 and LaF_3 as well as the concept of optical electronegativities by Jørgensen (Section 2.5.1), the $F^- \rightarrow Ln^{3+}$ transfer energies have been calculated as shown in Figure 2.9 [BEL99]. The $F^- \rightarrow Tm^{3+}$ CT band is predicted to be at 73 400 cm^{-1} (136 nm), whereas the $O^{2-} \rightarrow Tm^{3+}$ band is located at 52 400 cm^{-1}

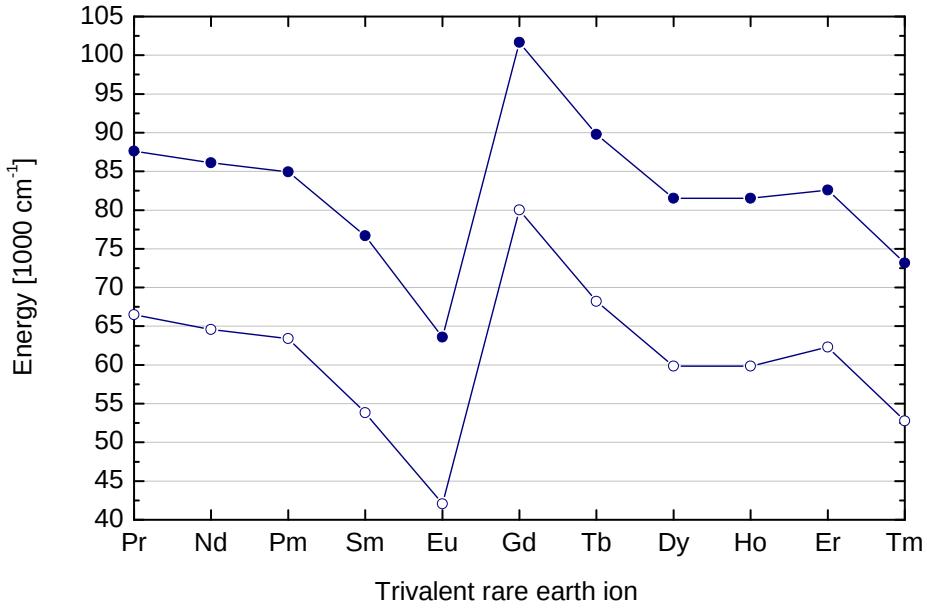

Figure 2.9: Energy of the charge transfer bands of trivalent RE doped fluorides (•) and oxides (○). Values taken from [BEL99].

(190 nm), yielding an energy difference of 21 000 cm^{-1}. However, one has to keep in mind that the energy values obtained are restricted to the specific crystal hosts.

In some fluoride hosts, the energy of the $F^- \rightarrow Ln^{3+}$ CT transition is obscured by $4f \rightarrow 5d$ or host absorption. Eu^{3+} ($4f^6$) and Yb^{3+} ($4f^{13}$) have the lowest CT energy, which is usually well below the $5d$ levels.

Oxygen impurities unintentionally introduced in fluorides during the sample preparation may lead to additional CT excitation bands in the spectra. Significant excitation or absorption due to oxygen impurities related CT bands has not been observed in the spectra presented in this work.

Charge transfer luminescence

CT luminescence, i.e. luminescence resulting from transitions from the CT state to the ground state or lower excited levels, is usually not observed in RE doped crystals. This is due to the overlap of electronic states with the CT state, resulting in efficient non-radiative energy transfer to the high-lying $4f$ states. In the configurational coordinate diagram in Figure 2.10 (a) this is depicted as intersection crossing by a thick arrow. The transition energy is plotted versus the configurational coordinate Q. The RE ions possess numerous $4f$ levels at

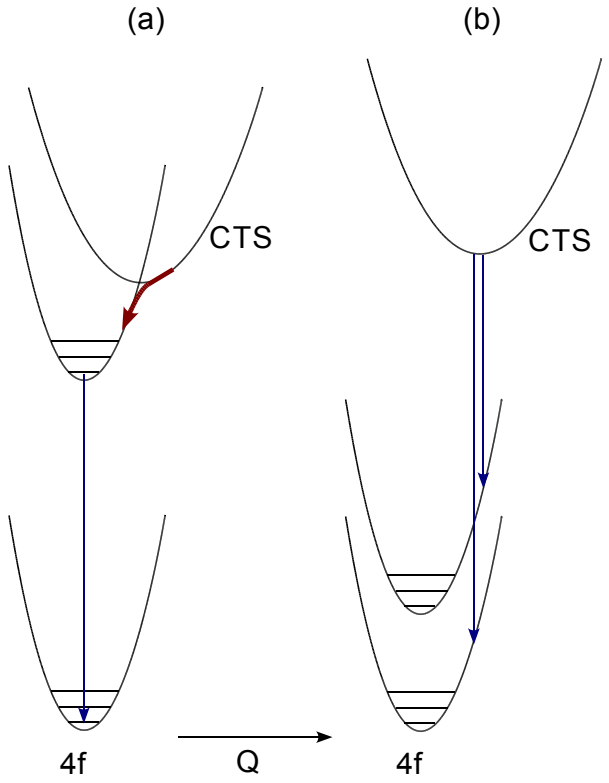

Figure 2.10: Configurational coordinate diagram of $4f$ states interacting with the CT state. (a) Usually fast relaxation from the CT state to high-lying $4f$ states occurs. (b) In Yb^{3+} and Ce^{4+} CT luminescence is observed, due to the lack of high-lying $4f$ states.

higher energy, increasing towards $4f^7$ (Gd^{3+}) electronic configuration (Figure 2.8), thus CT luminescence is typically not expected due fast non-radiative energy transfer to the $4f$ states.

CT luminescence has been observed for Yb^{3+} doped phosphates [NAK78], oxysulfides [NAK79], and recently for fluorides [PIE00]. The only excited $4f$ state $^2F_{5/2}$ in Yb^{3+} is located 10 000 cm^{-1} above the ground state, therefore fast relaxation from the CT state to the $4f$ states does not occur as shown in Figure 2.10 (b).

In most rare earths, also in Tm^{3+}, this luminescence is quenched even at low temperature due to fast relaxation of the overlapping $4f$ or $5d$ states.

Estimation of charge transfer energies

The position of $5d$ levels in trivalent [DOR00] and divalent [DOR03a] rare earth ions can be estimated relative to the position of Ce^{3+} in the respective host (Section 4.1.3). A similar approach is feasible for predicting CT transitions of trivalent RE ions relative to the

Eu^{3+} transition, which is well-established manifesting as separate excitation band in fluorides [GER94].

If the CT energy of one RE ion is known, the tabulated energy shift for all rare earths in this specific host can be estimated [DOR03b]. The CT energy in LiCAF:Tm^{3+} is predicted to be 13 470 cm^{-1} higher in energy than that of LiCAF:Eu^{3+}.

The $F^- \rightarrow Tm^{3+}$ charge transfer excitation of Tm^{3+} ($4f^{12}$) has been observed in fluoride crystals in this work around 127 nm (Section 4.4).

2.5.3 Charge transfer transitions in Mn^{2+}

In general, CT transitions in transition metal ions are not well investigated, unlike those in rare earth ions.

Manganese is known to exhibit strong CT transitions, depending on the oxidation state (Section 1.3.1). The intense $Cl^- \rightarrow Mn^{2+}$ CT band is placed at about 58 000 cm^{-1} [HIR82], while the $F^- \rightarrow Mn^{2+}$ band is shifted by 27 000 cm^{-1} to higher energies [LEV84], yielding approximately 85 000 cm^{-1} (118 nm) in fluorides.

2.6 Non-radiative transitions

Energy transfer in solid-state lattices [CAR23] has been modeled in the pioneering work of Förster [FOE48, FOE49], Dexter [DEX53], Inokuti and Hirayama [INO65]. Non-radiative transitions, i.e. without emission of photons, can be *intra-ionic* phonon-assisted or *inter-ionic* processes. The standard Inokuti-Hirayama model assumes a uniform distribution of acceptors and donors and a single interaction between them. Advanced models include non-uniform statistical acceptor-donor distributions applicable in cases of ion pairing (which changes the transfer radically) as well as energy transfer from multiple sites [ROT96].

Multi-phonon relaxation

In terms of the configurational coordinate model (Section 2.3), non-radiative transitions occur due to intersection crossings between two coordinate curves. The activation energy depends further on the temperature, which is accounted for quantum mechanically by considering lattice vibrations and the thermal population of the ground state. Temperature quenching of emission in all coupling cases can be explained in terms of crossing and tunneling processes as well as multi-phonon emission [STR75].

The radiative emission rate of levels close in energy is reduced by competitive non-radiative transitions of phonons coupled to the electronic state. The non-radiative transition rate for temperatures $T \to 0$ can be expressed as

$$\omega_{nr} = \alpha \exp\left(-\beta \frac{\Delta E}{E_{eff}}\right)$$

where α, β are constants of the lattice, ΔE is the energy distance of the corresponding levels, and E_{eff} is the effective phonon energy.

The number of phonons to be created simultaneously depends linearly on the energy between the states. As a rule of thumb, radiative emission becomes dominant if the energy gap exceeds four to five phonon energies for rare earths ions.

In general, fluorides have relatively low phonon energies of a few hundred cm^{-1}, therefore energy levels closer than 2000 cm^{-1} may be bridged by multi-phonon relaxation rather than emitting. With increasing phonon energy emission of further nearby states becomes quenched. In crystals such as $LiYF_4$ an energy gap of approximately 2500 cm^{-1} can be bridged by the creation of five phonons, the maximum phonon energy being $h\nu_{max} \approx 560\ \mathrm{cm}^{-1}$ [SAL97].

Chapter 3

Experimental methods

3.1 Crystal preparation

3.1.1 Solid state reaction

Highly-pure fluoride powders are mixed thoroughly, e.g. in the case of $LiCaAlF_6$ (LICAF) growth LiF, CaF_2, and AlF_3 powders with purity of 99.99%. A certain percentage of one ion type is substituted by the respective dopant, i.e. TmF_3 or MnF_2 with purity 99.999%. LiF is co-doped for charge compensation as needed, and 1% LiF is added in excess to compensate for evaporation losses of the same.

A small furnace at the *Institut für Laser-Physik der Universität Hamburg* (Germany) is used to apply a temperature curve to the powder mixture within N_2 atmosphere. The reduction of the surface material prevents water inclusions. Additional HF gas reduces oxygen impurities contained in the starting materials, which is hardly avoidable without fluorination.

If a certain temperature is reached and the correct composition is used, solid state reaction yields the desired compound as polycrystalline powder. This powder is useful for spectroscopic investigation, however, it may contain several crystal phases. The samples in this thesis have been tested for quality by X-ray diffraction, microprobe, and spectroscopic techniques. In a second step Czochralski growth can be performed with the polycrystalline material as described in the following section.

3.1.2 Czochralski growth of single crystals

The commercial setup of the company *Crystallox* has been made available by the *Institut für Laser-Physik* for Czochralski growth [CZO18] of single crystals [ELL98, WIL88]. The setup provides power up to 35 kW which is sufficient to grow large fluoride crystals that have generally moderate melting points.

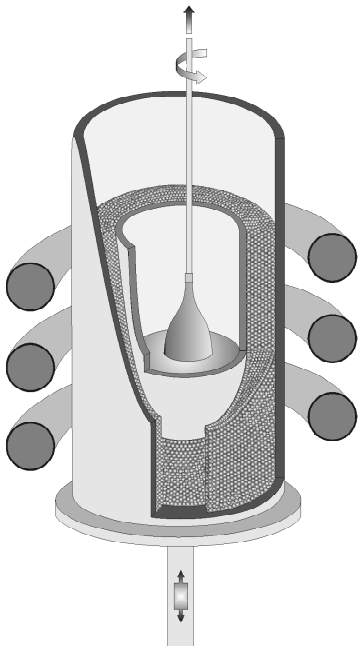

Figure 3.1: Czochralski growth of single crystal fluorides.

As starting material, the polycrystalline material prepared by solid state reaction (Section 3.1.1) is placed in a carbon crucible, which is located within a second larger crucible. A water-cooled induction coil with diameter 140 mm induces a high-frequency to the outer crucible, which transfers the heat through granulate carbon to the inner crucible.

In order to start the crystal growth, a water-cooled wire from the top is dipped into the melt just above the crystallization temperature. By measuring the total weight of the crucible setup, the diameter is controlled during the growth process. Deviations are compensated by the computer controlled PID (Proportional, Integral, Derivative) regulating the heating power. At the same time the wire is pulled upwards with 1 mm/h and rotated with 9 rpm. Oxygen inclusions are avoided by flushing several times with nitrogen. The crystal growth is carried out in N_2 atmosphere containing 5% reducing H_2.

For the purpose of this thesis, LiCAF:Tm^{3+}, LiCAF:Mn^{2+}, and LiCAF:Tm^{3+},Mn^{2+} single crystals have been successfully grown at the Institut für Laserphysik, Universität Hamburg. Faint cracks, especially at the bottom part of the crystal, can be recognized. This is introduced by thermal stress during the growth process and irrelevant for spectroscopic purposes.

However, Czochralski growth from polycrystalline material of LiSAF:Tm^{3+}, LiSAF:Mn^{2+}, LiSAF:Tm^{3+}, Mn^{2+} was unsuccessful. The growth of LiCAF and LiSAF single crystals has been reported without cracks or inclusions up to diameters of 50 mm by using special techniques [SHI00, SHI01a]. Part of the $LiSrAlF_6$ powders from the solid state reaction has been kept for spectroscopic purposes.

3.1.3 Crystal characterization

Powder diffractometry

The polycrystalline LiSAF:Tm^{3+}, LiSAF:Mn^{2+}, and LiSAF:Tm^{3+},Mn^{2+} samples have been proved to be single phase. The help of Dr. D. Schiffbauer (Universität Köln, Germany) in providing the X-ray powder diffractometry is acknowledged.

Quantitative analysis

		Tm^{3+}		Mn^{2+}
	melt	analysis	melt	analysis
LiCAF:Tm(A)	2.655	0.038 ± 0.010		
LiCAF:Mn(A)	-	-		0.055 ± 0.008
LiCAF:Tm,Mn(B)	2.654	0.030 ± 0.023	0.575	0.085 ± 0.022
LiCAF:Tm,Mn(A)	0.888	0.019 ± 0.019	0.289	0.027 ± 0.024
LiCAF:Tm,Mn(C)	2.322	0.010 ± 0.010	0.126	0.025 ± 0.017
BaY_2F_8 : Tm		0.679± 0.033		0.000
$Ba_{0.95}Mn_{0.05}\,(Y_{0.99}Tm_{0.01})_2\,F_8$ (N3)		0.000		$0.000^{\dagger}$
$(Ba_{0.99}Mn_{0.01})\,Y_2F_8$ (N4)		0.000		0.000
$Ba\,(Y_{0.99}Mn_{0.01})_2\,F_{7.98}$ (N5)		0.861±0.019		0.000
$Ba\,(Y_{0.94}Mn_{0.05}Tm_{0.01})_2\,F_8$ (N6)		0.873±0.033		0.000

Table 3.1: Ion concentration (in weight percent) in the original melt and after the growth. The standard deviation is denoted as result of several probes. †0.024% within inclusion.

The LiCAF and LiSAF samples exhibited very weak $f \rightarrow f$ luminescence, therefore a quantitative trace analysis has been performed in order to obtain the actual dopant concentrations (Table 3.1). Only a few percent of the Tm^{3+} and Mn^{2+} concentration which was originally in the melt is found in the crystal, which is nearly at the detection limit of the microprobe analysis. This is quite surprising regarding the fact that other rare earth and transition metal ions are incorporated very well into LiCAF or LiSAF, such as Ce^{3+} [SHI01a], Eu^{2+} [KIR05], and Cr^{3+} [PAY89].

An explanation can be only speculative, partially attributing this observation to the large Tm^{3+} ion which requires charge compensation which requires charge compensation if incorporated into the Ca^{2+} site of LiCAF. While during crystal growth, charge compensation has been provided by an excess of LiF (Li^{+} substituting Ca^{2+}), recent defect simulation studies proved Li^{+} or fluorine interstitials being a more probable compensation mechanism [AMA03, AMA04]. The Al^{3+} site is much smaller than the rare earth ions, nevertheless substitution of this site is clearly preferred in LiSAF.

The Mn^{2+} ion has only 80% of the size of Ca^{2+}(Section D). Similarly, the charge difference

between the Ce^{3+} impurity ion and the substitutional K^+ site in $KMgF_3$ is believed to be the main reason for the low level of doping concentration achieved [FRA97].

The samples LiCAF:Tm(A) and LiCAF:Tm,Mn(A) yielded the best spectroscopic results and have been used in the experiments presented in this thesis.

A single crystal BaY_2F_8 (BYF) doped with Tm^{3+} of good optical quality has been used for time-resolved and high resolution spectroscopy of $4f$ and $5d$ states, grown by T. Ouvarova from *General Physics Institut, Moscow, Russia*. However, the co-doped BYF crystals that have been ordered for extended analysis of this promising material exhibited large deviations from the nominal doping concentrations, even though Tm^{3+} is known to be incorporated very well. Mn^{2+} has been detected only in an inclusion, which suggests that Mn^{2+} is not incorporated into BYF host but manifests in a different phase. Due to the uncertainty concerning the crystal composition, a comprehensive discussion is beyond the scope of this thesis. Nevertheless, interesting excitation spectra have been measured in this work and are shown in Appendix A.

3.2 Overview of investigated samples

The spectroscopic properties of impurity ions depend on the local surrounding and site symmetry, thus a basic knowledge of the crystal structure is crucial for the evaluation of intra- and inter-configurational transitions, vibronic fine-structure, and intra-ionic energy transfer processes. Moreover, necessary charge compensation or color center formation influence the symmetries and optical properties.

$LiCaAlF_6$ (LiCAF) single crystals doped with Tm^{3+} and Mn^{2+} have been successfully grown by the Czochralski method in this work (Section 3.1.2). For comparison, polycrystalline samples of $LiSrAlF_6$ (LiSAF) have been obtained by solid state reaction (Section 3.1.1). $KMgF_3$:Mn^{2+} and MgF_2:Mn^{2+} were kindly provided by the *Institut für Laser-Physik*.

The selected fluoride crystals hosts have been investigated and exhibit advantageous properties, such as the capability of lasing with wider UV tunability of Ce^{3+} in LiCAF and LiSAF [MAR94b]. In addition the appealing possibility of co-doping one type of ion into the divalent and the other into the trivalent Al^{3+} site would defeat the need for charge compensation, while energy transfer via the shared F^- ion is a prospective possibility. From spectroscopic and further crystallographic considerations after the experiments it is found, however, that both Tm^{3+} and Mn^{2+}occupy the Ca^{2+} or Sr^{2+} site at rather low concentration.

$BaMgF_4$ offers the large Ba^{2+} as well as the Mg^{2+} lattice site. Two principal super-exchange paths have been proposed, permitting electron transfer between transition metal ions in $BaMgF_4$ and $KMgF_3$ [FER70]. In general, Mg^{2+} is well suited for Mn^{2+} doping due to the matching ion sizes and charge configurations.

The fluoro-perovskite $KMgF_3$ allows doping of rare earths with charge compensation. Energy migration between Er^{3+} substituting two Mg^{2+} sites and subsequent energy transfer to Mn^{2+} has been found in the perovskite $RbMgF_3$ and in a preliminary study of $KMgF_3$ [SHI82]. The charge compensation was determined to be predominantly non-local, thus leaving the local symmetry unchanged. The Mg^{2+} site does not require charge compensation for Mn^{2+} doping.

In this section the investigated crystals are briefly characterized. The computer software *Diamond 2.1* (Crystal Impact GbR) from the *Institut für Laserphysik* has been used to visualize the crystals. The corresponding lattice parameters are given in Table 3.2, and the symmetry of the space and point groups is summarized in Table 3.3. Ionic radii and weights of selected elements are tabulated in Appendix D.

3.2.1 LiCAF and LiSAF

Figure 3.2 shows the crystal structure of LiCAF and the iso-structural LiSAF compound, having Ca^{2+} (ionic radius 114 pm) substituted by Sr^{2+} (130 pm). Both are members of the *colquiriite* family of fluoride compounds LiMM'F_6 (M=Ca, Sr; M'=Al, Ga, Cr). They are

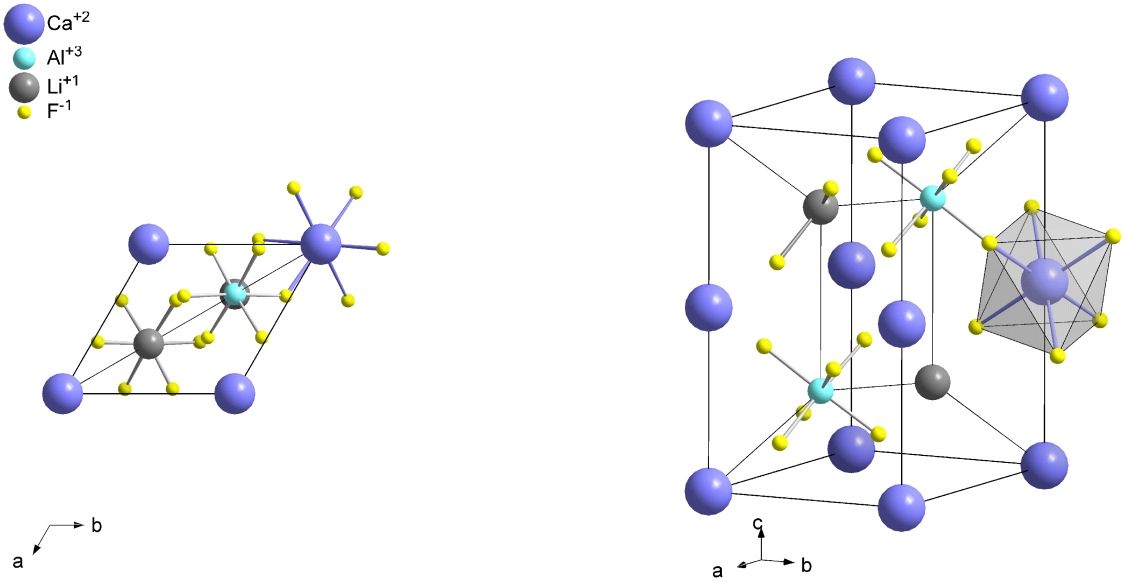

Figure 3.2: Crystal lattice structure of LiCAF and LiSAF.

considered to be the most promising materials for optical applications, such as lasers and scintillators [KLI99, PAY89]. LiCAF and LiSAF [DUB93a, DUB93b, MAR94b] doped with Ce^{3+} have proved successful in yielding large gain and tunable output. It was suggested that LiCAF is very stable concerning the creation of X-ray induced color centers as well as the gradual surface damage in air [SAT02a, SAT02b]. The spectra investigated, however, can be explained in terms of non-radiative energy relaxation, while the situation is different at low temperature (cf. Section 4.2).

Recently, refined lattice parameters of LiCAF and LiSAF have been obtained [GRZ04] in agreement with previous data [SCH91]. The crystal structure manifests in the hexagonal symmetry ($P\bar{3}1c$), an ordered derivative of the $LiZrF_6$ type. Each cation (Li^+, Ca^{2+}, Al^{3+}) occupies a distorted octahedral (O_h) lattice site. The deformation is correlated with the cation size [SCH91]. The ionic radius of Al^{3+} (67 pm) is much smaller than that of the trivalent RE (>100 pm) or Manganese (81 pm). Cr^{3+} ions occupying the Al^{3+} lattice site experience symmetry lowering distortions, while the deviation from O_h symmetry is not determined to be large [PAY89]. In this respect the valence of the Li^+ site (90 pm) is even more unfavorable.

In LiCAF crystal Tm^{3+} ions prefer entering the lattice on the divalent Ca^{2+} site regardless the ionization state, thus requiring charge compensation. EPR and site-selective laser spectroscopic studies of LiCAF:Gd^{3+} at low concentration suggested that three types of distinct centers were formed [ANT97, ABD01], attributed to Gd^{3+} on Ca^{2+} sites with charge compensation as well as Gd^{3+} on Al^{3+} sites, which is one order of magnitude less represented.

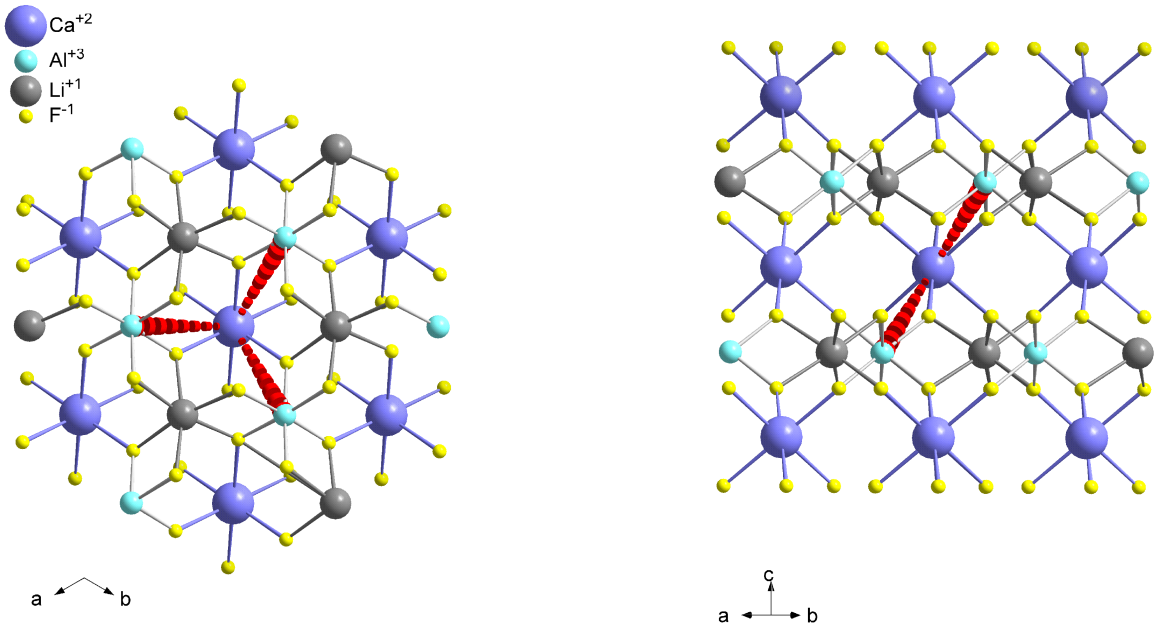

Figure 3.3: Super structure in LiCAF and LiSAF, emphasizing prospective energy transfer between Ca^{2+} and Al^{3+} sites (distance 3.764 Å).

Figure 3.3 shows the super structure of LiCAF and LiSAF, emphasizing the prospective energy transfer path, presumably mediated via the F^- ions. Possible substitutional lattice sites for Tm^{3+} and corresponding charge compensation schemes are discussed.

Recently, defect simulation and crystal field studies have been carried out for rare earth ions doped into LiCAF and LiSAF [AMA03, AMA04]. Charge compensation involving Li^+ vacancies has been proven to be the preferred in LiCAF. Two alternative mechanisms have only slightly higher potentials and may occur along with the previous one: Tm^{3+}may substitute an Al^{3+} ion despite the large size mismatch, thus requiring no further compensation. Furthermore, there are empty gaps between Ca^{2+} octahedrons in the *ab* plane which may contain next-nearest fluorine interstitials similar as the empty cubes in CaF_2 or SrF_2 [JAC71]. All charge compensation mechanisms in LiCAF have similar potentials from the defect simulation, leading to the assumption that more than one site will be occupied by Tm^{3+}.

The LiSAF structure is essentially the same, the larger cell parameters due to the larger Sr^{2+} ion lead to a reduced field at this lattice site. The size of Al^{3+} site in LiCAF is smaller than that of the rare earth ions, remaining the same in LiSAF. However, the larger lattice parameters of LiSAF allow relaxation of the local surrounding which is expressed in the Al^{3+} site being clearly the most favored one in LiSAF [AMA03]. The enlarged lattice provides more space for fluorine interstitials as charge compensation, whereas the potential calculated for this mechanism is lower compared to the occupation of Al^{3+} sites.

3.2.2 BaY_2F_8

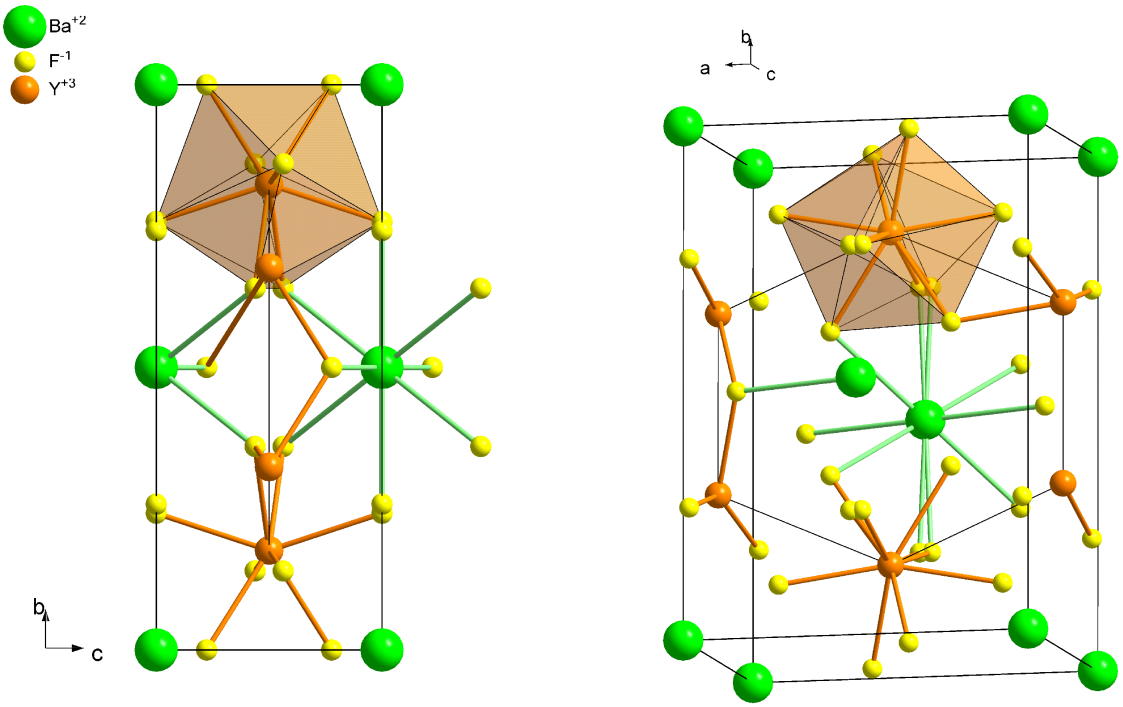

Figure 3.4: Crystal lattice structure of BaY_2F_8.

The BaY_2F_8 (BYF) crystal shown in Figure 3.4 has been reported to be of monoclinic $\beta - BaTm_2F_8$ structure with space group $C2/m$, which is maintained as such if rare earths ranging from Dy^{3+} to Lu^{3+} are incorporated [KAM86]. The single-center Y^{3+} site has point symmetry C_{2h} and is well-suited for doping with trivalent rare earth ions because of its size and ionization state. Although it is surrounded by ten nearest-neighbor F^-, the coordination is approximately eight-fold [KAM86] due to the close distance between two pairs of fluorine ions. The twelve-coordinated Ba^{2+} sites are connected to chains along the c-axis. The $b-$axis is the main symmetry axis.

BYF has phonon energies $\hbar\omega \approx 360 - 380$ cm^{-1} [SVE93], the maximum phonon energy being $\hbar\omega \approx 415$ cm^{-1} [KAM90]. Therefore, this is an attractive host and has been well-studied. Cross-relaxation processes involving $5d$ and $4f$ states of Er^{3+} have been studied in BYF [KIR02a]. Upconversion mechanisms are observed for various rare earth ions, including Tm^{3+} [NOG97], Er^{3+} [POL96], Ho^{3+} [OSI01], and Nd^{3+} [GUY93], as well as laser operation (Section 1.4.3). Time-resolved $5d \rightarrow 4f$ emission spectra of Tm^{3+} doped BaY_2F_8 single crystal (Section 4.5.5) as well as high resolution $d \rightarrow f$ and $f \rightarrow f$ emission spectra (Section 4.3.2) have been measured in this work.

3.2.3 $BaMgF_4$

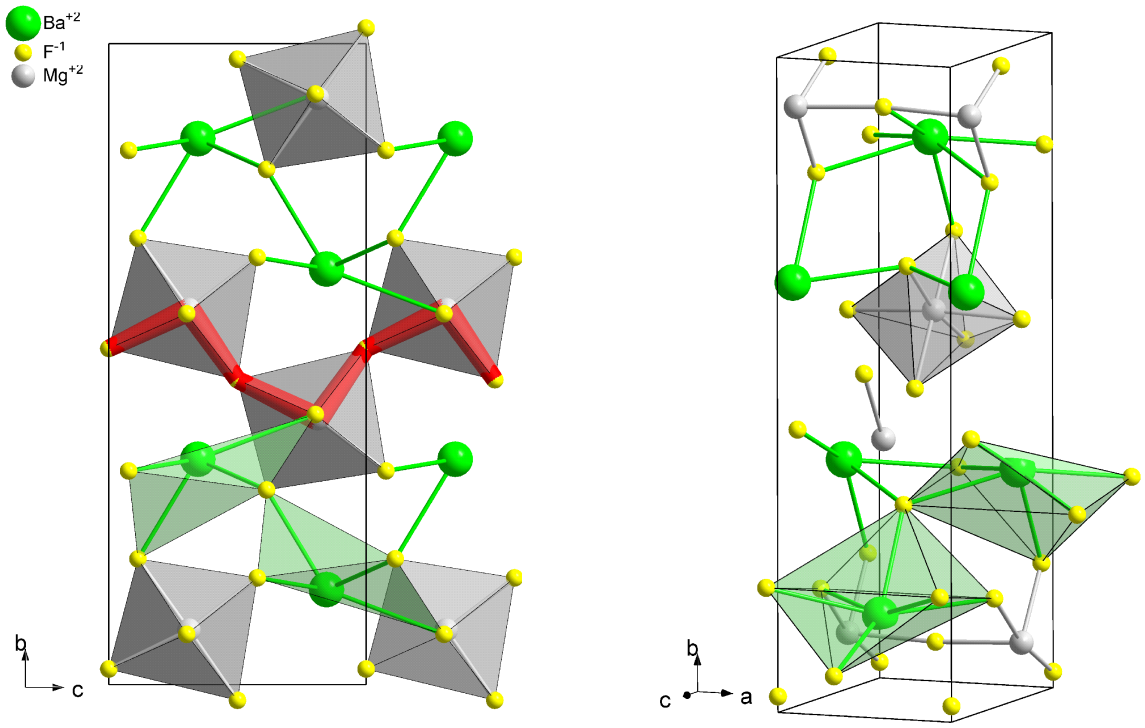

Figure 3.5: Crystal lattice structure of $BaMgF_4$.

$BaMgF_4$ (BMF) manifests in orthorhombic structure. The local surrounding of the Mg^{2+} sites consists of six F^- ions forming distorted octahedra, which are connected to long chains along the *c*-axis of the crystal lattice. Likewise octahedra are connected along the *a*-axis, yielding two principal super-exchange paths of which one is indicated by a broad line in Figure 3.5 (left). $Ni^{2+} \rightarrow Mn^{2+}$ and $Cu^{2+} \rightarrow Mn^{2+}$ electron transfer has been observed in this crystal host [FER70].

Ba^{2+} is surrounded by six fluorine ions forming a trigonal prism. Recently, the possible existence of symmetrically and magnetically non-equivalent sites has been pointed out [KOD01]. The two emphasized Ba^{2+} sites in Figure 3.5 would correspond to the different sites due to commensurate super-structures.

3.2.4 $KMgF_3$ and MgF_2

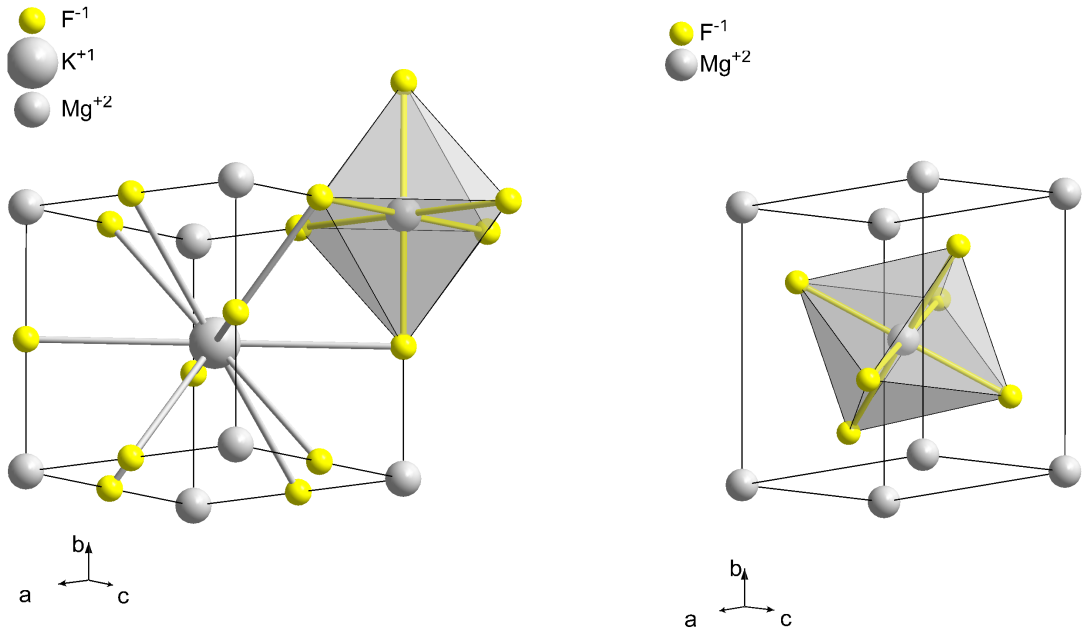

Figure 3.6: Crystal lattice structures of $KMgF_3$ (left) and MgF_2 (right).

$KMgF_3$ (KMF) has a cubic perovskite structure. Taking into account the ionic radii, Mn^{2+} ions preferentially enter the six-fold coordinated Mg^{2+} lattice site of octahedral symmetry without the need for charge compensation. The ionic radius of the twelve-fold coordinated K^+ lattice site is much larger (ionic radius $>$ 165 pm). Nevertheless, this is established being the substitutional site of Ce^{3+} and Pr^{3+} ions, which are found on the Na^+ site in the orthorhombically distorted perovskite $NaMgF_3$.

The Huang-Rhys factor has been obtained experimentally for KMF:Mn^{2+} being $S = 1.35$ [ROD91]. Strong absorption bands in the UV-visible (oscillator strength $\approx 10^{-2}$) and luminescence has been observed due to Mn^{2+} ions perturbed by F centers after irradiation [SIB73]. Ce^{3+}substituting for K^+ requires charge compensation. Two [FRA97], respectively, four [YAM00] different Ce^{3+} luminescent centers were assigned to Ce^{3+} ions perturbed by K^+ and Mg^{2+} vacancies.

Mn^{2+} impurities are incorporated into the KMF and MgF_2 host into Mg^{2+} lattice sites, thus charge compensation is not required. Due to the well matching charge configuration and ion sizes no symmetry distortions are expected. These hosts have been investigated in terms of a systematic study on the VUV spectral region of Mn^{2+} doped fluorides (Section 5.5).

	Z	a	b	c	V	angles	ρ	Ref.
$LiCaAlF_6$	2	4.9998	4.9998	9.6418	208.73	$\gamma = 120°$	2.98	[GRZ04]
$LiSrAlF_6$	2	5.1022	5.1022	10.2563	229.51	$\gamma = 120°$	3.45	[GRZ04]
BaY_2F_8	2	6.9829	10.519	4.2644	308.78	$\beta = 99.676°$	5.02	[GUI93]
$BaMgF_4$	4	4.126	14.518	5.821	348.69		4.53	[GIN97]
$KMgF_3$	1	3.9892	3.9892	3.9892	63.48		3.15	[MUR84]
MgF_2	2	4.628	4.628	3.045	65.22		3.17	[VID79]
CaF_2	4	5.462	5.462	5.462	162.95		3.18	[CHE71]

Table 3.2: Crystal properties and lattice constants of selected compounds. Z is the number of formulae per unit cell; a, b, c are the lattice parameters (Å); V is the unit cell volume (Å^3); ρ is the calculated density (g/cm^3). Only angles deviating from 90° are given.

	Space group		Point group			
$LiCaAlF_6$	$P\bar{3}1c$	trigonal	C_{3i}	Ca^{2+}	(6)	114
			$<O_h$	Al^{3+}	(6)	67.5
$LiSrAlF_6$	$P\bar{3}1c$	trigonal	C_{3i}	Sr^{2+}	(6)	132
			$<O_h$	Al^{3+}	(6)	67.5
BaY_2F_8	$C2/m$	monoclinic	C_{2h}	Y^{3+}	(8)	115.9
				Ba^{2+}	(11)	174
$BaMgF_4$	$Cmc2_1$	orthorhombic	C_s	Ba^{2+}	(6)	149
			$<O_h$	Mg^{2+}	(6)	86.0
$KMgF_3$	$Pm\bar{3}m$	cubic	O_h	K^+	(12)	174
			O_h	Mg^{2+}	(6)	86.0
MgF_2	$P4_2/mnm$	tetragonal	D_{2h}	Mg^{2+}	(6)	86.0
CaF_2	$Fm\bar{3}m$	cubic	O_h	Ca^{2+}	(8)	126

Table 3.3: Crystal space and point symmetry of selected compounds. The corresponding point group of each substitutional lattice site, the coordination number (in parenthesis), and the ion size (in pm) is given, data from [GUI93, KAM86, KEV69, KOD01, PAY89, SCH91].

3.3 The *Superlumi* experimental setup

Our *Superlumi* setup at HASYLAB, DESY, Hamburg has been used for acquiring most spectra by photo-luminescence spectroscopy with synchrotron radiation (Section 3.3.1). This unique experimental station renders possible the acquisition of high resolution excitation, emission, and absorption spectra in the infra-red (IR) to vacuum-ultra-violet (VUV) range [ZIM91]. Time-resolution measurements in the ns region are possible ranging from liquid Helium temperature up to 750 K using a high-temperature copper sample holder developed in our group [BEC98a]. Recently, thermoluminescence spectroscopy has been integrated to the setup as new feature of the enhanced custom-built acquisition software.

The multiple experimental possibilities make this setup predestinated for VUV range spectroscopy, which is particularly useful for investigating rare earth and transition metal ions in crystals or, e.g., rare gas solids [VIE03]. In this section a brief overview is given of the currently installed monochromators (Section 3.3.2) and detectors (Section 3.3.3), which are described in more detail in the given references and in the most recent theses of our group [BEC98a, LIC03, NEG03, SUL02, VIE03]. The time-correlated single photon counting (TCSPC) technique allows accurate time-resolved spectroscopy with superior signal-to-noise ratio (Section 3.3.4). The experimentally determined spectral response and the absolute photon flux of our setup are presented in Section 3.3.5.

3.3.1 Synchrotron radiation

Acceleration of charged particles by the bending magnets of the storage ring causes the emission of *synchrotron radiation*, which is polarized and covers a wide spectral range from IR to hard X-rays. The time characteristic of the particle bunches are well-defined, in the regular five-bunch operation a 150 ps light pulse is emitted every 192 to 196 ns. Single-bunch operation gives a pulse every 964 ns, which corresponds to the time for one revolution of the particles having velocities close to speed of light. The *Superlumi* setup is designed for using the wavelength region from 30 nm to 335 nm in excitation. Decay times in the range 0.2 to 2000 ns can be determined, by using the chopper up to 1 ms, and spectra in several time windows can be acquired simultaneously. The synchrotron luminescence is focused into a 10×0.2 mm image in the plane of the entrance slit. The beam line mirrors are adjusted before every beam time, which changes the image on the primary monochromator and requires measuring new calibration spectra (Section 3.3.5).

3.3.2 Monochromators

The primary monochromator having 2 m focal length is used for excitation by synchrotron radiation. Three secondary monochromators are currently available at our setup and have been used in this work (Table 3.4).

Monochromator	2 m (primary)		1 m	$\frac{1}{2}$ m	SpectraPro 308i		
Mounting	McPherson		McPherson	Pouey	Czerny-Turner		
Aperture ratio	$f:20$		$f:10$	$f:2.8$	$f:4$		
Focal length [mm]	2000		1000	500	300		
Spectral range [nm]	50-335	30-270	50-300	50-300	190-1100		
Grating size [mm^2]	$\varnothing$ 100	$\varnothing$ 100		130 × 130	64 × 84		
Grooves [mm^{-1}]	1200	1200	1200	1650†	300	300	1200
Blaze [nm]	100 (Al)	45 (Pt)	120	250	300	500	300
Dispersion [nm/mm]	0.4	0.4	0.8	1.0	10.8	10.8	2.7
Max. resolution [nm]	0.012	0.012	0.01	0.5	0.11	0.11	0.03
References	[GUE83, ROI84]		[MOE85]	[GUE83]			

Table 3.4: Monochromators at our experimental setup. †on average

Primary monochromator

The primary monochromator consists of an in situ changeable Aluminum and Platinum grating (1200 lines/mm) in 15° McPherson mounting [ROI84], having linear dispersion (0.4 nm/mm) [WIL83]. The entrance slits can be set to 30 μm, 100 μm, and 500 μm, corresponding to best achievable spectral resolutions of 0.02 nm, 0.05 nm, and, respectively, 0.23 nm. The surface quality of the gratings degrade slowly under the influence of the synchrotron radiation. The Platinum grating has not been used for the measurements presented in this thesis.

1 m monochromator

Recently, the 1 m monochromator, which was lent for testing experiments to the FEL, has been installed back at the *Superlumi* [MOE85]. It has a 1200 lines/mm grating in McPherson mounting and is equipped with a position sensitive multi-channel plate (MCP) detector, which allows measurements of emission in the VUV range at extraordinary high resolutions comparable to that of the excitation source.

The best achievable resolution is limited to 0.07 nm by the detector [HAR]. Detailed fine structure in $d \rightarrow f$ emission of Tm^{3+} has been observed for several crystals using this device in combination with the position sensitive MCP (Sections 4.5.2 and 4.5.5). A significant improvement of the resolution is achieved by recording the *second order* luminescence, yielding a resolution better than 0.04 nm as demonstrated for $d \rightarrow f$ emission in LiSAF:Tm^{3+} (Figure 4.12 on page 86).

Pouey type monochromator

The separated UHV chamber of the $\frac{1}{2}$ m Pouey type monochromator is equipped with two detectors. The open micro-sphere plate (MSP) [KOE97, NEG03] and a solar-blind (VUV)

photomultiplier tube. This monochromator has no entrance slit, therefore the resolution is limited by the size of the light spot on the sample. The best resolution achievable reaches about 0.5 nm if operating outside the main working range (150-250 nm) [GUE83]. A considerably large value of f : 2.8 is achieved by using a large toroidal grating in asymmetric mounting. This grating has a non-uniform groove distribution (1650 lines/mm on average).

Czerny-Turner type monochromator

An ARC SpectraPro 308i monochromator in Czerny-Turner mounting is available for measurements in the UV to IR spectral region. The software-controlled unit has three interchangeable gratings and two exit arms equipped with a CCD detector and a photomultiplier Hamamatsu R6358P.

The various detectors available at the *Superlumi* are described in the following section.

3.3.3 Detectors

Photomultiplier tubes

Detector	Hamamatsu R6836	Hamamatsu R6358P	Valvo XP2230B
Cathode (window)	CsTe (MgF_2)	LMA (UV glass)	SbKCs (boro-silicate)
Typical voltage [V]	-1500	-840	-2200
Operation temperature	RT	RT	-15°C
Dark pulses [s^{-1}]	3-5	20	50
Time resolution [ns]	4	1.4	0.7
Quantum efficiency	15% (at 240 nm)	23% (at 530 nm)	48% (at 400 nm)
Spectral range [nm]	115-320	190-830	250-650

Table 3.5: Photomultiplier tubes at our experimental setup.

Three photomultiplier tubes (PMT) for luminescence (Hamamatsu) and reflection (Valvo) spectroscopy are currently installed at our setup (Table 3.5). Single-photon counting photoluminescence measurements in the VUV have been carried out using the Hamamatsu R6836 solar blind PMT, which has a low dark current without cooling. The time resolution is limited, however, most luminescence investigated in this work has decay times in the μs range.

Time-resolved spectroscopy has been carried out using the Hamamatsu R6358P PMT, which is sensitive in the full visible to UV range. Since this is the only part of the setup not in UHV, the operation range is limited by the absorption of air at 190 nm and below.

Reflectivity is measured using the Valvo XP2230B PMT in conjunction with a thin layer of sodium salicylate that converts reflected light into 420 nm emission at a constant quantum yield. The high quantum efficiency at this wavelength with a comparable low background of the Peltier cooled detector yields a high signal-to-noise ratio.

CCD detector

Detector	Princeton Instruments
CCD pixels	1100×300
CCD pixel size	24×24 μm^2
Operation temperature	$-118°C$
Spectral range	190-1100 nm
References	[LIC03, NEG03]

Table 3.6: Charge coupled device (CCD) detector at our experimental setup.

A CCD detector consists basically of a closely spaced array of metal-oxide-silicon (MOS) diodes on an insulator (oxide) layer that covers a semiconductor substrate. The absorbed photo-electrons are collected by sweeping an electric field, described in more detail in [LIC03]. We use a Princeton Research CCD detector connected to the SpectraPro 308 spectrometer (Table 3.6). Operating at temperatures in the range $-119°C$ to $-116°C$ provides a stable signal-to-noise background [NEG03].

Photo diode

An AXUV-100 photo diode is mounted in the UHV sample chamber aligned with the excitation beam on the opposite side of the sample holder. Connected to a highly sensitive electrometer, direct absorption of transparent single crystal with very low doping concentration ($< 0.01\%$) has been measured (Sections 4.4.1 and 5.5.1) with high sensitivity. On the other hand intensities several orders of magnitude higher are still not saturating the diode.

3.3.4 Time-Correlated Single Photon Counting

Time-Correlated Single Photon Counting (TCSPC) has been one of the best techniques for recording light signals of low intensity with accurate time-resolution since conceived by Bollinger and Thomas [BOL61]. This method is based on measuring the time from the excitation pulse to the first photon detected (by PMT or MCP). This is achieved electronically by connecting the (pre-amplified) detector signal to the Constant Fraction Discriminator (CFD) which sends a precisely timed signal to start a linear voltage ramp in the Time-to-Amplitude Convertor (TAC). The time mark of the following bunch from the DORIS storage ring provides the stop signal, and the time difference between the bunches is accurately known. Running the TAC in inverted mode assures that each detected photon is counted.

The TCSPC method relies on the concept that the probability distribution for emission of a single photon after an excitation yields the actual intensity against time distribution of all the photons emitted as a result of the excitation. This probability is constructed from a large

number of synchrotron excitation pulses. This way excellent signal-to-noise ratio and time resolution are achieved.

On purpose, the excitation intensity is kept moderate at high resolution. In principal one could increase the counting rate to the limit that one photon is detected for each excitation pulse, however, on the expense of increased probability that there are two photons incident at the detector during its delay time. The upshot of high counting rates therefore is a bias towards early photons and hence shorter decay times which are inaccurate.

3.3.5 Spectral response

Sodium salicylate calibration for excitation intensity

Synchrotron radiation is the only convenient excitation source in a wide spectral region with excellent time characteristics, ranging in energy from infrared light to hard X-rays. Calibration curves of the intensity distribution have been recorded at the beginning of each beam time, since the spectral characteristics depend on the optimization of the mirrors of the beam line. In the long term the primary grating is slowly degrading, which is also accounted for by this approach.

Sodium salicylate is emitting at 420 nm with a constant quantum yield regardless the excitation energy as shown in Figure 3.7 (upper graph) and is therefore used as standard. If exciting at 200 nm, e.g., the second order of 100 nm exciting light will be present as well. In addition, a lithium fluoride (LiF) or quartz (SiO_2) filter can be inserted on the excitation side before the primary grating, which cuts of the exciting light below 110 nm (LiF) or below 155 nm (SiO_2). After the primary grating, the chopper valve actually consists of a thick LiF window which can be used as well. Thus, on the expense of intensity, excitation by higher orders at the primary grating can be avoided by applying the appropriate filters for the relevant energy range. The curves using SiO_2 and both available LiF filters are shown in Figure 3.7 along with the respective absolute flux.

After subtracting the background counts, the excitation spectra presented in this thesis have been divided by the respective sodium salicylate curves in order to obtain a quantum yield independent of the incident flux.

Photo diode calibration for excitation intensity

The absolute flux incident on the sample has been determined from measurements with a AXUV-100 photo diode (Section 3.3.3), which is shown in in Figure 3.7 (lower graph).

The photo diode is suitable for recording transmission of single crystals. Absorption has been determined for bi-planar LiCAF single crystals polished on both sides from such measurements (Section 4.4.1).

Calibration for detector sensitivity and monochromator transmission

The spectral response of the optics and the detectors is wavelength sensitive as well. A deuterium lamp (< 350 nm) and black body emitter (> 350 nm) has been used for recording the spectral sensitivity of the monochromator-detector system (Figure 3.8). The two curves have been appended, which causes local maxima artefacts in the overlap region. Obviously, the calibration curves for the CCD camera are more reliable than those for the PMT (except for that measured with the 300/500 grating).

The emission spectra presented in this thesis have not been corrected for the spectral response unless indicated otherwise, because a precise knowledge of emission intensities is usually not required for the discussion. Furthermore, the calibration curves are smooth and of comparable intensity in the relevant spectral range.

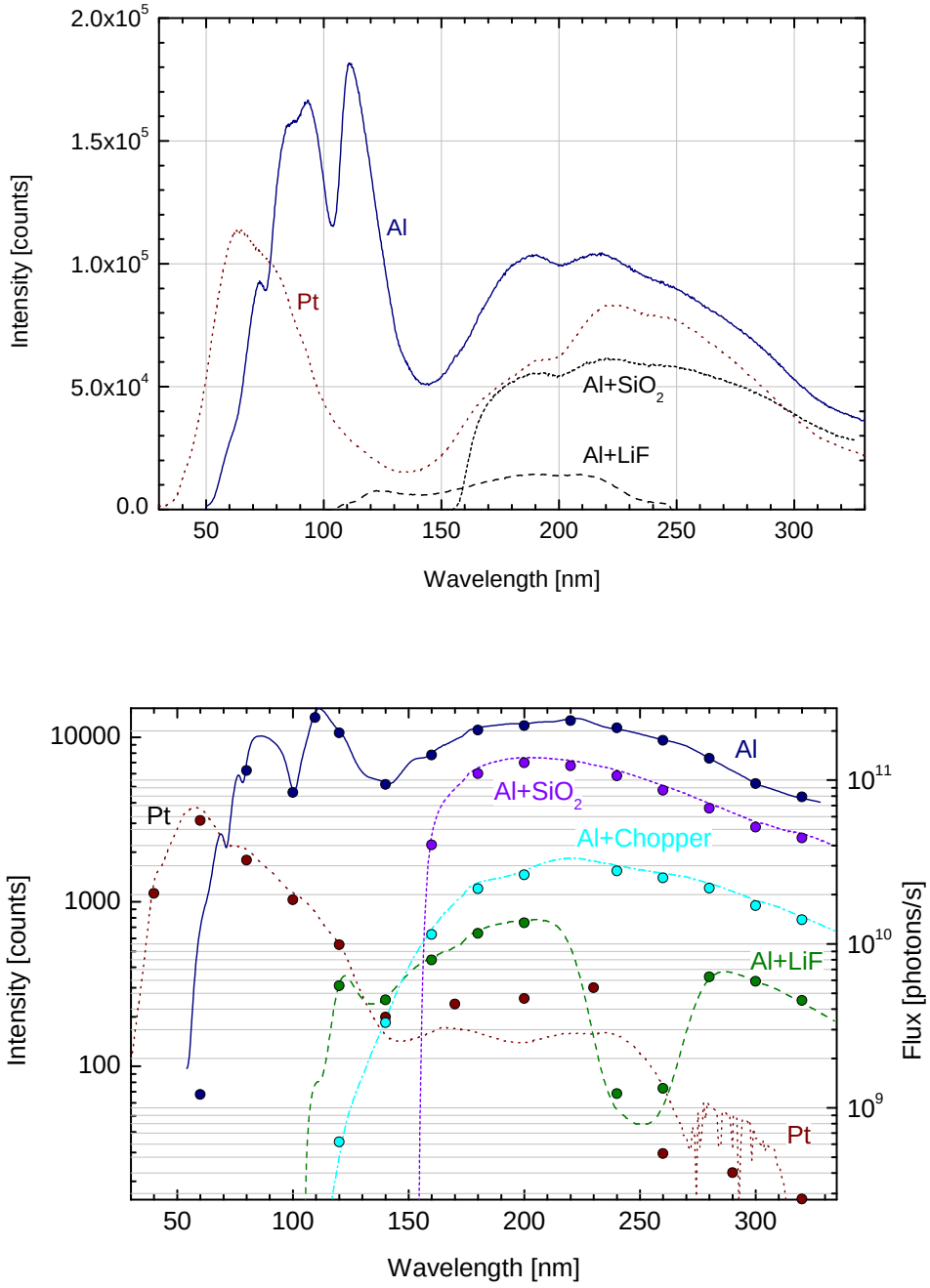

Figure 3.7: Upper graph: Sodium salicylate calibration curves with Al (—) and Pt (·····) primary grating (April 2^{nd}, 2002). Filters have been inserted on the excitation side, i.e. SiO_2 (----) or LiF (- - -) before as well as the LiF chopper valve (-·-·) after the primary grating. Lower graph: Absolute flux calibration curves measured with the AXUV photo-diode (October 10^{th}, 2003), including the direct current reading of the photo diode (○). Note the logarithmic intensity scale.

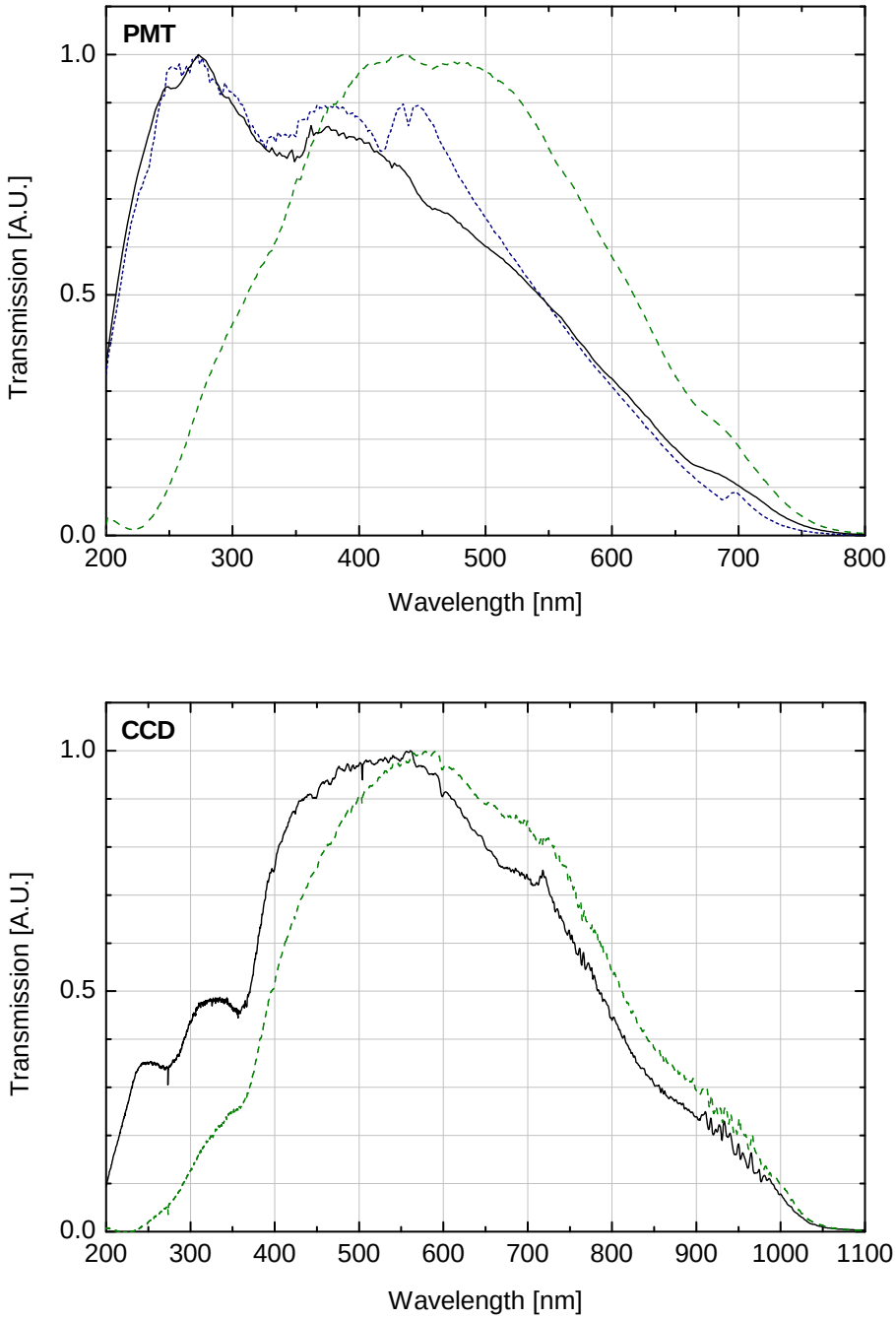

Figure 3.8: Transmission function of luminescence for the PMT R6358P (upper graph) and CCD (lower graph) detection setup at the *Superlumi*. The respective secondary gratings (lines/blaze wavelength) are 300/300 (—), 300/500 (---), and 1200/300 (----).

3.4 F_2 laser setup at the Debye Institut, Universiteit Utrecht

Supplementary measurements have been performed by kind permission of Prof. A. Meijerink at the Debye Institute, Universiteit Utrecht, Netherlands. The *ExciStar S* excimer laser setup operated with F_2 provides intense emission at 157.6 nm (63 450 cm^{-1}). The maximum pulse energy of 1 mJ has a duration of 15 ns (FWHM) at variable repetition rates. The sample is slightly off focus to avoid fast degradation of the sample due to the high laser intensity.

Two PMT are connected to the spectrometer (focal length 550 mm) for measurements in the VUV-UV and UV-IR range in combination with three changeable gratings (1200, 1800, and 3600 lines/mm). A flow-type cryostat attached to the sample holder allows cooling down to liquid Helium temperature.

The theoretically achievable dispersion with this setup is 1.5 nm/mm with the 1200 lines grating. Emission spectra at high resolution were measured with excellent signal-to-noise ratio, which have been used partially to assign electronic transitions between Stark components of Tm^{3+} ions in $4f \rightarrow 4f$ and $5d \rightarrow 4f$ transitions (Section 4.5). Unexpected differences are observed in the relative intensities compared with measurements carried out using synchrotron radiation at different excitation energy.

Chapter 4

Trivalent Thulium in fluorides

Among the *trivalent rare earth ions* Tm^{3+} has a concise energy level structure with only thirteen $4f$ levels (Section 2.4.2). The high $4f^{12}$ multiplet (^3P_J, $^1I_6$) is absorbing in the UV spectral region, while several transitions between lower-lying states are located in the visible. The Pr^{3+} ion ($4f^2$) has a similar level structure at reduced energy. The exceptionally close energy gap between the $4f^2$ state $^1S_0$ and the lowest $5d$ states about 47 000 cm^{-1} (213 nm) allows efficient photon cascade (quantum cutting) emission in some crystal host materials [PAP76, HEN00, KUE02]. An overview of various Pr^{3+} doped fluorides exhibiting quantum cutting under VUV synchrotron excitation with an internal quantum efficiency higher than one has been published recently [KUE03].

The $4f^{11}5d$ levels in Tm^{3+} have their onset between 58 000 and 65 000 cm^{-1} (170 and 150 nm) in fluorides depending on the host crystal, and are usually reaching into the bandgap. In less ionic crystals (oxides, chlorides, ...) the onset is located at considerably lower energy.

A quantum efficiency higher than one only considering $4f \rightarrow 4f$ transitions of Tm^{3+} cannot be achieved due to unfavorable branching ratios as shown for YF_3 [PAP76]. Transition metal ions such as Mn^{2+}, which is well-known to exhibit intense visible luminescence in many materials, are prospective transfer partners. Little attention has been devoted to the VUV region of transitions in Mn^{2+} so far, therefore the inter- and intra-configurational transitions of Mn^{2+} doped fluorides are subject to systematic investigation in Chapter 5.

In the current work, energy transfer processes and fine structure are investigated involving $5d$ and $4f$ states of (singly) Tm^{3+} doped fluorides. The well separated $4f$ energy levels, the substitutional lattice sites of different valences, the stability against under degradation of LiCAF, the low phonon energies, the large band gaps, and the long-living $5d$ states of LiCAF and LiSAF are suitable for efficient inter-ionic energy transfer as outlined in the motivation (Section 1.1). The unintentionally and surprisingly low doping concentration makes these samples well-suited for high resolution absorption and excitation spectroscopy, while little ion-ion interaction is expected due to the large mean distances between the dopants.

4.1 The energy level structure of Tm^{3+}

4.1.1 The $4f^{12}$ energy levels structure

The trivalent Thulium ion exhibits weak, narrow lines due to intra-configurational $f \rightarrow f$ transitions between the $4f$ sub-levels $^{2S+1}L_J$.

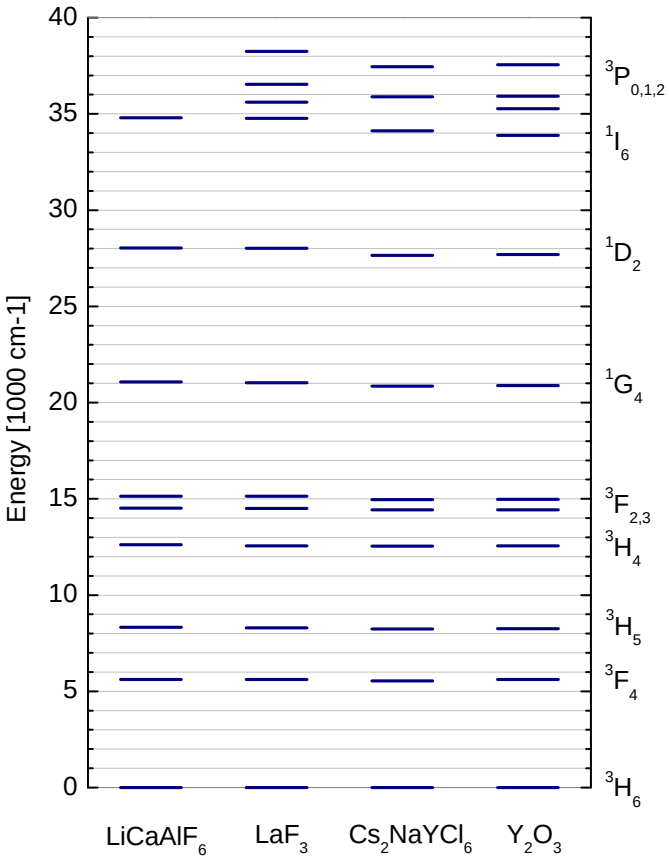

Figure 4.1: $4f^{12}$ energy levels of Tm^{3+} doped crystals LiCAF (this work), LaF_3 [CAR89], Cs_2NaYCl_6 [THO01], and Y_2O_3 [DIE68].

Figure 4.1 shows the $4f^{12}$ energy levels of Tm^{3+} in LiCAF (Appendix E), LaF_3 [CAR88, CAR89], Cs_2NaYCl_6 [THO01], and Y_2O_3 [DIE68], $^3H_6$ being the ground state. The $4f$ energy levels in fluoride, oxide, and chloride hosts closely resemble those of the free Tm^{3+} ion. Small shifts of the zero-phonon transitions up to a few hundred wavenumbers are exhibited, reaching the maximum for $^1I_6$ with a difference of about 900 cm^{-1} between LiCAF and Y_2O_3.

Luminescence is frequently observed from $^1I_6$, $^1D_2$, $^1G_4$, $^3F_3$, $^3H_4$, $^3H_5$, and $^3F_4$ as narrow,

weak lines. Non-radiative relaxation to the lowest level occurs within the $\left({}^3F_2, {}^3F_3\right)$ and $({}^3P_J, {}^1I_6)$ multiplets due to multi-phonon relaxation across the small energy gaps.

The lower $4f$ states are populated by several radiative cascades upon excitation of higher $4f$ levels, which contributes to intense luminescence in the infrared spectral region. This has to be considered concerning the quantum efficiency of visible luminescence.

The highest $4f$ state ${}^1S_0$ is theoretically predicted between 71 136 cm^{-1} in Cs_2NaYCl_6 [THO01] and 79 000 cm^{-1} in the range of strong absorption due to the $4f^{n-1}5d$ levels. Excitation within this range is followed by fast, non-radiative relaxation to the lowest $5d$ state and subsequent $d \rightarrow f$ emission (Section 4.3). Hence, transitions from or to the ${}^1S_0$ state have been observed neither in the literature nor in this work.

For the first time the energy level diagram of LiCAF:Tm^{3+} is established (Section 4.5), which comprises the $4f$ energy level scheme including the Stark level splitting of the ground state ${}^3H_6$ as well as emission due to the spin-forbidden $d \rightarrow f$ transition.

4.1.2 The $4f^{11}5d$ energy level structure

Due to the lack of tunable lasers in the VUV spectral region and experimental difficulties such as evacuated spectrometers required for absorption and excitation spectroscopy of the $5d$ energy level structure in trivalent rare earths, synchrotron radiation is the vital source for high resolution measurements (Section 4.5).

In 1966 the lower $4f \rightarrow 5d$ absorption bands for all trivalent rare earth ions were reported in CaF_2 [LOH66], and a few years later synchrotron radiation was used for studying the rare earths [ELI73, HEA76]. VUV emission originating from the lowest d-states has been observed for Nd^{3+}, Er^{3+}, and Tm^{3+} in tri-fluorides [YAN76, YAN78]. Fine structure has been observed in the absorption spectra of CaF_2:Tm^{3+} [SZC85].

In recent years extensive research on $d \rightarrow f$ emission in the VUV has been conducted at our experimental setup. Systematic investigations in the VUV of fluoride crystals ($LiYF_4$, LaF_3, and YF_3) doped with various rare earth ions (Ce^{3+}, Pr^{3+}, Nd^{3+}, Eu^{3+}, Tb^{3+}, Dy^{3+}, Ho^{3+},Er^{3+}, and Tm^{3+}) at RT have been carried out using luminescence excitation and diffuse reflection spectroscopy with synchrotron radiation [KRU97].

A few examples include detailed work on various Er^{3+} and Tm^{3+} containing fluorides [GES99], KYF_4 crystals doped with Nd^{3+}, Er^{3+}, Tm^{3+} [KHA00], $LiY_{1-x}Er_xF_4$ [MAK00], NaF-(Er,Y)F_3 [KAR01], and concentration series of $LiYF_4$:Er^{3+} [NEG03].

High resolution Tm^{3+} excitation spectra have been recorded for trivalent rare earth ions in $LiYF_4$, CaF_2, and YPO_4 using synchrotron radiation source at DESY [LIE02a, LIE02b]. Fine structure was observed for the lower energy $5d$ states and compared with theoretical calculation [REI00], but disappeared at higher energies. Only close to the band gap fine structure reappeared.

The Tm^{3+} ground state configuration $4f^{12}$ has a maximum of two unpaired spins, which corresponds to a total spin multiplicity $\Sigma = 3$ (spin quantum number of $S = 1$). The low-energy onset of the energy levels is a high-spin state with $S = 2$ ($2S + 1 = 5$). Hence, electric dipole transitions of this *high-spin* state to all lower $4f$ levels are spin-forbidden, having spin multiplicities $(2S + 1) = 1$ or 3. In addition the $4f^{11}5d$ low-spin state ($S = 1$) has its onset at slightly higher energy, which gives rise to spin-allowed transitions. Emission from the low-spin state is *not* observed in LiCAF and LiSAF as a result of this work (Section 4.3).

Since the d-levels are more sensitive to the crystal field than the f-levels (Section 2.4.3), the shifts in energy are not known prior to the measurement. A comprehensive work predicting the position of d-levels in various crystals is available [DOR00] and has been reviewed in terms of the obtained experimental data (Section 4.1.3).

For the first time $d \rightarrow f$ emission of Tm^{3+} in LiCAF and LiSAF has been observed (Section 4.3). High resolution spectra of LiCAF:Tm^{3+} have been recorded under synchrotron and excimer laser excitation in a wide spectral range (Section 4.5.2).

4.1.3 Review of predicted $5d$ levels of Tm^{3+} in fluorides

The energetic positions of the lowest spin-allowed and spin-forbidden $5d$ states can be predicted empirically for all rare earths in crystals, if at least one RE ion in this particular crystal is known [DOR00]. Spectroscopic data of $d \rightarrow f$ transitions of trivalent RE ions in various host materials has been collected from the literature, and average values for each host are tabulated. In particular, the Ce^{3+} ion has been investigated extensively in the past and has been chosen therefore as reference.

The procedure, based on empirical methods and assuming strong electron-phonon coupling, is outlined using Tm^{3+} as example. The predicted energy for the spin-allowed transition of a rare earth ion can be written

$$\Delta E^{RE,s-a} = 49340\,\mathrm{cm}^{-1} - D(A) + \Delta E^{RE,Ce} \tag{4.1}$$

where $D(A)$ is the crystal field depression of a compound A, and $\Delta E^{RE,Ce}$ is the energy difference between the first spin-allowed $d \rightarrow f$ transition in the RE ion and Ce^{3+}. These average values for each particular host have been obtained from a comprehensive analysis of absorption, excitation, and emission spectra of $d \rightleftarrows f$ transitions from the literature.

In the case of Tm^{3+} the energy difference is

$$\Delta E^{Tm,Ce} = 29300 \pm 1100\,\mathrm{cm}^{-1} \tag{4.2}$$

and the energy difference between the spin-allowed and spin-forbidden transition is

$$\Delta E^{sa,sf} = 2350 \pm 320\,\mathrm{cm}^{-1} \tag{4.3}$$

With the tabulated values, the predicted positions of the excitation energy levels are

$$\Delta E_{ex}^{Tm,sa} = 78640\ \mathrm{cm}^{-1} - D(A) \pm 1400\,\mathrm{cm}^{-1} \tag{4.4}$$

$$\Delta E_{ex}^{Tm,sf} = 76290\ \mathrm{cm}^{-1} - D(A) \pm 1720\,\mathrm{cm}^{-1} \tag{4.5}$$

A	$D(A)$	$\Delta S(A)$	$\Delta E_{ex}^{Tm,sa}$	$\Delta E_{ex}^{Tm,sf}$	$\Delta E_{em}^{Tm,sa}$	$\Delta E_{em}^{Tm,sf}$
free ion	0	0	78 640	76 290	78 640	76 290
$LiCaAlF_6$	13 344	1389	65 296	62 946	63 907	61 557
$LiSrAlF_6$	12 165	2452	66 475	64 125	64 023	61 673
$LiMgAlF_6$	10 878	5781	67 762	65 412	61 981	59 631
$LiGdF_4$	15 093	-	63 547	61 197	-	-
$LiYF_4$	15 262	1597	63 378	61 028	61 781	59 431
$NaYF_4$	8854	-	69 786	67 436	-	-
BaY_2F_8	16 047	2370	62 593	60 243	60 223	57 873

Table 4.1: Predicted $5d \rightarrow 4f$ transition energies (in cm^{-1}) of Tm^{3+} in different crystals. $D(A)$ is the crystal field depression of compound A; $\Delta S(A)$ is the Stokes' shift; $\Delta E_{ex}^{Tm,sa}$ and $\Delta E_{ex}^{Tm,sf}$ are the calculated energies of the lowest spin-allowed and spin-forbidden transition in excitation; $\Delta E_{em}^{Tm,sa}$ and $\Delta E_{em}^{Tm,sf}$ are those in emission.

The standard errors already contain the given uncertainty of 300 cm^{-1} for $D(A)$. The Stokes' shift $\Delta S(A)$ is tabulated as well, allowing to calculate the energy of the $d \rightarrow f$ *emission*. Table 4.1 shows selected crystal hosts and the calculated energies based on the parameters from [DOR00]. The question arises inasmuch the obtained values are comparable to the measurements.

High resolution spectra of $5d \rightarrow 4f$ emission of Tm^{3+} in LiCAF and LiSAF at 7.3 K were measured at the *Superlumi* experimental station in this work. The data is well suited for reviewing the empirical prediction outlined above, while the fine structure observed is discussed in more detail in Section 4.5 along with the high resolution $d \rightarrow f$ emission spectra.

Figure 4.2 shows the emission spectra (----) of (a) LiCAF:Tm^{3+} excited at 147.8 nm, (b) LiSAF:Tm^{3+} excited at 155.0 nm, and (c) BYF:Tm^{3+} excited at 158.3 nm. All spectra have been measured with the same spectral resolution, which ensures that the emission features limited and broadened by resolution are comparable.

In order to obtain the overall shape of each curve, a 50 point FFT smoothing filter has been applied (—). The smoothed curves have their maxima at 60 720 cm^{-1} (LiCAF), 60 660 cm^{-1} (LiSAF), and 58 600 cm^{-1} (BYF) corresponding to spin-forbidden $d \rightarrow f$ transitions of Tm^{3+}.

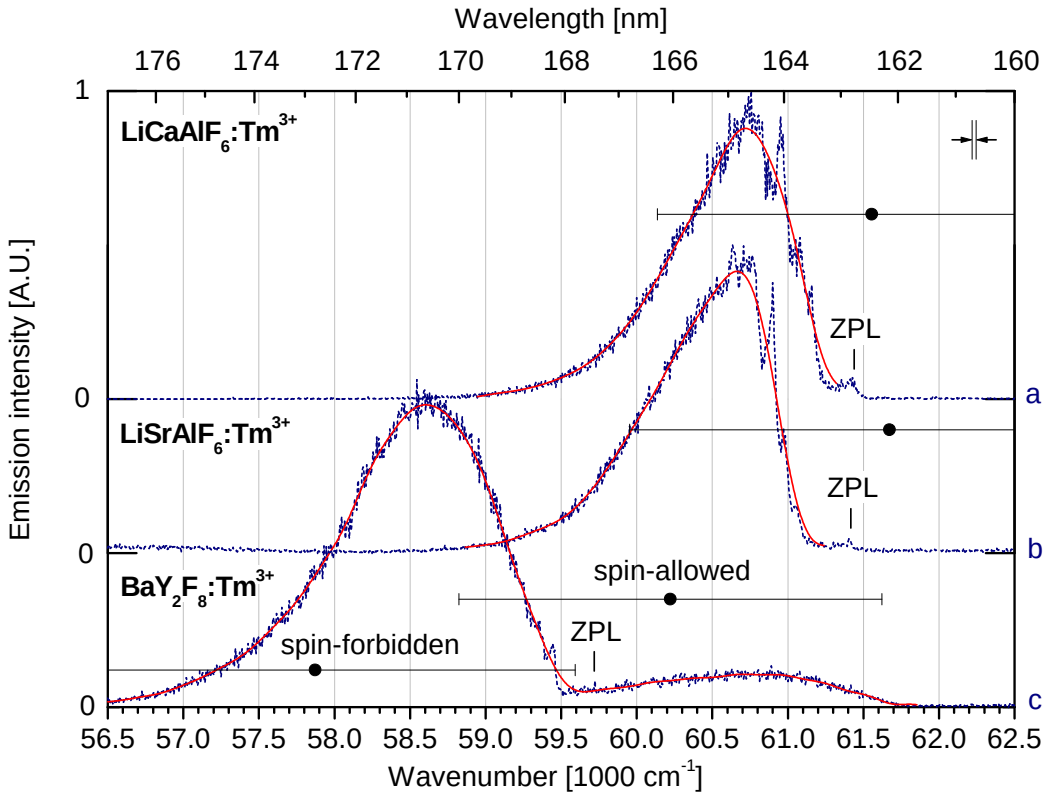

Figure 4.2: $5d \rightarrow 4f$ emission spectra at 7.3 K (----) of Tm^{3+} doped fluorides. (a) LiCAF, λ_{ex} =147.8 nm, τ_c =1000 s; (b) LiSAF, λ_{ex} =155.0 nm, τ_c =600 s; (c) BYF, λ_{ex} =158.3 nm, τ_c =600 s. FFT smoothed curves (—) exhibit the overall shape. The predicted transition energies (•) calculated from [DOR00] are given including the standard error. $\Delta\lambda_{em} \leq 0.08$ nm.

The spin-allowed emission is observed in BYF having its maximum at 60 700 cm^{-1}.

Due to the intermediate coupling expected in fluoride crystals, fine structure including zero-phonon lines (ZPL) due to $d \rightarrow f$ transitions can be exhibited in high resolution measurements, demonstrated in our recent publication for $LiYF_4$:Er^{3+} [CHE03] and for the first time for Tm^{3+} in LiCAF, LiSAF, and BYF crystals in this work (Section 4.5). It should be kept in mind that the model by Dorenbos [DOR00] assumes strong electron-phonon coupling and is thus not predicting ZPL.

The FFT smoothed curves have their peak maxima within the given standard error in all three crystal hosts. Going from LiCAF to LiSAF the maximum shifts 60 cm^{-1} to lower energy. The predicted value, however, shifts 116 cm^{-1} to higher energy, being within the given error boundaries. The predictions are reliable as proven in a large number of host materials, however, a limitation is imposed by impurity ions occupying non-equivalent lattice sites. As pointed out in Section 4.3.1 the Al^{3+} substitutional site is clearly preferred for Tm^{3+} in LiSAF due to the larger lattice constants, in contrast to the setting in LiCAF.

This disagreement of the predicted values concerning Tm^{3+} doped LiCAF and LiSAF can be interpreted as a result from occupation of non-equivalent lattice sites.

The ZPL in BYF is located outside the standard error of the empirical estimate (curve c), while it is close to the given values in LiCAF and LiSAF (curves a and b). The measured peak maxima of the spin-forbidden and spin-allowed $d \rightarrow f$ transitions agree within the predicted uncertainty range.

In summary, the experimentally derived $d \rightarrow f$ emission maxima in LiCAF, LiSAF, and BYF are compared with calculated values (Table 4.1) from empirical methods assuming strong coupling [DOR00]. The empirical data forming the basis of this method is predicting the peak maxima of spin-allowed and spin-forbidden transitions within the given standard error of 1420 and 1700 cm^{-1}, respectively. Regarding energy shifts between similar host lattices, the statistical error is too large to allow definite conclusions. The qualitative disagreement of the predicted values concerning Tm^{3+} doped LiCAF and LiSAF can be interpreted as a result from occupation of non-equivalent lattice sites.

4.1.4 Experimental and calculated $f \rightarrow d$ excitation in LiCAF:Tm

Figure 4.3 shows a comparison of the experimental (----) and theoretical (—) excitation due to $f \rightarrow d$ transitions in LiCAF:Tm^{3+}. The theoretical results have been kindly provided by M.F. Reid [REI03]. The calculated values are indicated by vertical lines at the bottom and have been convoluted by Gaussian bands (FWHM 40 cm^{-1}). Perfect octahedral symmetry and ambient temperature of 10.0 K have been assumed. The energy scale of the calculated curve has been shifted by approximately 10 nm, since the absolute transition energies are not accurately reproduced by the calculation. Details on the theoretical method can be found in [DUA03, REI00]. The inset shows the onset of $f \rightarrow d$ excitation on the low-energy side in enlarged scale.

The calculated ZPL at the lower wavelength has been shifted to the corresponding peak ζ_0 at 62 640 cm^{-1} (159.64 nm), clearly observed in the experimental spectrum. The following peak observed is ζ_1 at 63 188 cm^{-1} (158.26 nm). Z_0 indicates the ZPL of the spin-forbidden $d \rightarrow f$ transition, which has been determined from high resolution emission spectra (cf. Section 4.5.2). ζ_0 cannot be compared with the high resolution $d \rightarrow f$ emission spectra, since only the spin-forbidden transition has been observed (cf. Section 4.5).

The overall agreement of both spectra is good, the first five (broad) bands up to 80 000 cm^{-1} are in general coincidence, confirming the assignment of ζ_0 to a ZPL due to the spin-allowed transition. This is in agreement with the observed ZPL in emission of the spin-forbidden transition Z_0 at 61 410 cm^{-1} (162.84 nm), being 1230 cm^{-1} lower in energy. This value is about half compared to the average predicted by empirical methods (cf. Section 4.1.3), which is reasonable within the local surrounding of this particular host.

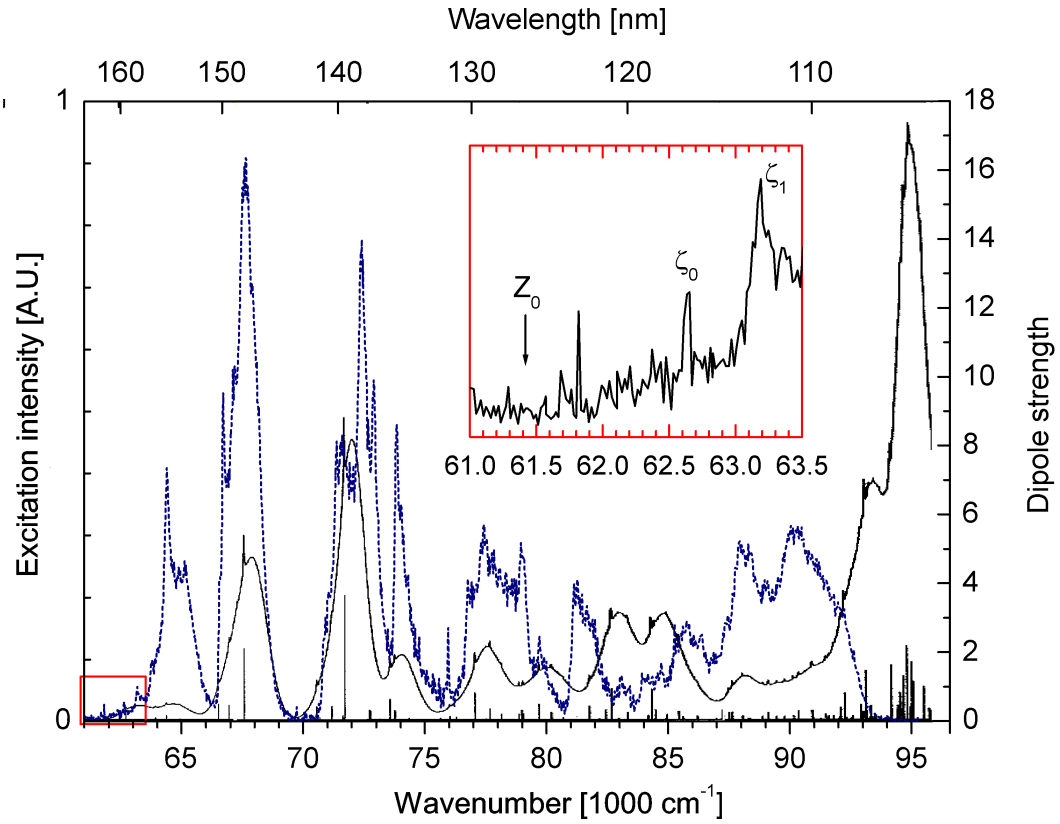

Figure 4.3: Experimental and calculated excitation spectra of $f \rightarrow d$ transitions in LiCAF:Tm^{3+}. (----) experimental spectrum, $\lambda_{em} = 165.4$ nm, $\Delta\lambda_{ex} = 0.05$ nm, $T = 7.4$ K; the theoretical dipole strength is indicated by vertical lines, convoluted with Gaussian curves (—). Inset: Enlarged scale, with ZPL ζ_0 and ζ_1 clearly observed. Z_0 indicates the ZPL of the spin-forbidden transition.

Numerous calculated lines have coinciding sharp peaks within the range 62 500 cm^{-1} to 80 000 cm^{-1}. In addition, many pronounced experimental peaks in this region have no corresponding partner in the calculated spectrum. This suggests a lower local symmetry of the substitutional lattice site and/or multiple sites (cf. Section 3.2.1).

Towards higher energies the theoretical bands are shifted compared to the experimental bands. Around 78 740 cm^{-1} (127 nm) strong absorption has been observed due to the CT state of Tm^{3+} which has significant influence on the absorption in this region. At energies approaching the fundamental absorption, excitonic and impurity excitation causes strong differences in both spectra.

The fine structure of the experimental excitation spectrum is furthermore in striking agreement with that in absorption (Section 4.4).

4.2 Experimental results: Nominally pure LiCAF

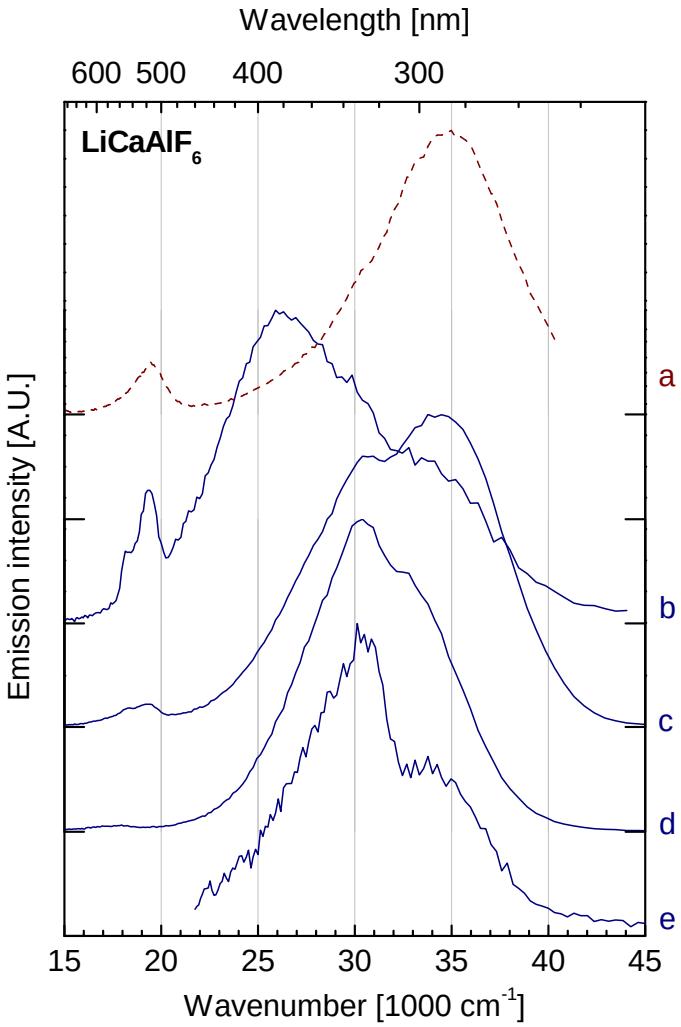

Figure 4.4: Emission spectra of nominally pure LiCAF. (a) λ_{ex} =85 300 cm^{-1}; (b) 87 000 cm^{-1}; (c) 92 250 cm^{-1}; (d) 122 700 cm^{-1}; (e) 100 eV. Curve a was recorded at RT, the other ones at 10 K. $\Delta\lambda_{em} \leq$10 nm.

In order to characterize the transparency range as well as host-related luminescence properties a nominally pure LiCAF single crystal has been investigated. Figure 4.4 shows emission spectra at various excitation wavelengths at RT (curve a) and 10 K (curves b-e). The relative intensities of the two overlapping main emission bands (peaking around 35 000 and 30 000 cm^{-1}) depend on the excitation energy (curves c and d). The higher-energetic part of the non-elementary emission band has been assigned to the radiative decay of self-trapped excitons (STE) [GEK03], studied recently in more detail [KIR04]. The emission curves a, c, d, and e are quite similar concerning the different excitation energies and sample temperatures.

The long-wavelength part arises from recombinations at intrinsic and extrinsic emission centers, being well excited in the transparency range of the host at 87 000 cm^{-1} (curve b). Weak luminescence arising from residual impurities or defects is observed around 20 000 cm^{-1} in the visible spectral region. This interpretation is supported by the observation of similar emission bands in the thermo-luminescence spectra after X-ray irradiation [SAT02a].

It is interesting to note that the dominant emission observed at RT (curve a) practically coincides with the short-wavelength part of that recorded under excitonic excitation (curve c). However, since the main excitation band at RT is located in the transparency range at 85 300 cm^{-1} (Figure 4.5, curve d), it is tentatively assigned to extrinsic origin.

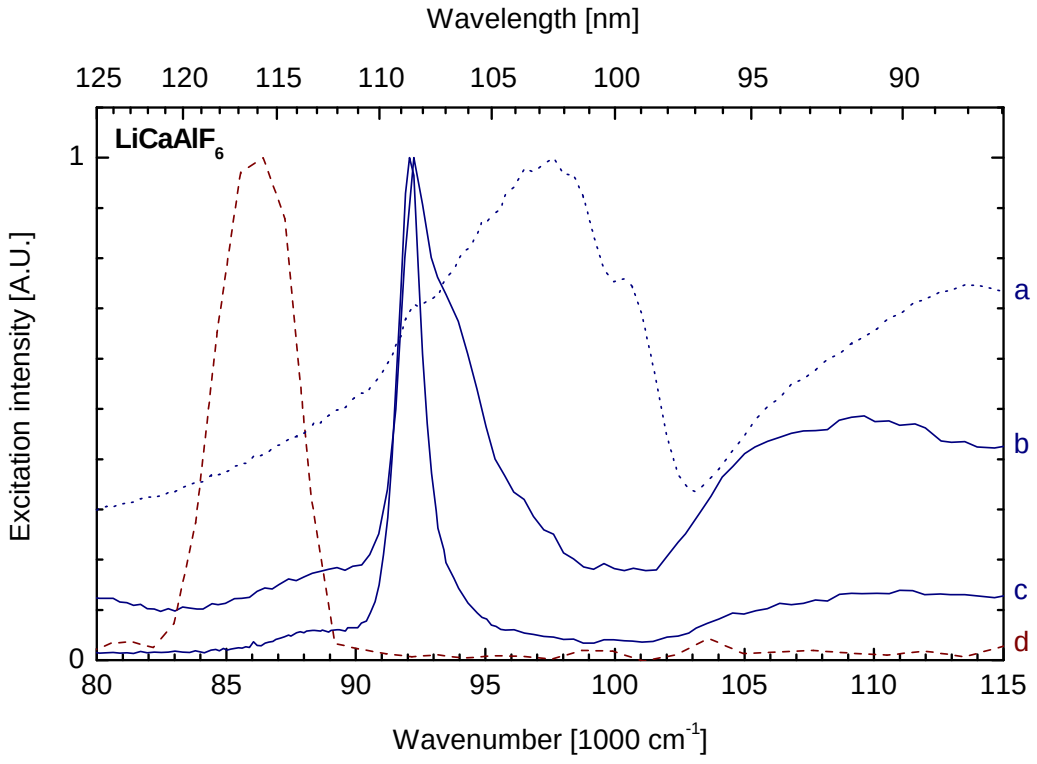

Figure 4.5: Excitation and reflection spectra of nominally pure LiCAF at 10 K. (a) reflection, T =10 K; (b) λ_{em} =350 nm, T =10 K; (c) λ_{em} =270 nm, T =10 K; (d) λ_{em} =270 nm, RT. $\Delta\lambda_{ex} = 0.32$ nm.

Figure 4.5 shows reflection (curve a) and excitation spectra (curves b-d) of nominally pure LiCAF at 10 K, only curve d was measured at RT. In order to decouple the STE and impurity/defect emission bands, the wavelengths to be monitored are chosen in the respective shoulders at 270 nm and 350 nm. STE emission is efficiently excited in the excitonic region (curve c) at 92 110 cm^{-1} (FWHM 1100 cm^{-1}). The onset of raising absorption is in good agreement with the transparency range determined earlier [SHI00]. The reflection spectrum

(curve a) shows a peak ascribed to excitonic excitation, supporting the assignment (curve a).

The emission intensity of the 30 000 cm^{-1} band is increased by electron-hole recombinations, which is indicated by the increasing excitation intensity in the region of fundamental absorption (curve b) above the excitonic excitation. Subsequent emission occurring due to the recombination of electrons and holes at impurity and/or defect sites is overlapping with the radiative transitions due to STE.

Only a single strong excitation band is observed at RT for the 270 nm emission. Its high-energy side coincides with the transmission edge (112 nm) [SHI01b]. Exciting within the intrinsic absorption of LiCAF yielded nearly no luminescence at RT, suggesting strongly that either non-radiative relaxation is prevailing or charge carriers are trapped separately. This may explain the results of Sato *et al.* reporting only weak emission of X-ray excited pure LiCAF [SAT02b]. Stable color centers have been found in the VUV absorption of as grown LiCAF crystals reported elsewhere [KIR02b].

The broad emission in the region 25 000 cm^{-1} to 40 000 cm^{-1} discussed in this section (Figure 4.4) is frequently observed in the spectra of the doped crystals as well.

4.3 Experimental results: $d \rightarrow f$ emission spectra

Time-resolved emission spectra have been recorded at low resolution in the VUV spectral region, excited with synchrotron radiation. $4f^{11}5d \rightarrow 4f^{12}$ transitions of Tm^{3+} doped LiCAF, LiSAF, and BYF are observed as expected. In Section 4.5.2 high resolution spectroscopy of $d \rightarrow f$ transitions of Tm^{3+} doped LiCAF and LiSAF is reported for the first time.

4.3.1 $LiCaAlF_6$ and $LiSrAlF_6$

Figure 4.6 shows emission spectra of Tm^{3+} doped LiCAF and LiSAF in the VUV spectral region at low temperature. Under excitation into the higher $4f^{11}5d$ states of LiCAF (curve a) inter-configurational $d \rightarrow f$ luminescence is observed. The most intense transition to the $4f^{12}$ ground state $^3H_6$ is peaking at 60 600 cm^{-1} (165.0 nm). In the 40× magnified curve weaker transitions are clearly observed, populating lower f-states up to $^1G_4$. Under intense excimer laser excitation population up to the highest f-levels ($^1I_6, ^3P_J$) has been observed (cf. Section 4.5), while the synchrotron radiation source appeared to be too weak.

The experimentally derived transition energies from Figure 4.6 and their assignment are shown in Table 4.2. The transition peak energy and FWHM were obtained from fitted Gaussian curves. The energy of each final state E_{4f} is calculated as difference to the transition from $5d$ to the ground state. Since peak energies are derived from this measurement and not zero-phonon energies, E_{4f} is *not* corresponding to the exact energy of the $4f$ state. E_{4f} appears to be somewhat lower than the values E_{LaF} of the Tm^{3+} energy levels in LaF_3

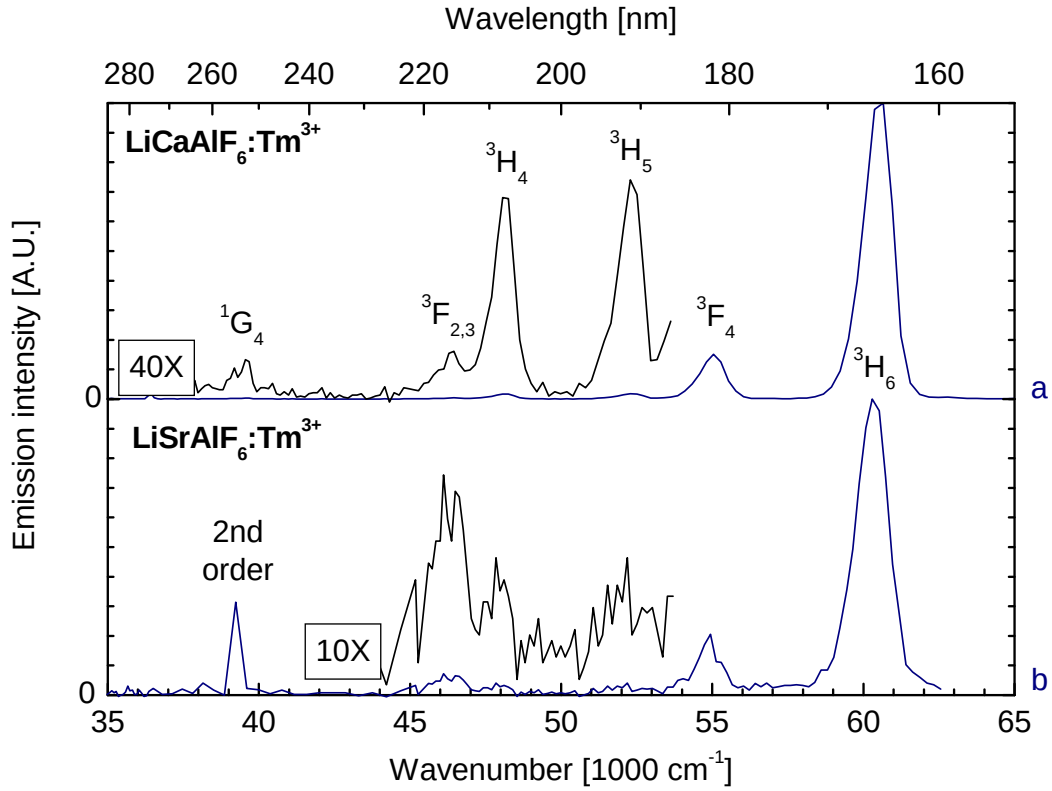

Figure 4.6: Emission spectra of $d \rightarrow f$ transitions. (a) LiCAF:Tm^{3+}, λ_{ex} =137.2 nm, T = 11 K; (b) LiSAF:Tm^{3+}, λ_{ex} =127 nm, T = 9 K. $\Delta\lambda_{em}$ = 1 nm.

(Section 2.4.2). High-resolution spectra revealing fine structure (zero-phonon and vibronic lines) are discussed for $d \rightarrow f$ (Section 4.5.2) and $f \rightarrow f$ (Section 4.5.3) transitions. As a result the energies of zero-phonon transitions between $4f$ levels in LiCAF are found to be at slightly higher energies than the emission peak positions.

The emission spectrum of LiSAF shown in Figure 4.6 (curve b) has its most intense peak at 60 300 cm^{-1} attributed to the spin-forbidden $d \rightarrow f$ transition to the $^3H_6$ ground state. Further transitions populating the lower f-states are observed, similar as in LiCAF:Tm^{3+}.

Only the spin-forbidden emission of Tm^{3+} doped LiCAF and LiSAF with a decay in the microsecond range was observed like in KYF_4:Tm^{3+} [KHA00]. The energy distance between the spin-allowed and spin-forbidden component is predicted to be 2350 cm^{-1} for both hosts (Section 4.1.3), which may be bridged by fast multi-phonon relaxation to the lowest (spin-forbidden) $5d$ level. The low doping concentration of both samples and the resulting weak signal also renders possible a fast component hidden by background noise. Due to this fact, a comparison of ZPL in the high resolution emission spectra (Section 4.5.2) with the corresponding peaks in excitation is not possible.

$4f$	$d \rightarrow f$ (LiCAF)	(LiSAF)	E_{4f} (LiCAF)	(LiSAF)	E_{LaF}
$^3H_6$	60 490 (890)	60 280 (1150)	0	0	0
$^3F_4$	55 000 (880)	54 870 (1040)	5490	5410	5615
$^3H_5$	52 300 (1070)	52 200	8190	8080	8305
$^3H_4$	48 130 (610)	48 000 *(650)*	12 360	12 280	12 561
$^3F_{3,2}$	47 400	46 300 *(1300)*	13 090	13 980	14 508
$^1G_4$	39 600	-	20 890	-	21 037

Table 4.2: $d \rightarrow f$ peak transition energies in cm^{-1} (and FWHM) from Gaussian fits of LiCAF:Tm^{3+} and LiSAF:Tm^{3+} *(not ZPL!)*. E_{4f} is the derived energy of the final state, E_{LaF} is the energy of the ZPL of that state in LaF_3 [CAR89], weak peaks in *italic*.

Practically no $d \rightarrow f$ luminescence is observed under band-to-band excitation, while at energies in the excitonic range both $d \rightarrow f$ and $f \rightarrow f$ transitions are observed. In other fluorides like BYF:Tm^{3+} the fast spin-allowed emission is also observed (Section 4.3.2).

4.3.2 BaY_2F_8

The VUV energy region, in particular concerning the $4f^{11}5d$ states, is investigated in BYF single crystal doped with Tm^{3+}. The Y^{3+} lattice site is well suited for substitution by RE ions, therefore Tm^{3+} is incorporated very well. At high (stoichiometric) concentrations the crystal structure changes to the $BaTmF_8$-type.

Emission spectra of BYF:Tm^{3+} in the VUV spectral region at 11 K are presented in Figure 4.7 (left side). Several emission peaks are observed due to $d \rightarrow f$ transitions (—) in agreement with earlier spectroscopic results obtained at the *Superlumi* station [BEC98b]. Time-resolved spectra have been recorded in a fast (•) time window of 17 ns length and a slow (∘) time window of 100-192 ns after the excitation pulse, which allows to assign each emission peak to spin-allowed and spin-forbidden transitions, having different f-levels as final states. The integrated and fast emission curves have been normalized to the maximum, the slow one is shown in enlarged scale.

Emissions corresponding to the slow spin-forbidden and the fast spin-allowed $d \rightarrow f$ transitions are summarized in Table 4.3 as indicated in the figure, the weaker spin-allowed transitions are printed in bold. No other emission is observed down to 35 000 cm^{-1}, indicating the good quality of the crystal.

The excitation spectrum (----) has been recorded monitoring $d \rightarrow f$ emission at 171 nm, which corresponds to the *spin-forbidden* transition to the ground state $^3H_6$. The observed $5d$ bands are mainly due to *spin-allowed* $f \rightarrow d$ absorption, relaxing non-radiatively to the lowest $5d$ states and subsequentally populating the lower $4f$ levels in a similar process as that observed for LiCAF and LiSAF (Section 4.3.1). The first (spin-forbidden) excitation band peaking

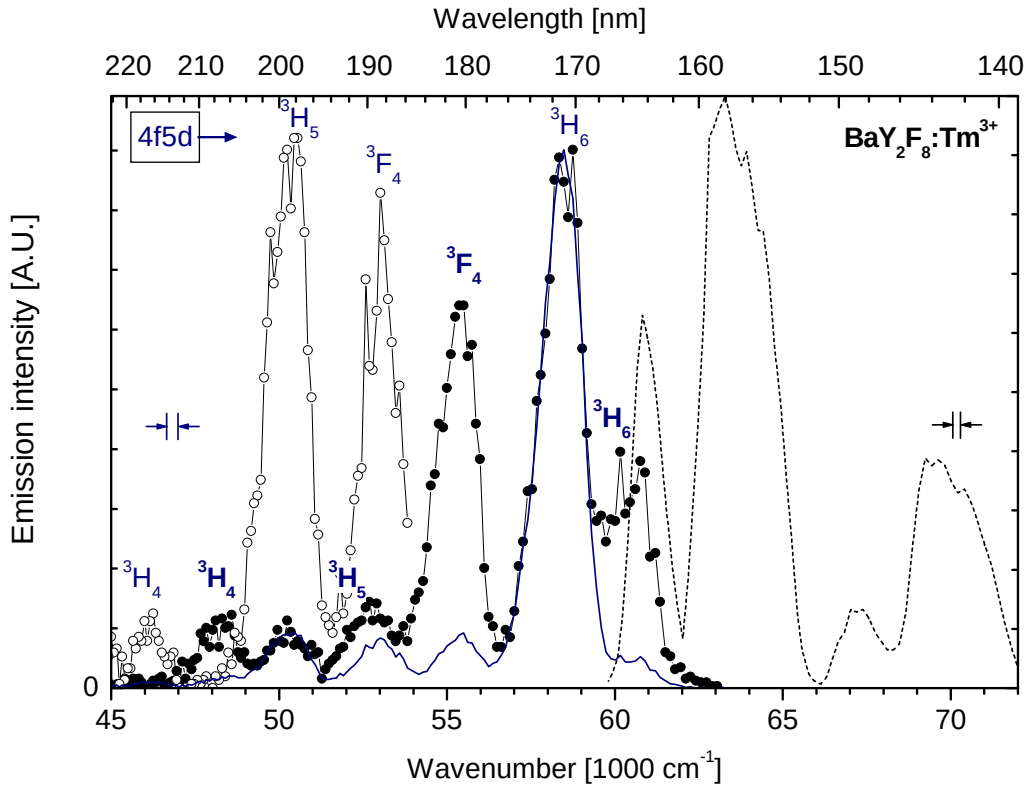

Figure 4.7: Emission and excitation spectra of $d \rightleftarrows f$ transitions in the VUV of BYF:Tm^{3+} at T =11 K. Left side: emission spectra, λ_{ex} =157.0 nm (63 700 cm^{-1}), $\Delta\lambda_{em}$ = 1 nm, integrated intensity (—), fast (•) and slow (∘) time windows. Right side: excitation spectrum, λ_{em} =171 nm (----).

at 60 820 cm^{-1} is overlapping with that of the (spin-allowed) emission to $^3H_6$, thus energy transfer to the spin-forbidden 5d states reduces the intensity of this emission band as seen in the figure. Further d-bands are observed up to 85 000 cm^{-1}, while at higher energy d-states are not excited in the region of excitonic and host absorption.

4.3.3 Conclusions

For the first time, the emission due to the spin-forbidden $d \rightarrow f$ transition of Tm^{3+} in LiCAF and the iso-structural LiSAF crystal has been observed, while the spin-allowed components are not present or extraordinary weak. Thus, this long-living state (life time $\tau \approx 5.6$ μs [TRU04b]) offers favorable energy transfer characteristics to a prospective co-dopant such as Mn^{2+} investigated in this thesis (Section 5). Unlike in BYF:Tm^{3+}, there is no overlap of the spin-forbidden emission and excitation spectra, therefore the respective ZPL are not available for comparison (cf. Section 4.4.1). The energy transfer characteristics are further investigated in Section 4.4. Emission due to the fast spin-allowed transition has been observed

$4f$	*allowed*	E_{4f}	*forbidden*	E_{4f}	E_{LaF}
$^3H_6$	60 750	0	58 500	0	0
$^3F_4$	55 400	5350	53 000	5500	5619
$^3H_5$	52 700	8050	50 450	8050	8309
$^3H_4$	48 300	12 450	46 250	12 250	12 565

Table 4.3: $d \rightarrow f$ emission peak energies *(not ZPL!)* in cm^{-1} (and FWHM) of BYF:Tm^{3+} of the spin-*allowed* and spin-*forbidden* component. E_{4f} is the derived energy of the final state, E_{LaF} is the energy of the ZPL of that state in LaF_3 [CAR89]

in BYF:Tm^{3+} along with the spin-forbidden component, in agreement with earlier results [BEC98b].

High resolution spectroscopy has been carried out based on these results, revealing for the first time detailed fine structure of $d \rightarrow f$ transitions in Tm^{3+} doped LiCAF and LiSAF (Section 4.5.2). A series of BYF samples co-doped with Tm^{3+} and Mn^{2+} has been obtained for further analysis of this interesting host, however, due to unexpected circumstances concerning the quality of the crystals some of the results are only briefly presented in Appendix A.

4.4 Experimental results: Absorption and excitation

Two important experimental techniques to characterize luminescence and energy transfer characteristics of impurities in a crystalline environment are absorption and excitation spectroscopy. Various excitation mechanisms exist for Tm^{3+} ions, populating the $4f$ and $5d$ levels differently, which is impossible to characterize only by absorption measurements (Section 4.4.1).

A detailed analysis of LiSAF:Tm^{3+} [TRU04a] and LiCAF:Tm^{3+} [TRU04b] single crystals in the VUV spectral region has been reported earlier as result of this work, and the main results are discussed briefly in Section 4.4.2.

4.4.1 Absorption and excitation of LiCAF:Tm^{3+}

Figure 4.8 shows the absorption (—) and excitation (----) spectrum of LiCAF:Tm^{3+} in the VUV spectral region. The sample has been polished, having a thickness of 0.4 mm. By trace analysis the crystal has been confirmed to be optically thin (cf. Section 3.1.3), which makes the crystal perfectly suited for measurements of strong absorption due to $f \rightarrow d$ transitions. The absorption of the crystal has been obtained from the transmission spectrum recorded at the *Superlumi* experimental station using the photo diode (cf. Section 3.3.3). This excitation spectrum has been found to be in agreement with that resulting from theoretical calculations (cf. Section 4.1.4).

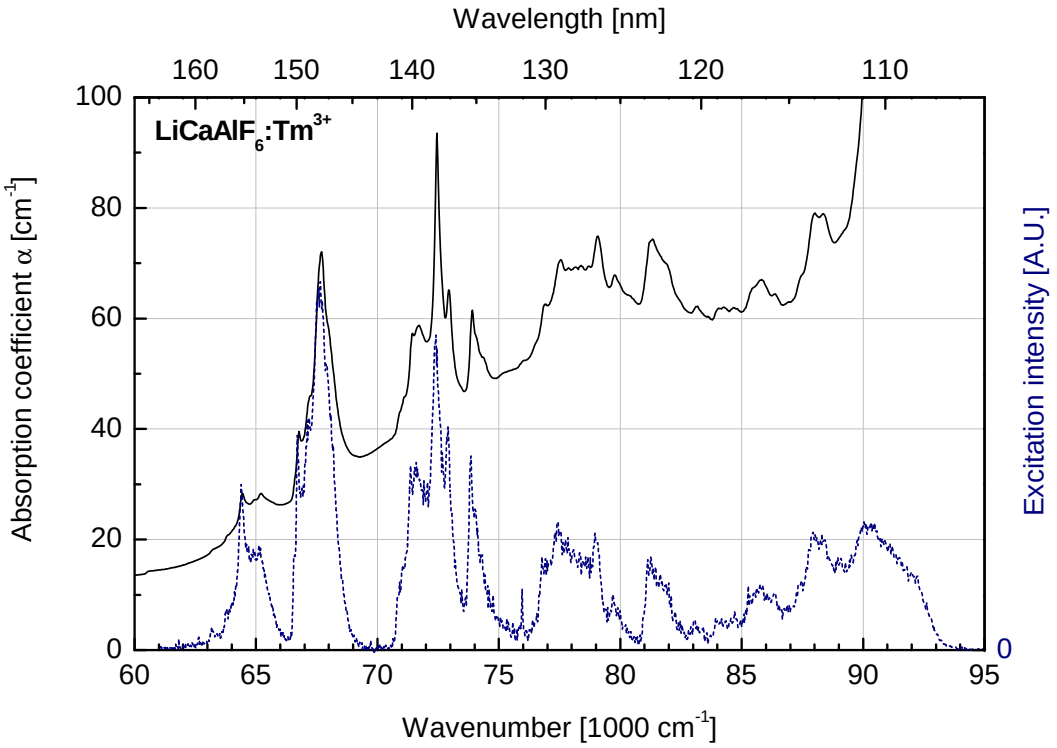

Figure 4.8: Absorption and excitation spectra of LiCAF:Tm^{3+} single crystal. (—) absorption, $T = 10$ K, (----) excitation, $T = 7.4$ K λ_{em} =165 nm. $\Delta\lambda_{ex} = 0.3$ nm.

The steep raise at 89 000 cm^{-1} (112 nm) comes from intrinsic absorption, in agreement with the results of nominally pure LICAF (cf. Section 4.2). A substantial background is observed in the absorption (—), causing the difference of both spectra. This background absorption appears to be largest around (130 nm) in the region of absorption due to the $F^- \rightarrow Tm^{3+}$ charge transfer state, which is a fully allowed transition (cf. Section 4.4.2).

The peaks of the absorption and excitation spectra coincide very well, confirming the nature of the features in the region 64 000-88 000 cm^{-1}, which arise due to $4f^{12} \rightarrow 4f^{11}5d$ transitions. In particular, the small peak at 63 000 cm^{-1} is *not* the ZPL of the spin-forbidden transition. This transition is located at clearly lower energy as observed in high resolution emission spectra (cf. Section 4.5.2), therefore the excitation spectra have not been included in the analysis of fine structure.

4.4.2 Excitation spectroscopy of Tm^{3+} doped LiSAF

Figure 4.9 shows excitation spectra for various emissions of LiSAF:Tm^{3+} recorded at 9 K in this work, which are discussed in more detail in [TRU04a]. Curve e exhibits fine structure in

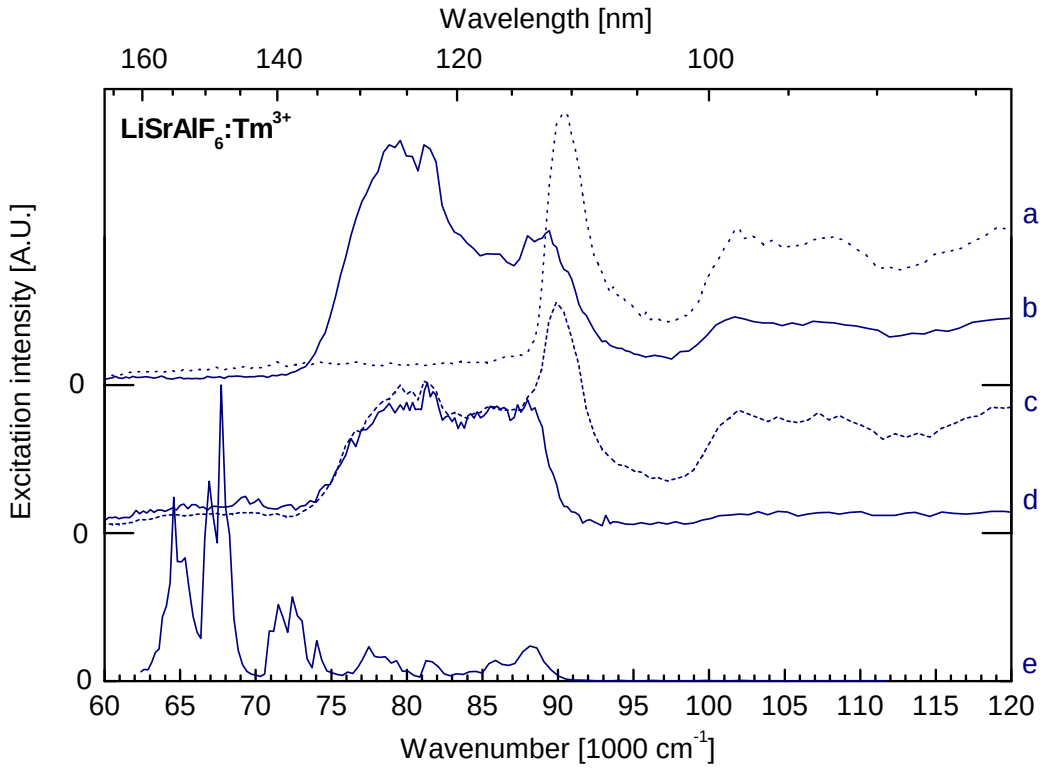

Figure 4.9: Excitation spectra of LiSAF:Tm^{3+} at T =9 K monitoring (a) STE emission at 320 nm, $f \rightarrow f$ emissions at (b) 293 nm, (c) 363 nm, (d) 455 nm; (e) $d \rightarrow f$ emission at 165.5 nm.

excitation monitoring the spin-forbidden $d \rightarrow f$ emission at 165.5 nm. The strong peaks are mainly due to spin-allowed $f \rightarrow d$ excitation into the low-spin state (spin-allowed transition). This luminescence is well excited in the lower d-bands (62 000-75 000 cm^{-1}), however, intensity is decreasing in the upper d-bands (75 000-90 000 cm^{-1}). No $d \rightarrow f$ luminescence is observed at higher excitation energies up to 120 000 cm^{-1}.

The excitation of the broad-band host emission at 320 nm (curve a) reaches its maximum at 91 000 cm^{-1}, which is ascribed to host exciton excitation. The intensity increase of the host emission above 98 000 cm^{-1} suggests that creation of free electron-hole pairs occurs, corresponding to the energy gap in LiSAF.

In order to analyze the population mechanisms of $^1I_6$ and $^1D_2$ states, the respective wavelengths for transitions to the ground state $^3H_6$ were chosen, 293 nm (curve b) and, respectively, 363 nm (curve c). The excitation of the Tm^{3+} $f \rightarrow f$ transitions at 10 K starts above 75 000 cm^{-1}. The excitonic peak at 91 000 cm^{-1} and increased host excitation observed in the spectra are due to an overlap with the broad-band host emission, while this is not the case for the emission at 455 nm (curve d), comprising both $^1I_6 \rightarrow {}^3H_4$ and $^1D_2 \rightarrow {}^3F_4$.

4.4.3 Discussion

The efficient excitation of $f \rightarrow f$ emissions is observed LiSAF:Tm^{3+} in the VUV spectral region. The underlying energy transfer processes are discussed after initial excitation with VUV photons.

Emission of more than one photon can be achieved by either *photon cascade emission* within one ion like in Pr^{3+} [PAP76] or a *cross-relaxation process* populating the lower lying state of two different ions [WEG99b]. Such cross-relaxations may play a role already at rather low doping concentration as shown for $LiYF_4$:Er^{3+} [KHA02].

Excitation into the higher d-states of Tm^{3+} is followed by rapid non-radiative relaxation to the lowest d-state, which can serve as initial state for cross-relaxation and radiative decay. However, since $f \rightarrow f$ emissions are efficiently excited only above 74 000 cm^{-1}, cross-relaxation can be excluded. Also a radiative cascade starting from the d state can be excluded for the same reason. Moreover, the $d \rightarrow f$ emission predominantly populates the ground state and $4f$ states up to $^3F_{2,3}$ (Figure 4.6).

The excitation of $f \rightarrow f$ emissions is not correlated with the strong $5d$ absorption and has its onset in the region of weak $5d$ absorption. Therefore this excitation originates from a different process. The charge transfer (CT) from anion to cation is well established (Section 2.5) manifesting as separate excitation band in Eu^{3+} doped fluorides [GER94]. For other rare earth ions the CT excitation bands overlap with the $5d$ bands and the assignment is based mostly on estimates available for fluorides and oxides [BEL99].

The position of CT transitions can be predicted relative to the position of the corresponding transition of Eu^{3+} in the same host [DOR03b]. According to our measurements the maximum of the CT excitation band in LiSAF:Eu^{3+} crystals is located at 65 300 cm^{-1} and that in LiCAF:Eu^{3+} at 65 300 cm^{-1} [KIR05], the respective CT transition is expected 13 300 cm^{-1} higher in energy [DOR03b]. In analogy, the excitation band peaking at 79 000 cm^{-1} is ascribed to CT absorption, populating the higher lying f-states ($^1I_6$, ^3P_J) non-radiatively as confirmed by the respective emission spectrum. The $5d$ states are bypassed in this process, hence subsequent emission due to $f \rightarrow f$ transitions is observed.

The excitation efficiency of transitions starting from $^1D_2$ is practically the same in the energy range of 78 000 to 90 000 cm^{-1}. At photon energies approaching the host absorption the $^1D_2$ state becomes presumably populated via radiative transfer from emission centers of extrinsic origin. In LiCAF and LiSAF the broad-band emission, arising from the radiative decay of near impurity excitons [CLU85] and impurity or defect centers, is shifted to longer wavelengths, which provides better overlap with lower-lying f-states.

A good knowledge of the population channels is useful for the following discussion of the drastic differences of $f \rightarrow f$ transitions that has been observed in the high-resolution emission spectra under different excitation mechanism (Section 4.5). In Chapter 6 excitation spectra of Tm^{3+} doped LiCAF are compared to those of the Tm^{3+} and Mn^{2+} co-doped crystals.

4.5 Experimental results: Spectroscopy at high resolution

Concerning spectroscopy of Tm^{3+} ions, which are subject to the intermediate electron-phonon coupling, fine structure of $4f^{12} \rightarrow 4f^{12}$ and $4f^{11}5d \rightarrow 4f^{12}$ transitions can be observed at sufficiently high spectral resolution. This allows a detailed analysis of the spectra and characterization of energy transfer processes.

Our experimental setup has a CCD camera installed for recording high resolution emission spectra in the UV to IR region under synchrotron radiation (SR) excitation. Due to the low doping concentration of the LiCAF and LiSAF crystals significant $f \rightarrow f$ emission intensity was only obtained upon excitation into the CT band of Tm^{3+} at 127 nm (78 740 cm^{-1}). Furthermore, the high resolution of the synchrotron excitation source is achieved intrinsically on the expense of intensity. Therefore, direct excitation of the $5d$ bands yields only very weak $f \rightarrow f$ luminescence in both LiCAF and LiSAF, which prevents the acquisition of spectra at the high resolution achieved under CT excitation even at significantly increased counting times.

Recently, the spectrometer with 1 m focal length equipped with a position sensitive VUV detector (Section 3.3.2), which was lent to the Free Electron Laser (FEL) for test experiments during some years, was installed back at our *Superlumi* experimental setup (Section 3.3). $d \rightarrow f$ emission spectra were measured in the VUV with high spectral resolution of Tm^{3+} doped LiCAF, LiSAF, and BYF, revealing a rich fine structure (Section 4.5.2).

An excimer laser setup (Section 3.4) was kindly made available by Prof. A. Meijerink at the *Debye Institute* of the *Universiteit Utrecht* (Netherlands). Operation with F_2 provides intense laser excitation at 157.6 nm (63 450 cm^{-1}), which is situated in the region of the lowest $5d$ bands of Tm^{3+} and is therefore well suited for further evaluation of the transfer characteristics. On the emission side two detectors are installed for acquisition of high resolution spectra in the UV to IR as well as in the VUV region.

Electron-phonon coupling of trivalent rare earth ions

From early systematic investigations of all trivalent RE ions (except for Pm^{3+}) doped into $Ln_2(SO_4)_3 \cdot 8H_2O$, a minimum of the electron-phonon coupling strength was found in the middle of the series (Gd^{3+}), increasing towards the beginning (Pr^{3+}) and the end (Tm^{3+}) measured at 80 K [HEL41]. This trend has been confirmed based on the relative intensities of vibronic lines in absorption spectra measured at RT using Y_2O_3 (doped with Pr, Nd, Eu, Er, Tm) and LaF_3 (Pr, Nd) single crystals [KRU66].

More recently, the intensity of several rare earth ions has been investigated, showing a strong dependence on the position of the opposite-parity configuration ($5d$) and on the polarizability and covalency of the local surrounding of the RE ion [BLA92]. The temperature-dependence of vibronic lines as narrow as 3.5 cm^{-1} has been investigated in $LiBaF_3$:Tm^{3+}

[MEI93]. A quantitative analysis based on vibronic transition probabilities was performed for Tm^{3+} [ELL96] in row with systematic investigations on Pr^{3+}, Gd^{3+}, Eu^{2+}, and Sm^{2+} (see [CAM00, ELL97] and references therein). Regarding one type of RE ions, the actual vibronic transition probabilities increase more than two orders of magnitude with increasing covalency of the host and decreasing energy distance to the $5d$ states due to enhanced contributions from opposite-parity states. Furthermore, the electron-phonon coupling strength differs for different transitions within the same sample [BAS96]. These experimentally observed characteristics are well reproduced by current theoretical models [CAM00].

At both experimental setups in Hamburg and Utrecht $f \rightarrow f$ and $d \rightarrow f$ emission spectra of Tm^{3+} doped crystals were recorded in the visible to VUV spectral range. Fine structure is observed, mainly consisting of zero-phonon lines (ZPL) and transitions involving the creation of vibrational quanta (phonons).

Outline

The splitting of the $^3H_6$ ground state in LiCAF:Tm^{3+} is deducted from the emission of a LiCAF:Tm^{3+}, Mn^{2+} under excimer laser excitation, being the spectrum with the highest resolution available (Section 4.5.1). At liquid Helium temperature transitions are originating from the lowest Stark level of $4f^{12}$ or $4f^{11}5d$ states. ZPL are observed corresponding to transitions to the Stark levels of the final state. The emission spectra due to the isolated $f \rightarrow f$ transitions $^1G_4 \rightarrow {}^3H_6$ are located around 500 nm in the visible, measured with energy resolutions down to 4 cm^{-1}. A tentative assignment of ground state Stark levels has been obtained from these spectra, being in general agreement with experimental and calculated results in other fluoride hosts.

High resolution $d \rightarrow f$ emission spectra excited with SR and laser are in good agreement (Section 4.5.2). Detailed fine structure arising from electronic and vibronic transition of Tm^{3+} in LiCAF and LiSAF is compared, allowing conclusions about the local symmetry and substitutional lattice site. The spectrum observed for the $^1G_4 \rightarrow {}^3H_6$ transitions in LiCAF is shifted in order to match the observed $d \rightarrow f$ emission spectra and to identify transitions to the Stark levels of the ground state.

Since the individual Stark levels could not be assigned, unlike in $LiYF_4$:Er^{3+} [CHE03], $d \rightarrow f$ and various $f \rightarrow f$ emission spectra having the same final state ($^3H_6$ and $^3F_4$) are compared (Section 4.5.3). The ZPL are tentatively assigned, being located at energies comparable to those in LaF_3 [CAR88, CAR89]. In Appendix E the experimentally determined peak energies are tabulated.

A comparison of $4f \rightarrow 4f$ transitions under SR excitation with those measured under laser excitation exhibits large differences in the relative intensities (Section 4.5.4), while the high resolution $d \rightarrow f$ emission spectra measured at both setups, on the other hand, are in good agreement. These differences cannot be attributed to the different excitation energies, thus

$4f \rightarrow 4f$ emission spectra have been re-measured at our setup. However, the emission at increased resolution has remained the same under SR excitation.

Due to the the Stark splitting of the $4f$ states into several levels and the intermediate strength of electron-phonon coupling it is not possible to obtain the coupling strength accurately from the emission intensities. Several weak peaks throughout the spectra are not discussed and may be electronic or vibronic transitions, being subject to additional selection rules. Transitions resulting from unwanted impurities are not excluded as well.

Notation

In the following Sections emission spectra are discussed, consisting mainly of ZPL and transitions to Stark levels of the same final state. $f \rightarrow f$ transitions are labeled A_0, A_1, ... $\left({}^1\mathrm{I}_6 \rightarrow {}^3\mathrm{H}_6\right)$, e.g., or G_0, G_1, ... $\left({}^1\mathrm{G}_4 \rightarrow {}^3\mathrm{H}_6\right)$. $d \rightarrow f$ transitions are labeled Z_0, Z_1, ... accordingly. Furthermore, replica involving vibrational quanta are observed corresponding to electronic transitions. The peaks arising due to a particularly strong vibrational mode ν_{vib} are labeled by (A'_0, A'_1, ...), (G'_0, G'_1, ...), etc.

4.5.1 Establishing some Stark levels of the ground state in LiCAF

The interpretation of fine structure in $4f \rightarrow 4f$ and $5d \rightarrow 4f$ transitions of rare earth ions requires knowledge of the Stark level splitting. For the LiCAF:Tm^{3+} crystal under investigation, neither experimental nor theoretical results beneficial in this respect have been found in the literature. The energy level positions, in particular those of the Stark levels, are fairly different in different hosts, which prohibits a quantitative comparison with other hosts.

Detailed work on $f \rightarrow f$ transitions of Tm^{3+} in $Y_3Al_5O_{12}$ (YAG) at high resolution has been reported previously based on absorption and fluorescence spectra as well as theoretical calculations [GRU89]. The dodecahedral coordinated Y^{3+} site (C_2 symmetry) in the oxide crystal implies a splitting of the ${}^3\mathrm{H}_6$ ground state in YAG into the maximum of 13 Stark levels, which is also expected for LiCAF:Tm^{3+} in the case of local charge compensation.

In a more recent publication excellent emission spectra of YAG:Tm^{3+} have been presented [LUP93]. Especially $f \rightarrow f$ emission peaks from higher f states are well resolved. Sharp ZPL are observed due to transitions originating from the lowest ${}^1\mathrm{G}_4$ level to several Stark levels of the ground state. The high-energetic emission peaks within this multiplet are quite sharp, presumably limited by resolution. Transitions to higher ${}^3\mathrm{H}_6$ Stark levels (at lower energy) have broader peaks due to electronic transitions, which is also observed for the ${}^3\mathrm{H}_4 \rightarrow {}^3\mathrm{H}_6$ transition. The emission spectra presented in this thesis exhibit similar general characteristics.

Figure 4.10 shows emission spectra at 7 K of LiCAF:Tm (curve a) and LiCAF:Tm,Mn (curve b) using laser excitation at 157.6 nm (63 450 cm^{-1}). The detailed fine structure of the ${}^1\mathrm{G}_4 \rightarrow {}^3\mathrm{H}_6$ transition agrees in both measurements. Since the latter spectrum (curve b)

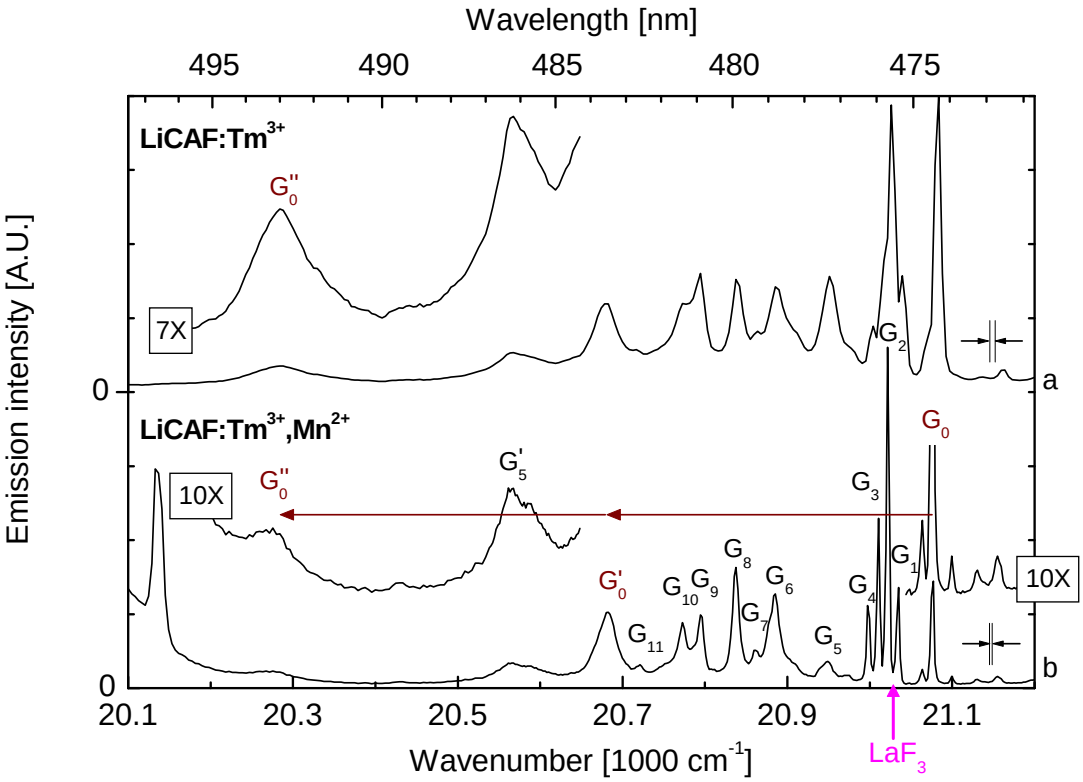

Figure 4.10: Emission spectra of the $^1G_4 \rightarrow {}^3H_6$ transition, $\lambda_{ex} = 157.6$ nm. (a) LiCAF:Tm, T =7.4 K $\Delta\lambda_{em} = 0.15$ nm; (b) LiCAF:Tm,Mn, T =7.3 K, $\Delta\lambda_{em} = 0.08$ nm.

is the measurement with the highest spectral resolution available, the Stark levels of the ground state are established on this basis. The corresponding energy resolution is below 4 cm^{-1} ($\Delta\lambda_{em}$ =0.08 nm). Only the stronger peaks are assigned, since numerous vibrational modes of the lattice couple to each electronic transition leading to weak peaks. Due to the lack of theoretical calculations the following assignment has to be regarded as tentative, since vibrational modes with narrow line width in Eu^{2+} [MEI93] as well as ZPL with broader width occur, as those observed in both spectra below 20 000 cm^{-1}. The resulting experimental peak positions and FWHM are tabulated in Table 4.4 as well as in Appendix E on page 151.

G_0 is observed as separate strong peak in curve b at 21 076 cm^{-1} (FWHM 2.6 cm^{-1}) attributed to a ZPL. The energy position of the same transition between lowest Stark components in LaF_3:Tm^{3+} is indicated by an arrow, being slightly below G_0. Two sharp peaks are located just next to G_0, which are not attributed to electronic transitions. If further peak were assigned to ZPL, the total number of Stark levels would exceed the maximum of 13 sub-levels. In addition, a comparison of experimental and calculated Tm^{3+} Stark levels in various crystals shows that generally an energy difference of some ten wavenumber is present between the first two zero-phonon lines in fluorides (cf. Figure 4.11 below). In the LiCAF:Tm spectrum (curve

a) the peak is broadened because of the lower resolution as indicated in the figure. The two weak peaks above 21 100 cm^{-1} are clearly broader and originate from a different transition (cf. Figure 4.18).

Intense narrow lines G_1 to G_4 attributed to electronic transitions are observed just above 21 000 cm^{-1}, having line widths comparable to that of G_0. The peaks below 21 000 cm^{-1} have a significant larger FWHM in common, which is the real width of the lines (and not resolution limited). Similarly, electronic transitions to higher Stark levels of Tm^{3+} in YAG are broader compared to those between lower Stark levels [LUP93]. On the other hand it is not excluded that some of the narrow or broader assigned peaks are of vibronic origin, since vibrational peaks may have a FWHM as low as 4 cm^{-1} as observed in $LiBaF_3$:Eu^{2+} [MEI93].

An emission band G_0' at 20 680 cm^{-1} (FWHM 25 cm^{-1}) is observed 400 cm^{-1} lower in energy than G_0 in both curves as indicated by long arrows. The width of this band is considerably larger than those of the electronic lines, and below only broad features are observed. A value for the phonon frequency of 452 cm^{-1} was given for Cr^{3+} ions occupy the Al^{3+} sites in LiCAF [PAY89]. The phonon energy may change due to a fairly changed surrounding or due to coupling of Tm^{3+} to a local mode on the charge compensated (distorted) lattice site. The possibility of coupling to a strong local mode is supported by the fact, that even the second order replica G_0'' is clearly observed peaking at 20 280 cm^{-1}. The FWHM is again significantly increased compared to that of G_0', and the energy difference equals again 395 cm^{-1}. A corresponding broad emission band is also observed for the transition G_5 at 20 560 cm^{-1}.

Recently, defect simulation and crystal field studies of LiCAF and LiSAF indicated a lower symmetry for rare earth ions doped into the Ca^{2+} or Sr^{2+} site due to charge compensation, which destroys inversion symmetry [AMA03]. As a result, the local symmetry of LiCAF:Eu^{3+} appeared to involve a C_2 element.

The observation of nearly the maximum of 13 Stark levels in the LiCAF spectra points to a symmetry-lowering mechanism of the local Tm^{3+} surrounding, while the symmetry of the Ca^{2+} site without distortions (C_{3i}) would correspond to only eight levels (Section 2.2.2).

The high resolution emission spectrum allowed the identification of 12 peaks G_0 to G_{11} as shown in Table 4.4, tentatively assigned to electronic transitions from $^1G_4$ to the Stark levels of the $^3H_6$ ground state. This assignment is compared with $5d$ (Section 4.5.2) and $4f$ transitions (Section 4.5.3) having the ground state as final state.

The replica are investigated in more detail in Section 4.5.4. In the following discussion the Stark levels of Tm^{3+} in various crystals are compared to those established above.

Stark level splitting in various crystal hosts

Figure 4.11 shows the Stark splitting of the Tm^{3+} ground state in LiCAF experimentally determined in this work from high resolution emission spectra compared to those of various

Peak	LiCAF:Tm	LiCAF:Tm,Mn	ΔE
G_0	21 082 (8)	21 076 (2.6)	0
G_1	*21 040*	21 034 (2.1)	42
G_2	21 026 (13)	21 022 (3.5)	54
G_3	*21 004*	21 010 (3.4)	66
G_4	-	20 998 (3.6)	78
G_5	20 952 (19)	20 950 (22)	126
G_6	20 888 (29)	20 884 (18)	192
G_7	*20 864*	20 860	216
G_8	20 839 (13)	20 837 (11)	239
G_9	20 794 (11)	20 796	280
G_{10}	20 774 (32)	20 773	303
G_{11}	*20 717*	20 721	355

Table 4.4: Emission peak energies (and FWHM) in cm^{-1} for the $^1G_4 \rightarrow {}^3H_6$ transition of LiCAF:Tm and LiCAF:Tm,Mn at 7 K. ΔE is the energy difference to the first ZPL. Weak peaks or shoulders denoted in *italic*.

crystals. The overall Stark splitting in LiCAF (row 0) is determined to be 355 cm^{-1}.

The substitutional Y^{3+} lattice site of the series of elpasolite crystals (1-5) has six-fold (octahedral) symmetry. The Stark level splitting is determined to be between 200 and 500 cm^{-1} and exhibits a reduction in the overall splitting when going from fluorides (1,2) to the chloride (3) and bromide (4), i.e. with increasing covalency. The overall Stark splitting of Tm^{3+} in $LiYF_4$ (6) and LaF_3 (10) agrees with that of LiCAF:Tm^{3+} (0), and also the $f \rightarrow f$ transition energies of LaF_3 have been found to match within some ten wavenumbers in these hosts as shown in the following discussion. Only the YAG and GdOCl host have a total ground state splitting of 800 cm^{-1}. The general agreement between the experimentally determined Stark levels in LiCAF:Tm^{3+} and other fluorides (1, 2, 6, 10) confirms the plausibility of the proposed assignment.

4.5.2 High resolution $d \rightarrow f$ emission spectra

In Section 4.3 the $4f^{11}5d \rightarrow 4f^{12}$ emission of Tm^{3+} doped LiCAF, LiSAF, and BYF has been established from time-resolved low resolution emission spectra under excitation with synchrotron radiation (SR). High resolution spectroscopy of the most intense transitions, having the ground state as final state, is presented in this section, which has been measured with our 1 m monochromator in combination with the position sensitive detector (cf. Section 3.3.2).

Due to the high resolution, distinct sharp peaks are observed due to $d \rightarrow f$ transitions of Tm^{3+} in LiCAF and LiSAF for the first time, comprising electronic transitions between the crystal field splitted Stark levels and vibrational lines. This is a consequence of the intermediate

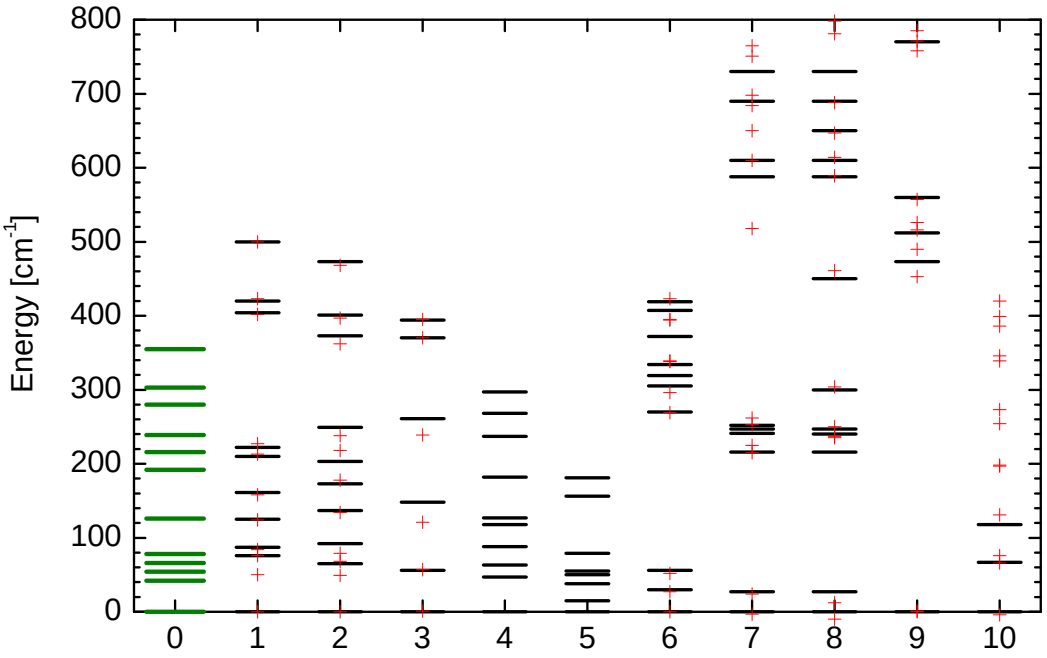

Figure 4.11: Experimental Stark levels of various Tm^{3+} doped crystals including calculated energies (+). 0 - LiCAF (this work), 1 - Rb_2NaTmF_6 [NIS99], 2 - Cs_2NaTmF_6 [NIN03], 3 - Cs_2NaYCl_6 [THO01], 4 -$Cs_2NaTmCl_6$ [NIN03], 5 -$Cs_2NaTmBr_6$ [NIN03], 6 - $LiYF_4$ [ELL96], 7 - YAG [GRU89], 8 - YAG [TIS95], 9 - GdOCl [HOE95], 10 - LaF_3 [CAR89].

electron-phonon coupling of Tm^{3+}. Intrinsically, in the strong coupling case applicable for transition metal ions such as Mn^{2+} detailed fine structure cannot be observed even though ZPL are resolved in some hosts, e.g. in MgF_2:Mn^{2+} (Section 5.2.4).

The high resolution emission spectra of LiSAF:Tm^{3+} under excitation with SR are presented. In the following discussion, spectra of LiCAF:Tm^{3+} excited with SR and laser are compared, being in good agreement. The peaks due to spin-forbidden $d \rightarrow f$ transitions to Stark levels of $^3H_6$ are compared with those of Tm^{3+} in LiSAF and with the $^1G_4 \rightarrow {}^3H_6$ transition utilized to establish the ground state splitting in Section 4.5.1.

Fine structure of $d \rightarrow f$ emission in LiSAF

Emission spectra due to the $5d \rightarrow 4f$ emission of LiSAF:Tm^{3+} are presented in Figure 4.12. The SR excitation at 155.0 nm is within strong absorption of the lowest (spin-allowed) $5d$-bands (cf. Figure 4.9). Figure 4.12 (curve a) shows luminescence recorded in second order

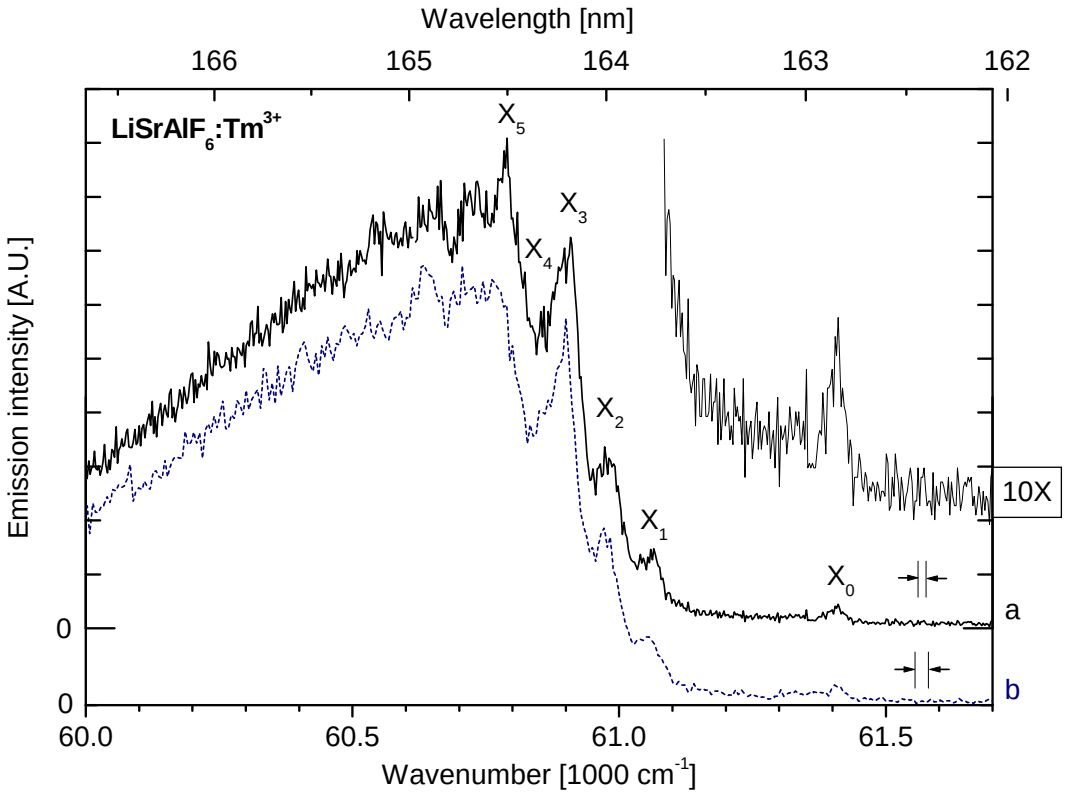

Figure 4.12: High resolution $d \rightarrow f$ emission spectra of LiSAF:Tm^{3+}, T =7.3 K, λ_{ex} = 155 nm. Emission was measured in (a) second order, $\tau_c = 4800$ s, $\Delta\lambda_{em} \leq 0.04$ nm; (b) first order, $\tau_c = 600$ s, $\Delta\lambda_{em} \leq 0.08$ nm.

of emission, reaching a resolution better than 0.04 nm, on expense of intensity, therefore a longer counting time $\tau_c = 4800$ s has been chosen. The observed peaks agree well with those measured in first order (curve b), which have been recorded close to the maximum resolution of 0.07 nm, limited by the detector.

The emission peak X_0 at 61 410 cm^{-1} (FWHM 30 cm^{-1}) is assigned to a ZPL. It should be pointed out, that nearly no emission occurs in the region between X_0 and X_1 (peaking at 61 060 cm^{-1}). Further peaks X_2 (60 970), X_3 (60 900), X_4 (60 850), and X_5 (60 790) are observed, which may be interpreted as ZPL to Stark levels of the ground state $^3H_6$. However, the energy of X_2 is already 437 cm^{-1} below X_0 in the range of multiple vibronic transitions, and the overall Stark splitting is expected in this region. Hence, the peaks X_3 to X_5 can be very well due electronic transition coupled to local modes.

The results are discussed subsequent to high resolution emission spectra of the iso-structural LiCAF compound presented below.

Fine structure of $d \rightarrow f$ emission in LiCAF

Figure 4.13 (curve a) shows the $d \rightarrow f$ emission spectrum of LiCAF:Tm^{3+} single crystal, measured at the *Superlumi* experimental station at 7.4 K using the position-sensitive detector in combination with the 1 m spectrometer. The excitation energy was 147.77 nm in the region of spin-allowed $f \rightarrow d$ absorption. Due to the high spectral resolution detailed fine structure is revealed, as observed recently in $LiYF_4$:Er^{3+} [CHE03].

The emission spectrum (curve b) of cleaved LiCAF:Tm^{3+}, Mn^{2+} has been measured at the excimer laser setup providing intense excitation pulses at 157.6 nm. This polished sample yields much better resolved peaks than the cleaved LiCAF:Tm^{3+} sample measured at the same setup (not shown), while a detailed comparison shows a good agreement of both spectra. This confirms the energy calibration of spectrum (curve a) as well as the absence of any impurity emission in this energy range. The laser excitation energy is just at the onset of the first $f \rightarrow d$ absorption (cf. Figure 4.8), while the SR was set to a maximum.

The emission spectrum of the $^1G_4 \rightarrow {}^3H_6$ transitions discussed in the previous Section (Figure 4.10) is shifted by 40 270 cm^{-1} in order to match the ZPL (G_0) with that of the $d \rightarrow f$ emission (Z_0).

The peak Z_0 at 61 410 cm^{-1} is assigned to the ZPL of the spin-forbidden transition from the lowest $5d$ level to the lowest level of the $4f$ ground state $^3H_6$ in agreement with the predicted value (Section 4.1.3). Further peaks are clearly observed as assigned in the figure, while the energy are tabulated in Appendix E. The $d \rightarrow f$ emission is characterized by strong vibrational modes contributing to the raise of intensity towards lower energy, which is not the case for the intra-configurational $f \rightarrow f$ transitions.

The Stark splitting of $d \rightarrow f$ and the $^1G_4 \rightarrow {}^3H_6$ transition of Tm^{3+} in LiCAF disagrees somewhat, not all peaks can be assigned to transitions to the Stark levels established in Section 4.5.1, whereas for Er^{3+} in $LiYF_4$ a clear assignment has been demonstrated [CHE03].

The narrow and closely spaced peaks G_1 to G_4 compare to the region of Z_1 in the $d \rightarrow f$ emission (curve b). In the SR excited spectrum, emission without distinct structure is observed in this region (curve a). The peaks G_5 to G_7 have no corresponding partner peak, while G_8 is matched with Z_2 observed as clear peak (a) and as shoulder (b). Z_3 and Z_5 are assigned corresponding to G_9 and G_{11}, respectively. G_{10} corresponds to a (local) intensity minimum in curve b, only the SR excited curve a may suggest this transition hidden in the shoulder.

Z_6 to Z_{11} have been tabulated together with other transition energies in Appendix E. These peaks are in the region of numerous vibrational transitions beyond the energy range of pure electronic lines, contributing to the overall rise of emission intensity for $d \rightarrow f$ transitions (Section 2.3).

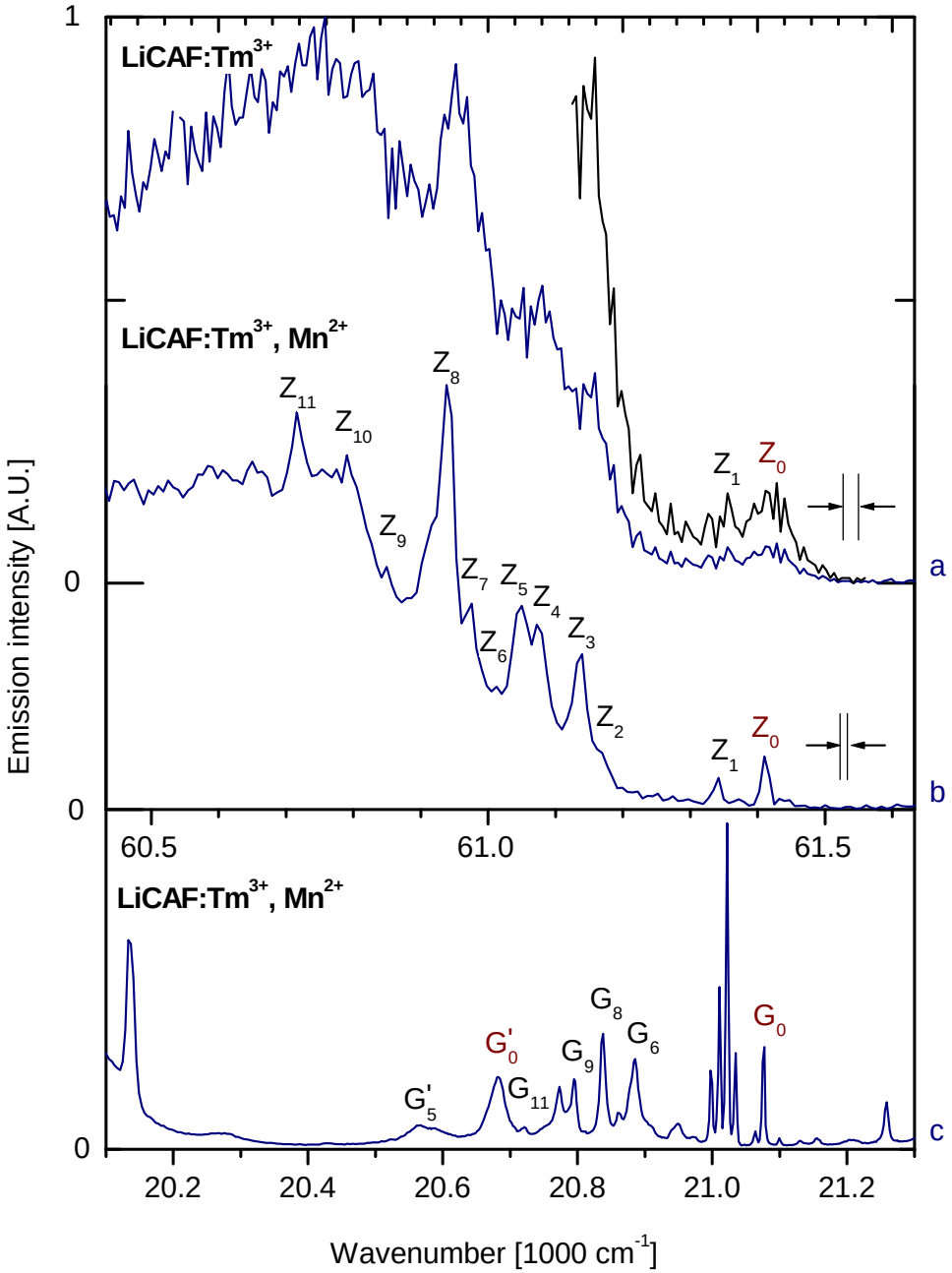

Figure 4.13: High resolution emission spectra of the (spin-forbidden) $d \rightarrow f$ transition in (a) LiCAF:Tm^{3+}, λ_{ex} = 147.77 nm, T = 7.4 K, τ_c =1000 s, $\Delta\lambda_{em}$ = 0.08 nm; (b,c) LiCAF:Tm^{3+},Mn^{2+}, λ_{ex} = 157.6 nm, T = 7.3 K, $\Delta\lambda_{em}$ = 0.025 nm; (c) $^1G_4 \rightarrow {}^3H_6$ emission to Stark levels (from Figure 4.10). Note the shifted energy scales.

Discussion

For the first time, detailed fine structure of $4f^{11}5d \rightarrow 4f^{12}$ transitions in Tm^{3+} doped LiCAF and LiSAF has been observed in high resolution emission spectra. Both measurements of LiCAF, using synchrotron radiation (SR) and excimer laser excitation, are in good agreement. The emission spectrum of LiSAF exhibits six peaks X_0 to X_5, while in LiCAF much more fine structure is observed.

Remarkably, the energy position is the same as that of X_0 in LiSAF in spite of the enlarged lattice, and the energy of the emission peak maxima is predicted to shift 116 cm^{-1} to higher energy when going from LiCAF to LiSAF. This fact is qualitatively understood from the Sr^{2+} lattice site yielding a weaker crystal field than that of the smaller Ca^{2+} site, hence the energy levels are expected to be blue-shifted towards the free-ion case. The results, however, are contradictory when comparing the experimental peak maxima of Tm^{3+} doped LiCAF and LiSAF (cf. Section 4.1.3), exhibiting a small red-shift of 56 cm^{-1}. Different sites due to Tm^{3+}-Tm^{3+} pairs can be excluded at the confirmed low doping concentration.

This phenomenom brings up the issue of charge compensation, which has been discussed in Section 3.2.1. In LiSAF the Al^{3+} site is clearly preferred when comparing the calculated potentials of different substitution schemes [AMA03]. For the LiSAF host the valence of the substitutional ion and lattice site are the same, but in LiCAF the *trivalent* Tm^{3+} substitutes a *divalent* Ca^{2+} ion. The most probable compensation scheme involves Li^{+} vacancies, while fluorine interstitials and substitution of the Al^{3+} site are only slightly less probable [AMA03].

According to Kramers theorem (Section 2.2.2) the ground state $^3H_6$ of Tm^{3+} ($4f^{12}$) is expected to split into a maximum of 13 non-degenerate states, while the point group of the substitutional Ca^{2+} site in LiCAF (C_{3i}) yields eight sub-levels. Note that not all the transitions may be observed due to their low probability or forbidden nature.

The spectra of LiCAF show clearly more fine structure, strongly suggesting a symmetry-lowering lattice distortion. Local charge compensation of any kind is expected to introduce sites of reduced symmetry, which should yield the maximum of non-degenerate states.

Taking into account the coincident energy of the ZPL in both crystals strongly suggests the occupation of different lattice sites, namely Ca^{2+} in LiCAF and Al^{3+} in LiSAF, which confirms the results from simulation of defect structures in the respective hosts [AMA03, AMA04]. This explains as well the red-energy shift of the $d \rightarrow f$ emission maximum in LiSAF, because the substitution lattice site is much smaller than that in LiCAF.

The observation, that two closely spaced transitions occur in LiCAF (Z_0 and Z_1), while only one is found in LiSAF (X_0), suggests that two occupied lattice sites in LiCAF are responsible for the additional emission features, which are the Ca^{2+} and Al^{3+} site. This may explain the coincident energy of Z_0 and X_0, both being incorporated on equivalent Al^{3+} sites in LiCAF and LiSAF. Z_1 would be a ZPL of Tm^{3+} on the charge-compensated distorted Ca^{2+} site, leading to a Stark splitting into 13 sub-levels of the ground state.

The proposed interpretation of the spectra involving the occupation of two sites in LiCAF is strongly supported by $f \rightarrow f$ emission spectra excited with SR and laser excitation, exhibiting strong differences under varied excitation conditions (Section 4.5.4).

4.5.3 Comparison of fine structure in $f \rightarrow f$ and $d \rightarrow f$ transitions

In the previous discussion transitions to lower Stark levels within $d \rightarrow f$ and the $f \rightarrow f$ transition $^1G_4 \rightarrow {}^3H_6$ have been discussed for Tm^{3+} doped LiCAF, while not all peaks could be assigned in both spectra. The $d \rightarrow f$ emission spectra recorded under synchrotron radiation (SR) excitation agrees well with that measured under excimer laser excitation at 157.6 nm (63 450 cm^{-1}).

In this section, several $f \rightarrow f$ transitions of LiCAF:Tm^{3+} single crystal are compared to $d \rightarrow f$ and $f \rightarrow f$ transitions having the same final state by shifting the respective spectra to match the ZPL. Only the laser excited spectra are discussed, because Stark levels of the $^3H_6$ ground state have been assigned by analyzing the laser excited spectra (Section 4.5.1). The resulting energy values are tabulated in Appendix E.

Excitation at 157.6 nm within the $5d$ bands leads to radiative transfer populating the $4f$ states in their lowest vibronic level. Emission due to the first step of this radiative cascade has been observed, populating $4f$ states up to the ($^1I_6$, ^3P_J) multiplets, while SR excitation has shown significant transition to states up to $^1G_4$ (Section 4.3). The second step of the cascade emission accounts for the $f \rightarrow f$ transition presented in Figure 4.14. The spectral resolutions are indicated.

Obviously, the individual $f \rightarrow f$ emission peaks to Stark levels of the ground state disagree, while the peaks A_0 and C_0 could be assigned to zero-phonon lines in good agreement with the corresponding transition energies in LaF_3:Tm^{3+} (indicated by short arrows). The following peaks in curves a and b have no obvious correspondence to the other spectra, which is attributed to strong electron-phonon coupling for these transitions.

A_0 and A_1 (curve a) exhibit partner peaks lowered by 400 cm^{-1}, which is the energy of a vibrational quanta identified for the $^1G_4 \rightarrow {}^3H_6$ transition (cf. Section 4.5.1). Furthermore, a broad band is observed at 34 080 cm^{-1} of presumably vibronic origin.

Besides C_0 only a very weak peak C_5 is identified (curve b) for the $^1D_2 \rightarrow {}^3H_6$ transition. On the other hand, a variety of pronounced peaks is observed between 27 200 cm^{-1} and 27 700 cm^{-1}, confirming a strong electron-phonon coupling for this particular transition.

Being aware that the question may arise concerning the origin of the peak at 21 138 cm^{-1} and the increasing intensity (curve c), the answer is provided as follows: This emission spectrum is that of the LiCAF:Tm,Mn sample, thus the intra-configurational $3d \rightarrow 3d$ transition $^4T_{1g} \rightarrow {}^6A_{1g}$ of Mn^{2+} has been recorded. The sharp peak is due to the corresponding zero-phonon line which is not observed at lower resolution (Section 5.2.3).

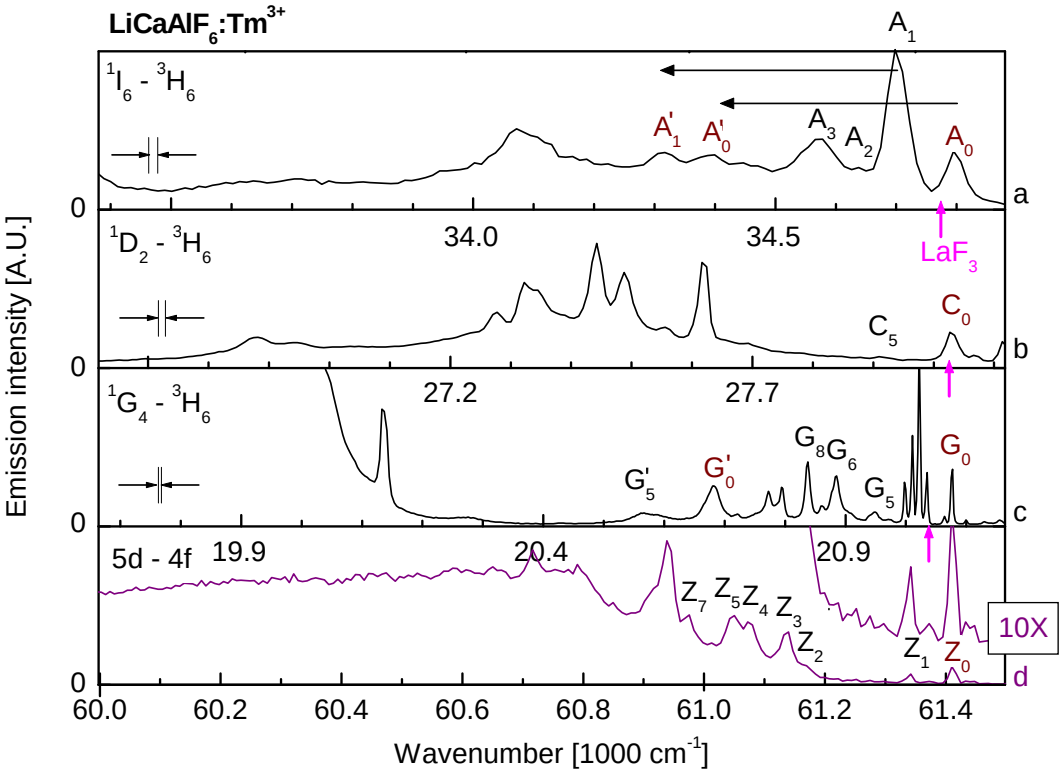

Figure 4.14: $d \rightarrow f$ and $f \rightarrow f$ emission spectra of LiCAF:Tm having $^3H_6$ as final state. λ_{ex} =157.6 nm, T =7.4 K, (a) $^1I_6 \rightarrow {}^3H_6$, $\Delta\lambda_{em}$ = 0.15 nm; (b) $^1D_2 \rightarrow {}^3H_6$, $\Delta\lambda_{em}$ = 0.15 nm; (c) LiCAF:Tm,Mn, $^1G_4 \rightarrow {}^3H_6$, $\Delta\lambda_{em}$ = 0.08 nm (cf. Figure 4.10); (d) $d \rightarrow f$ transition, T = 7.3 K, $\Delta\lambda_{em}$ = 0.025 nm (cf. Figure 4.13). Note the shifted energy scales.

In Figure 4.15 similar differences are observed when comparing $d \rightarrow f$ and $f \rightarrow f$ emission having $^3F_4$ as final state. By the preceeding assignment of ZPL, the energy levels $^1I_6$, $^1D_2$, and $^1G_4$ have been determined. Hence, the ZPL due to transitions to the $^3F_4$ state are expected at defined energies and the energy scales have been shifted accordingly.

Y_0 at 55 797 cm^{-1} is clearly due to a ZPL of the $d \rightarrow f$ in Tm^{3+}, having an energy difference of 5613 cm^{-1} to Z_0. This coincides very well with the energy of the lowest excited state ($^3F_4$) in LaF_3:Tm^{3+} at 5615 cm^{-1}, a value that hardly changes in different host (cf. Section 4.1.1). The closely spaced peaks Y_0 and Y_1 may be due to transitions to different Stark levels, but also a consequence of two occupational sites, reminding of the two peaks in Figure 4.14.

Concerning $f \rightarrow f$ transitions (curves a and b), a ZPL is clearly observed in both spectra coinciding with Y_0. This confirms the initial assignment of the zero-phonon lines. The peak B_1 (curve a) is attributed to the transition $^1I_6 \rightarrow {}^3F_4$, which has a vibrational partner peak 400 cm^{-1} lower in energy (indicated by a long arrow), similar to those observed for the $^1G_4 \rightarrow {}^3H_6$ and $^1I_6 \rightarrow {}^3H_6$ transitions. Considering the lower resolution of this spectrum

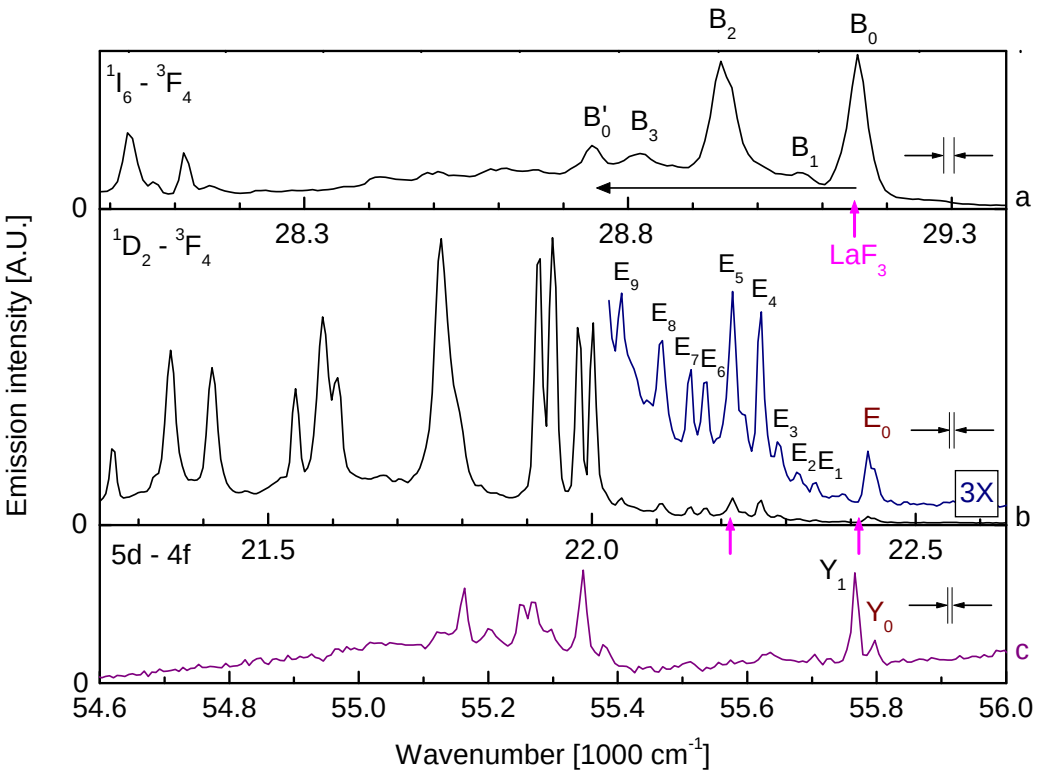

Figure 4.15: $d \rightarrow f$ and $f \rightarrow f$ emission spectra of LiCAF:Tm^{3+} having $^3F_4$ as final state, λ_{ex} =157.6 nm, T =7.4 K, $\Delta\lambda_{em}$ = 0.15 nm. (a) $^1I_6 \rightarrow {}^3F_4$ (B_x); (b) $^1D_2 \rightarrow {}^3F_4$ (E_x); (c) $d \rightarrow f$ transition (Y_x), λ_{ex} = 157.6 nm, T = 7.3 K, $\Delta\lambda_{em}$ = 0.025 nm. Note the shifted energy scales.

and the resulting width, this peak probably consists of more than one ZPL. This is also true for the following peaks.

In the energy range 22 000 cm^{-1} to 22 500 cm^{-1} (curve b) two pronounced transitions, namely $^1D_2 \rightarrow {}^3F_4$ and $^1I_6 \rightarrow {}^3H_4$, have their fine structure largely overlapping, which makes an exact assignment impossible. The peak E_0 at 22 426 cm^{-1} is weakly but clearly pronounced in the laser excited spectrum, attributed to a ZPL of the $^1D_2 \rightarrow {}^3F_4$ transition. Further peaks E_1 to E_9 of comparable intensity are observed down to 20 000 cm^{-1}, which may be a result of the $^3F_4$ crystal field splitting into the maximum of 9 Stark sub-levels. Due to the overlap in this region some peaks may be attributed to the $^1I_6 \rightarrow {}^3H_4$ transition, which has its ZPL in LaF_3 at 22 208 cm^{-1} as indicated in the figure by a short vertical arrow. The peaks observed below 22 000 cm^{-1} have a much higher intensity, being about one order of magnitude more intense. This suggests attributing them to electronic transitions of $^1I_6 \rightarrow {}^3H_4$.

The comparison of fine structure in $d \rightarrow f$ and $f \rightarrow f$ emission having the same final state exhibits large differences, rendering a reliable comparison and assignment of transitions to

Stark levels impossible. This can be very well a consequence of different selection rules between the transitions to individual Stark components. Since Tm^{3+} is subject to larger electron-phonon coupling than the rare earth ions in the middle of the series, the influence on selection rules for transitions between different multiplets appears quite pronounced for this type of ion. In contrast a good agreement has been observed when comparing $d \rightarrow f$ and $f \rightarrow f$ transitions in $LiYF_4$:Er^{3+} [CHE03].

4.5.4 Emission characteristics under excitation of the $5d$ levels versus the charge transfer state of Tm^{3+}

High-resolution $4f^{12} \rightarrow 4f^{12}$ emission spectra under excimer laser excitation within the lowest $5d$-band of Tm^{3+} in LiCAF have been discussed in the preceeding Section 4.5.3 in terms of Stark levels.

The synchrotron radiation (SR) excited spectra measured at our setup with the CCD camera and 1200 lines/grating at $T = 7.4$ K have not been discussed so far for the following reasons:

After the laser excited spectra had been measured, dramatic differences compared to the SR measurements became obvious. The energy calibration of both measurements have been checked reliably, proving to be very accurate. The $f \rightarrow f$ emission spectra have been re-measured several times at our experimental setup with increased resolution and/or counting times or with different crystal pieces, but the results did not change considerably.

Thus, an attempt of an explanation is presented in this concluding discussion, explaining the observed differences in fine structure and onset of $f \rightarrow f$ transitions in terms of more than one occupational lattice site for Tm^{3+} in LiCAF, namely the Al^{3+} site and the Ca^{2+} site with charge compensation, in agreement with results from very recent defect simulations [AMA03] (cf. Section 3.2.1 for details). Several replica of electronic transitions will be attributed to a strong local mode with energy $\nu_{vib} = 395$ cm^{-1} as mentioned in the previous discussion.

The respective energies of peaks are tabulated in Appendix E.

Figure 4.16 shows emission spectra resulting from the $^1I_6 \rightarrow {}^3H_6$ transition of Tm^{3+} in LiCAF single crystals. Synchrotron radiation was used to excite at 127 nm the charge transfer state (curve a), and excimer laser to excite into the lower d-states at 157.6 nm (curve b).

The distinct peak A_0 at 34 795 cm^{-1} (curve b) exhibits a relatively large FWHM of 36 cm^{-1}, while the energy resolution at this energy is about 18 cm^{-1}. It is assigned to a ZPL, or at least containing one or more ZPL. In the red spectral region resolutions are achieved below 6 cm^{-1}, which reveals more details in the following discussion. The peak is blue-shifted by 22 cm^{-1} compared to that in LaF_3:Tm^{3+} [CAR89]. However, no corresponding peak is observed in the CT excited spectrum (curve a). Further peaks A_1 to A_4 appear, whereas no coincidence of peaks in both spectra has to be admitted, indeed they seems to be almost anti-correlated.

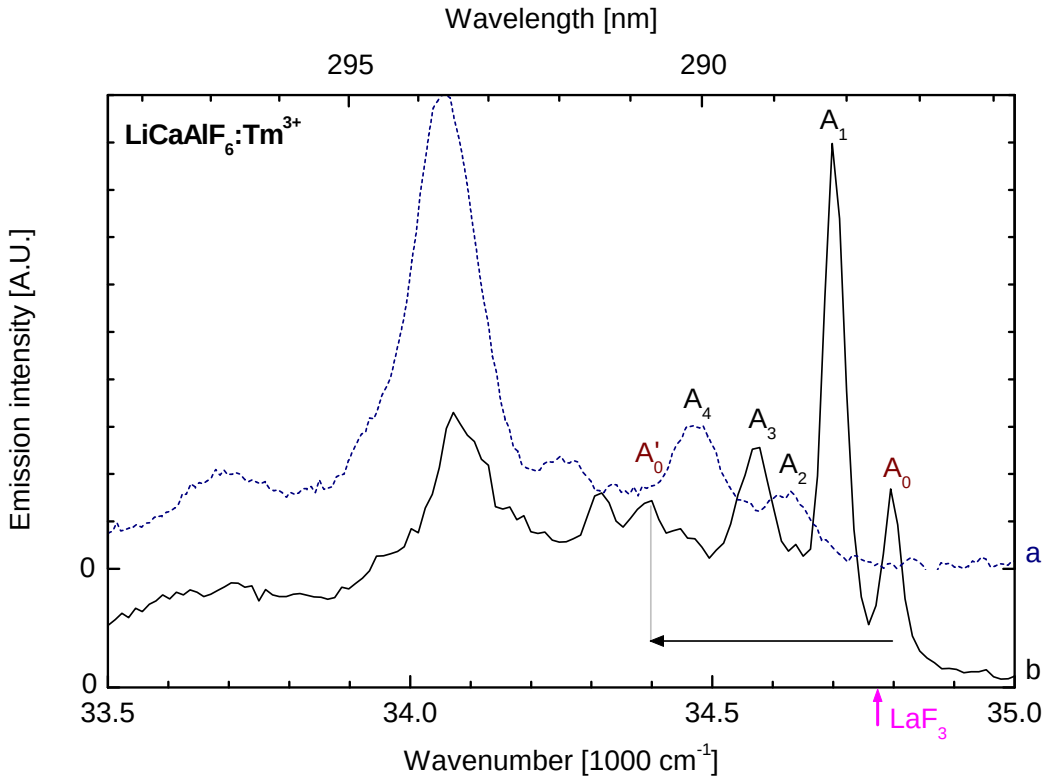

Figure 4.16: Emission spectra of the $^1I_6 \rightarrow {}^3H_6$ (A_x) transition in LiCAF:Tm^{3+}. (a) $\lambda_{ex} =$ 127 nm, $T = 10$ K, $\Delta\lambda_{em} \leq 0.5$ nm; $\lambda_{ex} = 157.6$ nm, $T = 7.4$ K, $\Delta\lambda_{em} = 0.15$ nm.

The long arrow represent the energy $\nu_{vib} = 395$ cm^{-1} of a strong vibrational mode, which is simultaneously excited along with the $f \rightarrow f$ transitions frequently observed in the spectra (cf. Sections 4.5.1 and 4.5.3). A possible vibronic satellite of A_0 is $A'_0 = A_0 - \nu_{vib}$ at 34 400 cm^{-1}. The broad peak around 34 000 cm^{-1} and further broad emission bands below that are attributed to transitions involving the creation of vibrational modes, in agreement in both spectra.

Under 127 nm excitation via the CT state with SR (curve b), the first emission peak observed on the high-energy side of the spectrum coincides with A_2, while A_2 is only a weak peak in curve a.

Figure 4.17 shows the energy region 25 000 cm^{-1} to 29 500 cm^{-1}, which comprises several $f \rightarrow f$ transitions. Drastic differences in the relative intensities are observed when comparing the emission spectra, similar as in the previous figure. The ZPL of the corresponding transitions are assigned from the excimer laser excited spectrum (curve b), in agreement with the ZPL determined for LaF_3:Tm^{3+} which are indicated by short arrows [CAR88, CAR89].

The first ZPL of the $^1I_6 \rightarrow {}^3F_4$ transition is assigned to B_0 at 29 155 cm^{-1}, clearly observed

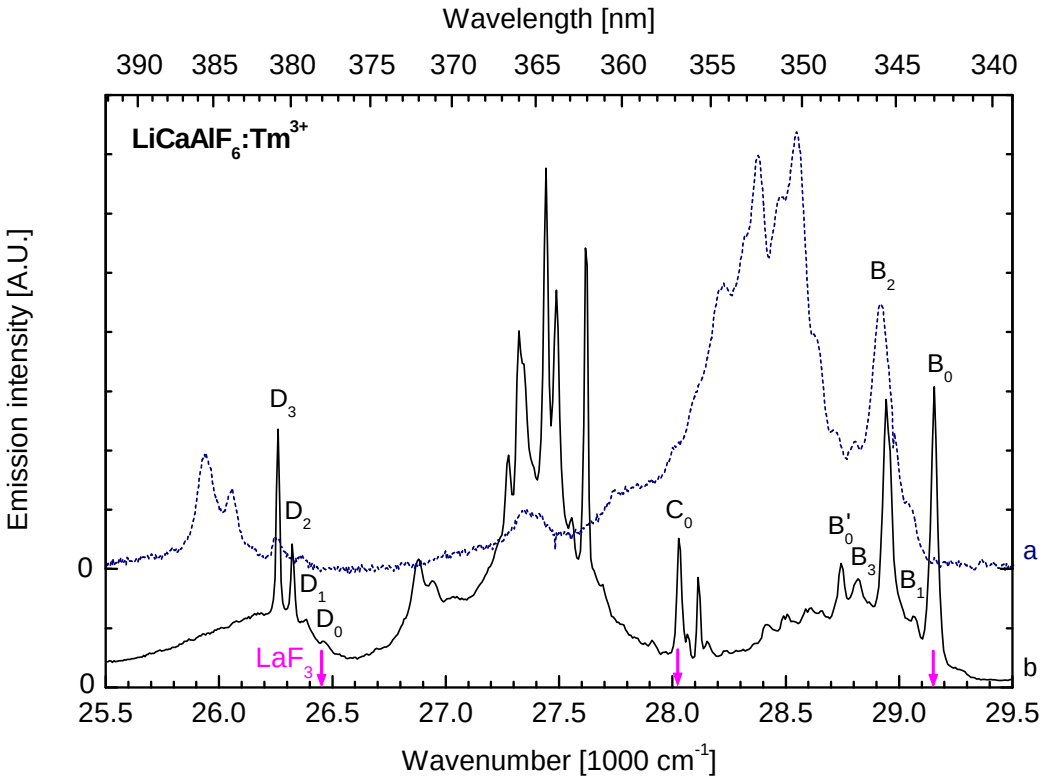

Figure 4.17: Emission spectra of the $^1I_6 \rightarrow {}^3F_4$ (B_x), $^1D_2 \rightarrow {}^3H_6$ (C_x), and $^1I_6 \rightarrow {}^3H_5$ (D_x) transitions in LiCAF:Tm^{3+}. (a) $\lambda_{ex} = 127$ nm, $T = 10$ K, $\Delta\lambda_{em} \leq 0.5$ nm; (b) $\lambda_{ex} = 157.6$ nm, $T = 7.4$, $\Delta\lambda_{em} = 0.15$ nm.

under excimer laser excitation (curve b). B_0' located at 28 750 cm^{-1} may be due to the vibrational mode $\nu_{vib} = 395$ cm^{-1}. Its FWHM is with approximately 60 cm^{-1} twice as large as that of B_0 (FWHM 28 cm^{-1}). The SR excited emission spectrum (curve a) has no corresponding peak B_0, however, the peak B_1 is observed as shoulder in this curve and as weak peak in curve b. B_2, B_3, and B_0' are observed in both spectra as well, even though the relative intensities vary strongly. In the energy region 28 000 cm^{-1} to 28 600 cm^{-1}, in which typically vibronic transitions are observed, the SR excited spectrum (curve a) emits a large part of the total emission. In contrast, curve b has some weaker peaks due to vibronic transitions.

The peak C_0 at 28 030 cm^{-1} (FWHM 23 cm^{-1}) is assigned to the ZPL of the $^1D_2 \rightarrow {}^3H_6$ transition, slightly above the ZPL of LaF_3:Tm^{3+} (cf. Figure 4.14). The peak of comparable intensity at even higher energy (28 115 cm^{-1}) seems to be too much shifted compared to LaF_3, first of all. Furthermore, adding 5613 cm^{-1} ($^3F_4$) the resulting energy should be coinciding with the ZPL E_0 of the $^1D_2 \rightarrow {}^3F_4$ transition (cf. Figure 4.15). This peak is again an indication of a (fairly different) substitutional site of Tm^{3+}.

For the $^1D_2 \rightarrow {}^3H_6$ transition the situation concerning the vibronic emission is different: Curve b exhibits at least five broad and most intense emission peaks, several 100 cm^{-1} below the assigned ZPL, and thus beyond pure electronic transitions. These structures are coinciding with a broad, structureless band in that region observed under SR excitation (curve a). However, the relative intensity of this particular transition is quite low in curve a.

The peaks in the region of the $^1I_6 \rightarrow {}^3H_5$ transitions (D_x) are rather difficult to assign. D_0 at 26 469 cm^{-1} corresponding to the $^1I_6 \rightarrow {}^3H_5$ transition is not very pronounced. For this multiplet only curve a exhibits strong vibronic bands as in the case of the $^1I_6 \rightarrow {}^3F_4$ transition.

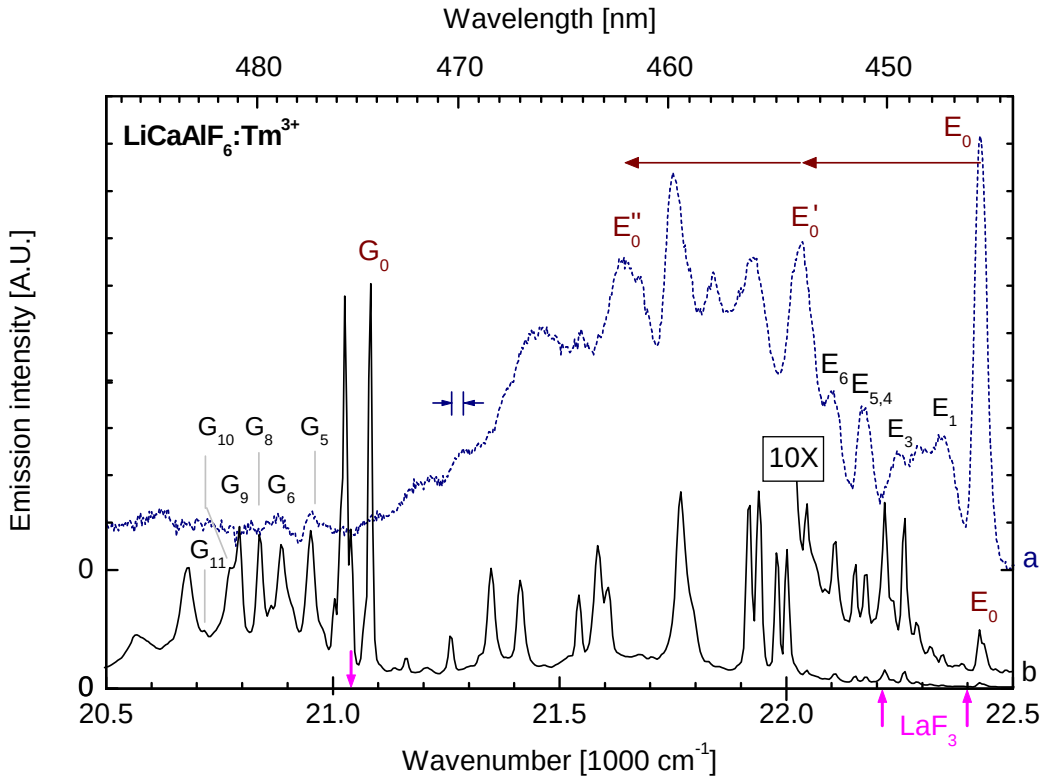

Figure 4.18: Emission spectra of the $^1D_2 \rightarrow {}^3F_4$ (E_x), $^1I_6 \rightarrow {}^3H_4$ (F_x), and $^1G_4 \rightarrow {}^3H_6$ (G_x) transitions in LiCAF:Tm^{3+}. (a) $\lambda_{ex} = 127$ nm, $T = 10$ K, $\Delta\lambda_{em} \leq 0.5$ nm; (b) $\lambda_{ex} = 157.6$ nm, $T = 7.4$ K, $\Delta\lambda_{em} = 0.15$ nm.

Figure 4.18 shows emission spectra in the energy range 20 500 to 22 500 cm^{-1}. The $^1D_2 \rightarrow {}^3F_4$ (E_x), and $^1I_6 \rightarrow {}^3H_4$ (F_x) transitions have a large overlap, which adds some difficulty to the assignment. The 10× magnified laser excited spectrum shows weak but pronounced peaks which have corresponding intense partner peaks in the synchrotron excited spectrum.

The ZPL is assigned to the peak E_0 observed at 22 430 cm^{-1} (FWHM 19 cm^{-1}) in both measurements, likewise further transitions are observed, terminating at higher Stark levels of

the final state ($^3F_4$). Peaks E_0' at 22 036 cm^{-1} and E_0'' at 22 642 cm^{-1} are clearly observed (curve a), being 394 cm^{-1} and 788 cm^{-1} lower in energy than E_0. Therefore these peaks are assigned to transitions coupled to a strong local mode having ν_{vib} = 395 cm^{-1} as discussed previously. The FWHM become apparently larger when going from E_0 to E_0' and again to E_0''.

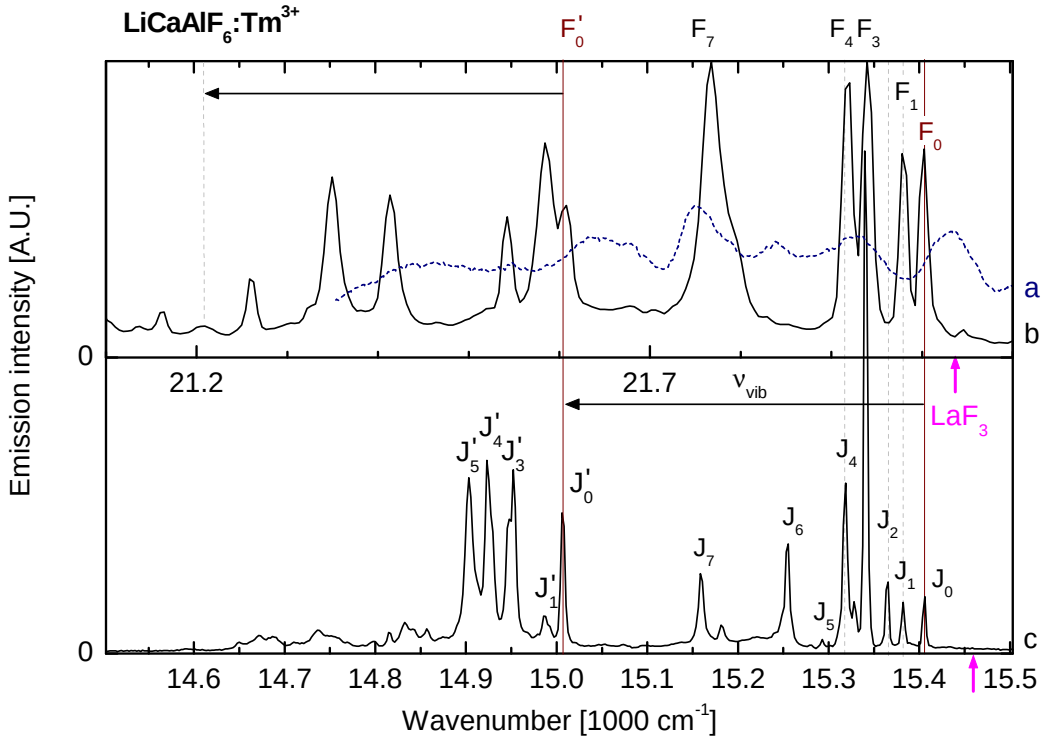

Figure 4.19: Emission spectra of the $^1I_6 \rightarrow {}^3H_4$ (F_x) and $^1D_2 \rightarrow {}^3H_4$ (J_x) transitions in LiCAF:Tm^{3+}. (a) λ_{ex} = 127 nm, T = 10 K, $\Delta\lambda_{em} \leq$ 0.5 nm; (b,c) λ_{ex} =157.6 nm, $\Delta\lambda_{em}$ = 0.15 nm. Note the shifted energy scales.

Figure 4.19 shows spectra of the the $f \rightarrow f$ emission due $^1I_6 \rightarrow {}^3H_4$ (F_x) and $^1D_2 \rightarrow {}^3H_4$ (J_x) transitions at low temperature. The SR excited spectrum (curve a) is only available of the $^1I_6 \rightarrow {}^3H_4$ and consists of about six broader bands. There is no coincidence with the peaks in curves b and c, and at first only the laser excited spectra are discussed.

Curves a and b exhibit clear peaks with striking coincidence, assigned to electronic transitions to the Stark levels of $^3H_4$. Furthermore, at ν_{vib} = 395 cm^{-1} lower in energy several partner peaks are observed corresponding to electronic transitions. This finally confirms the strong local mode which has been frequently observed throughout the discussion.

Conclusions

Only few peaks are observed in the various $f \rightarrow f$ emission spectra of LiCAF:Tm^{3+} excited by synchrotron radiation (SR). For example, in the region of electronic transitions about six peaks appeared in the SR excited spectrum of the $^1D_2 \rightarrow {}^3F_4$ (E_x) transitions (cf. Figure 4.18, curve a). In the respective spectrum under laser excitation (curve b) there are at least ten narrow peaks within the same energy region. This seems to be a general property of all $f \rightarrow f$ transitions. While one may argue this is due to the reduced resolution, this still does not explain the observed differences. In fact the spectra excited via the CT state (with SR) vs. the $5d$ bands (with laser) are dramatically different concerning the vibronic structure. It should be kept in mind that the two different excitation energies (for reasons given previously) will lead to different population mechanisms. This by itself does not explain the significant differences, since the emission spectra itself are due to the "same" $f \rightarrow f$ transitions.

A qualitative explanation can be given, considering the site symmetries of the substitutional lattice sites in $LiCaAlF_6$ (LiCAF), which are Al^{3+} and Ca^{2+} with additional charge compensation (cf. Section 3.2.1). If the Al^{3+} site (ionic radius 67.5 pm) is occupied by the much large Tm^{3+} ions (102 pm) a lattice distortion is expected. On the other hand, the deviation from octahedral symmetry for Cr^{3+} on Al^{3+} sites was not large in LiCAF and LiSAF [PAY89]. The proposed lattice sites (Al^{3+} and Ca^{2+}) are both feasible according to recent computer modeling of defect structure in LiCAF, while Ca^{2+} with Li^+ vacancies is the most probable compensation scheme [AMA03]. According to their calculations, LiSAF prefers clearly the Al^{3+} site crystal due to the increased lattice parameters.

Furthermore, under CT excitation with SR the penetration depth should be quite small due to a large absorption coefficient (cf. Section 4.4). SR excitation has been proven to result in weak $f \rightarrow f$ emission if excited at other energies than in the charge transfer (CT) state, being mainly due to the extraordinary low doping concentrations. Therefore, the presented $f \rightarrow f$ emission spectra have been excited at 127 nm into the established CT state. The absorption coefficient under laser excitation energy, in contrast, is almost one order of magnitude lower. Therefore, surface effects of the polished samples, such as reabsorption and line broadening, have to be considered for the SR excited spectra.

This would explain the reduced structure observed under SR excitation: Tm^{3+} is situated on (nearly) octahedral Al^{3+} lattice site preferably at the surface of the crystal, where a relaxation of the lattice in LiCAF is more probable.

Tm^{3+} prefers the Ca^{2+} lattice site with one or more charge compensation schemes in LiCAF. By using excimer laser, these centers are very well excited in the bulk material and have been used to establish Stark levels and ZPL of $d \rightarrow f$ and $f \rightarrow f$ transitions. The large number of observed peaks are due to the lower symmetry of the distorted (charge compensated) lattice site. In principal, several compensation mechanisms may occur at the same time with slightly changed characteristics.

The striking differences in the emission spectra of LiCAF:Tm^{3+} have been explained qualitatively in terms of two substitutional lattice sites in agreement with [AMA03], considering furthermore surface effects on the particular setting in LiCAF.

4.5.5 $f \rightarrow f$ and $d \rightarrow f$ emission in BaY_2F_8:Tm^{3+}

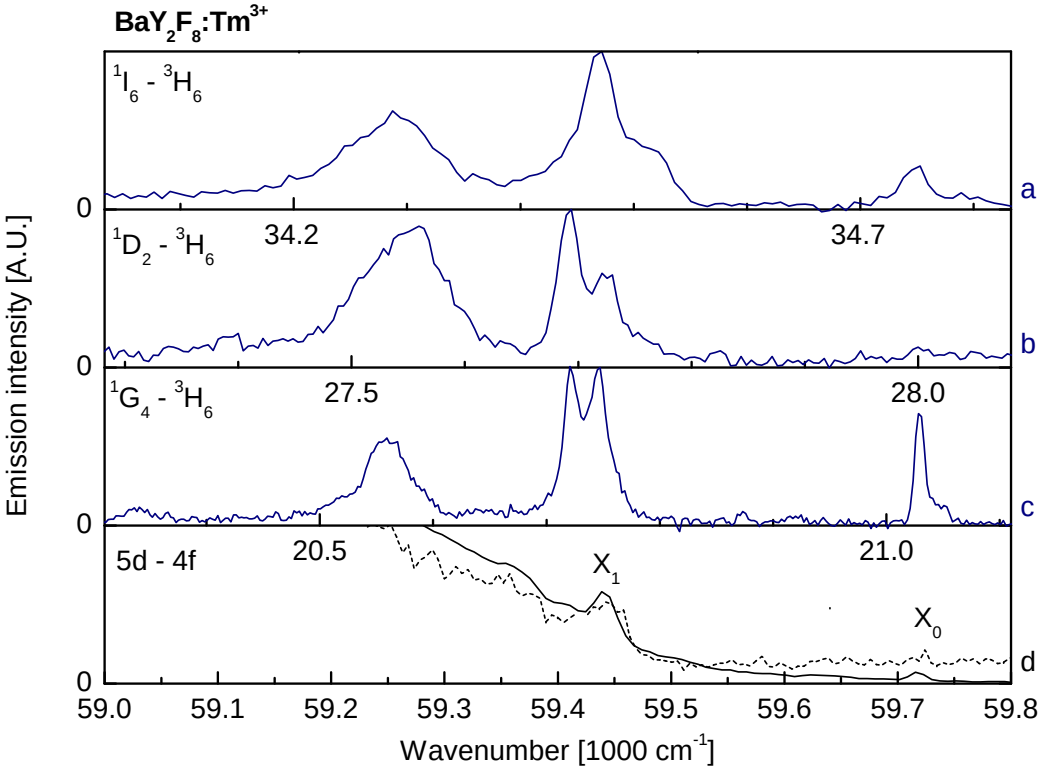

Figure 4.20: $d \rightarrow f$ and $f \rightarrow f$ emission spectra of BYF:Tm^{3+} at 7 K. (a) $^1I_6 \rightarrow {}^3H_6$; (b) $^1D_2 \rightarrow {}^3H_6$; (c) $^1G_4 \rightarrow {}^3H_6$, λ_{ex} =127 nm. (d) $d \rightarrow f$ emission spectra. (----) λ_{ex} =158.3 nm; and (—) λ_{ex} =157.6 nm.

A BaY_2F_8 (BYF) single crystal with 2% doping concentration of Tm^{3+} has been obtained by courtesy of T. Ouvarova. Intra-configurational $f \rightarrow f$ emission spectra have been measured, including for the first time fine structure due to inter-configurational $d \rightarrow f$ transitions. Figure 4.20 shows emission spectra of $f \rightarrow f$ transitions (a) $^1I_6 \rightarrow {}^3H_6$ shifted by 24 970 cm^{-1} to higher energy; (b) $^1D_2 \rightarrow {}^3H_6$ shifted 31 750 cm^{-1}; and (c) $^1G_4 \rightarrow {}^3H_6$ shifted 38 690 cm^{-1}.

High resolution emission spectra due to the spin-forbidden $d \rightarrow f$ transition to the ground state $^3H_6$ are shown in Figure 4.20 (curves d), recorded with synchrotron radiation excited at 158.3 nm (----) and under F_2 excimer laser excitation at 157.6 nm (—). The former curve measured at our setup is shown in its full extent in Section 4.1.3.

Both $d \rightarrow f$ emission spectra exhibit a consistent sharp peak at 59 720 cm^{-1}, which is attributed to the $d \rightarrow f$ zero-phonon transition. A range of 200 cm^{-1} below this ZPL remains clear of peaks, which has been observed as well in the $d \rightarrow f$ emission of LiCAF and LiSAF (cf. Section 4.5.2). Below 59 500 cm^{-1} a raise in emission intensity is observed due to an increased number of vibrational transitions.

The $f \rightarrow f$ emission spectra (curves a to c) support the assignment. They have been shifted until their ZPL are aligned with X_0. In the region of X_1 all spectra exhibit coinciding intense emission peaks. This is very different to the results for LiCAF discussed in Section 4.5.3, where several $f \rightarrow f$ emission spectra exhibited clear and narrow peaks in the region of missing peaks due to $d \rightarrow f$ transitions.

Due to the low point symmetry of the substitutional Y^{3+} site (C_{2h}) in the monoclinic BYF lattice (Section 3.2.2) all 13 sub-levels of the $^3H_6$ ground state are expected to be non-degenerate (cf. Section 2.2.2). Some may be not observed due to selection rules, low intensity, or resolution limitations.

The BYF host is known for having a low maximum phonon energy of 360-380 cm^{-1} [SVE93] or 415 cm^{-1} [KAM90], which points from the respective ZPL into the region of the broad emission band.

Inspired by the results on the pure BaY_2F_8:Tm^{3+} sample, a series of singly (Mn^{2+}) and co-doped (Tm^{3+}, Mn^{2+}) BYF crystals have been bought for extended analysis. Unfortunately, the nominal doping concentrations disagreed with the experimental spectra. Subsequently, a trace analysis had been performed, which confirmed the suspicion only very recently. In particular, Mn^{2+} was only detected within an inclusion, not in the bulk material. X-ray diffractometry could not be carried out in the scope of this thesis. Nevertheless, some of the measurements are presented in Appendix A without discussion for future reference, since the results seemed quite promising, which suggests further investigation in this respect.

Chapter 5

Divalent Manganese in fluorides

$3d^n$ transition metal ions utilized in efficient luminescent material are preferably $3d^5$ (Mn^{2+}, Fe^{3+}) or $3d^3$ (Mn^{4+}, Cr^{3+}) elements. Both have the lowest excited state, which is responsible for emission, in the visible spectral region. Mn^{2+} ions exhibit wide-range emission from 500 nm to 700 nm, depending on the host crystal. Hundreds of luminescent materials, in particular those used in fluorescent lamps (Section 1.4), have been developed based on Mn^{2+} as dopant or co-dopant with efficient energy transfer capabilities [FER70, SHI82, CAL03]. Example include the well-known amber emission of ZnS:Mn^{2+} used in thin films for electroluminescent phosphor, as well as $BaMg_2Si_2O_7$:Mn^{2+}, Eu^{2+} exhibiting $Eu^{2+} \rightarrow Mn^{2+}$ energy transfer [BAR70, YAO98].

In this chapter divalent Manganese is evaluated as optically active ion in several fluorides. In order to determine the energy level structure of $3d^n$ transition metal ions, Tanabe-Sugano diagrams are employed, while special attention is paid to Mn^{2+} (Section 5.1). The typical broad emission is observed in $LiCaAlF_6$, $LiSrAlF_6$, and MgF_2, as well as emission from multiple sites in $BaMgF_4$ and BaY_2F_8 (Section 5.3). Site-selective excitation spectra of the corresponding $3d \rightarrow 3d$ emissions are presented (Section 5.2). The initial level assignment is evaluated in terms of Tanabe-Sugano computation with a C++ brute force software fit, yielding in particular the crystal field splitting Dq (Section 5.4).

However, the Tanabe-Sugano diagram only comprises $3d^5$ energy levels. In various fluoride crystals excitation bands have been observed in the VUV spectral region, which are much more intense than the $d \rightarrow d$ transitions. Little research has been devoted to these bands, partially hampered by experimental difficulties.

The VUV spectral region has attracted exceeding interest in recent years for lighting applications and efficient down conversion processes, therefore insight into the nature of these bands is desired. Comprehensive studies of various transition metals doped into fluorides by McClure *et al.* using absorption spectroscopy provided convincing arguments in favor for $3d^5 \rightarrow 3d^4 4s$ transitions, while often only one band was resolved.

In Section 5.5 detailed excitation spectra in the VUV of a variety of Mn^{2+} doped fluorides reveal several distinct excitation bands, and two bands of each crystal are correlated with the corresponding crystal field splitting Dq. The oscillator strength has been calculated from absorption in LiCAF at low and RT, in agreement with the literature.

5.1 Tanabe-Sugano diagram for Mn^{2+}

The energy states of free $3d^n$ transition metal ions, observed in gaseous phase, are split strongly when introduced into a crystal lattice, because the $3d$ wave functions are spatially expanded and not shielded by outer shells like in $4f^n$ rare earth ions. The dependence on the crystal surrounding can be described in terms of the Racah parameters B, C and the crystal field splitting parameter Dq (Section 2.2.3). Tanabe and Sugano calculated the determinants of the electron interaction [TAN54a] and depicted the solution in *Tanabe-Sugano diagrams* for elements d^2 to d^8 [TAN54b].

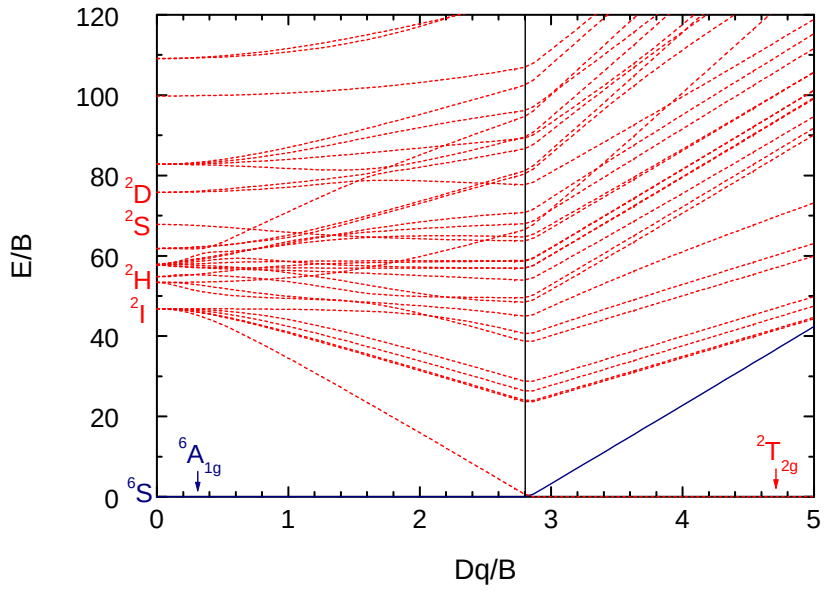

Figure 5.1: Tanabe-Sugano diagram for d^5 ions (Mn^{2+}, Fe^{3+}) in $O_h^{(6)}$ symmetry. (—) $^6A_{1g}$ (S) ground state; (----) doublet states, which are *not* observed in the spectra.

The doublet states shown in the Tanabe-Sugano diagrams for d^5 ions in $O_h^{(6)}$ symmetry (Figure 5.1) are not observed experimentally, since transitions from or to the ground state are of highly forbidden nature (parity forbidden, $\Delta S = 2$). In the case of non-radiative processes (multi-phonon relaxation, energy transfer) the multitude of doublet states should

be taken into account, but the following discussion is concerned with the optically relevant quartet states.

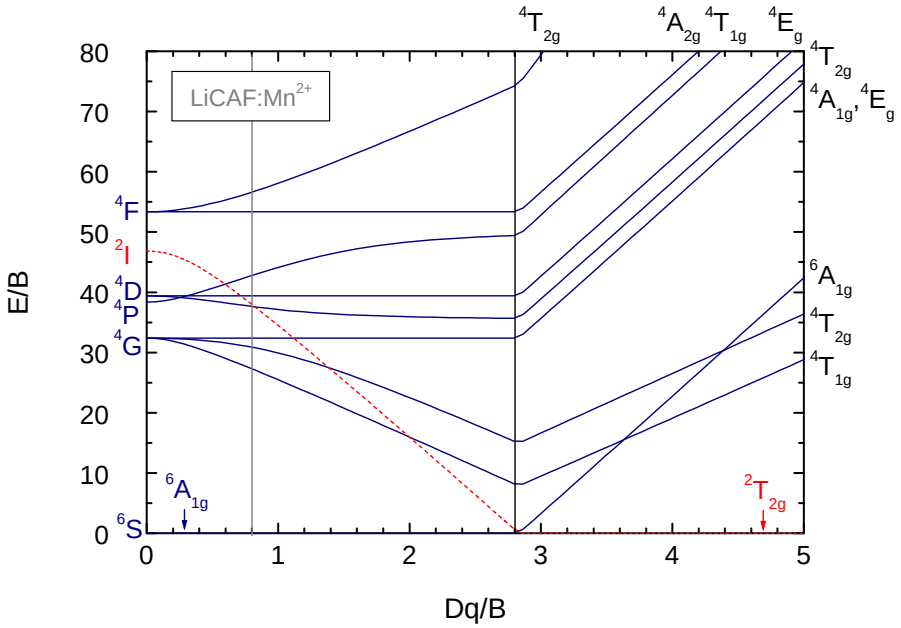

Figure 5.2: Tanabe-Sugano diagram for d^5 ions (Mn^{2+}, Fe^{3+}) in $O_h^{(6)}$ symmetry. (—) $^6A_{1g}$ (^{6}S) ground and quartet states; (----) doublet ^2P becomes ground state for $Dq/B \geq 2.8$.

The quartet states are usually considered for optical transitions in the Tanabe-Sugano diagram (Figure 5.2). The energy is plotted against the crystal field splitting Dq, both in units of the Racah parameter B.

The values of the crystal field splitting Dq within equivalent surroundings are of the order

$$Mn^{2+} < Ni^{2+} < Co^{2+} < Fe^{2+} < V^{2+} < Fe^{3+} < Cr^{3+} < V^{3+} < Co^{3+} < Mn^{4+}$$

For a specific metal ion, Dq depends on the ligand in the order of the *spectrochemical series*

$$I^- < Br^- < Cl^- < F^- < H_2O < NH_3 < NO_2^- < CN^-$$

Mn^{2+} in cubic or octahedral surrounding in fluorides is known to manifest in the high-spin configuration of the ground state $^6A_1$ (S) corresponding to $Dq < 2.8$. For higher values of Dq the $^6A_{1g}$ (S) state becomes the first excited state, and the lowest of the free ion ^2I doublet states represents the ground state. This is the reason for the sharp bend of the curves at $Dq \approx 2.8$.

In this approximation the ^6S ground state is are neither split nor shifted by the crystal field. The free-ion quartet states ^4G, ^4P, ^4D, and ^4F are split in octahedral configuration as shown in the diagram. The states $^4\mathrm{A}_{1g}$, $^4\mathrm{E}_g$ (G) and $^4\mathrm{A}_{2g}$ (F) are independent of the crystal field parameter Dq in the low field case ($Dq < 2.8$). In particular, their transitions appear as significantly sharper lines in the spectrum.

The only sextet state is the ground state $^6A_{1g}$ (S), therefore all $d \rightarrow d$ transitions are parity- and spin-forbidden and extremely weak with oscillator strengths of the order 10^{-7} to 10^{-6} [FRO98, KEE86, SIB73]. In direct absorption measurements, the $3d^5$ states are hardly observable and very few measurements exist. I could not record absorption bands in a 4 mm thick LiCAF:Mn^{2+} bi-planar polished single crystal, partially also due to the low doping concentration (Section 3.2).

The ground state of Mn^{2+} is split by the crystal field into the higher energetic doubly degenerate sublevel e_g and the lower triply degenerate sublevel t_{2g} (Section 2.2.3), having the electronic high-spin configuration $t_{2g}(\uparrow)^3 e_g(\uparrow)^2$ which is more stable than the low-spin configuration $t_{2g}(\uparrow)^3 e_g(\downarrow)^2$ in fluorides [SHE84]. The splitting is expected at an energetic distance of $10Dq$.

It has been shown theoretically and experimentally that B and C for MnF_6^{4-} are practically independent of the Mn-F distance R, while

$$10Dq \propto R^{-n} \tag{5.1}$$

A value of $n = 4.7$ has been determined for MnF_6^{4-} surrounding.

Besides excitation spectroscopy used as appropriate method in this work to examine $d \rightarrow d$ transitions, spin-polarized electron energy loss spectroscopy (EELS) with incident electrons of 26-130 eV yields energies of the spin-forbidden transitions [FRO98]. The dipole selection rule is removed for electrons of low energy, and electric multi-pole excitations become observable. Furthermore, EELS is quite surface sensitive. On the other hand, the resolution is lower compared to that in optical spectroscopy. EELS renders valence-band as well as core level electron excitation possible, and a detailed analysis has been performed on transitions within and across the band gap in MgO:Mn^{2+} [FRO98].

5.2 Experimental results: $^4\mathrm{T}_{1g} \rightarrow {}^6\mathrm{A}_{1g}$ emission

In comparison with $4f$ elements, the $3d$ transition metals show a much stronger electron-phonon coupling. Hence the rich energy level structure of Mn^{2+} (Figure 5.1) allows non-radiative relaxation even at liquid helium temperature to the lowest excited state $^4\mathrm{T}_{1g}$ (G) and subsequent emission $^4\mathrm{T}_{1g} \rightarrow {}^6\mathrm{A}_{1g}$ to the ground state. Several emission bands at different energies are observed, if Mn^{2+} is incorporated into different crystallographic sites. The emission bands have typically a FWHM of 1000 to 2000 cm^{-1} without any features, and are of a non-Gaussian *Pekarian* shape [HEN89]. This is due to the strong electron-phonon coupling of the $3d$ ions which prevents the observation of sharp electronic or vibrational lines, as opposed to rare earth ions.

5.2.1 Zero-phonon line of the $^4\mathrm{T}_{1g} \rightarrow {}^6\mathrm{A}_{1g}$ transition

In various crystals zero-phonon transitions have been observed at low temperature and rather low concentrations. Detailed vibronic fine structure was observed and first assigned to phonon-coupled electronic transitions in Mn^{2+} doped ZnS [LAN65]. Hence, the non-Gaussian shape of the broad band emission was attributed to the vibronic structure. At low temperature a steep raise on the high-energy side is caused by the zero-phonon transition. At higher temperature the band is extended towards the high-energy side as anti-Stokes' emission is activated, approaching the Gaussian shape to some degree.

Multiple zero-phonon lines, mainly due to Mn^{2+} pair interaction, have been observed Zn_2SiO_4, $ZnAl_2O_4$, $CdSiO_3$, ZnF_2 [LEV50], $MgGa_2O_4$ [BRO67], $LiAl_5O_8$ [NIC73], and in ZnS [BUS76] among others. Fe^{3+} , which possesses $3d^5$configuration as well, exhibits zero-phonon lines in $LiAl_5O_8$ [POT72] and $LiAlO_2$ [STO74].

Temperature-dependent emission peak shifts and variations of the FWHM in CaF_2:Mn^{2+} have been investigated systematically [RHO85].

5.2.2 Lattice sites

Crystals may have more than one lattice site, which is occupied by the dopant ions. If both sites are strongly varying in symmetry or size, the spectrum may change significantly. This is especially true for the $3d$ ions which are sensitive to the crystal field. Some crystals have intrinsically sites of the same point symmetry, which lead to slightly different emission energies. Such sites can be introduced by charge compensation as well, if the substitutional site has a different ionization state. The latter situation may be found in Mn^{2+} incorporated into the Y^{3+} lattice site of BaY_2F_8, while the Ba^{2+} site is different in size and coordination. An overview of the investigated crystals and substitutional lattice sites has been given in Section 3.2.

If the Mn^{2+} ion is substituted into a lattice site with octahedral symmetry, orange-red emission is typically expected due to the $^4T_{1g} \rightarrow {}^6A_{1g}$ transition, while in tetrahedral surroundings the crystal field at the substitutional lattice site is much smaller and the emission is usually green [PAL70, PAL71]. Most crystal investigated in this thesis have substitutional lattice sites of approximate octahedral configuration. However, if the Mn^{2+} ion in this surrounding is situated on a considerably larger lattice site, a lower crystal field is expected, resulting in a shift of the emission towards higher energy (cf. Figure 5.2). This is observed in crystals like SrB_6O_{10}:$Mn^{2+}$with emission at 512 nm [KOS85] and in GdF_3:Mn^{2+} with emission at 520 nm [POO97].

5.2.3 Emission spectra of LiCAF and LiSAF

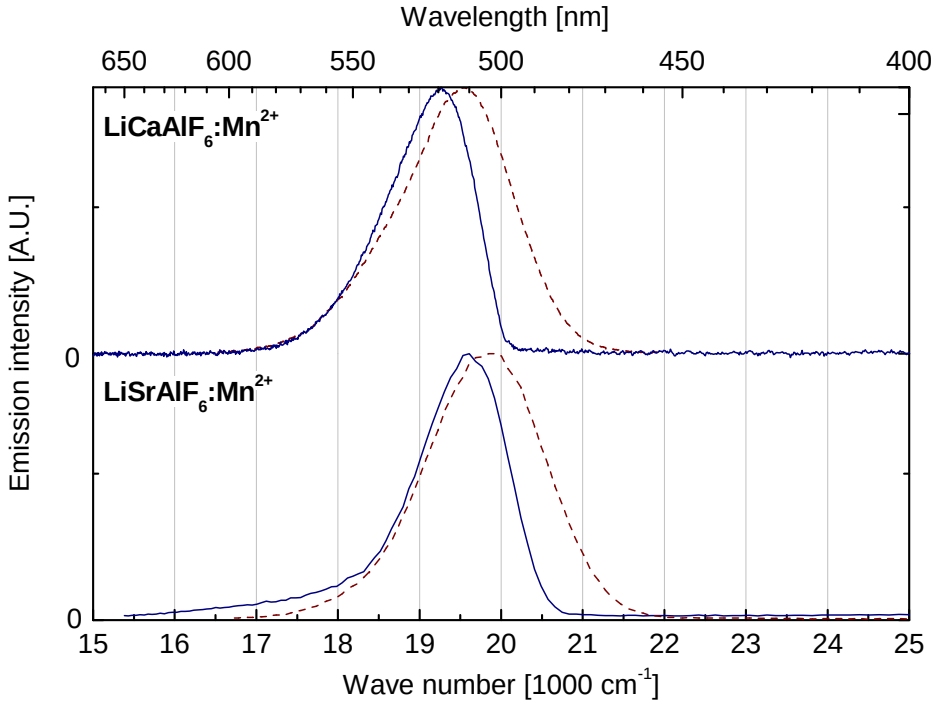

Figure 5.3: Emission spectra of the $^4T_{1g}(G) \rightarrow {}^6A_{1g}(S)$ transition in Mn^{2+} doped (a) LiCAF and (b) LiSAF at 9 K (—) and at 300 K (---).

Figure 5.3 (a) shows emission spectra of LiCAF:Mn^{2+} single crystals at 9 K (—) and 293 K (---) excited by 139.6 nm and 140.8 nm light, respectively. The broad emission band at 9 K peaking at 19 270 cm^{-1} (FWHM 1250 cm^{-1}) is assigned to the $^4T_{1g} \rightarrow {}^6A_{1g}$ intra-configurational $d \rightarrow d$ transition, which is parity- and spin-forbidden. At RT the band is broadened and its peak position is shifted to 19 540 cm^{-1} (1620 cm^{-1}). In high resolution emission spectra of LiCAF:Tm^{3+}, Mn^{2+} single crystal the zero-phonon line of this emission

is clearly observed at 21 138 cm^{-1} (cf. Section 4.5.3).

For the iso-structural polycrystalline LiSAF:Mn^{2+} emission bands of nearly identical widths are presented in Figure 5.3 (b). The peak is slightly shifted to higher energy 19 710 cm^{-1} (FWHM 1290 cm^{-1}) at 9 K (—) and 19 840 cm^{-1} (1690 cm^{-1}) at RT (---) as expected because of the larger Sr^{2+} ionic radius. Neither band is of Gaussian nor Lorentzian shape as reported in the literature. At low temperature the low-energy tail of the bands is more steep, while the overall shape approaches that of a Gaussian at RT. This leads further to a lower crystal field splitting Dq of LiSAF compared to LiCAF and raises the energy of the $^4T_{1g}$ (G) level according to the Tanabe-Sugano diagram (Figure 5.2).

The Al^{3+} lattice site is considerably smaller (ionic radius 67 pm) compared to Mn^{2+} (81 pm), which is unfavorable for substitution of this ion, while the Ca^{2+} (114 pm) or Sr^{2+} (132 pm) sites are much larger. Both the Al^{3+} and Ca^{2+} lattice sites have distorted octahedral symmetry. Nevertheless, green emission is detected for both crystals, which confirms that Mn^{2+} is incorporated into the only large Ca^{2+} or, respectively, Sr^{2+} site.

5.2.4 Emission spectra of MgF_2

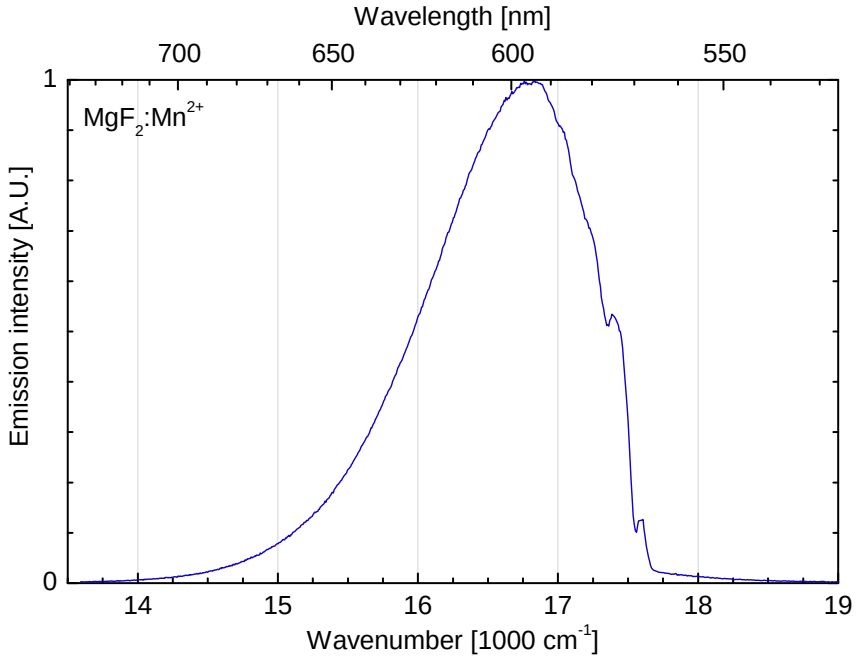

Figure 5.4: Emission spectrum of the $^4T_{1g}$(G) $\rightarrow$ $^6A_{1g}$(S) transition of MgF_2:Mn^{2+}, T =7 K, λ_{ex} = 112 nm, exhibiting ZPL at 17 385 and 17 606 cm^{-1}.

The emission spectrum of MgF_2:Mn^{2+} at 7 K has been recorded under excitation at 89 286 cm^{-1} (112 nm) with synchrotron radiation (Figure 5.4). The broad emission band, peaking at

16 800 cm^{-1} (595 nm) has a FWHM of 1476 cm^{-1} attributed. Because of octahedral coordination and similar ionic radii, Mn^{2+} emission in the red is expected (Section 5.2.2).

With spectral resolution better than 0.22 nm ($\approx$ 7 cm^{-1}), sharp lines at 17 385 and 17 606 cm^{-1} are observed, attributed to zero-phonon lines of the $^4T_{1g}(G) \rightarrow {}^6A_{1g}(S)$ transition. The FWHM is estimated being about 60 cm^{-1}. The zero-phonon line of $KMgF_3$:Mn^{2+} at 9 K is located at 17 222 cm^{-1} [MAR94a].

5.2.5 Emission spectra of $BaMgF_4$

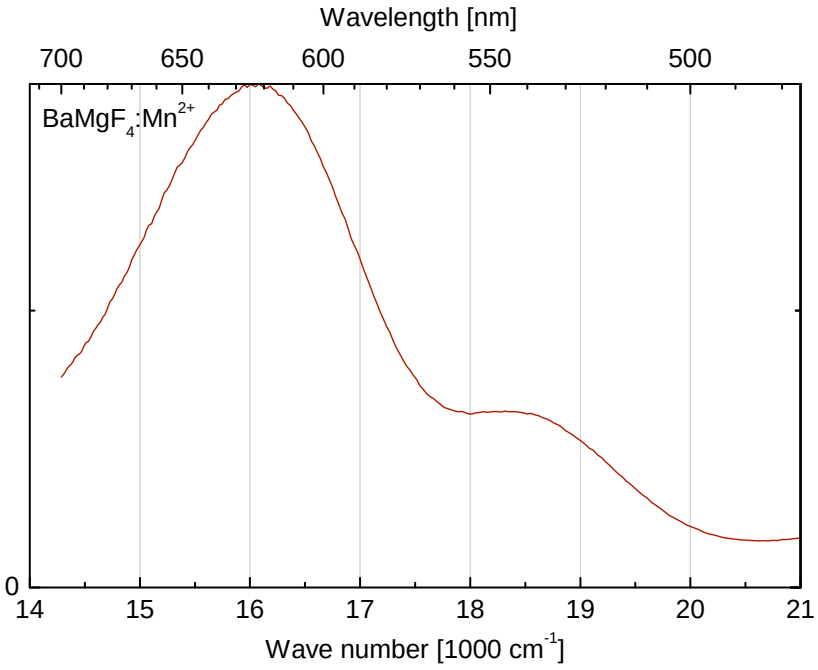

Figure 5.5: Emission spectrum in BMF:Mn^{2+} of the $^4T_{1g}(G) \rightarrow {}^6A_{1g}(S)$ transition resulting from two centers, $T = 300$ K, $\lambda_{ex} = 395$ nm.

The emission spectrum of BMF:Mn^{2+} at RT exhibits two broad bands peaking at 16 000 and 18 500 cm^{-1} (Figure 5.5), excited by 25 320 cm^{-1} (395 nm) photons. The FWHM of the intense emission band is determined being 2700 cm^{-1}. Because of the asymmetric shape and strong overlap the width of the second band at 18 500 cm^{-1} has not been estimated, since the deviation will be quite large.

The six-coordinated Ba^{2+} (ionic radius 149 pm) and Mg^{2+} (86 pm) lattice sites are considered for the Mn^{2+} (81 pm) ions. Since Mn^{2+} ions are well incorporated into the slightly larger octahedral Mg^{2+} site, the crystal field splitting leads to emission in the red, corresponding to the intense emission band at 16 000 cm^{-1}. The Ba^{2+} site is much larger, therefore a small fraction of the substitutional ions is expected to be found on this lattice site. The effective

crystal field is significantly lowered compared to the Mg^{2+} site, yielding the weak emission band at approximately 18 500 cm^{-1}. The assignment is confirmed by excitation spectra of the respective emissions.

5.2.6 Emission spectra of BaY_2F_8

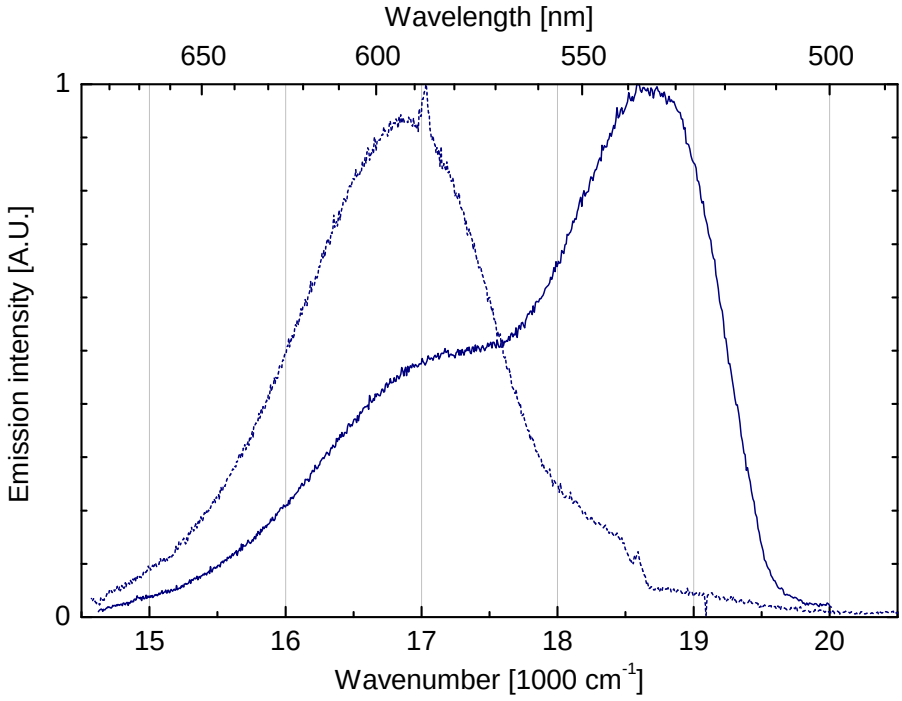

Figure 5.6: Emission spectra of the $^4T_{1g}(G) \rightarrow {}^6A_{1g}(S)$ transition of two distinct Mn^{2+} centers in BYF, T =8.5 K, λ_{ex} =157 nm (—) and 195 nm (----).

Figure 5.6 shows emission spectra of Mn^{2+} in BYF at 8.5 K. Excitation at 195 nm (----) results in the typical broad $^4T_{1g}(G) \rightarrow {}^6A_{1g}$ emission band at 16 850 cm^{-1} (FWHM 1500 cm^{-1}). Considering the local symmetry and ionic radii this emission is attributed to Mn^{2+} on Y^{3+} sites, while ions occupying the larger Ba^{2+} site have their emission peaking at 18 700 cm^{-1} (FWHM 1250 cm^{-1}) under excitation of 157 mm photons (—). This emission has a large overlap with the excitation band of $^4T_{1g}(G)$ of Mn^{2+} on the Y^{3+} site, and by energy transfer emission at 16 850 cm^{-1} is always observed in conjunction with the higher-energetic emission. The weak shoulder at 18 500 cm^{-1} (----) indicates energy transfer from Mn^{2+} on the Y^{3+} site to the Ba^{2+} site during non-radiative relaxation after initial excitation, but the transfer rate appears to be rather low.

Excitation in the visible to UV spectral region of the corresponding emission bands, presented in this section, are subject of the following discussion (Section 5.3).

5.3 Experimental results: $3d^5 \rightarrow 3d^5$ excitation

Excitation spectra of Mn^{2+} doped BMF, MgF_2, LiSAF, and LICAF in the visible to UV spectral region are shown in Figure 5.7. The spectra were measured at the Fluorolog setup at the *Institut für Laser Physik* (Universität Hamburg).

They show the typical intra-configurational transitions between $3d^5$ quartet states and the ground state, which are forbidden by spin and parity. The short vertical lines indicate the computational results by employing the appropriate Tanabe-Sugano diagram (Section 5.4). The computational results support the level assignment and confirm the proposed dopant sites.

The states $^4A_{1g}$,^4E_g (G) are only degenerate in perfect octahedral symmetry. Since its energy is independent of the crystal field [LEW94], a rather sharp peak is expected in the spectrum. A splitting observed is considered to reflect the reduction in symmetry [PAL70, PAL71].

	^4G				^4D		^4P	Ref.
	$^4T_{1g}$	$^4T_{2g}$	$^4A_{1g}$,^4E_g		$^4T_{2g}$	^4E_g	$^4T_{1g}$	
$\underline{Ba}MgF_4$	22 340	24 600	25 220	(25 380)	28 570	30 000		*this work*
$LiSrAlF_6$	21 720	21 800	(25 500)	25 840	29 370	30 700	32 360	*this work*
$LiCaAlF_6$	21 100	24 570	(25 290)	25 710	29 030	30 630	32 000	*this work*
$BaMgF_4$	18 620	23 020	25 100		28 210	29 940	32 520	*this work*
MgF_2	18 870	23 300	(25 190)	25 540	28 270	30 540	33 300	*this work*

Table 5.1: Experimentally observed energy levels (in cm^{-1}) for Mn^{2+} doped fluoride crystals from Figure 5.7. The substitutional lattice site is underlined. Energies in parenthesis are side-peaks.

All excitation spectra resemble the typical $3d^5$ level structure very well, except for the ($^4T_{1g}$) ^4P level which has not been included in the Tanabe-Sugano fitting procedure. The assigned energy levels from Figure 5.7 are given in Table 5.1. These values are further evaluated by computational methods in Section 5.4. A brief discussion of the spectra is given below.

$BaMgF_4$

Since two emission peaks have been observed for BMF (Section 5.2.5), the Mg^{2+} and Ba^{2+} lattice sites have been proposed as non-equivalent substitutional sites for the Mn^{2+} ion. Monitoring the corresponding emissions at 630 nm and 540 nm, respectively, two significantly different excitation spectra were obtained. This is due to the large difference of the crystal field of both lattice sites.

The excitation spectrum of Mn^{2+} on the Mg^{2+} site is very similar to that of MgF_2 as expected from the same occupational site.

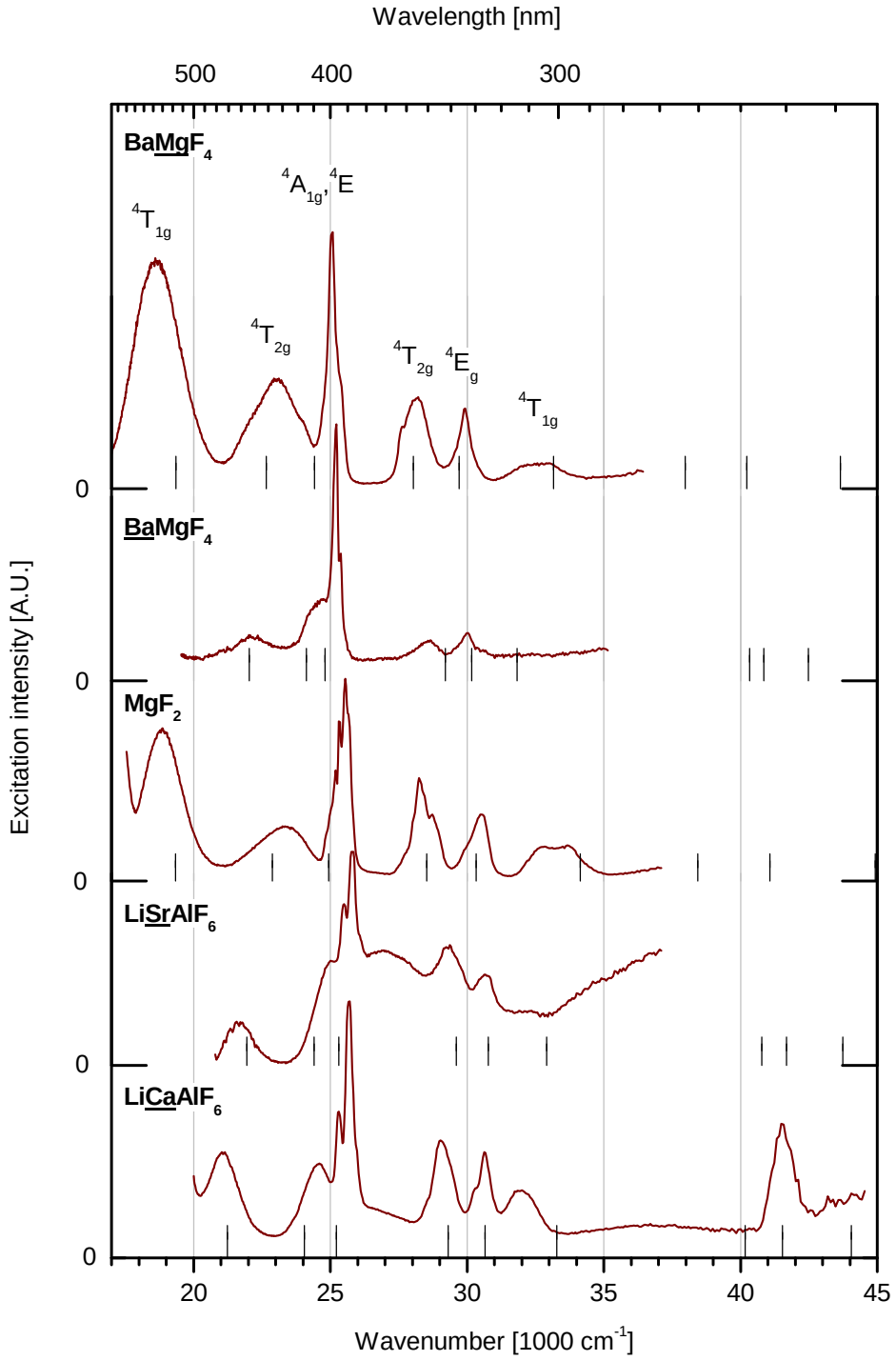

Figure 5.7: Excitation spectra of $d \rightarrow d$ transitions of Mn^{2+} doped fluoride crystals at RT. λ_{em}=630 nm ($BaMgF_4$), 540 nm ($BaMgF_4$), 600 nm (MgF_2), 510 nm (LiSAF), 520 nm (LiCAF). Vertical lines indicate the computed energy levels (Section 5.4). $\Delta\lambda_{ex} \leq 1$ nm.

MgF_2

The point symmetry of MgF_2 is $D_{2h}^{(6)}$ and thus considerably lower than O_h. Deviations from the applied Tanabe-Sugano diagram are present due to further splitting of the states. This is reflected in a significant broadening of the $^4A_{1g}$,^4E_g (G) line, whose degeneracy is lifted, and at least two additional sub-levels are observed as sharp peaks at 25 190 cm^{-1} and 25 320 cm^{-1} in addition to the main peak at 25 540 cm^{-1}.

LiCAF and LiSAF

Excitation spectra of LiCAF:Mn^{2+} single crystals are shown in Figure 5.7 (d). A distinct splitting of the $^4A_{1g}$,^4E_g (G) state into two components at 25 290 cm^{-1} and 25 710 cm^{-1} is revealed. The splitting of 420 cm^{-1} is attributed to the distorted octahedral Ca^{2+} site (3.2.1). Similar overlapping bands are observed for the ^4E_g (D) state.

The excitation spectrum of the LiSAF:Mn^{2+} powder sample shows an energy shift towards the free ion levels due to the large Sr^{2+} lattice site. Details as the splitted $^4A_{1g}$,^4E_g (G) state are present as well.

Charge compensation is not needed for Mn^{2+} doped into LiCAF and LiSAF, and the respective emission spectra (Section 5.2.3) show only one broad emission band. Thus all Mn^{2+} ions are expected to be found on the Ca^{2+} or, respectively, Sr^{2+} lattice site.

5.4 Computational results: $3d^5$ energy levels

Further evaluation of the excitation spectra presented in Section 5.3 is conducted by computational methods. I have written a software program in *C++* to compute the complete set of $3d^5$ energy levels using the appropriate Tanabe-Sugano diagram. The Racah parameters B and C as well as the crystal field splitting parameter Dq are obtained from experimental excitation energies of assigned $3d^5$ states in a *brute force fitting* process.

This allows calculation of all energy levels based on the computational parameters. A comparison confirms the initial level assignment (Figure 5.7) and site assignment in crystals, where multiple sites are occupied by the dopant.

5.4.1 Applied algorithm

The respective curves of the Tanabe-Sugano diagram for $3d^5$ ions in six-fold coordination ($O_h^{(6)}$) have been made available by R.J. Lancaster for Dq/B ranging from 0.0 to 5.59 [LAN04]. Included are calculated values for the ground state $^6A_{1g}$ (S), for 32 doublet states, and for the quartet states $^4T_{1g}$ (free ion term ^4G); $^4T_{2g}$ (G); $^4A_{1g}$,^4E_g (G); $^4T_{2g}$ (D); ^4E_g (D); $^4T_{1g}$

(P); $^4A_{2g}$ (F); $^4A_{2g}$ (F); $^4A_{2g}$ (F). The ground and quartet states have been used for the computation, except for $^4T_{1g}$ (F) which is strongly differing from the well-known diagrams in the literature.

A number n of experimentally determined excitation energy levels $E_{exp}(i)$ is used as basis for each calculation. The parameters are varied in the applicable range (B from 500 to 1200, Dq/B from 0.0 to 1.4). According to the Tanabe-Sugano diagram, the energy levels $E_{calc}(i)$ are calculated for the particular parameter set (B, Dq). The root mean square (RMS) deviation between E_{calc} and E_{exp} is calculated according to

$$\Omega_{rms}\,(B, Dq) = \sqrt{\frac{1}{n}\sum_{i=0}^{n}\left(E_{exp}(i) - E_{calc}(i)\right)^2} \tag{5.2}$$

In a brute force fitting process, all applicable variations of the two parameter B and Dq are calculated. Hence, the lowest Ω_{rms} value is assumed being the best fit for the respective crystal.

5.4.2 Racah and crystal field parameters

	CaF_2		$\underline{Ba}MgF_4$	$LiSrAlF_6$	$LiCaAlF_6$	$BaMgF_4$	MgF_2
n	9	10†	5	5	6	5	5
B	781.5	781†	765.6	781.1	778.3	766.4	777.5
Dq	437.6	420†	482.3	554.6	622.6	835.4	855.3
Dq/B	0.56	0.54†	0.63	0.71	0.80	1.09	1.1
Ω_{rms}	238	248	4312	281	267	288	356

Table 5.2: Computational results of the Tanabe-Sugano fit for Mn^{2+} doped fluoride crystals. The substitutional lattice site is underlined. n is the number of measured levels included in the fit, B is the Racah and Dq the crystal field parameter (in cm^{-1}), Ω_{rms} denotes the RMS deviation (in cm^{-1}). †values from [KEE86].

The computational results are listed in Table 5.2 including the number of fitted energy levels n, the calculated Racah parameter B, and the crystal field splitting parameter Dq. The value of Dq/B corresponds to the y-axis of the Tanabe-Sugano diagram. The RMS deviation between measured energies and calculated energies from the (B, Dq) parameters is denoted as Ω_{rms}.

CaF_2:Mn^{2+} has been used to probe the computational algorithm, a compound which has been studied thoroughly in the past. The position of the experimental energy levels for CaF_2 ($O_h^{(8)}$) are taken from the values given in the literature [KEE86]. The parameters obtained by this computation are $B = 781.2$ cm^{-1} and $Dq = 437.5$ cm^{-1}, which agrees with the reported values of $B = 781$ cm^{-1} and $Dq = 420$ cm^{-1} [KEE86]. However, the Tanabe-Sugano diagram

employed has been derived under the assumption of local six-fold coordination, while CaF_2 is eight-fold coordinated. Consequently, application of the appropriate Tanabe-Sugano diagram yields the correct parameters $B = 781$ cm^{-1} and $Dq = 570$ cm^{-1}, obtained by *ab initio* self-consistent field calculations [LEW94].

The crystal field parameter Dq is higher in LiCAF than in LiSAF as expected. This is caused by the larger Sr^{2+} (ionic radius 132 pm) compared to Ca^{2+} (114 pm), thus reducing the crystal field at the lattice site. The achieved RMS deviation Ω_{rms} between experiment and calculation is close to the resolution interval $\Delta E_{ex} \leq 110$ cm^{-1}.

In $BaMgF_4$ two lattice sites exist with significantly different ionic radii, namely Ba^{2+} (ionic radius 150 pm) and Mg^{2+} (86 pm), thus the Mn^{2+} ion (81 pm) is situated on lattice sites with strongly differing crystal field interaction (Section 3.2).

	$\underline{Ba}MgF_4$	$LiSrAlF_6$	$\underline{Ca}F_2$	$LiCaAlF_6$	$Ba\underline{Mg}F_4$	$\underline{Mg}F_2$
λ_{em}	*532*	*507*	495	*515*	*629*	*590*
r_{ion}	149	132	126	114	86	86
σ	$C_s^{(6)}$	$S_6^{(6)}$	$O_h^{(8)}$	$S_6^{(6)}$	$O_h^{(6)}$	$D_{2h}^{(6)}$
Dq	*508.2*	548.5	570‡	608.2	835.4	*855.3*
Dq/B	*0.66*	0.70		0.78	1.09	*1.1*

Table 5.3: Trend in the crystal field splitting parameter Dq of several Mn^{2+} doped fluorides. The substitutional lattice site is underlined. λ_{em} is the emission wavelength (in nm), r_{ion} the size of the lattice site (pm), and σ the symmetry (coordination). ‡values from [LEW94].

From the series of measurements a trend of the crystal field splitting parameter Dq is observed (Table 5.3). As the ionic radius r_{ion} of the dopant lattice site decreases, the crystal field splitting parameter increases. This results in more and more red-shifted emission $^4T_{1g}(G) \rightarrow {}^6A_{1g}$ peaking at λ_{em}. The reason is the reduced crystal field with increasing size of the substitutional site as immediately obvious from the Tanabe-Sugano diagram (Section), approaching the free ion case. This is a general argument, however, in the actual interaction in the appropriate symmetry has to be considered

More details on the crystal properties are given in Section 3.2.

5.4.3 Comparison of experimental and calculated energies

For the computational evaluation of the $3d^5$ levels in Mn^{2+} the peak positions of the respective excitation energy levels have been taken, since ZPL are not observable due to the strong-coupling applicable for transition metal ions. The actual ZPL should be located at the lower-energy onset of each peak.

The calculated energy of the $^4A_{1g}$ (G) state has a systematic energy mismatch, being lower than the experimental peak for all excitation spectra. It is known from the literature that the

energy of this level is insufficiently reproduced from ligand field calculations [KUE97]. The calculated values of the $^4T_{1g}$ (P) bands, on the other hand, are located on the high-energy side in all hosts. The ^4F multiplet (around 40 000 cm^{-1}) is not observed in the $3d$ spectra due to experimental limitations, an exception is LiCAF which has been specifically re-measured.

Under this condition the experimental (Figure 5.7) and the computational results (indicated by vertical lines) agree very well, confirming the initial energy level assignment.

5.5 Experimental results: VUV energy level structure

Optical properties [ALO81, DIA99, HER01, MAZ99, SER97, SHI84] and energy transfer processes [IVE80, MAO91, POO97, SHI84, SOH99, VIN01] of many systems containing divalent Manganese ions have been studied in the past. However, research has been focused primarily on the $3d^5$ states in the infrared to ultra-violet (UV) spectral region (down to 200 nm). Little research has been devoted to the vacuum-ultra-violet (VUV) spectral region.

Several broad excitation (and absorption) bands are observed in Mn^{2+} doped fluorides at energies between 50 000 cm^{-1} (200 nm) and the fundamental absorption. While the well-known $3d \rightarrow 3d$ transitions are hardly observable in absorption, large oscillator strengths are obtained in the VUV (Section 5.5.1). The absorption strength therefore differs strongly in the wide spectral region treated in this work (Section 5.5.2). Detailed investigation of these VUV bands in a variety of transition metal ions confirmed a $3d^4 4s$ character [LUS70, SAB75, CHA76, HAR81, DEN00, KOL03]. However, these studies are mainly based on absorption spectroscopy and lack systematic evaluation of the second and further excitation bands, clearly observed for Mn^{2+} doped fluorides in this work (Sections 5.5.3 and 5.5.4).

A comprehensive overview summarizing energies of VUV excitation and absorption bands determined in this and previous work is presented in Table 5.5 on page 126.

5.5.1 Absorption spectroscopy and oscillator strength of LiCAF:Mn^{2+}

Absorption and excitation spectra of polished LiCAF:Mn^{2+} single crystal plates with a thickness of 1.2 mm have been measured at 10 K in the VUV spectral region (Figure 5.8). The absorption coefficient α (—) of the two intense bands at 64 500 and 72 100 cm^{-1} achieves the value of 11.0 and 27.0 cm^{-1}, respectively. This is of the same magnitude as that of the spin-allowed $4f \rightarrow 5d$ absorption (Figure 4.8), suggesting at least some allowed character. The band at 64 500 cm^{-1} has a double peak structure split by 1000 cm^{-1}, which is consistent with the excitation spectrum recorded at 9 K (---) monitoring the $^4T_{1g} \rightarrow {}^6A_{1g}$ emission of Mn^{2+} at 519 nm (Section 5.5.3). The relative intensities of the two bands agree as well.

The low-energy part of the absorption up to 60 000 cm^{-1} (—) has been measured by inserting a LiF filter in the excitation arm. The absorption coefficient appears somewhat lowered, since the additional filter reduces the intensity of the incident beam.

A weakly pronounced band is reported for LiF:Mn^{2+} at 50 500 cm^{-1} [BAG74], which they assigned tentatively to a CT state similar to those that Kuwabara and Aoyagi observed. In the spectrum this band appears of comparable intensity to the $3d^5$ states (two orders of magnitude weaker) than the bands at higher energy, and therefore it is believed that a different origin than they claim is responsible.

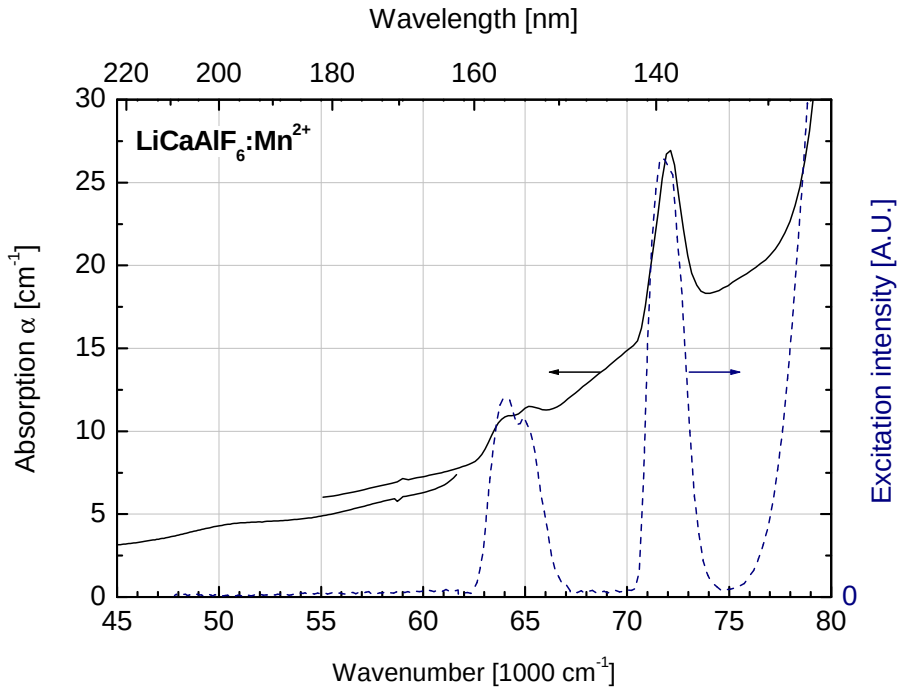

Figure 5.8: Absorption (—) and excitation spectrum (---) of LiCAF:Mn^{2+} at 10 K.

Experimentally derived oscillator strength

The measurement of the absorption coefficient α allows to calculate the approximate oscillator strength f of the transitions, if the refractive index n and the ion density ρ is known:

$$f = 1.13 \cdot 10^{12}\,\mathrm{cm}^{-1} \frac{9n}{\rho\,(n^2+2)^2} \int dE\,\alpha \tag{5.3}$$

The integrated absorption (∘) shown in Figure 5.9 is obtained by subtracting a straight base line from the original curve (Figure 5.8). Three Gaussian curves are fitted (---), and the resulting spectrum (—) is perfectly resembling the absorption curve (∘) at RT. At low temperature the fit is quite accurate, while additional absorption is observed on the low-energy side. The results from the fit and the following considerations are summarized in Table 5.4.

The refractive index for LiCAF:Mn^{2+} is calculated from the Sellmeier equations, an empirical relationship between refractive index n and wavelength λ (in μm) for a particular transparent medium [WOO91]. LiCAF is a bi-refractive material with small differences of the refractive index n_a along the crystal a axis, and n_c along the c axis:

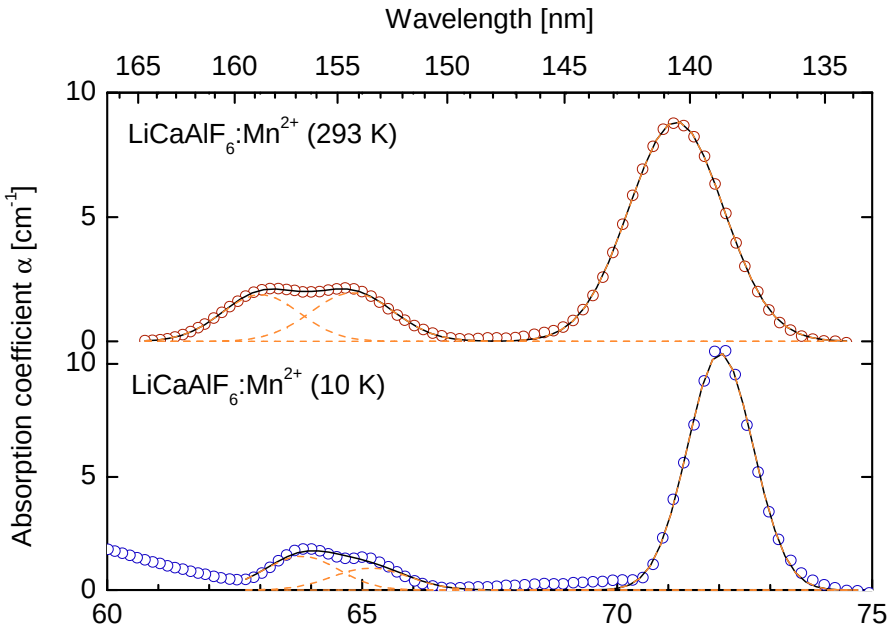

Figure 5.9: LiCAF:Mn^{2+} absorption spectra (∘) at 293 K (upper graph) and at 10 K (lower graph) after subtracting a straight line. Gaussian curves (---) have been fitted.

$$n_c^2 = 1.92155 + 0.00494/(\lambda^2 - 0.00617) - 0.00373\lambda^2 \quad (5.4)$$

$$n_a^2 = 1.92552 + 0.00492/(\lambda^2 - 0.00569) - 0.00421\lambda^2 \quad (5.5)$$

The absorption bands $E_1 = 64\,500$ cm^{-1} ($\lambda = 0.155$ μm) and 72 100 cm^{-1} ($\lambda = 0.139$ μm) have refractive indices $n_c(E_1) = 1.483$, $n_a(E_1) = 1.481$, $n_c(E_2) = 1.516$, $n_a(E_2) = 1.513$. The LiCAF crystals are grown non-oriented, and since n_c and n_a are only slightly deviating the arithmetic average used represents a good approximation.

The density $\rho = 2.988$ g $\cdot$ cm^{-3} and the weight of LiCAF $M = 187.99$ g $\cdot$ mol^{-1}. The ion concentration N at 100% doping into a cationic lattice site reads

$$N = \frac{\rho}{M} \cdot N_A = 9.54 \cdot 10^{21} \text{ cm}^{-3} \quad (5.6)$$

where $N_A = 6.022 \cdot 10^{23}$ mol^{-1} is the Avogadro constant.

The actual Mn^{2+} ion concentration equals 0.055 ± 0.08 weight-% (Section 3.1.3), accordingly

$$N\,[\text{atomic-\%}] = \frac{M}{n(\text{Mn})} \cdot N\,[\text{weight-\%}] \tag{5.7}$$

the atomic concentration is calculated being 0.188 atomic-%, where n(Mn) is the ionic weight.

	T [K]	E_{max}	ΔE_{FWHM}	$\int \alpha$	n	f
E_1	10	63 812	1445	2.7	1.482	$1.3 \cdot 10^{-4}$
E_1	293	63 008	1523	3.6	1.482	$1.7 \cdot 10^{-4}$
E_2	10	65 165	1485	1.8	1.482	$0.9 \cdot 10^{-4}$
E_2	293	64 806	1625	4.0	1.482	$1.9 \cdot 10^{-4}$
E_3	10	72 024	1287	16.91	1.514	$7.9 \cdot 10^{-4}$
E_3	293	71 158	1855	20.55	1.514	$9.6 \cdot 10^{-4}$

Table 5.4: Oscillator strength calculated from LiCAF:Mn^{2+} absorption. E_{max} is the peak energy (cm^{-1}), ΔE_{FWHM} the corresponding FWHM, $\int \alpha$ is the integrated absorption (in 1000 cm^{-2}), n the refractive index, f is the derived oscillator strength.

According to Equation 5.6 the ion density becomes $\rho = 1.79 \cdot 10^{19}$ cm^{-3}. From Equation 5.3 and the integrated absorption coefficient the oscillator strengths of the absorption bands are determined (Table 5.4). The oscillator strengths compare very well to those reported for Mn^{2+} in $KMgF_3$ at 4.2 K ($f = 1.9 \cdot 10^{-4}$) and 300 K ($f = 3.7 \cdot 10^{-4}$), and for MgF_2 at 4.2 K ($f = 8.8 \cdot 10^{-4}$) and 300 K ($f = 1.1 \cdot 10^{-3}$) [SAB75]. Typical values for the parity- and spin-forbidden $d \rightarrow d$ transition are of the order 10^{-7}.

The energy peak is shifting several 100 cm^{-1} towards higher energy when going from 10 K to room temperature. The partially allowed nature of the excitation bands E_1, E_2, and E_3 is confirmed by the clear temperature dependence. The oscillator strength of a fully allowed transitions is expected to be larger in magnitude and independent of temperature.

In order to further investigate these strong bands, excitation spectra of Mn^{2+} doped $LiCaAlF_6$, $LiSrAlF_6$, $BaMgF_4$, BaY_2F_8, and MgF_2 crystals have been analyzed. The corresponding experimental results on various crystal hosts are summarized in Table 5.5 on page 126 along with a detailed discussion of the results in Section 5.6.

5.5.2 Comparison of excitation in a wide spectral region

By means of excitation spectroscopy with synchrotron radiation of doped crystals electric dipole allowed transitions as well as the parity- and spin-forbidden $d \rightarrow d$ transitions can be measured very accurately. Figure 5.10 shows three excitation spectra of LiCAF:Mn^{2+} at low temperature, which have been appended by matching intensities within the spectral overlap. The broad $^4T_{1g} \rightarrow {}^6A_{1g}$ emission of Mn^{2+} is monitored at $\lambda_{em} = 520$ nm. On the low-energy side the free ion states are indicated that give rise to parity- and spin-forbidden

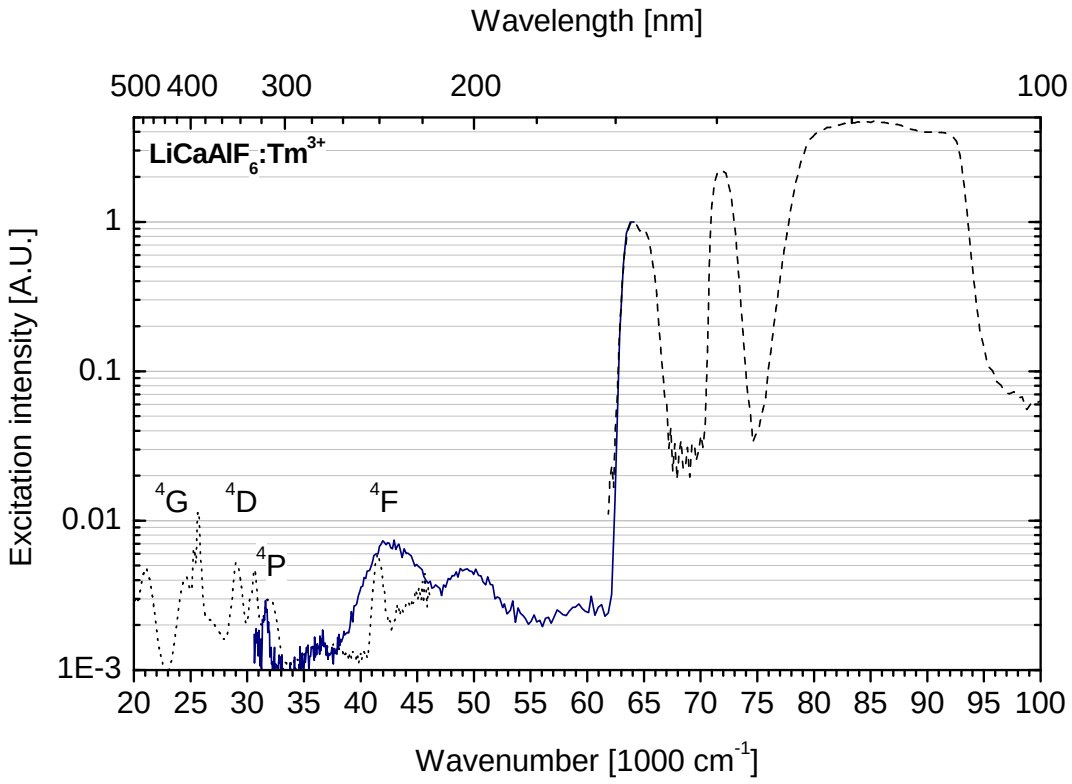

Figure 5.10: Three excitation spectra of LiCAF:Mn^{2+} at low temperature (λ_{em} = 520 nm), appended by matching intensities within the spectral overlap. Note the logarithmic scale.

$3d^5 \rightarrow 3d^5$ transitions (·····), measured at the Fluorolog setup. These transitions are very weak and hardly observable by absorption spectroscopy.

The second curve (—) of Figure 5.10 has been measured at the *Superlumi* setup by applying a quartz filter after the primary grating, which prevents second order excitation below 65 000 cm^{-1} (154 nm). The strong bands observed in this region would inevitably obscure the weak $3d^5$ structures. The intensity of the three excitation bands (---) between 50 000 and 100 000 cm^{-1} is at least two orders of magnitude higher than that of the $3d^5 \rightarrow 3d^5$ transitions and further evaluated by excitation spectroscopy.

In the overlap region around 300 nm the synchrotron radiation intensity is already substantially reduced (Figure 3.7 on page 58), therefore this graph should be regarded somewhat qualitatively. The oscillator strength of the $3d^5$ states is usually of the order 10^{-7}, being clearly lower compared with 10^{-4} determined for these VUV bands (Table 5.4).

5.5.3 Excitation spectra of LiCAF and LiSAF

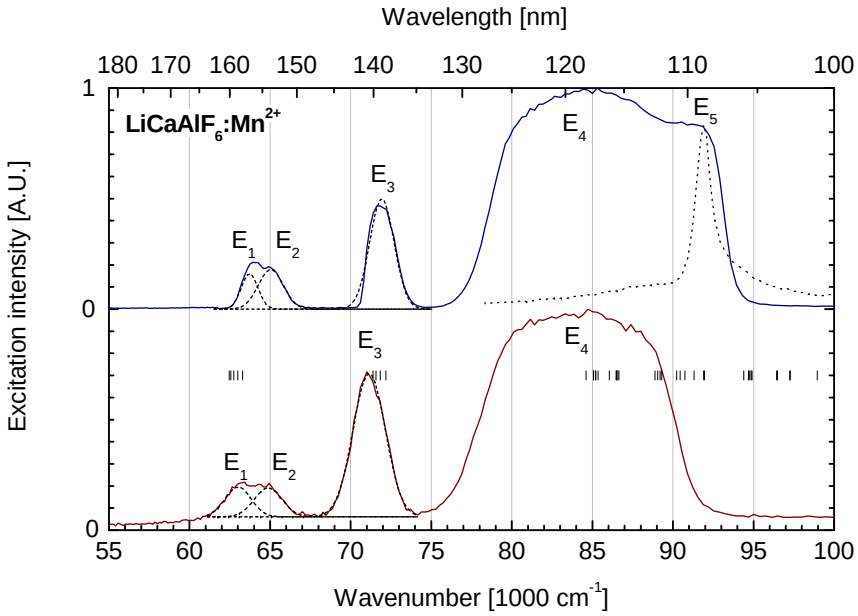

Figure 5.11: Excitation spectra of LiCAF:Mn^{2+}. (a) λ_{em} = 513 nm, T = 9 K; (b) λ_{em} = 519 nm, T = 300 K; (----) fitted Gaussian curves; (·····) excitonic peak, λ_{em} = 320 nm of pure LiCAF. The 4s (^6D, ^4D) and 4p states of the Mn^{2+} free ion are indicated by vertical lines.

Figure 5.11 shows excitation spectra of LiCAF:Mn^{2+} at 9 K (curve a) and at RT (curve b), discussed in more detail in [TRU04b]. The ^6D and ^4D multiplets of the free ion (configuration $3d^4 4s$) have their baycenters at 62 800 and 71 700 cm^{-1}, respectively, indicated by vertical lines [NIST]. The $3d^4 4p$ states commence at considerably higher energies (>85 000 cm^{-1}).

The intense excitation bands in the region of 60 000 to 75 000 cm^{-1} are decomposed of three components E_1, E_2, and E_3, being very well reproduced by three Gaussian bands (----). The values of all VUV excitation bands are tabulated with results from an extensive literature search in Table 5.5.

It should be noted that the single band E_3 at 71 000 cm^{-1} at 9 K is not exactly Gaussian, but exhibits a sharp raise on the low-energy side. These bands are shifted by some 100 cm^{-1} to lower energy when going from 9 K to RT, while the FWHM increases.

The very broad excitation band ranging from 75 000 to 90 000 cm^{-1} is composed of several excitation bands. The most intense band E_4 is mainly attributed to the fully allowed $F^- \rightarrow Mn^{2+}$ charge transfer transition. Further contributions arise from

The excitation feature E_5 at low temperature arises due to excitonic absorption of the host crystal (·····) and subsequent energy transfer to Mn^{2+}. At RT this excitonic mechanism is not active in the pure crystal and likewise disappears for LiCAF:Mn^{2+} (cf. Section 4.2).

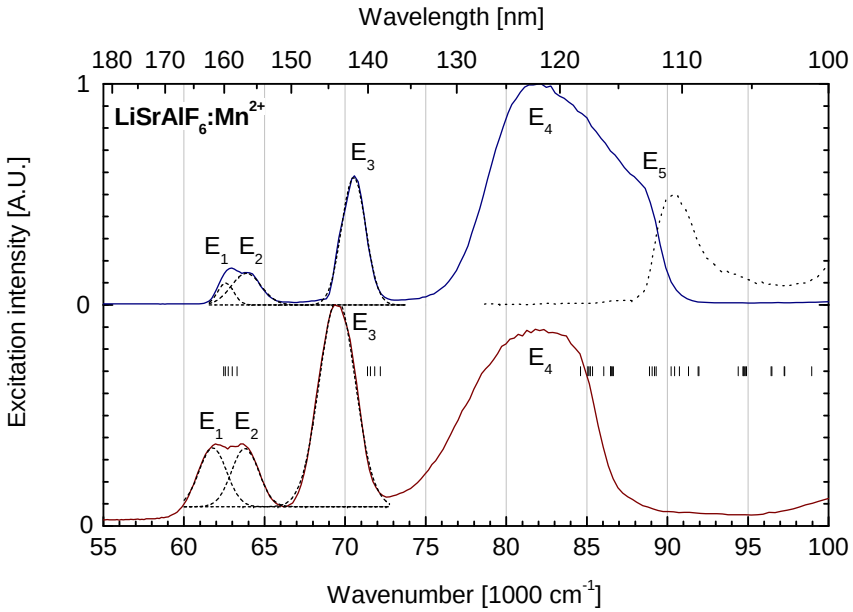

Figure 5.12: Excitation spectra of LiSAF:Mn^{2+} and fitted Gaussian curves (----). (a) λ_{em} =508 nm, T =10 K; (b) λ_{em} =515 nm, T =300 K; (·····) λ_{em} =320 nm (excitonic peak). The $4s$ (^6D, ^4D) and $4p$ states of the Mn^{2+} free ion are indicated by vertical lines.

Similar excitation bands are observed in LiSAF:Mn^{2+} as shown in Figure 5.12, being slightly blue-shifted compared to those in LiCAF. The previously reported measurement [TRU04a] has been fitted by three Gaussian bands E_1, E_2, and E_3 (----) and is further evaluated in comparison with the samples presented in this thesis. Small temperature-dependent energy shifts are observed as in LiCAF. The bands E_4 (charge transfer) and E_5 (excitonic) are explained analogously to LiCAF.

5.5.4 Excitation spectra of $BaMgF_4$

$BaMgF_4$ (BMF) offers two lattice sites for Mn^{2+} (ionic radius 81 pm), namely the Ba^{2+} (149 pm) and Mg^{2+} (86 pm) site, which leads to broad emissions at 520 nm and 630 nm, respectively (Section 5.2.5).

By monitoring each emission, excitation spectra of BMF:Mn^{2+} at low and RT have been measured, reflecting the influence of the local surrounding in clearly different excitation features. However, the 520 nm emission band is overlapping with the $^6A_{1g} \rightarrow {}^4T_{1g}$ absorption of Mn^{2+} on the Mg^{2+} site (Figure 5.7), thus monitoring the 630 nm emission unavoidably monitors the 520 nm emission as well.

Figure 5.13 shows excitation spectra of polycrystalline BMF monitoring *pure* emission of Mn^{2+} on Ba^{2+} sites. At 7.3 K (curve a) the excitation bands E_2 at 60 850 cm^{-1} (FWHM

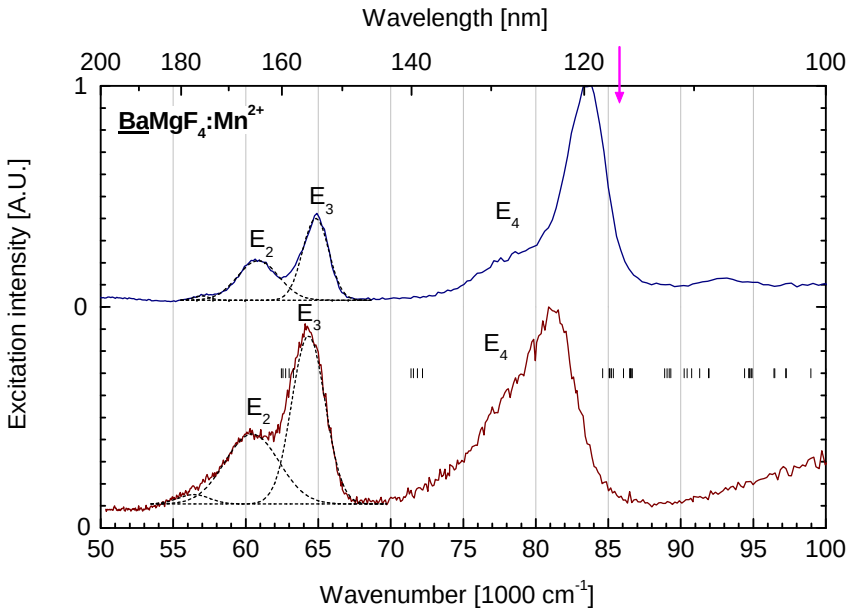

Figure 5.13: Excitation spectra of $BaMgF_4$:Mn^{2+} (substituting Ba^{2+}). (a) λ_{em} = 520 nm, T = 7.3 K ; (b) λ_{em} = 525 nm, T = 300 K ions incorporated into Ba^{2+} lattice sites. The excitonic peak is indicated by an arrow. The $4s$ (^6D, ^4D) and $4p$ states of the Mn^{2+} free ion are indicated by vertical lines.

2850 cm^{-1}) and E_3 at 64 830 cm^{-1} (1800 cm^{-1}) are clearly red-shifted compared to those observed in LiSAF and LiCAF. If the temperature is raised to 300 K, a small red-shift is experienced by E_2 to 60 440 cm^{-1} (FWHM 3670 cm^{-1}) and E_3 to 64 330 cm^{-1} (2290 cm^{-1}). While the width of E_3 compares very well to that in LiCAF and LiSAF, the width of E_2 appears to be twice as large. Thus, E_2 is actually decomposed of the components E_1 and E_2 observed in LiCAF and LiSAF.

The weak band around 57 000 cm^{-1} (FWHM 1050 cm^{-1}) at 7.3 K, shifting to 56 500 cm^{-1} (2200 cm^{-1}) at RT, corresponds to E_2 of Mn^{2+} on the other (Mg^{2+}) site in this host, which is also excited to some extent due to energy transfer between ions on both types of sites.

The most intense excitation is peaking at 86 000 cm^{-1} at 7.3 K (curve a), while it is almost quenched at RT (curve b). Since it is below the host excitonic peak identified by us in recent unpublished studies, it is attributed to a different process such as excitons created near impurity centers.

Figure 5.14 shows excitation spectra at 7.3 K (upper graph) and 300 K (lower graph), monitoring emission at 630 nm and 640 nm, respectively. This corresponds to emission of Mn^{2+} on Mg^{2+} sites. Shoulders marked with an asterix (*) are due to excitation of Mn^{2+} on the Ba^{2+} site and cannot be avoided as explained above.

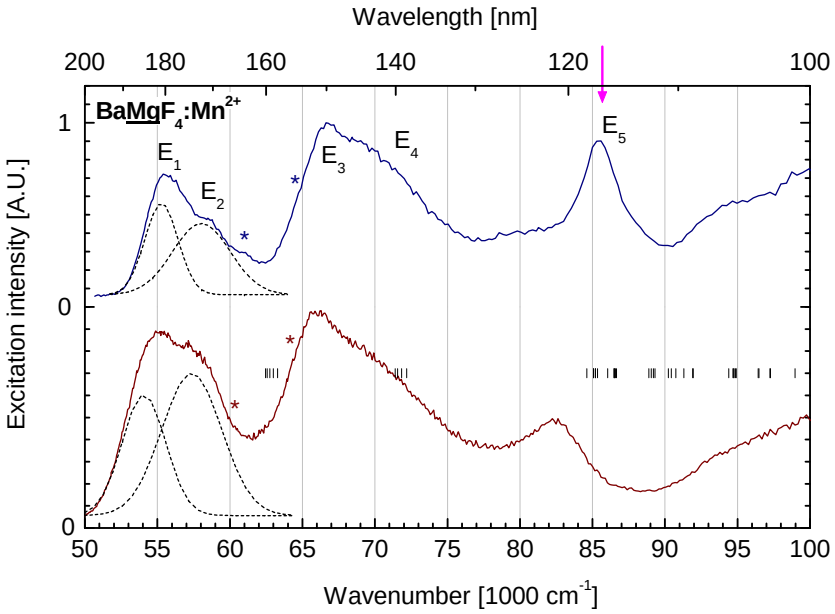

Figure 5.14: Excitation spectra of BMF:Mn^{2+} (substituting Mg^{2+}). (a) λ_{em} =630 nm, T = 7.3 K; (b) λ_{em} =640 nm, T = 300 K. *simultaneously excited due to the E_2 and E_3 bands of Mn^{2+} on Ba^{2+} sites. The excitonic peak is indicated by an arrow. The $4s$ (^6D, ^4D) and $4p$ states of the Mn^{2+} free ion are indicated by vertical lines.

Two excitation bands E_1 at 55 280 cm^{-1} (FWHM 2300 cm^{-1}) and E_2 at 58 040 cm^{-1} (4000 cm^{-1}) are observed at 7.3 K. The third peak E_3 is obscured by at least one broad excitation structure E_4.

The peak E_5 at 85 590 cm^{-1} is due to the excitonic absorption, being strongly quenched at RT. This is confirmed by recent unpublished studies of pure BMF carried out in our group. The energy of the excitonic peak is indicated by an arrow in the figure.

5.6 Discussion

Whereas the $3d^5$ states of Mn^{2+} are well known and investigated in many compounds, structureless broad bands at higher energy are difficult to assign due to the lack of theoretical calculations. Several excitation mechanisms exists in the VUV spectral region, which caused different interpretations in the literature.

The earliest study reporting such absorption bands of transition metals known to the author is concerning V^{2+}, Mn^{2+}, Ni^{2+}, Cu^{2+}, and Zn^{2+} in NaCl or NaF [KUW65]. One or two strong and temperature-insensitive bands were observed for ions with partly filled $3d$ shell, tentatively attributed to ligand-to-metal charge transfer (CT) transitions. Two or three weaker and temperature-sensitive bands were assigned to parity-forbidden intra-ionic transitions.

An early Estonian study reported intense VUV absorption bands in LiF:Mn^{2+} and CaF_2:Mn^{2+} at RT [LUS70], which are in agreement with later studies (cf. Table 5.5). They correlated these bands already with free ion $3d^4 4s$ energy levels ^{6}D and ^{4}D.

The investigation of LiF:Mn^{2+} by means of absorption spectroscopy in the region 140 to 600 nm revealed two bands at 50 500 cm^{-1} and 60 970 cm^{-1} [BAG74]. In order to observe the $d \rightarrow d$ transitions at lower energy in absorption, a sample containing 1000 ppm Mn^{2+} has been used, for the VUV bands a 20 ppm sample yield sufficient intensity. However, the presented absorption spectra have been measured at RT, and the structures are broad and very weakly pronounced.

McClure *et al.* contributed absorption measurements for various transition metals doped into CaF_2, $KMgF_3$, and MgF_2 fluorides [SAB75]. In conclusion, they attributed the VUV excitation band (corresponding to E_2 in this work) to transitions $3d^5 \rightarrow 3d^4 4s$. This was confirmed shortly afterwards by measurements of LiF and NaF [CHA76]. A more recent publication on CaF_2:Mn^{2+} powders at different doping concentrations was carried out using excitation spectroscopy [DEN00]. Two bands at 64 000 cm^{-1} and 70 000 cm^{-1} are assigned to partially transitions $3d^5 \rightarrow 3d^4 4s$ from the ground state ^{6}S to the excited ^{6}D term. The splitting of the ground state into two sub-levels by the crystal field into two sub-levels with energy difference $10Dq$ has been observed in the $d \rightarrow s$ excitation bands. In addition the $F^- \rightarrow Mn^{2+}$ charge transfer band was assigned. The energies of the bands agree in both studies, although McClure *et al.* state that they distrust the quality of this particular crystal and unfortunately did not include the measurement in their further evaluation.

Recently, excitation spectra in the VUV spectral region have been presented, exhibiting similar bands due to $d \rightarrow s$ transitions of Mn^{2+} in $CaAlF_5$, $SrAlF_5$, and $NaMgF_3$ [KOL03]. The spectra concerning the $SrAlF_5$ crystal are doubtful and thus not included in Table 5.5. The two peaks attributed to $d \rightarrow s$ excitation bands in $CaAlF_5$ are in good agreement with those of LiCAF (and LiSAF), and the energy difference between them agrees with the respective value $10Dq$. The systematic analysis presented in this work is straight forward in view of these results.

	σ	r_{ion}	T	E_1 (FWHM)	E_2 (FWHM)	E_3 (FWHM)	E_4	$(E_3 - E_2)$	Ref.	$10Dq$	Ref.
$\underline{Ba}MgF_4$	$C_s^{(6)}$	149	7.3	60 860 (2820)		64 830 (1790)		3970	*this*		
			RT	60 440 (3700)		64 330 (2290)		3890	*this*	*4823*	*this*
$LiSrAlF_6$	$C_{3i}^{(6)}$	132	10	62 600 (1000)	63 870 (1640)	70 530 (1500)		6660	*this*		
			RT	61 790 (1700)	63 790 (1670)	69 520 (2230)		5730	*this*	5546	*this*
$\underline{Ca}F_2$	$O_h^{(8)}$	126	4.2	-	64 800	70 700		5900	[SAB75]		
			85	-	64 530	70 170		5640	[DEN00]		
			RT	-	63 720 (4900)	69 360 (1400)		5640	[DEN00]	5700	[LEW94]
			RT	-	64 300	69 400		5100	[SAB75]		
				-	61 121	69 364			[LUS70]		
$LiCaAlF_6$	$C_{3i}^{(6)}$	114	9	63 730 (1020)	65 040 (1540)	71 940 (1510)		6900	*this*	6675	*this*
			RT	63 020 (1600)	64 890 (1730)	71 150 (2000)		6260	*this*	6226	*this*
$CaAlF_5$			12	62 770 *(2000)*	66 450 *(2300)*	71 380 *(2800)*		4930	[KOL03]		
$BaMgF_4$	$O_h^{(6)}$	86	7.3	55 280 (2300)	58 040 (3970)	66 800		8760	*this*		
			RT	54 070 (3000)	57 400 (4100)	66 000		8600	*this*	8354	*this*
$\underline{Li}F$	$O_h^{(6)}$	90	10	-	66 200	70 400		*3800*	[CHA76]		
			RT	-	65 300 *(3500)*	69 300 *(3900)*		*4000*			
					62 105	68 557		*6452*	[LUS70]	*8250*	
$KMgF_3$	$O_h^{(6)}$	86	4.2	-	60 600 *(2500)*	-		-	[SAB75]		
			RT	-	60 200 (3500)	-		-	[SAB75]		
			RT		57 700 *(6000)*	66 700 *(4000)*		8400	[KUE04]	8430	[SIB73]
$NaMgF_3$	$O_h^{(6)}$	86	12		58 800 *(7000)*	66 700		7900	[KOL03]		
$\underline{Mg}F_2$	$D_{2h}^{(6)}$	86	7		61 576 (3126)				*this*	*9550*	[SUZ87]
			4.2		62 500 *(3200)*			-	[SAB75]		
			RT		61 600 (4200)			-	[SAB75]		
			RT		60 600 *(6000)*	69 000		8400	[KUE04]	8550	*this*
$Ca_{0.9}Y_{0.1}F_{2.1}$			RT	56 200 *(5500)*	69 400 *(3500)*	76 900 *(6500)*			[KUE04]		

Table 5.5: Comprehensive overview of intense excitation bands E_1, E_2, and E_3 of Mn^{2+} doped fluorides in the VUV at temperature T (K). Energies are given in cm^{-1}, values in *italic* are tentative or inaccurate. The substitutional ion site is underlined, having point symmetry σ (coordination) and ion radius r_{ion} (pm). $10Dq$ is the crystal field splitting (in cm^{-1}). The references are given in the table.

In this work, excitation spectra of $d \rightarrow d$ transitions (Section 5.3) have been used to calculate the crystal field splitting $10Dq$ and the Racah parameters (Section 5.4). The VUV excitation spectra of Mn^{2+} doped into a variety of fluoride crystals were investigated, and the first two intense excitation bands are assigned to $3d^5 \rightarrow 3d^4 4s$ transitions. More specifically, these bands are due to transitions from the ground state $^6A_{1g}$ (^6S), which is split by $10Dq$ into mainly two sub-levels e_g and t_{2g}.

For the first time, the two observed excitation bands in the VUV are systematically analyzed and assigned to transitions from the crystal field splitted ground state to a highly excited state $3d^4 4s$. The energy difference between them equals $10Dq$. The following discussion shows that the energy differences of the $4s$ excitation bands of all samples are in striking agreement with the corresponding values $10Dq$. A comparison with the results from an extensive literature research is given in Table 5.5.

In order to investigate the origin of the intense VUV bands below the excitonic absorption, several excitation mechanisms are to be considered. The $3d^5 \rightarrow 3d^5$ have been discussed extensively in Section 5.3. The $F^- \rightarrow Mn^{2+}$ charge transfer state [FRO98, MOS01] is expected at rather higher energies around 84 000 cm^{-1} in LiCAF and 82 000 cm^{-1} in LiSAF (Section 5.5.3). Excitonic and inter-band excitations are located at even higher energies in the respective hosts. Mn^{2+}-Mn^{2+} pair interactions are excluded in view of the extraordinary low concentrations (Section 3.1.3). In principle unwanted impurities or color centers may contribute to the spectra, however, there have been no emissions observed in the visible to VUV spectral region other than those due to $d \rightarrow d$ transitions of Mn^{2+}. $3d^5 \rightarrow 3d^4 4p$ transitions [SIM77, HAR81, FRO98] are expected to have fully allowed character with accordingly increased oscillator strengths compared to those determined in this work (Section 5.5.1). A blue-shift on cooling of several 100 cm^{-1} has been observed for the bands E_1, E_2, and E_3 of all samples. This general property is a further confirmation of the assignment to $d \rightarrow s$ transitions localized on the ion as opposed to charge transfer transition and illustrated in Figure 5.15.

Mn^{2+} emission from the extraordinary large Ba-site in $BaMgF_4$ has been observed (Section 5.2.5). The VUV excitation bands E_2 and E_3 have their peak positions 3980 cm^{-1} and 3890 cm^{-1} apart at 7.3 K and RT, respectively, being only roughly in agreement with the obtained value $10Dq = 4823$ cm^{-1}. This is mainly resulting from the lower symmetry C_s of the Ba-site, supported by the fact that the full width at half maximum (FWHM) is broader compared to the other hosts with higher (O_h) symmetry. In addition, the weaker band E_1 around 57 000 cm^{-1} is likely due to a further splitting of the Mn^{2+} ground state terms e_g and t_{2g}, reflecting the lower symmetry. Applying the correct Tanabe-Sugano diagram for the corresponding symmetry would yield a slightly different value for Dq.

CaF_2:Mn^{2+} has been used to probe the computational method that has been applied to determine the crystal field splitting $10Dq$ (cf. Section 5.4). For CaF_2:Mn^{2+} the most recent value $10Dq = 5700$ cm^{-1} is given in the literature, whereby the appropriate Tanabe-Sugano

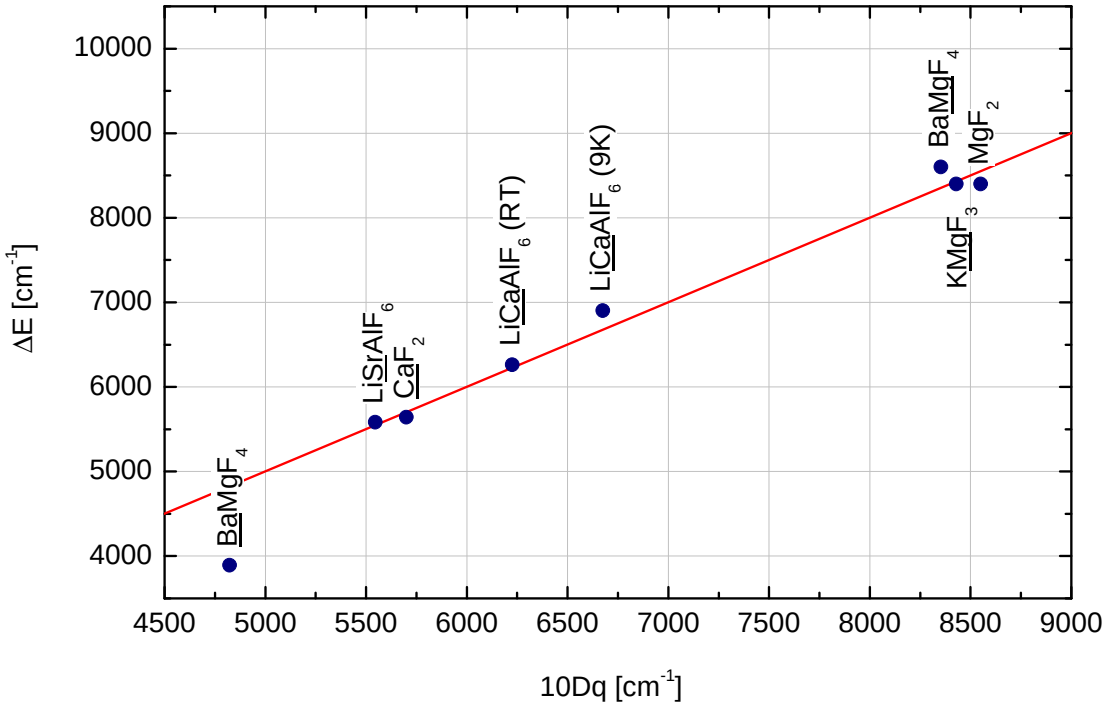

Figure 5.15: Correlation of Mn^{2+} doped fluoride crystals between the crystal field splitting $10Dq$ and the energy difference ΔE of the first two intense VUV excitation bands. The substitutional lattice site is underlined.

diagram in eight-fold coordination has been used. A calculation from the original measurement at RT using the diagram in six-fold coordination yielded $10Dq = 4200$ cm^{-1}. This corresponds to a factor of 1.4 when going from six-fold to eight-fold coordination. The revised value is in perfect agreement with the energy shift of 5640 cm^{-1} between E_2 and E_3 excitation bands [DEN00].

The crystal field splitting of LiCAF:Mn^{2+} has been determined in this work from excitation spectra at low and room temperature. At low temperature, the agreement of $10Dq = 6226$ cm^{-1} and $(E_3 - E_2) = 6260$ cm^{-1} is striking, which is also true for the values $10Dq = 6675$ cm^{-1} and $(E_3 - E_2) = 6900$ cm^{-1} obtained from RT measurements.

LiSAF:Mn^{2+} shows essentially the same luminescence and excitation characteristics, while Mn^{2+} is sensitive to the crystal field and experiences a reduction to $10Dq = 5546$ cm^{-1} at RT. The obtained energy difference $(E_3 - E_2) = 5580$ cm^{-1} of the VUV excitation bands coincides as well with the crystal field splitting.

For both LiCAF and LiSAF the peak on the lower-energy side is clearly decomposed of two sub-bands E_1 and E_2, $(E_2 - E_1) \approx 1300$ cm^{-1}. The E_1 band is attributed to the distorted

octahedral symmetry (cf. Section 3.2.1), similarly to that in $BaMgF_4$ discussed above. This causes a further splitting of the triply and doubly degenerate sub-levels of the ground state (cf. Section 2.2.3), similarly as the additional splitting observed in some peaks due to $d \rightarrow d$ excitation (cf. Section 5.3). Hosts having (nearly) octahedral symmetry (perovskites $KMgF_3$, $NaMgF_3$; MgF_2; CaF_2) exhibit only one band E_2, however, the FWHM is significantly larger than that of the sub-band E_1 and E_2 in LiCAF and LiSAF.

Mg^{2+} has approximately the same ionic size as Mn^{2+}, therefore a larger crystal field splitting for these hosts is reflected in high values of Dq.

The values of the crystal field splitting $10Dq$ and the energy difference $\Delta E = E_3 - E_2$ of the intense VUV excitation bands are shown in Figure 5.15 together with the *correlation function*

$$f(10Dq) = \Delta E \tag{5.8}$$

The experimentally derived values in this plot are in excellent agreement for LiCAF, LiSAF, $BaMgF_4$, $KMgF_3$, and MgF_2, and CaF_2, each having a close to octahedral surroundings. The substitutional lattice sites of MgF_2 and $\underline{Ba}MgF_4$ have lower symmetries, which explains the observed deviation from the correlation function. The value of $Ba\underline{Mg}F_4$, on the other hand, shows a smaller deviation from the correlation line, since the local symmetry of the Mg^{2+} site (O_h) is corresponding to that of the Tanabe-Sugano diagram used for calculating $10Dq$, whereby charge compensation is not needed.

In conclusion, the nature of the intense absorption bands in the VUV are confirmed being due to $3d^5 \rightarrow 3d^4 4s$ transitions. The sub-levels e_g and t_{2g} of the $3d^5$ ground state, splitted by the crystal field, are the initial states of this transitions and responsible for the two observed bands. These transition have ^6D as final state, i.e., they are due to transitions $^6S \rightarrow {}^6D$ of partially forbidden character in agreement with the oscillator strength determined for LiCAF. The energy of the free ion ^4D multiplet is close to that of the second excitation bands (E_3), however, the multiplicity would be not conserved for $^6S \rightarrow {}^4D$, thus these transitions are expected at much lower intensity than the intense bands under discussion.

Chapter 6

Spectroscopy of LiCAF:Tm, Mn

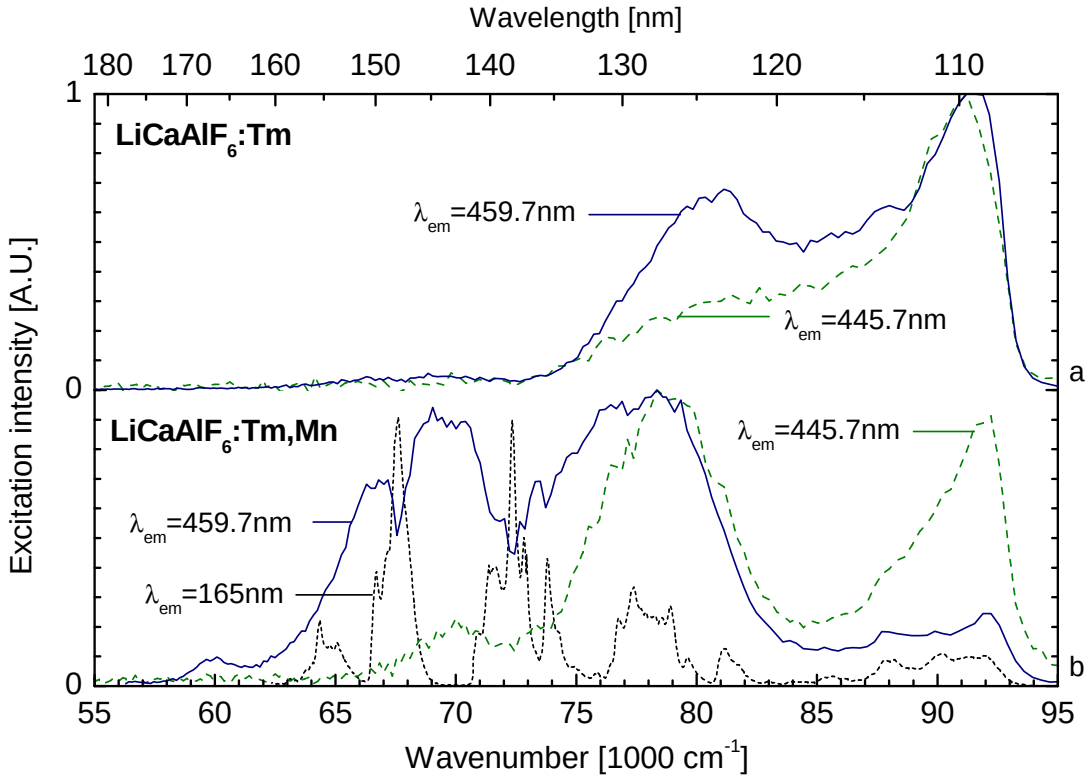

Figure 6.1: Excitation spectrum of Tm^{3+} and Mn^{2+} doped LiCAF crystal. (a) LiCAF:Tm^{3+}, $T = 9$ K, $\lambda_{em} = 459.7$ nm (—) and 445.7 nm (---); (b) LiCAF:Tm,Mn, $T = 17$ K, $\lambda_{em} = 459.7$ nm (—), 445.7 nm (---), and 165 nm (----).

Figure 6.1 presents excitation spectra of $LiCaAlF_6$ (LiCAF) singly doped with Tm^{3+} (curves a) and co-doped with Tm^{3+}, Mn^{2+} (curves b) at low temperature. The transitions $^1D_2 \rightarrow {}^3F_4$ (E_x) at 445.7 nm (cf. Figure 4.18) and a peak at 459.8 nm (cf. below) have been monitored

selectively ($\Delta\lambda_{em} \leq 1.3$ nm). The excitation spectra of the singly doped crystal are discussed in more detail in [TRU04b]. The peak at 115 nm is due to excitonic excitation, and the broad band around 127 nm is mainly due to the $F^- \rightarrow Tm^{3+}$ charge transfer (CT) transition.

At energies lower than 75 000 cm^{-1} the $f \rightarrow f$ transitions are only faintly excited in LiCAF:Tm (curves a), in agreement with the results for LiSAF:Tm (Section 4.4.2), but in contrast to the excitation of LiCAF:Tm,Mn (curves b). An additional wide excitation band of large intensity is observed exclusively in the co-doped samples. Similar results have been obtained for the other Tm,Mn co-doped LiCAF crystals (cf. Section 3.1.3).

The question arises, if the origin of this band can be attributed to an inter-ionic energy transfer process, e.g. cross relaxation as proposed in Section 1.1. Following the initial excitation within the region of absorption due to spin-allowed $4f^{12} \rightarrow 4f^{11}5d$ transitions, non-radiative relaxation occurs to the lowest d-state, which has a life-time of 5.6 μs at RT [TRU04b]. From this long-living state a cross relaxation may occur, involving relaxation to one of the lower $4f$ levels along with excitation of the numerous $3d^5$ states of Mn^{2+} ion. Subsequently, two visible photons are expected resulting from $f \rightarrow f$ transitions of Tm^{3+} as well as the $d \rightarrow d$ transition of Mn^{2+}.

In order to pursue this idea, various emission spectra have been recorded at low and room temperature, at various excitation energies, and by applying additional filters. Selected spectra representative for this discussion are shown below, recorded with our CCD camera at moderate resolution ($\Delta\lambda_{em} \leq 0.5$ nm). This way, the low intensity of $f \rightarrow f$ transitions under $d \rightarrow f$ excitation is partially compensated for.

Figure 6.2 shows emission spectra of LiCAF:Tm^{3+}, Mn^{2+} excited with synchrotron radiation at 9 K. All curves have been normalized to the largest peak around 19 000 cm^{-1}, which is due to the well-known Mn^{2+} emission (cf. Section 5.2.3).

The spectra on the left-hand side (curves a-c) have been measured without additional filters. A LiF filter has been inserted after the primary grating for the spectra on the right-hand side (curves d-f), preventing higher order excitations. The low signal-to-noise ratio in curves d-f is partly due to the LiF filter. A comparison with the spectra measured without filter (curves a-c) shows a good agreement for these measurements at low temperature.

The emission spectra measured at RT without filter exhibit large differences to those measured with LiF or SiO_2 filters, since energy transfer to Mn^{2+} states is efficiently excited by second-order via the intrinsic absorption of LiCAF at RT. This process is quenched at low temperature. On the other hand, broad emission intrinsically excited in LiCAF and LiSAF is observed predominantly at low temperature (cf. Section 4.2). The broad background emission is observed in the emission spectra presented in Figure 6.2.

The intense double peaks are observed for all co-doped LiCAF samples and can be literally excited in a large spectral range, while the singly Tm^{3+} doped high resolution emission spectra did not exhibit this double peak (cf. Sections 4.5.3 and 4.5.4).

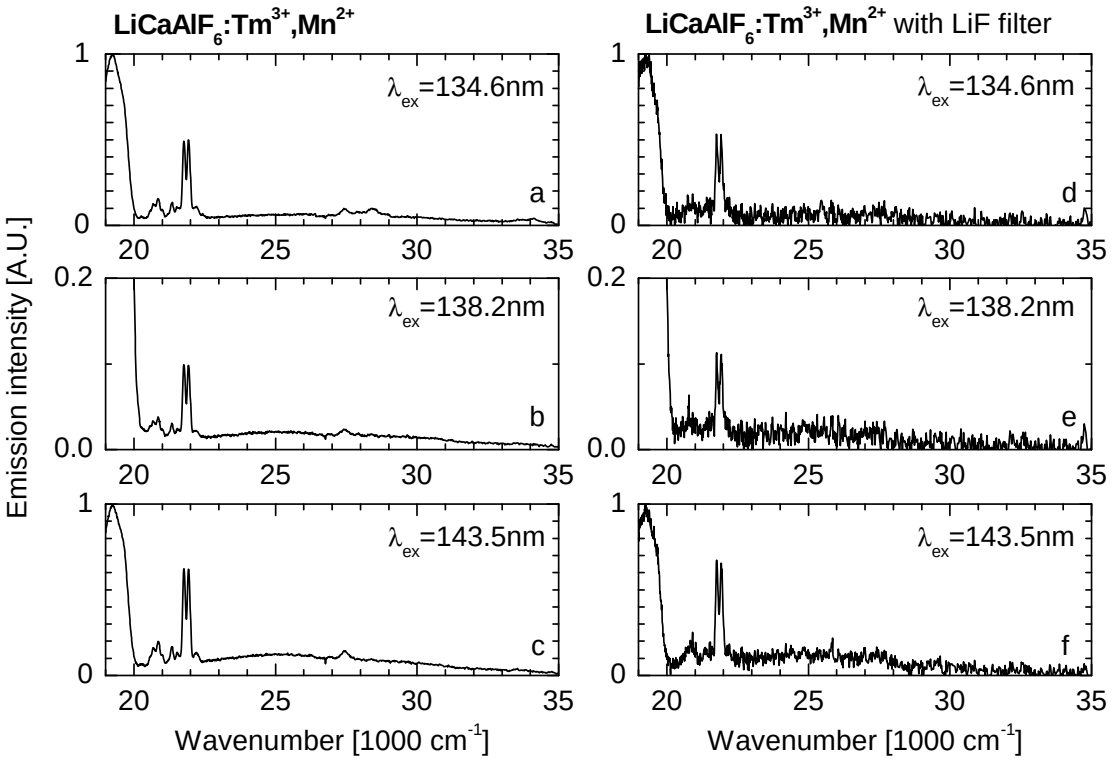

Figure 6.2: Emission spectra of LiCAF:Tm^{3+}, Mn^{2+} under various excitation energies, $T = 9$ K, $\Delta\lambda_{em} \leq 0.5$ nm. (a,d) $\lambda_{ex} = 134.6$ nm; (b,e) $\lambda_{ex} = 138.2$ nm; (c,f) $\lambda_{ex} = 143.5$ nm. LiF filter has been inserted after the primary grating for curves c to f.

Attributing this double peak to an $f \rightarrow f$ emission is doubtful, since the transitions to other f-states are missing in the emission spectra. Furthermore, the extraordinary low doping concentrations of both ions (cf. Section 3.1.3) have to be considered. Cross relaxation requires interaction of the participating ions, which is de facto vanishing in view of the low doping concentrations, assuming statistical distribution of the dopants.

Due to these limitations new samples were required, and therefore a series of the promising BaY_2F_8 host has been bought for extended analysis. However, a strong disagreement of the nominal and probed doping concentrations has been determined. This is also reflected in the spectra, which are presented in Appendix A.

Chapter 7

Conclusions and Outlook

The present work has been motivated by the search for efficient lighting materials applicable in mercury-free discharge lamps, being part of the BMBF project "VUV Leuchtstoffe für quecksilberfreie Entladungslampen". Rare earth and transition metal ion doped $LiCaAlF_6$ (LiCAF) and $LiSrAlF_6$ (LiSAF) crystals, among others, have been investigated as promising candidates for intra-ionic energy transfer, including a systematic analysis of absorption bands in the VUV.

Crystal growth

Czochralski growth of LiCAF single crystals, singly doped with Tm^{3+} and Mn^{2+} and co-doped with both ions, has been carried out successfully at the *Institut für Laserphysik*. Whereas growth of LiSAF under similar conditions has been reported in the literature, several attempts to grow LiSAF single crystals have been unsuccessful due to missing experience in the beginning and problems beyond control in the following attempts (power failure). Hence, growth of the respective LiSAF crystals should be possible under more auspicious circumstances.

Part of the LiSAF powder obtained by solid state reaction for the Czochralski growth has been kept for spectroscopic purposes. X-ray diffractometry confirmed that these samples are single phase. The achieved doping concentrations of the novel samples were determined by trace analysis to be substantially (two orders of magnitude) lower than the initial concentrations, close to the detection limit of the microprobe. Thus, spectroscopy of (partially) forbidden transitions yielded low intensities. As outlined in the following discussion, rare earth and transition metal ion doped LiSAF is a most interesting candidate for prospective inter-ionic energy transfer processes.

Additional samples have been obtained from different sources. Several Mn^{2+} doped fluoride crystals have been obtained from the *Institut für Laserphysik, Universität Hamburg* for extended investigation along with LiCAF:Mn^{2+} and LiSAF:Mn^{2+}. Several crystals BaY_2F_8

(BYF) singly and co-doped with Tm^{3+} and Mn^{2+} have been provided by T. Ouvarova from the *General Physics Institute, Moscow, Russia*.

Emission, excitation and absorption spectroscopy of Tm^{3+} doped LiCAF and LiSAF as well as nominally pure LiCAF has been carried out at low and room temperature. Various energy transfer mechanisms have been identified, involving $4f$ and $5d$ states. Excitation in the region of the $F^- \rightarrow Tm^{3+}$ charge transfer (CT) state at around 127 nm yielded significant $f \rightarrow f$ emission, bypassing the $5d$ states by non-radiative relaxation. This process has been used for detailed characterization of the respective transitions, while it is not applicable for efficient photon cascade emission, as it yields only one photon in the visible per absorbed photon.

Since a variety of energy transfer processes can occur in the VUV spectral region, the singly doped crystals have been characterized in the first place.

Tm^{3+} doped fluoride crystals

For the first time, a rich fine structure due to $d \rightarrow f$ transition of Tm^{3+} doped LiCAF, LiSAF, and BaY_2F_8 (BYF) crystals is exhibited in high resolution emission spectra measured at our setup. While in LiCAF and LiSAF only the spin-forbidden transition has been observed, both components are exhibited in BYF in agreement with earlier results. The energies of the peak maxima are compared with the predicted values from the literature, and a general agreement is confirmed within the given error boundaries. The observed fine structure agrees well with measurements of LiCAF:Tm,Mn under fluorine excimer laser excitation performed at the *Debye Institute, Universiteit Utrecht, Netherlands*.

Significant differences, on the other hand, have been observed when comparing the fine structure of LiCAF and LiSAF. While in LiSAF only six distinct peaks occurred, the $d \rightarrow f$ emission in LiCAF exhibits clearly more structure. Considering the number of identified Stark levels in the applicable local surroundings, occupation of more than one lattice site is suggested. This is further supported by comparison of the fine structure in our experimental excitation spectra with that resulting from theoretical calculations, provided by courtesy of M.F. Reid, *University of Canterbury, New Zealand*. Even though the spectra agree in general, the measurements appeared to be clearly more structured, which has been attributed to the reduced symmetry in the real crystals.

The laser excited $f \rightarrow f$ emission of the isolated $^1G_4 \rightarrow {}^3H_6$ transition in LiCAF is the spectrum with the highest energy resolution available (4 cm^{-1}), thus the Stark level splitting of the $^3H_6$ ground state has been established tentatively on this basis. Zero-phonon lines (ZPL) of the observed $f \rightarrow f$ transitions are assigned, having similar energies as those well-studied in LaF_3:Tm^{3+}.

In the analysis of $d \rightarrow f$ and $f \rightarrow f$ transitions having the same final state, the respective spectra are shifted in such a way that the zero-phonon lines of all transitions are aligned.

However, unlike in $LiYF_4$:Er^{3+}, differences have been observed in the fine structure due to transitions to the Stark levels of the ground state, several lines had no corresponding peaks. Difficulties arise from the large number of Stark levels expected in low-symmetry surroundings, which causes a splitting into the maximum of 13 sub-levels. Furthermore, more than one site are expected to be occupied in LiCAF. Among the rare earth ions Tm^{3+} is subject to strong electron-phonon coupling, and for each transition varying coupling strengths are qualitatively observed. Thus, an assignment of intra-configurational $d \rightarrow f$ transitions to individual Stark levels has been skipped.

The supplementary measurements of LiCAF:Tm^{3+} excimer laser excitation have been motivated and was mandatory due to the fact, that SR excitation of $f \rightarrow f$ emission yielded significant intensity *only* when exciting within the $F^- \rightarrow Tm^{3+}$ charge transfer (CT) state established in this work. This is especially painful since comparing the SR and laser excited $f \rightarrow f$ emission spectra exhibited drastic differences, and excimer laser excitation is restraint to a few specific wavelengths. Consequently, the CT excited emission spectra have been remeasured at our setup, while the initial measurements were only confirmed. A feasible explanation is given in terms of more than one substitutional lattice sites in LiCAF, namely the Ca^{2+} and Al^{3+} site, which are differently excited via the $5d$ and the CT states.

Mn^{2+} doped fluoride crystals

Initially, LiCAF and LiSAF crystals doped with Mn^{2+} have been investigated. Emission has been observed due to the lowest intra-configuration $3d^5 \rightarrow 3d^5$ transition, along with the corresponding $d \rightarrow d$ excitation spectra. In the VUV spectral region, several excitation bands have been observed at low and room temperature. From absorption measurements the oscillator strengths associated with these bands are determined being of the order 10^{-4}, and a clear temperature dependence confirmed the partially allowed nature.

While the UV and VUV bands of rare earth ions in crystals have been investigated extensively in the last decades, little attention has been paid to this spectral region concerning transition metal ions. Earlier investigations on various transition metals ascribed the VUV absorption bands to $3d^n \rightarrow 3d^{n-1}4s$ transitions, mainly based on absorption measurements.

Hence, a systematic investigation of Mn^{2+} has been carried out in crystal hosts such as LiCAF, LiSAF, $BaMgF_4$, $KMgF_3$, MgF_2, and BaY_2F_8.

From $d \rightarrow d$ excitation spectra, the crystal field splitting ($10Dq$) and the Racah parameters have been determined using the Tanabe-Sugano diagram for d^5 elements. A brute force fitting algorithm has been written for accurate computation of the parameters, successfully tested with the well-studied CaF_2:Mn^{2+} crystal.

The ground state of Mn^{2+} in crystals is known to split into a doubly and triply degenerate sub-level in octahedral symmetry. The energy difference corresponds to $10Dq$, being also

observed in the $d \rightarrow d$ excitation spectra. The energy differences of two excitation peaks due to $3d^5 \rightarrow 3d^4 4s$ transitions is in striking agreement in all samples with the corresponding values $10Dq$.

Thus, theoretical calculations of $3d^5 \rightarrow 3d^4 4s$ transitions would be a rewarding subject, since oscillator strengths as well as energy positions have been determined experimentally with high confidence.

Co-doped crystals and outlook

Concerning the proposed intra-ionic energy transfer via the $5d$ state in Tm^{3+} it can be concluded that the main problem is based on the low doping concentrations achieved in the crystals. A much better result should be achieved under improved crystal growth conditions, which holds true especially for the $LiSrAlF_6$ (LiSAF) samples. The $5d$ and $4s$ states of Tm^{3+} and Mn^{2+} ions overlap in the VUV, which may impose additional energy transfer between these states. Further investigation concerning the branching ratios would be required to allow definite conclusions.

For extended analysis, a series of Tm^{3+} and Mn^{2+} co-doped BaY_2F_8 (BYF) samples have been bought. However, a severe disagreement between the nominal and experimental doping concentrations has been observed, e.g., Mn^{2+} was only detected within an inclusion in the very recent trace analysis of the crystals. Therefore, selected results are presented in the Appendix for future reference, while a comprehensive discussion has been omitted.

Nevertheless, interesting excitation spectra have been observed, which may point to cross relaxation processes in this material. A second attempt to grow BYF single crystals co-doped with Tm^{3+} and Mn^{2+} is strongly suggested, and the resulting crystals can be investigated readily at our setup.

Concerning the design of novel luminescent materials, the desired initial situation would be the Al^{3+} site occupied with one type of ion and the Ca^{2+} or Sr^{2+} site with another one. This setting has been concluded for LiSAF:Tm^{3+}, Mn^{2+} as a result of this work, since Tm^{3+} clearly prefers the Al^{3+} site and Mn^{2+} is situated on the Sr^{2+} site. This is contradictory to the initial expectation one might have, considering size and valence of the ions. If a higher doping concentration of a few percent (as initially targeted) can be achieved for LiSAF, the investigation of the co-doped sample in terms of $Tm^{3+} \rightarrow Mn^{2+}$ energy transfer would be definitely worthwhile. Charge compensation is not required in this setting.

Thus, LiSAF co-doped with transition metal and rare earth ions enables a great number of novel materials with prospective energy transfer capability. While the rare earth ions in many hosts have been investigated in the VUV spectral region extensively in the past decades, research on transition metal ions in the VUV has been neglected. This includes experimental and theoretical analysis of the $3d^{n-1}4s$ (and $3d^{n-1}4p$) energy levels as well as intra- and inter-ionic energy transfer processes.

The search for phosphors exhibiting efficient down conversion (quantum cutting) has to be concluded with this insight into a wide range of fluoride crystal hosts, such as $LiCaAlF_6$, with rare earth and transition metal ion impurities. In view of the similar large variety of limitations concerning energy transfer efficiencies, it is definitely a challenging task to find an appropriate compound concerning the desired process of quantum cutting . BaY_2F_8 and $LiSrAlF_6$ are considered to be promising candidates concerning energy transfer capabilities, and doping with Tm^{3+} and Mn^{2+} or similar combinations of ions are expected to yield inter-ionic energy transfer in the VUV, for example via cross relaxation.

Appendix A

Spectroscopy of BYF:Tm, Mn

Excitation spectra of several BaY_2F_8 (BYF) crystals singly doped with Mn^{2+} and co-doped with Tm^{3+}, Mn^{2+} have been measured in this work. However, the quantitative micro probe analysis (Section 3.1.3) and the nominal doping concentrations disagree strongly. Therefore, further investigations would be required to discuss reliably the interesting excitation features.

The following discussion should be regarded as supplementary information to the spectra in order to facilitate future efforts.

Figure A.1 shows excitation spectra of various BYF crystals singly doped with Mn^{2+} and co-doped with Tm^{3+}, Mn^{2+}. The emission monitored is due to the transition of Mn^{2+} incorporated into two lattice sites, while the emission around 525 nm is attributed to the large Ba^{2+} site, and the emission around 620 nm to the Y^{3+} site.

The investigated samples are $Ba\,(Y_{0.94}Mn_{0.05}Tm_{0.01})_2\,F_8$ (N6), $Ba\,(Y_{0.99}Mn_{0.01})_2\,F_{7.98}$ (N5), $(Ba_{0.99}Mn_{0.01})\,Y_2F_8$ (N4), $Ba_{0.95}Mn_{0.05}\,(Y_{0.99}Tm_{0.01})_2\,F_8$ (N3) according to the source.

The excitonic excitation is indicated around 85 000 cm^{-1} (c). In this region, the spectra at low temperature exhibit strong excitation of the 525 nm emission, while at RT the respective excitation curves have their intensity strongly decreasing. In the region at energies below the excitonic peak, strong excitation of Mn^{2+} on both lattice sites is observed. The spectra recorded when monitoring 525 nm emission are anti-correlated to those monitoring 620 nm emission. The 525 nm emission is reabsorbed by the lowest d-state of Mn^{2+} and subsequently emitted as 620 nm photons, thus the excitation of the 620 nm emission (Y^{3+} substitutional site) inadvertly monitors 525 nm as well (Ba^{2+}). Hence, the excitation of the 620 nm is not further discussed at this point.

While these spectra are similar to the excitation of several fluorides discussed in this work (cf. Section 5.5), there are significant differences. First of all, the *pure* excitation of the 525 nm emission exhibits 5 distinct excitation bands in the region, where $3d^5 \rightarrow 3d^4 4s$ transitions are expected. In the fluoride samples investigated in this work, only two sub-band (E_2, E_3) associated with $d \rightarrow s$ transitions ${}^6S \rightarrow {}^6D$ have been observed (cf. Section 5.6). For LiCAF

and LiSAF the band E_2 was further splitted into sub-bands $E_1$and E_2 due to the reduced local symmetry of the substitutional lattice site (C_{3i}). The corresponding excitation spectra of Mn^{2+} on the Ba^{2+} lattice site in $BaMgF_4$ are not advantageous for comparison, since this site has a regular six-fold coordination.

The BYF crystal structure and lattice sites are briefly discussed in Section 3.2.2. The Ba^{2+} site is BYF has a high coordination number and a low local symmetry. This may explain the observed excitation bands: the Mn^{2+} ($3d^5$) ground state is splitted into five non-degenerate sub-levels due to the reduced symmetry, which are the initial states responsible for the observed transitions.

Excitation spectra of various transitions of Tm^{3+} in BaY_2F_8 at 8 K are shown in Figure A.2. Figure A.2 (c) shows $d \rightarrow f$ excitation spectra of samples N3, N5, N6, monitoring 171 nm emission, coinciding in all samples. The most intense band is peaking at 63 450 cm^{-1}.

Comparing the excitation spectra of 348 nm emission of the different sample (a), (b), (d), and (e) shows a strong and broad band peaking around 77 000 cm^{-1} (130 nm) in agreement in all spectra. This band is tentatively assigned to the $F^- \rightarrow Tm^{3+}$ charge transfer (CT) transition, very similar to that determined in LiCAF and LiSAF.

Obviously, $f \rightarrow f$ emission monitored at 456 nm (d) is excited via a radiative cascade after excitation within the $5d$ states down to 70 000 cm^{-1}, which has been observed similarly under laser excitation in LiCAF:Tm,Mn (Chapter 6). The 350 nm emission of this sample (N3) if excited in the same way, exhibiting four excitation peaks. The one around 77 000 cm^{-1} is attributed tentatively to CT excitation. The two bands at lower energy do not coincide with the $d \rightarrow f$ emission peaks (c). For unknown reasons, the $d \rightarrow f$ emission corresponding to this sample (N3) is also deviation from the usual ones.

Most interesting is the enhanced excitation of the Mn^{2+} emission (525 nm) along with $f \rightarrow f$ emission of Tm^{3+} (350 nm), observed in curves (a) and (b). Judging by appearance, the most pronounced excitation band around 63 500 cm^{-1} in the respective spectra result from the same energy transfer process, as it is observed in striking coincidence for *both* excitation curves of Tm^{3+} and Mn^{2+} (a) as well as in $d \rightarrow f$ excitation (c). This strongly suggests an energy transfer, e.g. cross relaxation as outlined in Section 1.1, excited via the d-states and resulting in emission of photons in the visible via $f \rightarrow f$ transitions of Tm^{3+} and $d \rightarrow d$ transitions of Mn^{2+}.

However, due to the uncertainties concerning the crystal structure and doping concentration, the results need to be investigated further to allow definite conclusion.

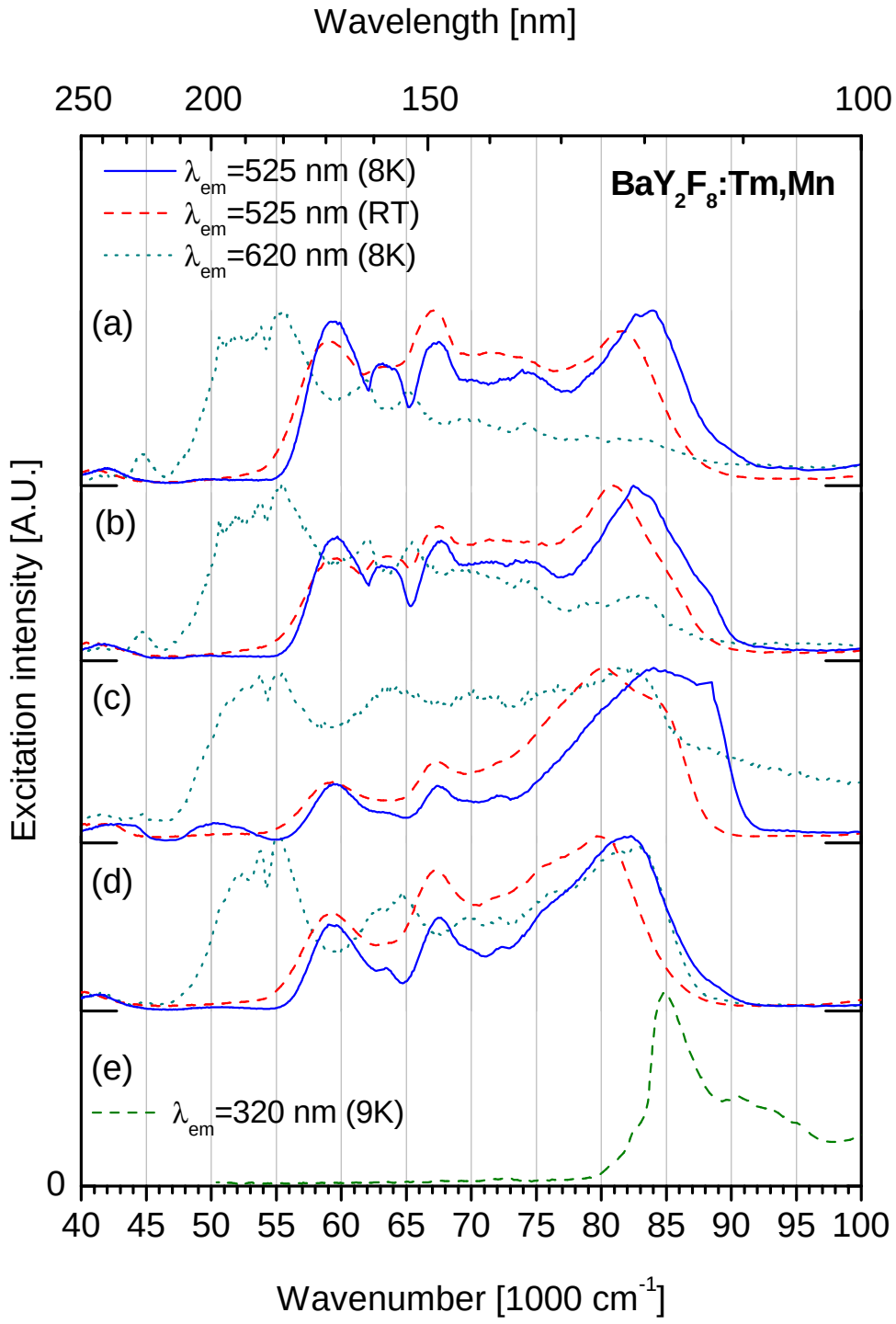

Figure A.1: Excitation spectra of Mn^{2+} and Tm^{3+} doped BYF, (a-d) spectra of samples N6, N5, N4, N3. (—) λ_{em} =525 nm, T =8 K; (---) λ_{em} =525 nm, T =300 K; (∘) λ_{em} =620 nm, T =8 K; (e) BYF:Tm, λ_{em} =320 nm, T =9 K.

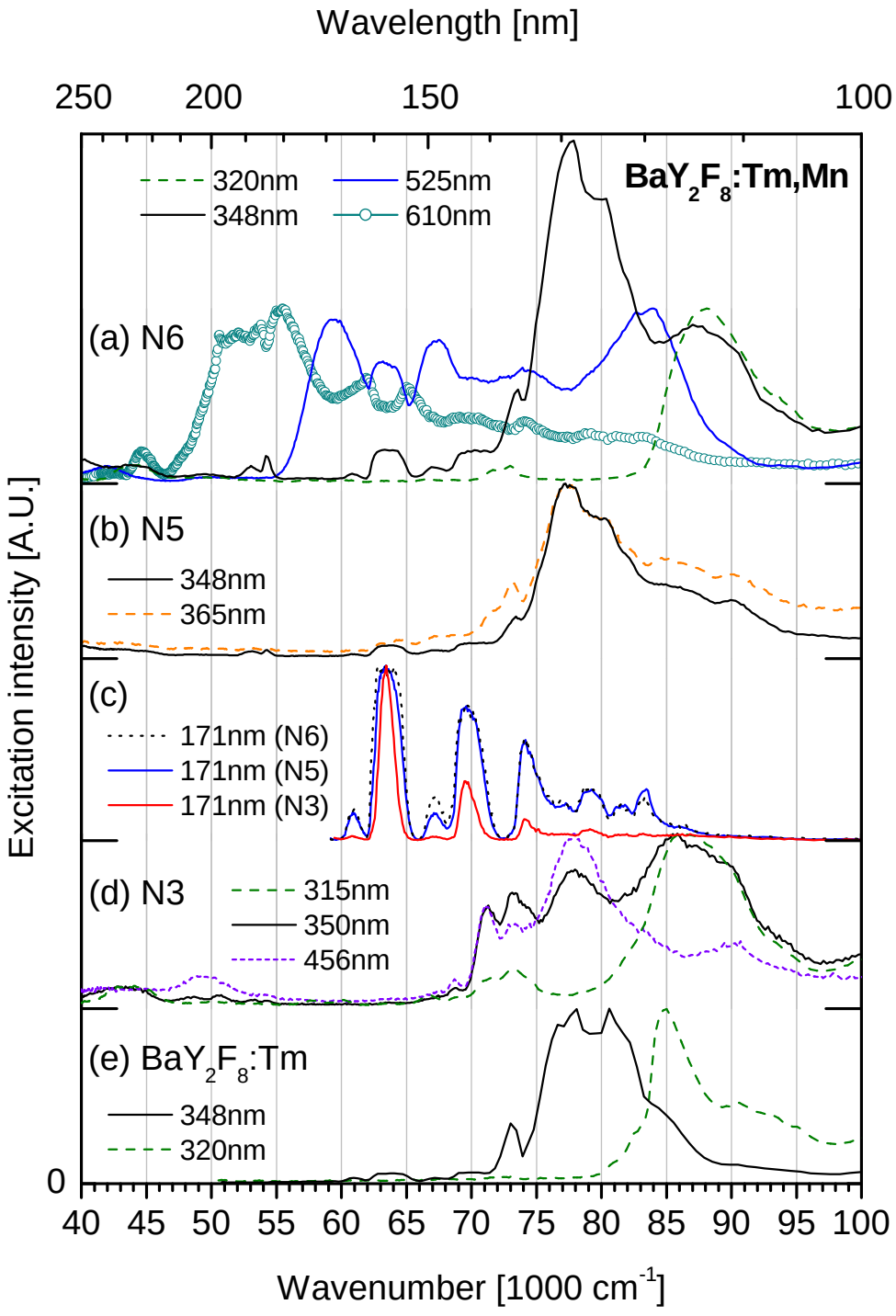

Figure A.2: Excitation spectra of Mn^{2+} and Tm^{3+} doped BaY_2F_8, $T = 8$ K, monitored emission wavelengths are indicated. (a) N6; (b) N5; (d) N3; (e) BYF:Tm; (c) $d \rightarrow f$ excitation spectra for samples N3, N5, N6.

Appendix B

The Periodic Table of Elements

The Periodic Table of Elements shown on the following page is provided for convenience due to the variety of elements discussed.

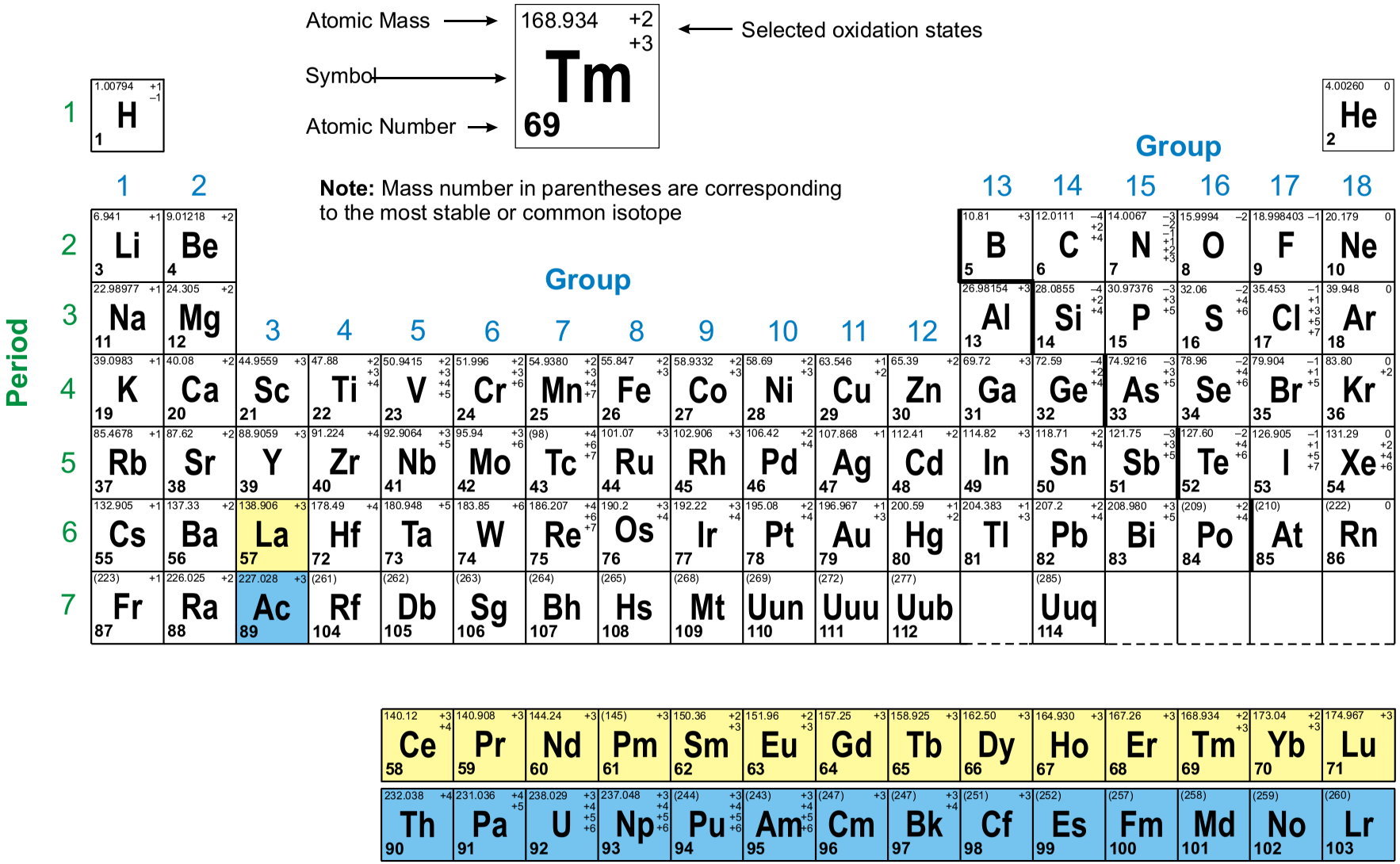
Atomic Mass
Symbol
Atomic Number
168.934 +2 +3
Tm
69
Selected oxidation states
Note: Mass number in parentheses are corresponding to the most stable or common isotope
Group
Period
1 2 3 4 5 6 7 8 9 10 11 12 13 14 15 16 17 18
1 H 1 1.00794 +1 −1
He 2 4.00260 0
2 Li 3 6.941 +1
Be 4 9.01218 +2
B 5 10.81 +3
C 6 12.0111 −4 +2 +4
N 7 14.0067 −3 −2 −1 +1 +2 +3
O 8 15.9994 −2
F 9 18.998403 −1
Ne 10 20.179 0
3 Na 11 22.98977 +1
Mg 12 24.305 +2
Al 13 26.98154 +3
Si 14 28.0855 −4 +2 +4
P 15 30.97376 −3 +3 +5
S 16 32.06 −2 +4 +6
Cl 17 35.453 −1 +1 +3 +5 +7
Ar 18 39.948 0
4 K 19 39.0983 +1
Ca 20 40.08 +2
Sc 21 44.9559 +3
Ti 22 47.88 +2 +3 +4
V 23 50.9415 +2 +3 +4 +5
Cr 24 51.996 +2 +3 +6
Mn 25 54.9380 +2 +3 +4 +7
Fe 26 55.847 +2 +3
Co 27 58.9332 +2 +3
Ni 28 58.69 +2 +3
Cu 29 63.546 +1 +2
Zn 30 65.39 +2
Ga 31 69.72 +3
Ge 32 72.59 −4 +2 +4
As 33 74.9216 −3 +3 +5
Se 34 78.96 −2 +4 +6
Br 35 79.904 −1 +1 +5
Kr 36 83.80 0 +2
5 Rb 37 85.4678 +1
Sr 38 87.62 +2
Y 39 88.9059 +3
Zr 40 91.224 +4
Nb 41 92.9064 +3 +5
Mo 42 95.94 +3 +6
Tc 43 (98) +4 +6 +7
Ru 44 101.07 +3
Rh 45 102.906 +3
Pd 46 106.42 +2 +4
Ag 47 107.868 +1
Cd 48 112.41 +2
In 49 114.82 +3
Sn 50 118.71 +2 +4
Sb 51 121.75 −3 +3 +5
Te 52 127.60 −2 +4 +6
I 53 126.905 −1 +1 +5 +7
Xe 54 131.29 0 +2 +4 +6
6 Cs 55 132.905 +1
Ba 56 137.33 +2
La 57 138.906 +3
Hf 72 178.49 +4
Ta 73 180.948 +5
W 74 183.85 +6
Re 75 186.207 +4 +6 +7
Os 76 190.2 +3 +4
Ir 77 192.22 +3 +4
Pt 78 195.08 +2 +4
Au 79 196.967 +1 +3
Hg 80 200.59 +1 +2
Tl 81 204.383 +1 +3
Pb 82 207.2 +2 +4
Bi 83 208.980 +3 +5
Po 84 (209) +2 +4
At 85 (210)
Rn 86 (222) 0
7 Fr 87 (223) +1
Ra 88 226.025 +2
Ac 89 227.028 +3
Rf 104 (261)
Db 105 (262)
Sg 106 (263)
Bh 107 (264)
Hs 108 (265)
Mt 109 (268)
Uun 110 (269)
Uuu 111 (272)
Uub 112 (277)
Uuq 114 (285)
Ce 58 140.12 +3 +4
Pr 59 140.908 +3
Nd 60 144.24 +3
Pm 61 (145) +3
Sm 62 150.36 +2 +3
Eu 63 151.96 +2 +3
Gd 64 157.25 +3
Tb 65 158.925 +3
Dy 66 162.50 +3
Ho 67 164.930 +3
Er 68 167.26 +3
Tm 69 168.934 +2 +3
Yb 70 173.04 +2 +3
Lu 71 174.967 +3
Th 90 232.038 +4
Pa 91 231.036 +4 +5
U 92 238.029 +3 +4 +5 +6
Np 93 237.048 +3 +4 +5 +6
Pu 94 (244) +3 +4 +5 +6
Am 95 (243) +3 +4 +5 +6
Cm 96 (247) +3
Bk 97 (247) +3 +4
Cf 98 (251) +3
Es 99 (252)
Fm 100 (257)
Md 101 (258)
No 102 (259)
Lr 103 (260)

Appendix C

Abbreviations

Abbreviation	Description
BMF	$BaMgF_4$
BYF	BaY_2F_8
CCD	Charge Coupled Device
CFD	Constant-Fraction Discriminator
CRI	Color Rendering Index
CRT	Cathode Ray Tube
CT	Charge Transfer
CTH:YAG	Cr^{3+}, Tm^{3+}, Ho^{3+}:YAG
CTS	Charge Transfer State
DESY	Deutsches Elektronen-Synchrotron
FWHM	Full Width at Half Maximum
HASYLAB	Hamburger Synchrotronstrahlungs-Labor
IR	Infra-Red
IUPAC	International Union of Pure and Applied Chemistry
KMF	$KMgF_3$
λ_{em}	Emission wavelength or energy
$\Delta\lambda_{em}$	Spectral resolution in emission
λ_{ex}	Excitation wavelength or energy
$\Delta\lambda_{ex}$	Spectral resolution in excitation
LASER	Light Amplification by Stimulated Emission of Radiation
LCD	Liquid Crystal Display
LiCAF	$LiCaAlF_6$
LiSAF	$LiSrAlF_6$
MCP	Multi-Channel Plate
MSP	Micro-Sphere Plate
OLED	Organic Light Emitting Diode

Abbreviation	Description
PDP	Plasma Display Panels
PMT	Photo-Multiplier Tube
RE	Rare Earth
RMS	Root Mean Square
RT	Room Temperature
SR	Synchrotron Radiation
STE	Self-Trapped Exciton
Superlumi	Our experimental station at HASYLAB, DESY, Germany
T	Temperature
τ_c	Counting time
TAC	Time-to-Amplitude Converter
TCSPC	Time-Correlated Single Photon Counting
UHV	Ultra-High Vacuum
UV	Ultra-Violet
VUV	Vacuum-Ultra-Violet ($\lambda < 200$ nm)
YAG	$Y_3Al_5O_{12}$
YSGG	$Y_3Sc_{2.5}Ga_{2.5}O_{12}$
ZPL	Zero-Phonon Line

Appendix D

Ionic radii and weights

Shannon *ionic radii and weights* of selected elements [WIN04, HUH93, SHA76, SHA69] are shown for four-fold (tetrahedral T_d), six-fold (octahedral O_h), and eight-fold coordination. Tabulated is the effective ionic radius for fluorides assuming the ionic radius of fluorine $r(F^-) = 1.33\,\text{Å}$ and oxide $r(O^{2-}) = 1.40\,\text{Å}$, depending on the coordination number an the spin-state for transition metals. The older Shannon crystal radii are based on $r(F^-) = 1.19\,\text{Å}$ in six-fold coordination and are 14-18% larger than the effective ionic radii.

Z denotes the atomic number, and the atomic weight is given as ratio of the average mass per atom of the element to $\frac{1}{12}$ of the mass of ^{12}C in its ground state.

Ion	Z	Atomic weight	Shannon ionic radius [pm]		
			4-coord.	6-coord.	8-coord.
Al^{3+}	13	26.981538(2)	53	67.5	-
Ba^{2+}	56	137.327(7)	-	149	156
Ca^{2+}	20	40.078(4)	-	114	126
Ce^{3+}	58	140.116(1)	-	115	128.3
Ce^{4+}	58	140.116(1)	-	101	111
Cr^{3+}	24	51.9961(6)	-	75.5	-
Cs^{+}	55	132.90545(2)	-	181	188
Dy^{3+}	66	162.500(1)	-	105.2	116.7
Er^{3+}	68	167.259(3)	-	103.0	114.4
Eu^{2+}	63	151.964(1)	-	131	139
Eu^{3+}	63	151.964	-	108.7	120.6
F^{-}	9	18.9984032(5)	117	119	-
Ga^{3+}	31	69.723	-	76.0	-
Gd^{3+}	64	157.25	-	107.8	119.3
Ho^{3+}	67	164.93032(2)	-	104.1	115.5
K^{+}	19	39.0983(1)	151	152	165
La^{3+}	57	138.9055(2)	-	117.2	130.0
Li^{+}	3	6.941(2)	73.0	90	106
Lu^{3+}	71	174.967(1)	-	100.1	111.7
Mg^{2+}	12	24.3050(6)	71	86.0	103
Mn^{2+}	25	54.9380	80	81	110
Nd^{3+}	60	144.24(3)	-	112.3	124.9
Pm^{3+}	61	145	-	111	123.3
Pr^{3+}	59	140.90765(2)	-	113	126.6
Pr^{4+}	59	140.9076	-	99	110
Rb^{+}	37	85.4678(3)	-	166	175
Sm^{2+}	62	150.36(3)	-	-	141
Sm^{3+}	62	150.36(3)	-	109.8	121.9
Sr^{2+}	38	87.62(1)	-	132	140
Tb^{3+}	65	158.92534(2)		106.3	118.0
Tm^{2+}	69	168.93421(2)	-	117	
Tm^{3+}	69	168.93421(2)	-	102.0	113.4
Yb^{2+}	70	173.04(3)	-	116	128
Yb^{3+}	70	173.04	-	100.8	112.5
Y^{3+}	39	88.90585(2)	-	104.0	115.9

Appendix E

Peak energies of LiCAF:Tm^{3+}

Experimental emission peak energies (and the corresponding FWHM) of Tm^{3+} in LiCAF are tabulated below. The corresponding spectra are discussed in detail in Section 4.5. The FWHM is calculated from Lorentzian curves fitted to the spectra. ΔE is the energy difference within a multiplet of each transitions to its first ZPL. Energies are denoted in cm^{-1}, values in *italic* correspond to weak peaks or shoulders in the spectra.

The zero-phonon transition energies of Tm^{3+} (and of all other rare earth ions) in LaF_3 have been well-studied [CAR88, CAR89] and are given for comparison. In several spectra, replica of zero-phonon lines have been observed due to a strong local vibronic mode $\nu_{vib} = 395$ cm^{-1}. The replica are denoted, e.g., by A_0' corresponding to A_0. Only clearly observed peaks of significant intensity have been tabulated.

		E (FWHM)	ΔE	LaF_3
$^1I_6 \rightarrow {}^3H_6$	A_0	34 795 (32)	0	34 769
	A_1	34 698 (35)	97	
	A_2	34 638	157	
	A_3	34 570	225	
	A_4	34 480	315	
	A'_0	34 400	$\nu_{vib} - 5$	
	A'_1	34 317	$\nu_{vib} + 83$	
$^1I_6 \rightarrow {}^3F_4$	B_0	29 155 (28)	*0*	29 154
	B_1	*29 070*	85	
	B_2	28 943	212	
	B_3	28 819 (61)	336	
	B'_0	28 744	$\nu_{vib} - 5$	
$^1D_2 \rightarrow {}^3H_6$	C_0	28 033 (23)	0	28 021
	C_5	27 909	124	
$^1I_6 \rightarrow {}^3H_5$	D_0	26 469	0	26 464
	D_1	26 385	84	
	D_2	26 325	144	
	D_3	26 260	209	
$^1D_2 \rightarrow {}^3F_4$	E_0	22 430	0	22 406
	E_2	22 346	84	
	E_3	22 316	114	
	E_4	22 287	143	
	E_5	22 262	168	
	E_6	22 217	212	
	E'_0	22 036	$\nu_{vib} - 1$	
	E''_0	21 642	$2 \cdot \nu_{vib}$-2	
$^1I_6 \rightarrow {}^3H_4$	F_0	22 002 (9)	0	22 208
	F_1	21 980 (4)	22	
	F_3	21 940 (11)	62	
	F_4	21 918 (9)	84	
	F_7	21 767	235	
	F'_0	21 607 (13)	ν_{vib}	
	F'_1	21 585 (16)	$\nu_{vib} + 22$	
	F'_3	21 542 (9)	$\nu_{vib} + 65$	
	F'_7	21 464	$\nu_{vib} + 143$	
$^1G_4 \rightarrow {}^3H_6$	G_0	21 076 (2.6)	0	21 037
	G_1	21 034 (2.1)	42	
	G_2	21 022 (3.5)	54	
	G_3	21 010 (3.4)	66	

		E (FWHM)	ΔE	LaF_3
	G_4	20 998 (3.6)	78	
	G_5	20 950 (22)	126	
	G_6	20 884 (18)	192	
	G_7	20 860	216	
	G_8	20 837 (11)	239	
	G_9	20 796	280	
	G_{10}	20 773	303	
	G_{11}	20 721	355	
	G'_0	20 680	$\nu_{vib}+1$	
	G'_5	20 570	$\nu_{vib}+111$	
$^1I_6 \rightarrow {}^3F_3$		20 289 (95)		20 261
$^1D_2 \rightarrow {}^3H_5$	H_0	19 720	0	19 716
	H_1	19 681	39	
	H_2	19 658	62	
	H_3	19 600	120	
$^1D_2 \rightarrow {}^3H_4$	J_0	15 405 (4)	0	15 460
	J_1	15 382 (5)	23	
	J_2	15 365 (3)	40	
	J_3	15 341 (3)	64	
	J_4	15 318 (6)	87	
	J_5	*15 293*	*112*	
	J_6	15 254 (6)	151	
	J_7	15 159 (6)	246	
	J'_0	15 007 (4)	ν_{vib}+3	
	J'_1	14 988 (9)	ν_{vib}+22	
	J'_2	*14 968*	ν_{vib}+*42*	
	J'_3	14 948 (7)	ν_{vib}+59	
	J'_4	14 924 (4)	ν_{vib}+86	
	J'_5	14 903 (10)	ν_{vib}+107	
	J'_6	14 857	ν_{vib}+153	
	J'_7	14 672	ν_{vib}+338	
$d \rightarrow f$ ($^3F_4$)	Y_0	55 797	0	
	Y_1	55 766	31	
	Y_2	55 377	420	
	Y_3	55 346	451	
$d \rightarrow f$ ($^3H_6$)	Z_0	61 410	0	
	Z_1	61 342	68	
	Z_2	61 170	240	
	Z_3	61 140	270	

	E (FWHM)	ΔE	LaF_3
Z_4	61 072	338	
Z_5	61 050	360	
Z_6	61 013	397	
Z_7	60 976	434	
Z_8	60 938	472	
Z_9	60 850	560	
Z_{10}	60 790	630	
Z_{11}	60 716	704	

Bibliography

[ABD01] R.Yu. Abdulsabirov, M.A. Dubinskii, S.L. Korableva, A.K. Naumov, V.V. Semashkov, V.G. Stepanov, M.S. Zhuchkov. *Crystal growth, EPR and site-selective laser spectroscopy of Gd^{3+}-activated $LiCaAlF_6$ single crystals.* J. Lumin. **94-95** (2001) 113.

[ALO81] P.J. Alonso, R. Alcalá. *Excitation Spectra and Fluorescent Lifetime Measurements of Mn^{2+} in CaF_2 and CdF_2.* J. Lumin. **22** (1981) 321.

[AMA03] J.B. Amaral, D.F. Plant, M.E.G. Valerio, R.A. Jackson. *Computer modelling of defect structure and rare earth doping in $LiCaAlF_6$ and $LiSrAlF_6$.* J. Phys.: Condens. Matter **15** (2003) 2523.

[AMA04] J.B. Amaral, M.E.G. Valerio, M.A. Couto dos Santos, R.A. Jackson. *Defect simulation and crystal field studies of Ln^{3+}:$LiCaAlF_6$ and $LiSrAlF_6$.* Nucl. Instrum. Methods **218** (2004) 232.

[ANT97] I.I. Antonova, I.N. Nizamutdinov, R.Yu. Abdulsabirov, S.L. Korableva, N.M. Khasanova, A.A. Galeev, V.G. Stepanov, N.M. Nizamutdinov. *EPR of Gd^{3+} in Single Crystal Colquiriite and Analysis of the Spin Hamiltonian Tensors B_4 and B_6.* Appl. Magn. Res. **13** (1997) 3.

[ARM89a] G. Armagan, B. Di Bartolo, A. M. Buonchristiani. *Spectroscopic investigation of Cr to Tm energy transfer in yttrium aluminum garnet crystals.* J. Lumin. **44** (1989) 129.

[ARM89b] G. Armagan, B. Di Bartolo, A. M. Buonchristiani. *Kinetics and microscopic interaction parameters of Cr to Tm energy transfer in yttrium aluminum garnet crystals.* J. Lumin. **44** (1989) 141.

[BAG74] R.K. Bagai, R.K. Jain, A.V.R. Warrier. *Optical Properties of LiF:Mn.* J. Phys. C: Solid State Phys. **7** (1974) 1219.

[BAG76] R.K. Bagai, A.V.R. Warrier. *Ultraviolet Absorption Spectrum of CaF_2:Mn^{2+}.* Phys. Stat. Sol. (b) **73** (1976) K123.

[BAR70] T. L. Barry. J. Electrochem. Soc. **117** (1970) 381.

[BAS96] T.T. Basiev, Yu.V. Orlovskii, K.K. Pukhov, V.B. Sigachev, M.E. Doroshenko, I.N. Vorob'ev. *Multiphonon relaxation rates measurements and theoretical calculations in the frame of non-linear and non-Coulomb model of a rare-earth ion-ligand interaction.* J. Lumin. **68** (1996) 241.

[BAT02] L.E. Batay, A.A. Demidovich, A.N. Kuzmin, A.N. Titov, M. Mond, S. Kück. *Efficient tunable laser operation of diode-pumped Yb,Tm:KY$(WO_4)_2$ around 1.9 μm.* Appl. Phys. **B 75** (2002) 457.

[BEC92] T. Becker. *Einfluss interionischer Wechselwirkung auf die Effizienz und das dynamische Verhalten von Cr,Tm:YAG- und Cr,Tm,Ho:YAG-Lasern.* Dissertation, Universität Hamburg, Germany (1992).

[BEC98a] J. Becker. *Lumineszenzspektroskopische Untersuchung der intrinsischen Emissionen von BaF_2 und der Energietransfer-Prozesse in BaF_2:Dy.* Dissertation, Universität Hamburg, Germany (1998).

[BEC98b] J. Becker, J.Y. Gesland, N.Yu. Kirikova, J.C. Krupa, V.N. Makhov, M. Runne, M. Queffelec, T.V. Uvarova, G. Zimmerer. *VUV Emission of Er^{3+} and Tm^{3+} in Fluoride Crystals.* J. Lumin. **78** (1998) 91.

[BEL91] R.F. Belt, R. Uhrin. J. Cryst. Growth **109** (1991) 340.

[BEL99] A.N. Belsky, J.C. Krupa. *Luminescence Excitation Mechanisms of Rare Earth Doped Phosphors in the VUV Range.* Displays **19** (1999) 185.

[BIC95] K. Bickelmann. *Untersuchungen zur Effizienz eines CTH:YAG-Lasers und deren Umsetzung in ein mobiles Lasersystem für den medizinischen Einsatz.* Diploma thesis, Universität Kiel (1995).

[BLA92] G. Blasse. lnt. Rev. Phys. Chem. **11** (1992) 71.

[BLA94] G. Blasse, B.C. Grabmaier. *Luminescent Materials.* Springer Verlag, Berlin, Germany (1994).

[BOL61] L.M Bollinger, G.E. Thomas. *Measurement of the time dependence of scintillation intensity by a delayed coincidence method.* Rev. Sci. Instrum. **32** (1961) 1044.

[BOR27] M. Born, J.R. Oppenheimer. Ann. d. Physik **84** (1927) 457.

[BRA00] A. Braud, S. Girard, J.L. Doualan, M. Thuau, R. Moncorgé, A.M. Tkachuck. *Energy-transfer processes in Yb:Tm-doped KY_3F_{10}, $LiYF_4$, and BaY_2F_8 single crystal for laser operation at 1.5 and 2.3 μm.* Phys. Rev. **B 61** (2000) 5280.

[BRA01] A. Braud, P.Y. Tigréat, J.L. Doualan, R. Moncorgé. *Spectroscopy and CW operation of a 1.85 mm Tm:KY_3F_{10} laser.* Appl. Phys. B **72** (2001) 909.

[BRO67] Jr. J.J. Brown. J. Electrochem. Soc. **114** (1967) 245.

[BUR62] G. Burns. *Shielding and Crystal Fields at Rare-Earth Ions.* Phys. Rev. **128** (1962) 2121.

[BUS76] W. Busse, H.E. Gumlich, B. Meissmer, D. Theis. J. Lumin. **12/13** (1976) 693.

[BYE69] W. Byers et al. *The Charge-Transfer Spectra of Pyridine n-Oxide Metal Complexes. Determination of Optical Electronegativities.* J. Am. Chem. Soc. **91** (1969) 1329.

[CAI75] J.A. Caird, L.G. DeShazer, J. Nella. *Characteristics of room-temperature 2.3- m laser emission from Tm^{3+} in YAG and $YAlO_3$.* IEEE J. Quantum Electr. **11** (1975) 874.

[CAL03] G. U Caldiño. *Energy transfer in CaF_2 doped with Ce^{3+}, Eu^{2+} and Mn^{2+} ions.* J. Phys.: Condens. Matter **15** (2003) 7127.

[CAM00] A. F. Campos, A. Meijerink, C. de Mello Donegá, O. L. Malta. *A theoretical calculation of vibronic coupling strength: the trend in the lanthanide ion series and the host-lattice dependence.* J. Phys. Chem. Solids **61** (2000) 1489.

[CAR23] G. Carlo, J. Franck. Z. Phys. **17** (1923) 202.

[CAR70] W.T. Carnall, P.R. Fields, J. Morrison, R. Sarup. *Absorption Spectrum of Tm^{3+}:LaF_3.* J. Chem. Phys. **52** (1970) 4054.

[CAR83] W.T. Carnall, H. Crosswhite. *Further interpretation of the spectra of Pr^{3+}-LaF_3 and Tm^{3+}-LaF_3.* J. Less-Common Metals **93** (1983) 127.

[CAR88] W.T. Carnall, G.L. Goodman, K. Rajnak, R.S. Rana. Argonne National Laboratory, Argonne, Illinois, USA (1988) 70.

[CAR89] W. T. Carnall, G. L. Goodman, K. Rajnak, R. S. Rana. *A systematic analysis of the spectra of the lanthanides doped into single crystal LaF_3.* J. Chem. Phys. **90** (1989) 3443.

[CHA76] D.B. Chase, D.S. McClure. *The $3d \rightarrow 4s$ bands of transition metal ions in LiF and NaF.* J. Chem. Phys. **64** (1976) 74.

[CHE71] A.K. Cheetham, B.E.F. Fender, M.J. Cooper. *Defect structure of calcium fluoride containing excess anions: I. Bragg scattering.* J. Phys. **C 4** (1971) 3107.

[CHE03] Y. Chen, M. Kirm, E. Negodin, M. True, S. Vielhauer, G. Zimmerer. *Zero-phonon lines in the d-f luminescence of $LiYF_4$:Er^{3+}.* Phys. Stat. Sol. (b) **240** (2003) R1.

[CHR98] T. Christie, B. Brathwhite, A. Tullach. *Mineral Commodity Report 17: Rare Earths and Related Elements.* New Zealand Mining **24** (1998) 7.

[CLU85] D.S. McClure, C. Pedrini. *Excitons trapped at impurity centers in highly ionic crystals.* Phys. Rev. **B 32** (1985) 8465.

[COR04] F. Cornacchia, D. Parisi, C. Bernardini, A. Toncelli, M. Tonelli. *Efficient, diode-pumped Tm^{3+}:BaY_2F_8 vibronic laser.* Opt. Express **12** (2004) 1982.

[CZO18] J. Czochralski. *Ein neues Verfahren zur Messung der Kristallisations-geschwindigkeit der Metalle.* Z. Phys. Chemie **92** (1918) 219.

[DEN00] V.P. Denks, M.P. Kerikmyae, A.L. Lust, T.I. Savikhina. *Photoluminescence of Concentration Series of CaF_2 : Mn^{2+} Phosphors Excited by VUV Radiation.* Phys. Solid State **42** (2000) 261.

[DEP93] S.W. Depp, W.E. Howard. Sci. Am. **260** (1993) 40.

[DEX53] D.L. Dexter. J. Chem. Phys. **21** (1953) 836.

[DIA99] M. Díaz, F. Lahoz, B. Villacampa, R. Cases, B. Sobolev, R. Alcalá. *Optical Properties of Mn^{2+} Ions in Solid Solutions of Fluorite-Type Crystals.* J. Lumin. **81** (1999) 53.

[DIE68] G.H. Dieke, edited by H.M. Crosswhite, Hannah Crosswhite. *Spectra and Energy Levels of Rare Earth Ions in Crystals.* John Wiley & Sons, USA (1968).

[DIE98] A. Diening, P.E.-A. Möbert, G. Huber. J. Appl. Phys. **84** (1998) 5900.

[DOR00] P. Dorenbos. *The 5d Level Positions of the Trivalent Lanthanides in Inorganic Compounds.* J. Lumin. **91** (2000) 155.

[DOR03a] P. Dorenbos. *Energy of the first $4f^7 \rightarrow 4f^6 5d$ transition of Eu^{2+} in inorganic compounds.* J. Lumin. **104** (2003) 239.

[DOR03b] P. Dorenbos. *Systematic Behaviour in Trivalent Lanthanide Charge Transfer Energies.* J. Phys.: Condens. Matter **15** (2003) 8417.

[DOW96] E. Downing, L. Hesselink, J. Ralston, R. MacFarlane. Science **273** (1996) 1185.

[DUA03] C.K. Duan, M.F. Reid. *A simple model for $f \rightarrow d$ transitions of rare-earth ions in crystals.* J. Solid State Chem. **171** (2003) 299.

[DUB93a] M.A. Dubinski. Laser Phys. **3** (1993) 216.

[DUB93b] M.A. Dubinski. J. Mod. Opt. **40** (1993) 1.

[EHR78] D.J. Ehrlich, P.F. Moulton, R.M. Osgood. Opt. Lett. **4** (1978) 184.

[ELI73] L.R. Elias, Wm.S. Heaps, W.M. Yen. Phys. Rev. **B 8** (1973) 4989.

[ELL96] A. Ellens, S. Schenker, A. Meijerink, G. Blasse. *Vibronic transitions of Tm^{3+} in various lattices.* J. Lumin. **69** (1996) 1.

[ELL97] A. Ellens, S. Schenker, A. Meijerink, G. Blasse. *Vibronic transitions of Tm^{3+} in various lattices. A comparison with Pr^{3+}, Eu^{3+} and Gd^{3+}.* J. Lumin. **72** (1997) 183.

[ELL98] S.R. Elliott. *The Physics and Chemistry of Solids.* John Wiley & Sons (1998).

[ERD72] P. Erdös, J.H. Kang. *Electronic Shielding of Pr^{3+} and Tm^{3+} Ions in Crystals.* Phys. Rev. **B 6** (1972) 3393.

[EST67] L. Esterowitz, J. Noonan, J. Bahler. Appl. Phys. Lett. **10** (1967) 126.

[FAN87] T.Y. Fan, G. Huber, R.L. Byer, P. Mitszcherlich. *Continuous wave operation at 2.1mm of a diode laser pumped, Tm-sensitized Ho:YAG laser at 300K.* Opt. Lett. **12** (1987) 678.

[FAN88] T.Y. Fan, G. Huber, R.L. Byer, P. Mitzscherlich. *Spectroscopy and Diode Laser-Pumped Operation of Tm, Ho:YAG.* IEEE J. Quantum Electr. **24** (1988) 924.

[FAR94] R.A. MacFarlane. J. Phys. IV **4** (1994) C4-289.

[FEL01] C. Feldmann, T. Jüstel, C.R. Ronda, D.U. Wiechert. *Quantum efficiency of down-conversion phosphor $LiGdF_4 : Eu$.* J. Lumin. **92** (2001) 245.

[FER70] J. Ferguson, H.J. Guggenheim. *Electron-Transfer States of Pairs of Unlike Transition-Metal Ions in Perovskite Fluroides.* Phy. Rev. **B 1** (1970) 4223.

[FOE48] T. Förster. Ann. Physik **2** (1948) 55.

[FOE49] T. Förster. Z. Naturforsch. **4a** (1949) 321.

[FOR69] H. Forest, G. Ban. J. Electrochem. Soc. **116** (1969) 474.

[FRA97] R. Francini, U.M. Grassano, L. Landi, A. Scacco, M. D'Elena, M. Nikl, N. Cechova, N. Zema. *Ce^{3+} luminescent centers of different symmetries in $KMgF_3$ single crystals.* Phys. Rev. **B 56** (1997) 15109.

[FRA00] C.A. DiFrancesco, J.B. Hedrick. *Rare Earths Statistics: Survey Open-File Report 01-116.* U. S. Geological Survey, Tucson, AZ (2000).
http://minerals.usgs.gov/minerals/pubs/of01-006/

[FRO98] B. Fromme, U. Brunokowski, E. Kisker. *d-d excitations and interband transitions in MnO: A spin-polarized electron-energy-loss study.* Phys. Rev. **B 58** (1998) 9783.

[GES99] J.Y. Gesland, N.M. Khaidukov, N.Yu. Kirikova, M. Kirm, J.C. Krupa, V.N. Makhov, T.V. Ouvarova, M. Queffelec, G. Zimmerer. *VUV Emission of Stoichiometric Er^{3+}- and Tm^{3+}-Containing Fluoride Crystals.* J. Electron Spec. and Rel. Phenomena **101-103** (1999) 579.

[GEK03] A.V. Gektin, N.V. Shiran, S.V. Neicheva, M.J. Weber, S.E. Derenzo, W.W. Moses. *Energy transfer in $LiCaAlF_6$:Ce^{3+}.* J. Lumin. **102-103** (2003) 460.

[GER94] I. Gérard, J. C. Krupa, E. Simoni, P. Martin. J. Alloys Comp. **207-208** (1994) 120.

[GIN97] F. Gingl. Z. Anorg. *$BaMgF_4$ and $Ba_2Mg_3F_{10}$: New Examples for Structural Relationships between Hydrides and Fluorides.* Allg. Chemie **623** (1997) 705.

[GRE98] N.N. Greenwood, A. Earnshaw. *Manganese, Technetium and Rhenium in Chemistry of the Elements.* Butterworth Heinemann, Oxford, UK (1998).

[GRU89] J.B. Gruber, M. E. Hills, R.M. Macfarlane, C.A. Morrison, G.A. Turner, G.J. Quarles, G.J. Kintz, L. Esterowitz. *Spectra and energy levels of Tm^{3+}:$Y_3Al_5O_{12}$.* Phys. Rev. **B 40** (1989) 9464.

[GRZ04] A. Grzechnik, V. Dmitriev, H. Weber, J. Gesland, S. van Smaalen. *The Crytal Structure of Pressure-Induced $LiSrAlF_6$-II and $LiCaAlF_6$-II.* J. Phys.: Condens. Matter **16** (2004) 1033.

[GUE83] P. Gürtler, E. Roick, G. Zimmerer, M. Pouey. *SUPERLUMI: A high flux spectroscopic device for luminescence measurements.* Nucl. Instr. Methods **208** (1983) 835.

[GUI93] L.H. Guilbert, J.Y. Gesland, A. Bulou, R. Retoux. *Structure and Raman spectroscopy of Czochralski-grown barium yttrium and barium ytterbium fluorides crystals.* Mater. Res. Bull. **28** (1993) 923.

[GUY93] S. Guy, M. F. Joubert, B. Jacquier, M. Bouazaoui. *Excited-state absorption in BaY_2F_8:Nd^{3+}.* Phys. Rev. **B 47** (1993) 11001.

[HAR81] J.G. Harrison, C.C. Lin. *Electronic strucuture of an associated impurity-vacancy defect in ionic crystals: V^{2+} in LiF.* Phys. Rev. **B 24** (1981) 6060.

[HAR] H. Harding. Dissertation, Universität Hamburg.

[HEW69] R.A. Hewes, J.F. Sarver. *Infrared Excitation Processes for the Visible Luminescence of Er^{3+}, Ho^{3+}, and Tm^{3+} in Yb^{3+}-Sensitized Rare-Earth Trifluorides.* Phys. Rev. **182** (1969) 427.

[HEA76] Wm.S. Heaps, L.R. Elias, W.M. Yen. *Vacuum-ultraviolet absorption bands of trivalent lanthanides in LaF_3.* Phys. Rev. **B 13** (1976) 94.

[HED00] J.B. Hedrick. *Metal Prices in the United States through 1998.* U. S. Geological Survey, Tucson, AZ (2000) p. 109-126.
http://minerals.usgs.gov/minerals/pubs/metal_prices/

[HEI95] F. Heine, V. Ostroumov, E. Heumann, T. Jensen, G. Huber, B.T.H. Chai. *Cw Yb,Tm:LiYF$_4$ upconversion laser at 650, 800, and 1500 nm.* OSA Proc. Adv. Solid-State Lasers **24** (1995) 77.

[HEL41] A.M. Hellwege. Ann. Phys. **40** (1941) 529.

[HEL49] K.H. Hellwege. *Elektronen und Strahlung von Atomen in Kristallen.* Ann. Physik **4** (1949) 95-126, 127-135, 136-142, 143-149, 150-160, 357-358.

[HEN83] S.T. Henderson, A.M. Marsden. *A Manual of Lamps and Lighting.* Thorn EMI Lighting Ltd., New York, USA (1983).

[HEN89] B. Henderson, G.F. Imbusch. *Optical Spectroscopy of Inorganic Solids.* Oxford University Press, UK (1989).

[HEN00] M. Henke, G. Huber, S. Kück, K. Rademaker, I. Sokólska. *Investigation of high-energetic transitions in Pr^{3+} and Yb^{2+}- doped fluoride and oxide crystals.* HASYLAB annual report I (2000).

[HER92] T. Hebert, R. Wannemacher, R.M. Macfarlane, W. Lenth. *Blue continuously pumped upconversion lasing in Tm:YLiF$_4$.* Appl. Phys. Lett. **60** (1992) 2592.

[HER01] J.A. Hernández *et al. Red and Green Fluorescence of Mn^{2+} in NaCl.* Opt. Mat. **17** (2001) 491.

[HIR82] S. Hirako, R. Onaka. J. Phys. Soc. Jpn. **51** (1982) 1255.

[HOE95] J. Hölsä, R.-J. Lamminmäki, E. Antic-Fidancev, M. Lemaitre-Blaise, P. Porcher. *Observation and simulation of the energy levels of the trivalent thulium ion in gadolinium oxychloride.* J. Phys.: Condens. Matter **7** (1995) 5127.

[HUB88] G. Huber, E. W. Duczynski, K. Petermann. *Laser Pumping of Ho-, Tm-, Er-Doped Garnet Lasers at Room Temperature.* J. Quantum Electr. **24** (1988) 920.

[HUH93] J.E. Huheey, E.A. Keiter, R.L. Keiter. *Inorganic Chemistry: Principles of Structure and Reactivity.* HarperCollins, New York, USA (1993).

[HUT64] M. T. Hutchings. Solid State Phys. **16** (1964) 227.

[INO65] M. Inokuti, F. Hirayama. J. Chem. Phys. **43** (1965) 1978.

[IVE80] M.V. Iverson, W.A. Sibley. *Optical Properties of $RbMnF_3 : Er^{3+}$.* Phys. Rev. **B 21** (1980) 2522.

[JAC71] I.T. Jacobs, G.D. Jones, K. Zdánský, R.A. Satten. *Electron-Phonon Interaction Effects in the Spectra of Hydrogenated, Deuterated, and Tritiated Crystals of Calcium and Strontium Fluorides Containing Cerium.* Phys. Rev. **B 3** (1971) 2888.

[JAM92] A.M. James, M.P. Lord. *Macmillan's Chemical and Physical Data.* Macmillan, London, UK (1992).

[JOH71] L.F. Johnson, H.J. Guggenheim. Appl. Phys. Lett. **19** (1971) 44.

[JOR62] C.K. Jørgensen. Mol. Phys. **5** (1962) 271.

[JOR70] C.K. Jørgensen. Progr. Inorg. Chem. **12** (1970) 101.

[JOR71] C.K. Jørgensen. *Modern Aspects of Ligand-Field Theory.* North-Holland, Amsterdam (1971).

[JUD62] B.R. Judd. *Optical Absorption Intensities of Rare-Earth Ions.* Phys. Rev. **127** (1962) 750.

[JUE98] T. Jüstel, H. Nikol, C.R. Ronda. Angew. Chem. Int. Ed. **37** (1998) 3084.

[JUE00] T. Hüstel, C. Feldmann, C.R. Ronda. *Leuchtstoffe für aktive Displays.* Physikalische Blätter **56** (2000) 55.

[KAM86] A.A. Kaminskii, S.E. Sarkisov. *Stimulated-Emission Spectroscopy of Pr^{3+} Ions in Monoclinic BaY_2F_8 Fluoride.* Phys. Stat. Sol. (a) **97** (1986) K163.

[KAM90] A.A. Kaminskii, S.E. Sarkisov, F. Below, H.J. Eichler. Opt. Quantum Electron. **22** (1990) S95.

[KAR01] D.N. Karimov, M. Kirm, V. N. Makhov, T.V. Ouvarova, S. Vielhauer, G. Zimmerer. *VUV spectroscopy of a new fluoride system NaF-(Er,Y)F_3.* Opt. Mat. **16** (2001) 437.

[KAY93] G.W.C. Kaye, T.H. Laby. *Tables of physical and chemical constants.* Longman, London, UK, 15th edition (1993).

[KEE86] S.W.S. McKeever, B. Jassemnejad, J.F. Landreth. *Manganese Absorption in $CaF_2 : Mn$.* J. Appl. Phys. **60** (1986) 1124.

[KEV69] E.T. Keve, S.C. Abrahams, J.L. Bernstein. *Crystal structure of pyroelectric Barium Magnesium Fluoride, $BaMnF_4$.* J. Chem. Phys. **51** (1969) 4928.

[KHA00] N.M. Khaidukov, M. Kirm, S.K. Lam, D. Lo, V.N. Makhov, G. Zimmerer. *VUV Spectroscopy of KYF_4 Crystals Doped with Nd^{3+}, Er^{3+} and Tm^{3+}.* Opt. Comm. **184** (2000) 183.

[KHA02] N.M. Khaidukov, N.Yu. Kirikova, M. Kirm, J.C. Krupa , V.N. Makhov, E. Negodin, G. Zimmerer. Proc. of SPIE **4766** (2002) 154.

[KIR02a] M. Kirm, H. Lichtenberg, V.N. Makhov, E. Negodin, T.V. Ouvarova, E. Suljoti, M. True, G. Zimmerer. *Inter- and Intraconfigurational Luminescence of Er^{3+} Ions in BaY_2F_8 under VUV Excitation.* Rad. Effects and Defects in Solids **157** (2002) 911.

[KIR02b] M. Kirm, H. Lichtenberg, E. Negodin, E. Suljoti, M. True, S. Vielhauer, G. Zimmerer. HASYLAB annual report I (2002) 449.

[KIR04] M. Kirm, M. True, S. Vielhauer, G. Zimmerer, N.V. Shiran, I. Shpinkov, D. Spassky, K. Shimamura, N. Ichinose. *VUV spectroscopy of pure $LiCaAlF_6$ crystals.* Nucl. Instrum. Methods A (2004), in press.

[KIR05] M. Kirm, Y.Chen, S. Neicheva, K. Shimamura, N. Shiran, M. True, S. Vielhauer. *VUV spectroscopy of Eu doped $LiCaAlF_6$ and $LiSrAlF_6$ crystals.* Phys. Stat. Sol. (c), in press.

[KLI99] D. Klimm, P. Reiche. Cryst. Res. Technol. **34** (1999) 145.

[KOD01] N. Kodama, T. Hoshino, M. Yamaga, N. Ishizawa, K. Shimamura, T. Fukuda. *Optical and Structural Studies on $BaMgF_4$:Ce^{3+} Crystals.* J. Cryst. Growth **229** (2001) 492.

[KOE71] M. Koedam, J.J. Opstelten. Light. Res. Technol. **3** (1971) 205.

[KOE97] S. Körding. *Lumineszenzspektroskopische Untersuchung der Erzeugung und Relaxation elektronischer Ein- und Mehrfachanregungen in Festem Xenon.* Diploma thesis, Universität Hamburg (1997).

[KOL03] E. van der Kolk, P. Dorenbos, C.W.E. van Eijk, A.P. Vink, M. Weil, J.P. Chaminade. *Luminescence Excitation Study of the higher energy states of Mn^{2+} in $SrAlF_5$, $CaAlF_5$ and $NaMgF_3$.* HASYLAB Annual Report I (2003).

[KOS85] T. Koskentalo, M. Leskelä, L. Niinistö. Mater. Res. Bull. **20** (1985) 265.

[KRA30] H. A. Kramers. Koniki. Ned. Akad. Wetenschap. Proc. **B 33** (1930) 959. Proc. Acad. Sci. Amsterdam **2** (1930) 432.

[KRO03] P. van der Krogt. *Elementymology & Elements Multidict.* Universiteit Utrecht, Netherlands (2003).
http://elements.vanderkrogt.net

[KRU66] W.F. Krupke. Phys. Rev. **145** (1966) 325.

[KRU97] J.C. Krupa, M. Queffelec. *UV and VUV optical excitations in wide band gap materials doped with rare earth ions: $4f - 5d$ transitions.* J. Alloys Comp. **250** (1997) 287.

[KUE97] S. Kück, K. L. Schepler, B. H. T. Chai. J. Opt. Soc. Am. **B 14** (1997) 957.

[KUE01] S. Kück. *Laser-related spectroscopy of ion-doped crystals for tunable solid-state lasers.* Appl. Phys. **B 72** (2001) 515-562.

[KUE02] S. Kück, I. Sokólska, M. Henke, M. Döring, T. Scheffler. *Investigation of the quantum cutting processes in Pr^{3+}-doped fluoride crystals.* HASYLAB Annual Report I (2002).

[KUE03] S. Kück, I. Sokólska, M. Henke, M. Döring, T. Scheffler. *Photon cascade emission in Pr^{3+}-doped fluorides.* J. Lumin. **102-103** (2003) 176.

[KUE04] S. Kück. PTB, Braunschweig, Germany. *Private communication.*

[KUS69] T. Kushida. *Linewidths and Thermal Shifts of Spectral Lines in Neodymium-Doped Yttrium Aluminum Garnet and Calcium Fluorophosphate.* Phys. Rev. **185** (1969) 500.

[KUW65] Goro Kuwabara, Kiyoshi Aoyagi. *Ultraviolet absorption of transition metal ions in alkali halides.* Japan. J. Appl. Phys. , Suppl. **4**(1) (1965), Vol. Date (1964) 627-30.

[LAN65] D. Langer, S. Ibuki. *Zero-Phonon Lines and Phonon Coupling in ZnS:Mn.* Phys. Rev. **138** (1965) A809.

[LAN04] R.J. Lancaster. University of the West Indies, Kingston, Jamaica (2004). http://wwwchem.uwimona.edu.jm/courses/Tanabe-Sugano/TSspread.html

[LEV50] H.W. Leverenz. *An Introduction to Luminescence of Solids.* John Wiley&Sons, New York (1950).

[LEV84] A.B.P. Lever. *Inorganic Electronic Spectroscopy.* Elsevier, New York (1984).

[LEW94] A.C. Lewandowski, T.M. Wilson. *Ab Initio Multiconfiguration Self-Consistent-Field Calculations of the Excited States of a Mn Impurity in CaF_2.* Phys. Rev. **B 50** (1994) 2780.

[LI93] Cheng Li, R. Moncorgé, J.C. Souriau, Ch. Wyon. *Efficient 2.05 μm room temperature Y_2SiO_5:Tm^{3+} cw laser.* Opt. Comm. **101** (1993) 356.

[LI00] Cheng Li, Deyuan Shen, Jie Song, Nam Seong Kim, Ken-ichi Ueda. *Flash-lamp pumped high-power Cr-Tm:YAG and Cr-Tm-Ho:YAG lasers operating at 2-μm wavelength.* Proc. SPIE **3889** (2000) 274.

[LIC03] H. Lichtenberg. *Quantum cutting in $LiKGdF_5$:Er^{3+},Dy^{3+}.* Diploma thesis, Universität Hamburg, Germany (2003).

[LIE02a] L. van Pieterson, M. F. Reid, R. T. Wegh, S. Soverna, A. Meijerink. *$4f^n \rightarrow 4f^{n-1}5d$ transitions of the light lanthanides: Experiment and theory.* Phys. Rev. **B 65** (2002) 045 113.

[LIE02b] L. van Pieterson, M. F. Reid, G. W. Burdick, A. Meijerink. *$4f^n \rightarrow 4f^{n-1}5d$ transitions of the heavy lanthanides: Experiment and theory.* Phys. Rev. **B 65** (2002) 045 114.

[LOH66] E. Loh. *Lowest $4f \rightarrow 5d$ Transition of Trivalent Rare-Earth Ions in CaF_2 Crystals.* Phys. Rev. **147** (1966) 332.

[LUP93] A. Lupei, C. Tiseanu, V. Lupei. *Correlation between spectra and strctural data of YAG:Tm^{3+} and YAG:Tm^{3+}.* Phys. Rev. **B 47** (1993) 14 084.

[LUS70] N.E. Lushchik, Kh. A. Soovik. *Spectroscopy of Crystals.* Nauka, Moscow (1970) 258 *(in Russian).*

[MAK00] V.N. Makhov, N.M. Khaidukov, N.Yu. Kirikova, M. Kirm, J.C. Krupa, T.V. Ouvarova, G. Zimmerer. *VUV emission of rare earth ions doped into fluoride crystals.* J. Lumin. **87-89** (2000) 1005.

[MAK02] V.N. Makhov, N.Yu. Kirikova, N.M. Khaidukov, M. Kirm, E. Negodin, G. Zimmerer, S.K. Lam, D. Lo, J.C. Krupa, J.Y. Gesland. *VUV Spectroscopy of Crystalline Emitters Based on 5d-4f Transitions in Rare Earth Ions.* Surface Rev. Lett. **9** (2002) 621.

[MAO91] O. Maoz, S.R. Rotman, A.M. Weiss, R. Reisfeld, M. Eyal. *Anomalously Fast Energy Transfer between Manganese and Thulium in Fluoride Glasses.* J. Lumin. **48 & 49** (1991) 213.

[MAR94a] M. C. Marco de Lucas, F. Rodríguez, M. Moreno. *Zero-phonon transitions and the Stokes' shift of Mn^{2+}-doped perovskites: Dependence on the metal-ligand distance.* Phys. Rev. **B 50** (1994) 2760.

[MAR94b] C.D. Marshall, J.A. Speth, S.A. Payne, W.F. Krupke, G.J. Quarles, V. Castillo, B.H.T. Chai. J. Opt. Soc. Am. **B 11** (1994) 2054.

[MAS03] N.J.M. Le Masson, A.P. Vink, P. Dorenbos, A.J.J. Bos, C.W.E. VanEijk, J.P. Chaminade. *Ce^{3+} and Pr^{3+} 5d-energy levels in the (pseudo) perovskites $KMgF_3$ and $NaMgF_3$.* J. Lumin. **101** (2003) 175.

[MAZ99] Z. Mazurak, A. Ratuszna, Ph. Daniel. *Optical Properties of Mn^{2+} in $KCaF_3$ Single Crystals.* Spectr. Acta **A 55** (1999) 375.

[MEI93] A. Meijerink. *Spectroscopy and vibronic transitions of divalent europium in $LiBaF_3$.* J. Lumin. **55** (1993) 125.

[MOE85] T. Möller, T. Kloiber, G. Zimmerer. *Der neue 1-m-Monochromator zur Lumineszenzanalyse ist in Betrieb.* HASYLAB Annual Report (1985).

[MOS94] W.W. Moses, S.E. Derenzo, M.J. Weber, A.K. Ray Chaudhuri, F. Cerrina. *Scintillation Mechanisms in Cerium Fluoride.* J. Lumin. **59** (1994) 89.

[MOS01] A.S. Moskvin. *One-center charge transfer transitions in manganites.* arXiv:cond-mat/0111198 (2001)

[MUR84] L.A. Muradyan, V.E. Zavodnik, I.P. Makarova, K.S. Aleksandrov, V.I. Simonov. *Thermal vibrations of atoms in the structure of $KMgF_3$ at 293 and 123 K.* Kristallografiya **29** (1984) 392.

[NAK78] E. Nakazawa. Chem. Phys. Lett. **56** (1978) 161.

[NAK79] E. Nakazawa. *Charge transfer type luminescence of Yb^{3+} ions in RPO_4 and R_2O_2S (R=Y, La, and Lu).* J. Lumin. **18-19** (1979) 272.

[NEG03] E. Negodine. *Inter- and Intraconfigurational Luminescence of $LiYF_4$:Er^{3+} under Selective VUV Excitation.* Dissertation, Universität Hamburg, Germany (2003).

[NGU89] D.C. Nguyen, G.E. Faulkner, M. Dulick. *Blue-green (450-nm) upconversion Tm^{3+}:YLF laser.* Appl. Opt. **28** (1989) 3553.

[NIC73] B.D. McNicol, G.T. Pott. J. Lumin. **6** (1973) 320.

[NIN03] L. Ning, P.A. Tanner, X. Shangda. *Unit cell group analysis of rare earth elpasolites.* Vibrational Spectroscopy **31** (2003) 51.

[NIS99] B. Nissen, T. Luxbacher, W. Strek, C.D. Flint. *Luminescence and electronic absorption spectra of $Rb_2NaY_{0.95}Tm_{0.05}F_6$. Chem.* Phys. Lett. **303** (1999) 235.

[NIST] NIST Atomic Spectra Database. http://www.nist.gov/srd/

[NOG97] M. A. Noginov, M. Curley, P. Venkateswarlu, A. Williams, H. P. Jenssen. *Excitation scheme for the upper energy levels in a Tm:Yb:BaY_2F_8 laser crystal.* J. Opt. Soc. Am. **B 14** (1997) 2126.

[OFE62] G.S. Ofelt. *Intensities of crystal spectra of rare-earth ions.* J. Chem. Phys. **37** (1962) 511.

[OKA94] F. Okada, S. Togawa, K. Ohta. J. Appl. Phys. **75** (1994) 49.

[ORG95] L.E. Orgel. J. Chem. Phys. **23** (1995) 1004.

[ORR02] G.J. Orris, R.I. Grauch. *Rare Earth Element Mines, Deposits, and Occurrences: U.S. Geological Survey Open-File Report 02-189*, U.S. Geological Survey, Tucson, USA (2002). http://geopubs.wr.usgs.gov/open-file/of02-189

[OSI01] E. Osiac, I. Sokólska, S. Kück. *Upconversion-induced blue, green and red emission in* Ho^{3+}*:*BaY_2F_8. J. Alloys Comp. **283** (2001) 323.

[OSI03a] E. Osiac, E. Heumann, S. Kück, G. Huber, E. Sani, A. Toncelli, M. Tonelli. *Orange and red upconversion laser pumped by an avalanche mechanism in* Pr^{3+}, Yb^{3+}*:*BaY_2F_8. App. Phys. Lett. **82** (2003) 3832.

[OSI03b] E. Osiac, S. Kück, E. Heumann, G. Huber, E. Sani, A. Toncelli, M. Tonelli. *Spectroscopic investigation of the upconversion avalanche mechanism in* Pr^{3+}, Yb^{3+}*:*BaY_2F_8. Opt. Mat. **24** (2003) 537.

[PAL70] D.T. Palumbo, Jr. J.J. Brown. J. Electrochem. Soc. **117** (1970) 1184.

[PAL71] D.T. Palumbo, Jr. J.J. Brown. J. Electrochem. Soc. **118** (1971) 1159.

[PAP76] R. Pappalardo. J. Lumin. **14** (1976) 159.

[PAY89] A. Payne, L.L. Chase, G.D. Wilke. *Optical Spectroscopy of the New Laser Materials,* $LiSrAlF_6 : Cr^{3+}$ *and* $LiCaAlF_6 : Cr^{3+}$. J. Lumin. **44** (1989) 167.

[PIE00] L. van Pieterson, M. Heeroma, E. de Heer, A. Meijerink. *Charge Transfer Luminescence of* Yb^{3+}. J. Lumin. **91** (2000) 177.

[PIN94] J.F. Pinto, L. Esterowitz, G.H. Rosenblatt. Tm^{3+} *:YLF laser continuously tunable between 2.20 and 2.46 Mum.* Opt. Lett. **19** (1994) 883.

[PIP74] W.W. Piper, J.A. DeLuca, F.S. Ham, J. Lumin. **8** (1974) 344.

[POL87] S.A. Pollack, D.B. Chang, I. Fu Shih, R. Tseng. Appl. Opt. **26** (1987) 4400.

[POL96] M. Pollnau, W. Lüthy, H. P. Weber, K. Krämer, H. U. Güdel, R. A. McFarlane. *Excited-State Absorption in Er:*BaY_2F_8*, and* $Cs_3Er_2Br_9$ *and Comparison to Er:*$LiYF_4$. Appl. Phys. **B 62** (1996) 339.

[POO97] S.H.M. Poort, A. Meijerink, G. Blasse. *On the Luminescence of* GdF_3*:*Ce^{3+}, Mn^{2+}. Solid State Comm. **103** (1997) 537.

[POT72] G.T. Pott, B.D. McNicol. *Zero-Phonon Transition and Fine Structure in the Phosphorescence of* Fe^{3+} *Ions in Ordered and Disordered* $LiAl_5O_8$. J. Chem. Phys. **11** (1972) 5246.

[QUA90] J. Quarles, A. Rosenbaum, C. L. Marquardt, L. Esterowitz. *Flash-lamp pumped, efficient room temperature Cr,Tm:YAG laser operation at 2.01 mm wavelength.* Opt. Lett. **15** (1990) 42.

[RAY63] D.K. Ray. *Investigation into the Origin of the Crystalline Electric Field Effects on Rare Earth Ions: II. Contributions from the Rare Earth Orbitals.* Proc. Phys. Soc. **82** (1963) 47.

[REI00] M.F. Reid, L. van Pieterson, R. T. Wegh, A. Meijerink. *Spectroscopy and calculations for* $4f^n \rightarrow 4f^{n-1}5d$ *transitions of lanthanide ions in* $LiYF_4$*.* Phys. Rev. **B 62** (2000) 14744.

[REI03] M.F. Reid. University of Adelaide, New Zealand. *Private communication.*

[RHO85] Joanne F. Rhodes, R.J. Abbundi, D. Wayne Cooke, V.K. Mathur, M.D. Brown. *Temperature dependence of fluorescence spectra from x-ray-excited single-crystal* $CaF_2 : Mn(x)$ *(*$x = 0.1$, 1.0, 3.0 *at. %).* Phys. Rev. **B 31** (1985) 5393.

[ROD91] F. Rodríguez, H. Riesen, H.U. Güdel. J. Lumin. **50** (1991) 101.

[ROI84] E. Roick. *Relaxationsprozesse in festen Edelgasen untersucht mit energie- und zeitaufgelöster Lumineszenzspektroskopie.* Dissertation, Universität Hamburg (1984).

[RON02] C. Ronda. *Luminescent materials with quantum efficiency larger than 1, status and prospects.* J. Lumin. **100** (2002) 301.

[ROT96] S.R. Rotman, E. Luria, N. Yitzhaki, A. Eyal. *Practical models for energy transfer between ions in solids.* Opt. Mat. **5** (1996) 1-33.

[RUB91] J. Rubio O. *Doubly-Valent Rare-Earth Ions in Halide Crystals.* J. Phys. Chem. Solids **52** (1991) 101.

[SAB75] J.F. Sabatini, A.E. Salwin, D.S. McClure. *High-Energy Optical-Absorption Bands of Transition-Metal Ions in Fluoride Host Crystals.* Phys. Rev. **B 11** (1975) 3832.

[SAI92] H. Saito, S. Chaddha, R.S.F. Chang, N. Djeu. *Efficient 1.94-*μm Tm^{3+} *laser in* YVO_4 *host.* Opt. Lett. **17** (1992) 189.

[SAL97] S. Salaun, M.T. Fornoni, A. Bulou, M. Rousseau, P. Simon, J.Y. Gesland. J. Phys.: Condens. Matter **9** (1997) 6941.

[SAT02a] H. Sato, K. Shimamura, A. Bensalah, N. Solovieva, A. Beitlerova, A. Vedda, M. Martini, H. Machida, T. Fukuda, M. Nikl. *Induced Absorption Phenomena, Thermoluminescence and Colour Centres in* $KMgF_3$*,* $BaLiF_3$ *and* $LiCaAlF_6$ *Complex Fluorides.* Jpn. J. Appl. Phys. **41** (2002) 2028.

[SAT02b] H. Sato, H. Machida, K.Shimamura, A. Bensalah, T. Satonaga, T. Fukuda, E. Mihokova, M. Dusek, M. Nikl, A. Vedda. *Color centers in* $LiCaAlF_6$ *single crystals and their suppression by doping.* J. Appl. Phys. **91** (2002) 5666.

[SCH91] K.I. Schaffers, D.A. Keszler. Acta Cryst. **C 47** (1991) 18.

[SER97] J. Ramírez-Serrano, E. Madrigal, F. Ramos, U.Caldiño Garcia. *Optical Spectroscopy of Mn^{2+} Ions in $CdCl_2$ Crystals.* J. Lumin. **71** (1997) 169.

[SHA69] R.D. Shannon, C.T. Prewitt. *Effective Ionic Radii in Oxides and Fluorides.* Acta Cryst. **B 25** (1969) 925.

[SHA70] R.D. Shannon, C.T. Prewitt. Acta Cryst. **B 26** (1970) 1046.

[SHA76] R.D. Shannon. *Revised Effective Ionic Radii and Ssystematic Studies of Interatomic Distances in Halides and Chalcogenides.* Acta Cryst. **A 32** (1976) 751.

[SHE84] D.M. Sherman. Am. Mineral. **69** (1984) 788.

[SHE96] R. Scheps. *Upconversion laser processes.* Progr. Quantum Electr. **20** (1996) 271-358.

[SHI82] M.D. Shinn, J.C. Windschleif, D.K. Sardar, W.A. Sibley. *Optical transitions of Er^{3+} ions in $RbMgF_3$ and $RbMgF_3$:Mn.* Phys. Rev. **B 26** (1982) 2371.

[SHI84] M.D. Shinn, W.A. Sibley. *Eu^{2+}-Sensitized Mn^{2+} Luminescence in $RbMgF_3$: Eu, Mn.* Phys. Rev. **B 29** (1984) 3834.

[SHI96] C. Shi, J. Deng, X. Lu, J. Becker, G. Zimmerer, G. Hu, L. Xu, Z. Ying. *Electronic states of CeF_3 in UV and VUV region.* Chinese J. Lumin. **17**, Suppl. (1996) 66.

[SHI99] S. Shionoya, W.M. Yen, et al. *Phosphor Handbook.* Phosphor Research Society. Boca Raton, FL, CRC Press (1999).

[SHI00] K. Shimamura, S.L. Baldochi, N. Mujilatu, K. Nakano, Z. Liu, H. Othake, N. Sarukura, T. Fukuda. *Growth of Ce-doped $LiCaAlF_6$ and $LiSrAlF_6$ single crystals by the Czochralski technique under CF_4 atmosphere.* J. Cryst. Growth **211** (2000) 302.

[SHI01a] K. Shimamura, S.L. Baldochi, I.M. Ranieri, H. Sato, T. Fujita, V.L. Mazzocchi, C.B.R. Parente, C.O. Paiva-Santos, C.V. Santilli, N. Sarukura, T. Fukuda. *Crystal growth of Ce-doped and undoped $LiCaAlF_6$ by the Czochralski technique under CF_4 atmosphere.* J. Cryst. Growth **223** (2001) 383.

[SHI01b] K. Shimamura, H. Sato, A. Bensalah, V. Sudesh, H. Machida, N. Sarukura, T. Fukuda. *Crystal Growth of Fluorides for Optical Applications.* Cryst. Res. Technol. **36** (2001) 801.

[SIB73] W.A. Sibley, S.I. Yun, W.E. Vehse. *Colour Centre Luminescence in $KMgF_3$: Mn crystals.* J. Phys. C: Solid State Phys. **6** (1973) 1105.

[SIM77] J. Simonetti, D. McClure. *The $3d \rightarrow 4p$ transitions of Cu^+ in LiCl and of transition-metal ions in crystals.* Phys. Rev. **B 16** (1977) 3887.

[SIU88] G.G. Siu. *Contributions to the ground-state splitting of S-stae ions: II. A theoretical framework for the $3d^5$ ^6S ground-state splitting of Mn^{2+}.* J. Phys. C: Solid State Phys. **21** (1998) 3927.

[SOH99] K. Sohn, B. Cho, H.D. Park. *Excitation Energy-Dependent Photoluminescence Behavior in Zn_2SiO_4 : Mn Phosphors.* Mat. Let. **41** (1999) 303.

[SOM74] J.L. Sommerdijk, A. Bril, A.W. de Jager. *Two photon luminescence with ultraviolet excitation of trivalent praseodymium.* J. Lumin. **8** (1974) 341.

[STE66] R.M. Sternheimer. *Shielding and Antishielding Effects for Various Ions and Atomic Systems.* Phys. Rev. **146** (1966) 140.

[STO74] W.H.J. Stork, G.T. Pott. J. Phys. Chem. **78** (1974) 2496.

[STO90] R.C. Stoneman, L. Esterowitz. *Efficient, broadly tunable, laser-pumped Tm:YAG and Tm:YSGG cw laser.* Opt. Lett. **15** (1990) 486.

[STR75] C.W. Struck, W.H. Fonger. *Unified Model of the Temperature Quenching of Narrow-Line and Broad-Band Emissions.* J. Lumin. **10** (1975) 1.

[STU67] M.D. Sturge. Solid State Phys. **20** (1967) 91.

[SUL02] E. Suljoti. *Electronic relaxation of Er^{3+} $5d$ excitations in different fluoride matrices.* Diploma thesis, Universität Hamburg, Germany (2002).

[SUZ87] Y. Suzuki, W.A. Sibley, O.H.El. Bayoumi, T.M. Roberts, B. Bendow. *Optical properties of transition-metal ions in zirconium-based metal fluoride glasses and MgF_2 crystals.* Phys. Rev. **B 35** (1987) 4472.

[SVE93] E.B. Svesnikova, A.A. Stroganov, N.T. Timofeev. Opt. Spektrosk. **64** (1993) 43.

[SZC85] T. Szczurek, M. Schlesinger. *Proceedings of the International Symposium on Rare Earth Spectroscopy, edited by B. Jezowska-Trebiatowska, J. Legendziewicz, W. Strek.* World Scientific, Singapore (1985) 309.

[TAN54a] Y. Tanabe, S. Sugano. J. Phys. Soc. Jpn. **9** (1954) 753.

[TAN54b] Y. Tanabe, S. Sugano. J. Phys. Soc. Jpn. **9** (1954) 766.

[THO71] W.A. Thornton. J. Opt. Soc. Am. **61** (1971) 1155.

[THR94] R. J. Thrash, L. F. Johnson. *Upconversion laser emission from Yb3+-sensitized Tm^{3+} in BaY_2F_8.* J. Opt. Soc. Am. **B 11** (1994) 881.

[TIP70] H.H. Tippins. *Charge-Transfer Spectra of Transition-Metal Ions is Corundum.* Phys. Rev. **B 1** (1970) 126.

[TIS95] C. Tiseanu, A. Lupei, V. Lupei. *Energy levels of Tm^{3+} in ytttrium aluminum garnet.* J. Phys.: Cond. Mat. **7** (1995) 8477.

[THO01] J.R.G. Thorne, Q. Zeng, R.G. Denning. *Evidence for a spin-correlated crystal field two-photon spectroscopy of thulium III in the elpasolite Cs_2NaYCl_6:Tm^{3+}.* J. Phys.: Condens. Matter **13** (2001) 7403.

[TRU04a] M. True, M. Kirm, E. Negodine, S. Vielhauer, G. Zimmerer. *VUV Spectroscopy of Tm^{3+} and Mn^{2+} Doped $LiSrAlF_6$.* J. Alloys Comp. **374** (2004) 36.

[TRU04b] M. True, M. Kirm, Y. Chen, S. Vielhauer, G. Zimmerer. *VUV spectroscopy of pure and Tm^{3+} doped $LiCaAlF_6$ crystals.* To be published.

[VER74] J.M.P.J. Verstegen, D. Radielovic, L.E. Vrenken. J. Electrochem. Soc. **121** (1974) 1627.

[VID79] G. Vidal-Valat, J.P. Vidal, C.M.E. Zeyen, K. Kurki-Suonio. *Neutron diffraction study of magnesium fluoride single crystals.* Acta Cryst. **B 35** (1979) 1584.

[VIE03] S. Vielhauer. *Innerschalenanregungen und sekundäre Exzitonen in Edelgasfestkörpern.* Dissertation, Universität Hamburg, Germany (2003).

[VIN00] A.P. Vink. *Electron-phonon coupling and pair interactions of transition metal ions.* Dissertation, Universiteit Utrecht, Netherlands (2000).

[VIN01] A.P. Vink, M.A. de Bruin, S. Roke, P.S. Peijzel, A. Meijerink. *Luminescence of Exchange Coupled Pairs of Transition Metal Ions.* J. Electrochem. Soc. **E 148** (2001) 313.

[VUG73] N. van Vugt, T. Wigmans, G. Blasse. J. Inorg. Nucl. Chem. **35** (1973) 2602.

[WEG99a] R.T. Wegh. *Vacuum ultraviolet spectroscopy and quantum cutting for trivalent lanthanides.* Dissertation, Universiteit Utrecht, Netherlands (1999).

[WEG99b] R.T. Wegh, H. Donker, K.D. Oskam, A. Meijerink. *Visible Quantum Cutting in $LiGdF_4$:Eu^{3+} through Downconversion.* Science **283** (1999) 663.

[WIL51] F.E. Williams, M.H. Hebb. *Theoretical Spectra of Luminescent Solids.* Phys. Rev. **84** (1951) 1181.

[WIL83] H. Wilcke, W. Böhmer, R. Haensel, N. Schwertner. Nucl. Instr. Methods **208** (1983) 59.

[WIL88] K.T. Wilke. *Kristallzüchtung.* Harri Deutsch, Thun, Frankfurt/Main (1988).

[WIN04] M. J. Winter. *WebElements^{TM}.* University of Sheffield and WebElements Ltd., U.K. (1993-2004). http://www.webelements.com

[WOO91] B. W. Woods. J. Opt. Soc. Am. **B 8** (1991) 970.

[YAM00] M. Yamaga, T. Imai, N. Kodama. *Optical Properties of Two Ce^{3+}-Site Centers in $BaMgF_4$:Ce^{3+} Crystals.* J. Lumin. **87-89** (2000) 992.

[YAM99] H. Yamamoto. *Phosphor handbook: Fundamentals of luminescence.* CRC Press LLC, Boca Raton (1999).

[YAN76] K.H. Yang, J.A. DeLuca. *VUV fluorescence of Nd^{3+}-, Er^{3+}-, and Tm^{3+}-doped trifluorides and tunable coherent sources from 1650 to 2600 Å.* Appl. Phys. Lett. **29** (1976) 499.

[YAN78] K.H. Yang, J.A. DeLuca. *Vacuum-ultraviolet excitation studies of $5d^1f^{n-1}$ to $4f^n$ and $4f^n$ to $4f^n$ transitions of Nd^{3+}-, Er^{3+}-, and Tm^{3+}-doped trifluorides.* Phys. Rev. **B 17** (1978) 4246.

[YAO98] G. Q. Yao, J. H. Lin, L. Zhang, G. X. Lu, M. L. Gong, M. Z. Su. *Luminescent properties of $BaMg_2Si_2O_7$:Mn^{2+}, Eu^{2+}.* J. Mater. Chem. **8** (1998) 585.

[YEN64] W.M. Yen, W.C. Scott, A.L. Schawlow. *Phonon-Induced Relaxation in Excited Optical States of Trivalent Praseodymium in LaF_3.* Phys. Rev. 136 (1964) A271.

[ZAC98] M. Zachau, F. Zwaschka, F. Kummer. *Proceedings of the Sixth International Conference on Luminescent Materials, edited by C. R. Ronda, T. Welker.* Electrochem. Soc. (1998) 314.

[ZIM91] G. Zimmerer. *Status report on luminescence investigations with synchrotron radiation at HASYLAB.* Nucl. Instrum. Methods Phys. Res. **A 308** (1991) 178.

Acknowledgments

This work has been carried out during the years 2001 to 2004 at the *Institut für Experimentalphysik, Universität Hamburg*, affiliated to HASYLAB at DESY.

I would like to express my sincere thanks to Prof. Dr. G. Zimmerer for the great opportunity and latitude to carry out the present work in its full extent, including rewarding advice on the interpretation of the spectra. In particular, I appreciated the collaboration and fruitful discussions with Dr. Marco Kirm now at the *Institute of Physics, University of Tartu, Estonia*. Many thanks to my co-workers Dr. Sebastian Vielhauer and Dr. Evgueni Negodine as well as our recent diploma students Edlira Suljoti and Henning Lichtenberg.

I am much obliged to Prof. Dr. G. Huber for the close collaboration of the *Institut für Laserphysik, Universität Hamburg*, with special thanks to Dr. Markus Henke and Dr. Sebastian Bär for the continuous assistance during crystal growth and supplementary measurements. The initial suggestion of the crystal host and discussion of spectroscopic results with Dr. Stefan Kück are greatly acknowledged.

I am indebted to Prof. Dr. A. Meijerink for the kind permission and support to use the excimer laser setup at the *Debye Institut, Universiteit Utrecht*, *Netherlands*, and to Peter Vergeer for the assistance during the measurements. Many thanks to Prof. Dr. A. Meijerink and Prof. Dr. V. Makhov from the *Lebedev Institut*, *Moscow*, *Russia*, for the discussion of the high resolution spectra.

The microprobe trace analysis of many crystals carried out by Mrs. B. Cornelisen of the *Mineralogisch-petrographisches Institut* of the *Universität Hamburg* and the X-ray diffractometry provided by Dr. Daniel Schiffbauer of the *Universität zu Köln* are acknowledged.

For support and advice concerning the design of the thesis and much more I express my special thanks to Tuyet-Trinh *Jenn* Tran.

This work was partly supported by the BMBF collaboration project “VUV-Leuchtstoffe für Hg-freie Entladungslampen”, grant no. 03N8019D.